UPC CTTC

Numerical modeling of complex heat transfer phenomena in cooling applications

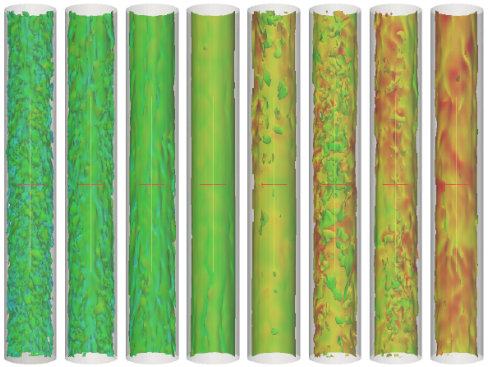

Centre Tecnològic de Transferència de Calor
Departament de Màquines i Motors Tèrmics
Universitat Politècnica de Catalunya
Xiaofei Hou
Doctoral Thesis

Numerical modeling of complex heat transfer phenomena in cooling applications

Xiaofei Hou

TESI DOCTORAL

presentada al

Departament de Màquines i Motors Tèrmics
E.T.S.E.I.A.T.
Universitat Politècnica de Catalunya

per a l'obtenció del grau de

Doctor per la Universitat Politècnica de Catalunya

Terrassa, May 2015

Numerical modeling of complex heat transfer phenomena in cooling applications

Xiaofei Hou

Directors de la Tesi

Dr. Carles Oliet Casasayas

Dr. Oriol Lehmkuhl Barba

Dr. Joaquim Rigola Serrano

Tutor de la tesi

Dr. Assensi Oliva Llena

Tribunal Qualificador

Dr. José Fernández Seara
Universidad de Vigo

Dr. Jesús Castro González
Universitat Politècnica de Catalunya

Dr. Maria Manuela Prieto González
Escuela Politécnica de Ingeniería de Gijón

This thesis is dedicated to
my parents, YunXi and YanLin,
my wife, Maggie Chen

When I am down and, oh, my soul, so weary; When troubles come and my heart burdened be; Then I am still and wait here in the silence, Until you come and sit awhile with me.

There is no life - no life without its hunger; Each restless heart beats so imperfectly; But when you come and I am filled with wonder, Sometimes, I think I glimpse eternity.

You raise me up, so I can stand on mountains; You raise me up to walk on stormy seas; I am strong when I am on your shoulders; You raise me up to more than I can be.

You rise me up - Westlife

Acknowledgements

Looking back to the whole Ph.D period from 2008 till now, I have been completely reshaped. If there is a parable to describe my life staying in CTTC, I would like to say “It is a Metamorphosis from a seed in debris to a small tree of vigour”.

I must express my deepest appreciation to my academic supervisor, Prof. Joaquim Rigola. It is him who picked me up-a seed in debris and gave me an opportunity to enter the numerical world. During these years, he gave me countless help, guidance, support and understanding. Most important, I could not have completed the study without his encouragement. In my memory, he always says ”good work”, ”well done” even when my work does not go smoothly. For my first publication, he spent much time and energy helping me improve it. Without his guidance, there would have been no publication.

I wish to appreciate Prof. Assensi Oliva, head of CTTC, for his support in finance. Without his assistance, it would have been impossible for me to carry out the present work. I got a lot of help in dealing with the daily life throughout my studying abroad. He directed me in many aspects as one of the elders and seniors. He really is a kind and friendly person.

I am very grateful to Oriol Lehmkuhl, one of my advisors, for his many significant guidance in the numerical work, especially in turbulent simulation and Termofluids software. He broadened my view in the field of science. I was deeply impressed by his good knowledge of fluid mechanics and he set a good example for my studying in the future.

I am also pleased to thank Carles Oliet for his patient help and guidance during all the simulation cases. Seating next to me, our discussions are more like between friends, instead of between student and advisor. Without his careful and patient checking of the content and language of my thesis, the present thesis would have never ended to this point.

There are several people who have either directly or indirectly made this work possible. Special thanks to Jordi Chiva for his teaching and assistance in C++. It is him that helped me improve my ability to write code from zero to the present level. Whenever I encountered problems, he never hesitated to give me a hand. He is always willing to help others and explain anything with enough patience. Meanwhile during the whole work, Jordi Muela and Jordi Ventosa also provided me with their numerical code, which gave me good tools to speed up my work and reduced many unnecessary by-pass.

There are also several people in the CTTC community that I would like to thank. First, my colleagues Lluís Jofre and Joan Farnós who illustrated the catalan culture to me and lead me into the local life. They let me recognize the life style of occidental

Ph.D students. They also provided many guidance in life and study to me. Also thanks to Alex, Aleix and Roser. They showed me many strange things-calçot, hiking and the typical catalan cottage.

Thanks to Santiago, Willy, Federico and Pedro for their company. With them, my life in Terrassa became more colorful and enriched, and my Spanish language reached to a daily communication level. Their optimistic, cheerful characters brought me many happiness.

My good Chinese colleague Hao Zhang gave me many encouragements and good advices. Without him, the thesis would have been surely delayed six months. During the frequent communication, he brought me the latest domestic news and situations on our academic fields. Thanks to his company during our stay in CTTC.

I am grateful to my beloved wife, Maggie Chen whose constant encouragement, patience, love, and care has made it possible for me to carry out the present work. She frequently flew here to meet me with great effort, it was my greatest pleasure to meet you. I also feel appreciated to her Boss -Mr. Timmermans, my Profs. Assensi, Joaquim, Oriol and Carles for their understanding and support. With their permission, we could meet once each two months and keep our relation alive.

Finally, I would like to thank my parents, who have brought me up and taught me many principles even though they do not have a high level of education. To my brothers, who take care of my parents in my absence. To my uncles, who pour much attention to my studies through primary and middle school. Thank you for always being there.

I am also very much in debt to many excellent colleagues whom I am fortunate to meet and cannot list here. They all gave me a lot of assistance both in work and life. They are both mentors and friends. During the six years far from home, I have felt so much enthusiasm and numerous fun from my colleagues in CTTC. They are all valuable experience in my life.

CTTC is my other home and I will never forget it.

Contents

Abstract

Multiphase and multicomponent flows are frequently encountered in the cooling applications due to combined heat transfer and phase change phenomena. Two-fluid and homogeneous mixture models are chosen to numerically study these flows in the cooling phenomena. Therefore this work is divided in two main parts. In the first part, a two-fluid model algorithm for free surface flows is presented. The two fluid model is usually used as a tool to simulate dispersed flow. With its extension, it may also be applied to large interface (separated) flow, considering liquid and gas phases in a same control volume. In the second part, the homogeneous mixture model for the multicomponent flow is employed to solve evaporation problems. Finally the simulation is focused on the mixed transitional or turbulent flow with and without evaporation. The long-term objective is to couple the two models, which can solve all the flow regimes and application to industrial problems.

In detail, this thesis consists of six chapters. The first chapter is devoted to an introduction to the two-fluid and homogeneous mixture models employed in the multiphase/multicomponent flow. The multiphase classification is explained and the previous works on the two models are reviewed.

The second chapter is mainly focused on the application of the Fractional step method algorithm in the two-fluid model. In addition, the Conservative Level Set method(interface sharpening) is applied to overcome the weakness of the two-fluid model (numerical diffusion of the interface), which is often encountered in the simulations using this model. With the proposed algorithm, the two-fluid model suitable for the dispersed flow is extended to the separated flow.

The homogeneous mixture model is introduced in the third chapter. As an application of this model, different evaporation cases have been tested. A hydrodynamically fully developed laminar flow in a horizontal duct is firstly studied. It is used to verify the model in a laminar flow considering constant physical properties. Water falling films are often applied to enhance the heat transfer. Therefore the second case analyzes the natural convection in a cavity with liquid film (assuming variable physical properties), and validates the falling film model. Finally, a third case is focused on mixed convective flow interacting with a water falling liquid film. The effects of heat flux on the evaporation rate and the flow structure are investigated employing numerical experiments.

In the fourth chapter, the laminarization phenomena of turbulent forced flow in a vertical pipe with constant heat flux is studied. These studies validate the prediction ability of large eddy simulation in this complex situation. Afterwards additional cases in a long vertical pipe (100 times diameters) are conducted and the results are compared with the existing experimental data. Throughout the whole pipe, the flow

state follows a complicated process, which includes turbulent-laminar and laminar-turbulent transitions. This problem is of great significance in industrial applications for it may result in the enhancement or impairment of heat transfer.

Based on the previous verification of the model in turbulent and transitional flow, the simulation of the cooling in a uniformly heated vertical tube is conducted in the fifth chapter with an ascending flow of air and a falling film. This case also involves the transitional complex flow and boundary conditions of falling film with simultaneous heat/mass transfer. The variable factors affecting the evaporation and thermal efficiency have been analyzed.

In Appendix C, as an application in engineering of the work developed within the thesis, a series of flows in a complex geometry of a refrigerator chamber without or with fins are simulated to obtain their effects on the flow distribution and mixing feature.

In the last chapter, the main conclusions are summarized and the future works are listed.

List of Figures

List of Tables

1

Introduction

1.1 Motivation for the thesis

In the many industrial and engineering fields, a certain value of low temperature is required for systems to work correctly. An air flow with pure sensible heat transfer is sometimes not enough to remove the excess heat. In order to improve the heat transfer, the phase change with latent heat transfer is usually introduced for the cooling objective. It includes the multiphase and multicomponent flows. A typical application is the cooling tower in power plant. In the system, the upward mixture flow also is directly reacting with the falling liquid droplet or film and the liquid is cooled due to evaporation. Inside the tube of refrigeration cycle, the flow is at multiphase state while it is multicomponent flow outside the tube consisting of moisture and air. The coolant inside the tube could change into gas or liquid due to heating or cooling. The vapor in the moisture air can be condensed into liquid at the surface of the heat exchanger and the mixture is directly touched with liquid surface. An evaporator or condensor in domestic refrigerator is one of application examples. Other applications includes passive cooling for critical point in nuclear engineering, noise control and optimization in the variable speed air-conditioner. Due to the wide application of phase change heat transfer, our present study focuses on the multiphase and multicomponent flows, especially on mixed transitional/turbulent flow with strong buoyancy force.

Multiphase flow with phase change includes evaporation and boiling [1]. Boiling is the liquid-vapor phase change that occurs at a solid-liquid interface when the surface temperature of the solid exceeds the saturation temperature of the liquid. This process of characterized by the formation of vapor bubbles, which are initiated at the solid surface then grow and detach. Different from the boiling process occurring at a solid-liquid interface, evaporation is a liquid-to-vapor transformation process that occurs across a liquid-vapor interface. The phase change is caused by the concentration difference between components. During the evaporation process, there are no vapor

bubbles formed.

In the cooling phenomenon, a falling liquid film is often employed to enhance the heat transfer. In this situation, the physics can be reduced to a two phase flow with a large scale interface in the whole domain. It also is a multicomponent flow in the core of the tube with air-vapor mixture. Inside the liquid film, the nucleate boiling may happen if wall temperature is over its saturation temperature. Meanwhile the surface evaporation usually exists at the liquid-gas interface due to the concentration difference. If the wall temperature is not high enough to generate the nucleate boiling, there only exists surface evaporation. Moreover if the liquid flow rate is small and its thickness is very thin, its thickness can be neglected and only a simplified boundary condition can used to solve the air-moist multicomponent flow. This case is one focus of the present thesis.

The first part of this thesis focuses on the numerical simulation of the gas-liquid two phase flow. The regimes of two-phase flow can be classified into three major groups according to the rule of Ishii and Hibiki [2]: separated flow (stratified flow), transitional or mixed flow and dispersed flow. In the tube of refrigeration cycle, two-phase flow can be at any regime of the above mentioned flow. Two-fluid model is selected to model the two-phase flow. Two-fluid model is originally suitable for dispersed flow, however it is extended to the stratified flow with Fractional step method. In the present work, it is only limited to momentum interaction, without considering the phase change or nucleate boiling.

In the second part of this work, in order to study the multicomponent flow, the homogeneous mixture model is firstly applied to laminar evaporation flow. Forced convection, natural convection and mixed convection flow has been studied respectively in the evaporation application, and the effects of different parameters on heat transfer has been analyzed. Meanwhile the thermophysical properties are accurately calculated in TermoFluids software. A simplified discontinous model of liquid film has been developed to take into account the thermodynamic characteristics of liquid film.

The multicomponent flow is not limited to laminar regime. In many applications, it is the transitional/turbulent flow. Due to the significant variation of physical property caused by heat and mass transfer, buoyancy force plays an important role and the flow is usually at the mixed convection state. The existence of buoyancy forces can result in laminarization or turbulization in the mixed flow. Moreover it can lead to impairment or enhancement of heat and mass transfer process. It is significant on improvement of heat and mass transfer efficiency, noise control and geometry configuration optimization. Therefore the main attention for multicomponent flow is placed on the mixed transitional/turbulent flow with strong buoyancy force. In order to simulate the transitional/turbulent flow with evaporation phase change, a pure air mixed flow with strong buoyancy force has been implemented to validate the

turbulent model and to study the effects of buoyancy force on flow characteristics using Large-eddy Simulations techniques.

Based on the simplified discontinuous model of liquid film and the validated turbulent model, the evaporation heat transfer of multicomponent flow has been investigated by means of three-dimensional simulations of the turbulent flow. The effect of variable parameters on flow state and evaporation are obtained.

The long-term aim is the coupling of the two methods. It can be used to model the mixed multiphase and multicomponent flow with the nucleate boiling and surface evaporation/condensation, such as annular flow with wall nucleation and steam in the core. The present work makes a fundamental studying of the coupling of these methods for the future, and builds a strong basis for the future coupled model and industrial applications from the developed modes.

1.2 Review on two-fluid model

There are a large number of scientific articles dedicated to the numerical methods for two-phase flow. Depending on the flow state and particular physics, different approaches have been developed to model two-phase flow in the past decades, but none of them is available to all the flow regimes. Models for the two-phase flow may be classified into the following two categories [3]: Interface-capturing methods and interface-tracking methods.

In the interface capturing methods the interface is reconstructed from the properties of suitable field variables [4]. Volume of Fluid (VOF) [5] and Level Set (LS) methods [6] are two very popular techniques of interface-capturing method. Specially speaking, the interface is represented as a discontinuity line in VOF, which is reconstructed from the volume fraction values. The reconstruction of the interface can effectively eliminate the numerical diffusion caused by the continuity equation. The reconstruction approach is important since it may significantly affect the accuracy of the interface shape. There are many reconstruction techniques developed by different researchers [7–9]. In the LS methods, a continuous level set function advected with the velocity is employed to represent the interface. The function is positive in the space occupied by the first fluid and negative in the space of the other fluid. From the function, the interface and its geometric properties are calculated. Its weakness is that they are not conservative in mass. However a conservative level set algorithm recently developed by Olsson and Kreiss [10, 11], can keep the mass conservative.

Within the Heat and Mass Transfer Technological Center (CTTC) research group, a new VOF method on 3-D Cartesian and unstructured meshes was developed by Jofre et al. [3, 12]. In their study, the interface was reconstructed as first- and second-order piecewise planar approximation (PLIC). The volume was advected in a single unsplit Lagrangian-Eulerian geometrical algorithm, based on constructing flux polyhedrons

by tracking back the lagrangian trajectories of the cell-vertex velocities. The situations of overlapping between flux polyhedrons were minimized in his new method. VOF has a robust and accurate polyhedral library for interface capturing while the accurate geometrical properties of interface (curvature) can be obtained by LS method. The two methods were combined in Balcazar's study [13]. In addition, a novel multiple marker level-set method was also introduced to perform the simulation of droplet collision in his work.

In the interface-tracking methods, the interface is always tracked by some techniques as the flow evolves. It can be further decomposed into two groups: (1) Moving mesh methods [14], in which the grid deforms with the interface at each time step. Each individual node of the computational mesh follows the associated particle during motion. (2) Particle-tracking methods, in which the fluid is comprised of a finite number of massless or volumeless particles. The particles are transported in a Lagrangian manner and the interface can be calculated by the distribution of the particles. The well-known techniques of particle-tracking methods includes Smoothed Particles Hydrodynamics (SPH), Marker and Cell(MAC) [15] and Lattice-Boltzmann method (LBM). In these techniques, the fluid is comprised of a finite number of interacting particles. Each of the fluid particles are tracked with a fixed grid or without grid in the implementation and the fluid system is determined by the finite ensemble of particles.

Both interface-capturing and interface-tracking methods have its advantages and disadvantages. Interface-capturing methods can accurately calculate the interface, keep the interface sharp and conserve the mass; the disadvantage of interface capturing method is critical: it is impossible to reconstruct the surface when the chunks of the particular fluid are smaller than the grid cell in a dispersed flow, and the result of the interface-capturing methods loses their physical meaning. Particle-tracking methods can track the fluid with the particles smaller than the grid, it fails to provide the premise interface. To obtain the exact location of the interface is necessary to greatly increase the number of particles with an expensive CPU time cost. In addition, even with particle-tracking methods, it is very difficult to track the particles in Lagrangian way in the dispersed flow since it will be beyond the computation power for large number of particles.

Is here in the situation of the dispersed flow, with numerous small bubble or droplets where the two-fluid method shows its advantages over the two techniques above. The two-fluid model, obtained by averaging local equations, enables both mechanical and thermal non-equilibrium to be taken into account [16–18]. Assuming that both the continuous and dispersed phases can be represented as two separate, but intermixed continua. Each phase is governed by its own set of conservation laws and the interactions of mass, momentum and energy are treated explicitly as transfer terms. Therefore it is only concerned in the average variable and is very suitable for

the dispersed or mixed flows. The two-fluid model is one of our focuses in the present thesis.

As it is suitable for dispersed/mixed flows, many researchers have paid attentions on the numerical simulation of two-fluid model in the dispersed/mixed flows. Antal et al. [19] analyzed a laminar bubbly two-phase flow in vertical pipe. With the adequate model for the lateral lift force and wall force. The obtained results showed a good agreement with the available data. Sun et al. [20] employed a modified two-fluid model-a simplified approach-for the flow regimes spanning from bubbly, cap bubbly, slug to churn-turbulent flow. In his model, bubbles were categorized into two groups. The velocities of Group 1 bubbles (spherical/distorted bubbles) and Group 2 bubbles (cap/slug/churn-turbulent bubbles) were assumed to be different. Thus, compared to the conventional model, one more continuity equation for the gas phase was added in the field equations for the modified two-fluid model. But the same momentum equation for Group 1 and Group 2 was used with the determined velocity difference between them. Similar work was done by Brooks et al. [21, 22]. The closure of the modified two-fluid model was proposed, in which weighted Group-1 and Group-2 gas velocities and momentum covariance were considered.

Although there are many works on two-fluid model, most of them are mainly focused on the flow pattern - the dispersed/mixed flows for which it is suitable. At some certain situations, both free surface and dispersed flow coexist in the same computation domain, which causes a more challenging problem. It is of significance to employ a model to solve the two flow patterns simultaneously. Fortunately, there are still some works which extend the two-fluid model to stratified flow. For example, the two-fluid model was used for modeling stratified flows with curved interfaces in the work of Brauner et al. [23]. All the input dimensionless parameters were identified for the solution of the stratified flow pattern. In their following work [24], a new closure relation for the wall and interfacial shear stress was formulated in terms of the commonly used single-phase-based expressions. In particular, the expressions obtained for the wall shear were capable of representing the change in the direction of the wall shear-stress when gravity driven backflow of either of the phases was encountered in the near wall region (i.e., in the heavy phase in concurrent up-flow, or in the light phase in concurrent down-flow), and also was valid for turbulent gas-liquid stratified flow. Furthermore, in the study of Vladimir et al. [25], the multi-fluid model was applied to the simulation of bubbly, churn and annular flow. In their simulation, the different interfacial momentum transfer formulations was employed for the different flow patterns. It was found that the accuracy of the bubbly and churn-turbulent flow prediction strongly depended on the interfacial momentum transfer. The annular flow simulation was most sensitive to the prediction of the droplets entrainment, deposition and liquid-film gas core interfacial friction.

In the two-fluid model, the coupling between two phases is strong. In the dispersed

flow of small droplets/bubble, the relative velocity between them is small. Contrarily, the relative velocity between them is large in the flow with big droplets/bubbles, which means a stiff term (drag force) in the momentum equation. The stiff drag force term requires a small time step during the simulation and presents a difficulty to the solution of governing equations. Concerning the problem, Coquel et al. [26] developed a splitting technique to solve the two-fluid model. Based on suitable kinetic upwind schemes, the whole scheme preserves the positivity of all the thermodynamic variables under a fairly unrestrictive CFL-like condition. Their approach presented an advantage in efficiency. Evje and Flätten [27] constructed a semi-implicit numerical scheme for two-fluid model, allowing the violation of the CFL criterion for sonic wave while maintaining a high level of accuracy and stability on volume fraction waves. In their study, the first-order weakly implicit mixture flux (WIMF) was combined with an advection upstream splitting method (AUSMM) type of upwind flux to obtain a scheme WIMF-AUSMD. Comparisons with an explicit Roe scheme [28, 29] indicated that the proposed scheme was highly efficient, robust and accurate on slow transients while it was more diffusive on pressure waves. It allows a larger time step by a coupling between the pressure wave component of the mixture flux, the cell center momentum and the cell interface pressure.

In the simulation of two-fluid model for the stratified and dispersed mixed flow, two-fluid model is not suitable for the solution of the stratified flow since the numerical diffusion can be caused by the continuity equation. Thus two-fluid model alone is not used to model the mixed flow. Regarding to this kind of flow, Cerne and Petelin [30], Yan and Che [31] respectively coupled VOF and two fluid model to simulate the complex flow where the stratified flow and dispersed flow coexist. In their approaches, VOF was used to capture the interface of the free surface while two-fluid model was used to simulate the dispersed flow. The coupling simulation retained the accuracy of the interface-capturing technique for a simple two-phase flow and eliminated the need for the special closure relations of two-fluid model for the same simple flow.

Although the coupling algorithm can accurately capture the large-scale interface and can also calculate the dispersed flow, two governing equations have to be employed simultaneously. Hence, the resulting model has increased complexity and computational cost. The long-term objective of many researchers is to employ a model to cover as many patterns as possible with a suitable cost. Within CTTC group, Morales et al. [32] numerically studied the thermal and fluid dynamic behaviour of the two-phase inside the evaporator and condensers using two-fluid model. In his study, one-dimensional simulation of phase change phenomena in the horizontal evaporator was implemented using R134a as refrigerant fluid. The obtained results were compared with the data of quasi-homogeneous model (QHM) [33]. Two-fluid model could give more detailed information about the fluid flow. In addition, the two-dimensional simulation of the stratified flow was also done, but the numerical dif-

fusion was not avoided in his work. Therefore following his work, the two-fluid model in the present study is used to calculate the interface through the coupling with a conservative level set method. It can avoid the serious numerical diffusion problem and accurately capture the interface in the stratified flow. Compared to the coupling with VOF, LS method is more efficient since the interface reconstruction is avoided. Furthermore, Fractional step method is employed to avoid the iterative pressure correction procedure appearing in the SIMPLE algorithm. A operator splitting method is used to overcome the limitation of stiff source term on the time step. A larger time step can be adopted for the good efficiency. It could be used to study the nucleate boiling in the cooling application for the future. Moreover, with further developing the model can be used to study the nucleate and surface mixed vaporization using the combination of two-fluid and mixture model.

1.3 Reviews of homogeneous mixture model

The moist-air multicomponent flow is commonly encountered in cooling application like air-cooled evaporator and condensor, cooling tower and desalination. It can greatly improve the efficiency of the heat transfer and reduce the temperature of the industrial equipments. Many research works have been carried out both experimentally and numerically.

1.3.1 Literature on laminar flow and falling film

Laminar convection with simultaneous heat and mass transfer between a flowing gas and the wet walls has a wide application in industrial engineerings. Among these flows, the influence of variable factors, e.g. heat flux, velocity and buoyancy force on the evaporation and condensation is of significance. The earlier studies on the effects of mass transfer were concerned with the natural convection along a vertical flat plate [34] or a vertical cylinder [35]. The combined effects of mass and thermal buoyancy forces on the developing laminar flow in the inclined channels were reported numerically by Orfi and Galanis [36] and Yan [37]. Their results showed that close to the tube inlet forced convection boundary layer development dominated. As the fluid flowed downstream, the buoyancy force became predominated. The effect of buoyancy forces in the laminar flow were also simulated in others literatures [38–40].

Lin et al. [41], He and Tzeng [42] performed a numerical study to examine the buoyancy effects of thermal and mass diffusion on laminar forced convection in the entrance region of a horizontal square channel. Their results, including the developments of temperature and concentration contours, described in detail the effects of the bottom wall temperature, relative humidity of air, aspect ratio and Rayleigh number on the local Nusselt number and Sherwood number. A two-dimensional heat and mass transfer during drying of a rectangular moist object was studied by Kaya and Dincer [43], with the convective boundary conditions at all surfaces of the moist

object. The external flow, temperature field and local distributions of convective heat transfer coefficients were numerically obtained. Furthermore, the influence of the aspect ratio on the heat and mass transfer was also studied. It was found, that the convective heat and mass transfer coefficients varied greatly with the aspect ratios. In the work of Boukadida and Ben [44] on evaporation inside a two-dimensional horizontal channel, the effect of the thermal radiation on Nusselt and Sherwood numbers were studied. They found that the thermal radiation could cause the Nusselt and Sherwood numbers increase, and the radiation could break analogy between heat and mass transfer, which only appeared at low free stream temperatures and vapor concentrations. Jang and Yan [45] examined the effects of the buoyancy force and the amplitude of wavy surface on the Nusselt and Sherwood number.

Many of cooling applications for the evaporation and condensation involve a thin falling film because of its potential for high heat and mass transfer rates with the minimal pressure drops. A significant amount of research works concerning the evaporation and condensation with liquid film or liquid film itself were carried out over the last few decades.

The laminar falling film has been firstly investigated and its main shortcoming is the assumption of a smooth liquid film, whereas the actual falling films have a wavy interface at practically all flow rates of interest. The wavy laminar regime, which prevails at low flow rates, is characterized by large waves that travel along a thin laminar substrate. These waves carry a significant portion of the mass flow and induce secondary circulation in the laminar bulk, resulting in enhancement of heat and mass transfer above the predicted value by the classic theory [46]. Extensive experiments on the falling film characteristics have been pursued. Drosos et al. [47] has experimentally studied the developing free falling films in a vertical rectangular channel. The wavy film surface and wave celerity were observed and the length of wave free area tended to increase with both increasing surface tension and Re. Energy analysis has been performed to examine the behavior of wavy interface for thin evaporating falling film in the study of Du et al. [48]. The interfacial capillary waves were formed by the balance of works done by inertial force, surface tension on phase-change interface, and also capillary force on tube wall. Based on the theory, they gave the rational explanations to film instability enhancement due to increase of Reynolds number and perturbation wavelength. It was found that the higher wall heat flux on the tube could increase the film breakup. It was mainly because the surface tension waving was enhanced with high heat flux and therefore the stability effect of capillary adherence on tube wall was weakened. The flow condition of wavy laminar films has been investigated experimentally by Adomeit and Renz [49] at falling film Reynolds numbers ranging from 27 to 200. A fluorescence intensity imaging technique was used to measure the film thickness distribution and the velocity distribution within the wavy film was measured by particle image velocimetry (PIV). They concluded

that both three-dimensional effects and the wave collision frequency increased with the increasing film flow rate. The wave shapes at 200 became completely unsteady and approximately every second wave collision caused the formulation of a turbulent spot.

The falling film is actually a kind of flow with large scale interface. It can be considered as the Kelvin-Helmholtz instability problem. In order to accurately model the falling film, the two-phase fluid model, such as VOF, LS and two fluid model, should be adopted. However, it is not easy to model the film liquid phase due to its instability, thin thickness ($10^{-4}m$) and the possible turbulent flow. Therefore, a simplified film liquid model was adopted in the numerous investigations [37, 50–53]. To facilitate the analysis, the inertia terms in the liquid-film momentum equation were neglected, for it was small compared with the diffusion term(viscous term) in momentum equation of liquid film. In the literatures [46, 54], different models were summarized in detail. In the present study, the simplified film liquid model is firstly validated against the published experiment results. Based on the verification, the test cases in the different situations are conducted with the constant or variable physical properties. The affecting parameters, such as inlet velocity, heat flux and water flow rate are studied in the laminar flow.

1.3.2 Literature on transitional flow of dry air for mixed convection

Among heat and mass transfer phenomenon, large property variation caused by heat and mass transfer results in more complicated flows, which usually involve mixed convection heat transfer, as well laminar and turbulent flow. More than one flow state exist in most of the above applications and they often appear combined together. The transition process in which a flow initially laminar becomes turbulent or inverse, is especially encountered in these kinds of applications. The laminarization may cause serious impairment of heat transfer, on the contrary, the turbulization can enhance the energy and mass transfer greatly. Therefore the location of transition and the extent of transition significantly influence the performance and efficiency of many devices.

Before investigating the mixed convection transitional/turbulent flow of air-vapor mixture in simultaneous heat and mass transfer problems, it is necessary to study the turbulent or transitional flow under the heated dry air flow. A considerable amount of experiments and numerical studies have been done to study the effects of buoyancy force in turbulent or transitional flow of different configurations. Chang et al. [55] did a experimental investigation of flow and heat transfer characteristics of a vertical narrow channel with uniform heat flux condition and analyzed the effect of wall heating on the laminar to turbulent transition. They found that the wall heating leads to the delay of laminar to turbulent transition. The critical Reynolds number where the laminar flow breakdown increases with the rise of the fluid temperature difference. Tsuji, Hattori and Abedin et al. [56–63] conducted a series of experiments and DNS on a

turbulent convection boundary layer along a vertical heated plate in mixed convection flow. The range of local Reynolds number and Grashof number were $0 - 1.9 \times 10^6$ and $1.3 \times 10^8 - 3.5 \times 10^{11}$, respectively. In the experiment, laminarization behaviour was clearly demonstrated. They found that Nu number was reduced drastically with a slight reduction of free stream (aiding flow) velocity and the reduction behaviour of Nu number was caused by laminarization. The transition from laminar to turbulence delayed for aiding flow and quickened for opposing flow as the freestream velocity increased. Poskas et al. [64] did a detailed analysis on experimental investigation of the local opposing mixed convection heat transfer in the vertical flat channel with symmetrical heating in the laminar-turbulent transition region. They found that for the higher than ambient air pressure in some Reynolds number region, heat transfer was more intensive than for the turbulent flow. Meanwhile a determination correlation of the critical Re number was proposed.

The laminar-turbulent transition flow phenomena has been also studied through large-eddy simulation (LES) by several authors. Among these investigations, some researchers [65–71] focused on LES for laminar-to-turbulent transition in a spatially developing boundary layer, but without heat transfer. In the study on the mixed convection with heating [72–78], only fully developed flow has been simulated in a number of studies using the periodic or stepwise periodic conditions. Regarding to LES of transitional flow, Padilla [79] performed a transition to turbulence study of natural convection in a annular cavity and confirmed that subgrid models can be used to predict transition to turbulence problems. Darious and Barhaghi et al. [80, 81] studied the turbulent natural boundary layer using LES and direct numerical simulation (DNS). They found that among the Smagorinsky model (SMG), Wall-adapting local eddy-viscosity (WALE) and the dynamic SGS model (DYN), DYN model was the only model capable of predicting the location of the transition from laminar to turbulent flow correctly. Few work has been done on the transition from turbulence to laminar in the mixed convection flow with strong buoyancy force using LES. Following the experiment by Shehata and McEligot [82], Xu et al. [83], Michal et al. [84], Satake et al. [85] and Bae et al. [86], respectively conducted a numerical simulation of laminarization in a vertical tube using LES and DNS. In their LES and DNS study, the detailed information on laminarization and thermal structure were revealed. However, due to the short tube, the fully developed condition was not approached. With upward flow where buoyancy aids the motion and turbulence production is inhibited, the process of the flow development is slowed down and fully development is only approached in a very long tube [87], especially in serious impaired situations.

Due to the long tube requirement, the simulation of LES and DNS on the development process is computationally expensive. Thus, most of investigations on the development process were conducted through Reynolds-Averaged Navier-Stokes

model (RANS). Minkowycz and Abraham [88,89] conducted a series of numerical simulations on the laminar breakdown in channel (Length/Width=600) flow using the transitional shear stress transport (SST) model. Under the condition of non-heating, the effects of the inlet velocity profile and inlet turbulence intensity on the transitions between laminar, intermittent and turbulent flows were investigated. In their second paper [90], the change of flow regime from turbulent through intermittent to laminar was studied using the same method. The flow passing a conical diffuser was decelerated and the laminarization occured. It was concluded from the two tests that the model adopted by them worked well for both turbulization and laminarization. On the basis of this validation, the model was used to predict the heat transfer coefficient in the laminar, intermittent and turbulent regimes in their following work [91]. With a long round pipe (Length/Diameter=200), the cases with the uniform heat flux and uniform wall temperature boundary conditions were tested. The maximum Reynolds number was up to 40,000 in their simulations. The results obtained were supported well by the experimental data. They also proposed a equation of Nusselt number for the transition regime with Reynolds number between 2300 and 3100. Unfortunately, buoyancy forces were not considered in their simulations. Behzadmehr et al. [92–95] implemented a series of numerical and experimental tests of mixed convection of air flowing through a vertical tube (100 times diameter) with uniform wall heat flux. The temperature and velocity fluctuation characteristics in the case of airflows undergoing transition were studied in detail both experimentally and numerically for low Reynolds number($Re < 2000$) over a wide range of Grashof numbers. In their simulation, using the Launder and Sharma low Reynolds $k - \epsilon$ model, the flow field underwent two transitions for upward flow as the Grashof number increased: laminar, turbulent and laminar again. The effects of inlet turbulent intensity on the hydrodynamic and thermal fields were also studied, and it was found that the increase of inlet turbulent intensity caused a significant decrease of wall temperature and of the skin friction coefficient at a certain $Re - Gr$ combinations.

Li and Jackson [96, 97] also carried out experiments with a long heated tube in which a fully developed condition was achieved. The Launder Sharma low Reynolds $k - \epsilon$ model was used to study the flow in their work. The inlet Reynolds number with a large range from 1000-35000 was employed and Nusselt ratio with the forced flow were given in the different buoyancy forces. Shome [98] numerically studied the turbulent heated flow in a quite long tube (Length/Diameter=100) using SST model and proposed a criterion of laminarization in term of Reynolds shear stress.

In addition, it is important to mention the work within CTTC research group on DNS and LES. Trias et al. [99, 100] studied the two and three dimensional DNS in a differentially heated air-filled cavity. A general symmetry-preserving discretization method was extended to unstructured mesh and it provided a good tool for the present study. With the Rayleigh numbers up to 10^{10}, the detailed flow features

were obtained under the condition of the pure natural convection. Lehmkuhl et al. [101–104] studied numerically turbulent flows on complex geometries. Different models including Smagorinsky model, Dynamic Eddy-viscosity model, QR model, WALE model and WALE model within a variational multiscale frame work (VMS-WALE) were tested through the flow past a airfoil and in a cylindrical enclosure. The result showed that both VMS-WALE and QR-model preformed good capability of predicting separation and transition to turbulence in the wake with symmetry-preserving unstructured meshes. In addition, the corresponding DNS were also carried out to compare with the LES results. However in their studies, few attention were paid on the mixed convection, in particular the laminarization or turbulization caused by the heating or buoyancy force.

As indicated above, very little work has been done on simulating the variation of spatial developing flow in a very long heated tube, in particular using LES. The flow structure in laminarization or turbulization process is hard to obtain by experiment. RANS models are dependent on empirical coefficients, hence is difficult for a RANS model to give accurate results in all flows without ad hoc adjustments with empirical data. Moreover RANS model is based on time averaging and can not provide the transient flow structure. In the present study, one of the objectives is to simulate the flow process in a vertical tube with strong buoyancy forces using LES.

1.3.3 Literature on turbulent mixed convection with mass transfer

The equipment heated could be cooled by a turbulent air flow over its surface, however, in some situations, this mechanism alone might not be sufficient to remove heat effectively from a system and to keep the temperature of it below the required level. One approach of enhancing the effectiveness of cooling is to introduce the evaporation which can increase the heat transfer greatly. A water falling film flowing a surface of the system is an efficient way in improving the performance of cooling. Thus, it has been recently a hot topic.

The introduction of evaporation coupled with heating can lead to the significant physical property variation. Therefore the turbulent flow with surface evaporation becomes a mixed convection with strong buoyancy force influence. There are several numerical experiments performed to study the turbulent mixed convection with a liquid film. Groff et al. [105] conducted a numerical study of turbulent downward flow in a vertical pipe with a falling condensation film. In their study, each phase had its governing equations including a turbulence model. Three turbulence modeling approaches were implemented: (1) Pletcher's mixing length model for both phases, (2) Jones and Launder low Reynolds $k-\epsilon$ model for both phase, (3) $k-\epsilon$ model for mixture and Pletcher's mixing model for liquid film. An approach developed by Siow [106] for condensation in parallel-plate channels was applied. Correlation equations for the coupling of two phases was not required in his study. Instead, a simplified evaporation boundary condition was employed to calculate heat and mass transfer. Considering

the changing thickness of liquid film, a moving mesh was adopted to maintain the interface. Through comparison with the experiment, it was found that the $k-\epsilon$ could predict the result best.

Yan [107, 108], Jang and Yan [109] and Feddaoui et al. [110, 111] investigated numerically a turbulent mixed convection of heat and mass transfer with film evaporation, respectively. Yan's work was mainly on channel flow while Feddaoui's work paid attention to the tube flow. In their studies, there was a common point that a simplified governing equation for the liquid film were used while a $k-\epsilon$ model was applied on the gas-vapor side. In addition, downward flow with opposing-buoyancy forces were employed in their works. Their result showed that opposing-buoyancy forces caused an enhancement in turbulent heat and mass transfer. Compared with the corresponding results of turbulent forced convection, the extent of the augmentation increased with the increase in the inlet film temperature or heat flux. A higher Reynolds number of gas flow caused a better mass and heat transfer. Li [112] published a condensation study of water vapour for turbulent flow in a vertical cylindrical condenser tube. $k-\epsilon$ model was conducted using ANSYS FLUENT commercial software. The novelty of the study was the non assumption of constant wall temperature or heat flux, instead, that gas mixture was cooled by the flowing coolant in the annulus channel. It involved the coupling of three zones: gas-vapor mixture, liquid film and coolant in the annulus channel. His results clearly showed that the average axial velocity decreased rapidly as water vapour was condensed, since the density of the gas mixture increased across the condenser tube and along the condenser. The axial velocity of the gas mixture at the interface between the gas mixture and the condensate film was not small and can not be neglected. It should be taken into account in the simulation.

Till now, few works on evaporation and condensation were conducted using LES. Dong et al. [113] employed a LES technique to predict the turbulent mass transfer at high-Schmidt numbers and to analyze the behavior of turbulent mass diffusion from a solid boundary to the adjacent shear flow at different Schmidt numbers from 0.1 up to 200. At low and medium Schmidt numbers, the concentration fluctuation was high in the whole channel except the wall region. However, at high-Schmidt number, the concentration fluctuation over the central part of the channel was negligibly small because the gradient of mean concentration was nearly zero. Similar simulation was performed by Calmet and Magnaudet [114] through a solid boundary. They showed that the high-Schmidt-number mass transfer at a solid wall was governed by the low-frequency part of the normal velocity fluctuation gradient at the wall. This was why the LES approach using efficient subgrid-scale models seems to be a powerful and accurate tool to study many features of mass transfer problems which are very difficult to describe in the experiments. Further study [115] was conducted to two different kinds of interfaces, namely a shear-driven interface and a shear-free surface.

With no shear on the interface, the concentration field was organized in large patches that mirrored the upwelling structures coming from the core of the flow. In contrast, the concentration field was organized in elongated structures of much smaller spanwise extent. The shape of these structures was found to result from the combined effect of advection by the streamwise velocities which are themselves organized in streaks, and of the vertical motions induced by bursting events. All the above literatures of LES only involved the fully developed turbulent flow.

To wrap up, there are a certain amount of works on evaporation. Most of them on turbulent mass transfer with a falling liquid film are only concerned with $k-\epsilon$ model and downward flow. There is short of LES on it. The existing large eddy simulations on mass transfer are only for the fully developed turbulent flows or neglecting the buoyancy force. Due to the margin of the existing research, it is interesting to investigate the transitional phenomena in a upward flow with a falling film using the large eddy simulation. A better understanding of the mechanisms controlling the turbulent mass transfer with a falling film and the laminar-turbulent transition phenomenon in the buoyancy-influenced flow, is expected to be achieved as a result of this LES study.

1.4 Outline of the thesis

In this introduction, the multiphase/multicomponent flows is introduced for the cooling application. Based on the type of the multiphase/multicomponent flows and the vaporization, different techniques are disclosed. In this thesis, the two-fluid model and mixture evaporation model are chosen as the main study objectives. Therefore, the previous works on two-fluid and mixture model was reviewed.

In Chapter 2, the two-fluid model is introduced and extended to solve free surface flow. Different from the other authors, the fractional step method is applied to the two-fluid model firstly to avoid the pressure-momentum correction procedure. The conservative LS method is coupled with two-fluid model for overcoming the numerical diffusion. A operator splitting method is used to overcome the limitation of stiff source term on the time step and a large CFL time step can be adopted. Finally, the free surface and dispersed flows are tested using the proposed method.

Chapter 3 provides three evaporation and condensation tests in laminar flow. In the first case, the mixture model is validated in the laminar forced flow considering constant physical properties. In the second case, a falling liquid film is imposed on the wall. In order to the solve the coupling of liquid film and water vapor mixture, a simplified liquid film model is validated against the experimental data. The mixture model is validated in the pure natural convection considering variable property. A mixed convection flow with combined heat and mass transfer is considered as the third case to analyze its affecting factors. Meanwhile the falling film is also treated as boundary condition.

In Chapter 4, large eddy simulation is applied to the transitional flow under the heated cylindrical pipe. In the simulation, the fluid is pure air, and the evaporation or condensation are not considered. A laminarization case is firstly used as benchmark test to validate the WALE model under the condition of strong heating. A flow in a long tube is considered as the second case, in which laminarization and turbulization happen. It is adopted to study the structure variation in the transitional flow. In general, this chapter is mainly focused on the validation of WALE in mixed convection under the strong influence of buoyancy force flow.

Combined the verified discontinous model in Chapter 3 with turbulence model in Chapter 4, the turbulent or transitional flow with evaporation or condensation is computationally conducted in Chapter 5. The detailed variations of flow parameters are given and the effects of water flux, water inlet temperature and air Reynolds number on evaporation and wall temperature are measured. The results in the present simulation are compared with the data obtained by RANS model. It is found that WALE model presents clear different performance in the transitional evaporation flow.

Chapter 6 gives the main conclusions that can be drawn from this thesis. To finish, further works are listed for the future.

References

[1] Amir Faghri and Yuwen Zhang. *Transport phenomena in multiphase systems*. Academic Press, 2006.

[2] Mamoru Ishii and Takashi Hibiki. *Thermo-Fluid Dynamic Theory of Two-Phase Flow*. Springer, 1975.

[3] Lluís Jofre, Oriol Lehmkuhl, Jesús Castro, and Assensi Oliva. A 3-d volume-of-fluid advection method based on cell-vertex velocities for unstructured meshes. *Computers & Fluids*, 94:14–29, 2014.

[4] Anton Smolianski. *Numerical Modeling of Two-Fluid Interfacial Flows*. PhD thesis, Univeristy of Jyväskylä, 2001.

[5] C.W Hirt and B.D Nichols. Volume of fluid (VOF) method for the dynamics of free boundaries. *Journal of Computational Physics*, 39(1):201–225, January 1981.

[6] S.Osher and J.A.Sethian. Fronts propagating with curvature-dependent speed:algorithms based on hamilton-jacobi formulations. *Journal of Computational Physics*, 79(1):12–49, November 1988.

[7] G.Yadigaroglu M.Meier and B.L.Smith. A novel technique for including surface tension in PLIC-VOF methods. *European Journal of Mechanics - B/Fluids*, 21(1):61–73, 2002.

[8] J.H.Jeong and D.Y.Yang. Finite element analysis of transient fluid flow with free surface using VOF (volume-of-fluid) method and adaptive grid.

[9] J.Y Poo N Ashgriz. Flair: Flux line-segment model for advection and interface reconstruction. *Journal of Computational Physics*, 93(2):449–468, April 1991.

[10] G.Kreiss E.Olsson. A conservative level set method for two phase flow. *Journal of Computational Physics*, 210(1):225–246, November 2005.

[11] G.Kreiss E.Olsson. A conservative level set method for two phase flow II. *Journal of Computational Physics*, 225(1):785–807, July 2007.

[12] Lluís Jofre Cruanyes. *Numerical simulation of multiphase immiscible flow on unstructured meshes*. PhD thesis, 2014.

[13] Néstor Vinicio Balcázar Arciniega et al. *Numerical simulation of multiphase flows: level-set techniques*. PhD thesis, 2014.

[14] Svend Tollak Munkejord. *Analysis of the two-fluid model and the drift-flux model for numerical calculation of two-phase flow*. PhD thesis, Norwegian Univeristy of Science and Technology, 2005.

[15] Francis H.Harlow and J.Eddie Welch. Numerical calculation of time-independent viscous incompressible flow of fluid with free surface. *The Physics of Fluids*, 8(12):2182–2189, December 1965.

[16] T Bo Anderson and Roy Jackson. Fluid mechanical description of fluidized beds. equations of motion. *Industrial & Engineering Chemistry Fundamentals*, 6(4):527–539, 1967.

[17] H Bruce Stewart and Burton Wendroff. Two-phase flow: models and methods. *Journal of Computational Physics*, 56(3):363–409, 1984.

[18] DZ Zhang and A Prosperetti. Ensemble phase-averaged equations for bubbly flows. *Physics of Fluids (1994-present)*, 6(9):2956–2970, 1994.

[19] SP Antal, RT Lahey Jr, and JE Flaherty. Analysis of phase distribution in fully developed laminar bubbly two-phase flow. *International Journal of Multiphase Flow*, 17(5):635–652, 1991.

[20] Xiaodong Sun, Mamoru Ishii, and Joseph M. Kelly. Modified two-fluid model for the two-group interfacial area transport equation. *Annals of Nuclear Energy*, 30(16):1601 – 1622, 2003.

[21] Caleb S. Brooks, Sidharth S. Paranjape, Basar Ozar, Takashi Hibiki, and Mamoru Ishii. Two-group drift-flux model for closure of the modified two-fluid model. *International Journal of Heat and Fluid Flow*, 37(0):196 – 208, 2012.

[22] Caleb S. Brooks, Basar Ozar, Takashi Hibiki, and Mamoru Ishii. Two-group drift-flux model in boiling flow. *International Journal of Heat and Mass Transfer*, 55(21–22):6121 – 6129, 2012.

[23] N. Brauner, D. Moalem Maron, and J. Rovinsky. A two-fluid model for stratified flows with curved interfaces. *International Journal of Multiphase Flow*, 24(6):975 – 1004, 1998.

[24] A. Ullmann and N. Brauner. Closure relations for two-fluid models for two-phase stratified smooth and stratified wavy flows. *International Journal of Multiphase Flow*, 32(1):82 – 105, 2006.

[25] Stevanović Vladimir, Prica Sanja, and Maslovarić Blaženka. Multi-fluid model predictions of gas-liquid two-phase flows in vertical tubes. *FME Transactions*, 35(4):173 – 181, 2007.

[26] F. Coquel, K. El Amine, E. Godlewski, B. Perthame, and P. Rascle. A numerical method using upwind schemes for the resolution of two-phase flows. *Journal of Computational Physics*, 136(2):272 – 288, 1997.

[27] Steinar Evje and Tore Flåtten. Weakly implicit numerical schemes for a two-fluid model. *SIAM J. Sci. Comput.*, 26(5):1449 – 1484, 2005.

[28] Ph L Roe. The use of the riemann problem in finite difference schemes. In *Seventh International Conference on Numerical Methods in Fluid Dynamics*, pages 354–359. Springer, 1981.

[29] Philip L Roe. Approximate riemann solvers, parameter vectors, and difference schemes. *Journal of computational physics*, 43(2):357–372, 1981.

[30] Gregor Cerne and Stojan. Petelin. Coupling of the interface tracking and the two-fluid models for the simulation of incompressible two-phase flow. *Journal of Computational Physics*, 171(2):776–804(29), 2001.

[31] Kai Yan and Defu Che. A coupled model for simulation of the gas-liquid two phase flow with complex flow patterns. *International Journal of Multiphase flow*, 36(4):333–348, 2010.

[32] Sergio Morales Ruiz et al. Numerical simulation of the thermal and fluid dynamics behaviour of liquid-vapour two-phase flow in evaporators and condensers. 2009.

[33] Joaquim Rigola, Sergio Morales, Gustavo Raush, and Carlos D Perez Segarra. Analysis of two-phase flow in double-pipe condensers and evaporators with special emphasis on transition zones: Numerical model and experimental comparison. In *the 2004 International Refrigeration and Air Conditioning Conference at Purdue*, pages 1–10, 2004.

[34] B Gebhart and L Pera. The nature of vertical natural convection flows resulting from the combined buoyancy effects of thermal and mass diffusion. *International Journal of Heat and Mass Transfer*, 14(12):2025 – 2050, 1971.

[35] T.S. Chen and C.F. Yuh. Combined heat and mass transfer in natural convection along a vertical cylinder. *International Journal of Heat and Mass Transfer*, 23(4):451 – 461, 1980.

[36] Jamel Orfi and Nicolas Galanis. Developing laminar mixed convection with heat and mass transfer in horizontal and vertical tubes. *International Journal of Thermal Sciences*, 41(4):319 – 331, 2002.

[37] Wei-Mon Yan. Transport phenomena of developing laminar mixed convection heat and mass transfer in inclined rectangular ducts. *International Journal of Heat and Mass Transfer*, 38(15):2905 – 2914, 1995.

[38] C. Debbissi, J. Orfi, and S. Ben Nasrallah. Evaporation of water by free or mixed convection into humid air and superheated steam. *International Journal of Heat and Mass Transfer*, 46(24):4703 – 4715, 2003.

[39] Zouhair Ait Hammou, Brahim Benhamou, Nicolas Galanis, and Jamel Orfi. Laminar mixed convection of humid air in a vertical channel with evaporation or condensation at the wall. *International Journal of Thermal Sciences*, 43(6):531 – 539, 2004.

[40] Kuan-Tzong Lee, Hon-Ling Tsai, and Wei-Mon Yan. Mixed convection heat and mass transfer in vertical rectangular ducts. *International Journal of Heat and Mass Transfer*, 40(7):1621 – 1631, 1997.

[41] J. N. Lin, F. C. Chou, W. M. Yan, and P. Y. Tzeng. Combined buoyancy effects of thermal and mass diffusion on laminar forced convection in the thermal entrance region of horizontal square channels. *The Canadian Journal of Chemical Engineering*, 70(4):681 – 689, 1992.

[42] J.N. Lin and P.Y. Tzeng. Convective instability of heat and mass transfer for laminar forced convection in the thermal entrance region of horizontal rectangular channels. *International Journal of Heat and Fluid Flow*, 13(3):250 – 258, SEPTEMBER 1992.

[43] Ahmet Kaya and Ibrahim Dincer. Numerical modeling of heat and mass transfer during forced convection drying of rectangular moist objects. *International Journal of Heat and Mass Transfer*, 49(17 - 18):3094 – 3103, AUGUST 2006.

[44] Noureddine Boukadida and Sassi Ben Nasrallah. Mass and heat transfer during water evaporation in laminar flow inside a rectangular channel-validity of heat and mass transfer analogy. *International Journal of Thermal Sciences*, 40(1):67 – 81, 2001.

[45] Jer-Huan Jang and Wei-Mon Yan. Mixed convection heat and mass transfer along a vertical wavy surface. *International Journal of Heat and Mass Transfer*, 47(3):419 – 428, 2004.

[46] Abdulmalik A. Alhusseini and John C. Chen. Transport phenomena in turbulent falling films. *Industrial Engineering Chemistry Research*, 39(6):2091–2100, 2000.

[47] E.I.P Drosos, S.V Paras, and A.J Karabelas. Characteristics of developing free falling films at intermediate reynolds and high kapitza numbers. *International Journal of Multiphase Flow*, 30(7–8):853 – 876, 2004.

[48] Xiao-Ze Du, Bu-Xuan Wang, Shao-Rong Wu, and Sheng-Yao Jiang. Energy analysis of evaporating thin falling film instability in vertical tube. *International Journal of Heat and Mass Transfer*, 45(9):1889 – 1893, 2002.

[49] Philipp Adomeit and Ulrich Renz. Hydrodynamics of three-dimensional waves in laminar falling films. *International Journal of Multiphase Flow*, 26(7):1183 – 1208, 2000.

[50] V. Dharma Rao, V. Murali Krishna, K.V. Sharma, and P.V.J. Mohana Rao. Convective condensation of vapor in the presence of a non-condensable gas of high concentration in laminar flow in a vertical pipe. *International Journal of Heat and Mass Transfer*, 51(25–26):6090 – 6101, 2008.

[51] W.M. Yan and T.F. Lin. Evaporative cooling of liquid film through interfacial heat and mass transfer in a vertical channel—ii. numerical study. *International Journal of Heat and Mass Transfer*, 34(4–5):1113 – 1124, 1991.

[52] Feng Zhang, Dong-Lei Tang, Jiao Geng, Zhi-Xiang Wang, and Zhi-Bing Zhang. Study on the temperature distribution of heated falling liquid films. *Physica D: Nonlinear Phenomena*, 237(7):867 – 872, 2008.

[53] M'barek Feddaoui, El Mustapha Belahmidi, Ahmed Mir, and Abdelaziz Bendou. Numerical study of the evaporative cooling of liquid film in laminar mixed convection tube flows. *International Journal of Thermal Sciences*, 40(11):1011 – 1020, 2001.

[54] Nikhin Mascarenhas and Issam Mudawar. Investigation of eddy diffusivity and heat transfer coefficient for free-falling turbulent liquid films subjected to sensible heating. *International Journal of Heat and Mass Transfer*, 64(0):647 – 660, 2013.

[55] Wang Chang, Gao Pu-zhen, Wang Zhan-wei, and Tan Si-chao. Experimental study of transition from laminar to turbulent flow in vertical narrow channel. *Annals of Nuclear Energy*, 47(0):85 – 90, 2012.

[56] T. Tsuji and Y. Nagano. Turbulence measurements in a natural convection boundary layer along a vertical flat plate. *International Journal of Heat and Mass Transfer*, 31(10):2101 – 2111, 1988.

[57] T. Tsuji and Y. Nagano. Velocity and temperature measurements in a natural convection boundary layer along a vertical flat plate. *Experimental Thermal and Fluid Science*, 2(2):208 – 215, 1989.

[58] Yasuo Hattori, Toshihiro Tsuji, Yasutaka Nagano, and Nobukazu Tanaka. Characteristics of turbulent combined-convection boundary layer along a vertical heated plate. *International Journal of Heat and Fluid Flow*, 21(5):520 – 525, 2000.

[59] Yasuo Hattori, Toshihiro Tsuji, Yasutaka Nagano, and Nobukazu Tanaka. Effects of freestream on turbulent combined-convection boundary layer along a vertical heated plate. *International Journal of Heat and Fluid Flow*, 22(3):315 – 322, 2001.

[60] Yasuo Hattori, Toshihiro Tsuji, Yasutaka Nagano, and Nobukazu Tanaka. Effects of free stream velocity on turbulent natural convection flow along a vertical plate. *Experimental Heat Transfer*, 13(3):183 – 195, 2000.

[61] Mohammad Zoynal Abedin, Toshihiro Tsuji, and Yasuo Hattori. Direct numerical simulation for a time-developing natural-convection boundary layer along a vertical flat plate. *International Journal of Heat and Mass Transfer*, 52(19 - 20):4525 – 4534, 2009.

[62] Mohammad Zoynal Abedin, Toshihiro Tsuji, and Yasuo Hattori. Direct numerical simulation for a time-developing combined-convection boundary layer along a vertical flat plate. *International Journal of Heat and Mass Transfer*, 53(9 - 10):2113 – 2122, 2010.

[63] Mohammad Zoynal Abedin, Toshihiro Tsuji, and Jinho Lee. Effects of freestream on the characteristics of thermally-driven boundary layers along a heated vertical flat plate. *International Journal of Heat and Fluid Flow*, 36(0):92 – 100, 2012.

[64] P. Poskas, R. Poskas, A. Sirvydas, and A. Smaizys. Experimental investigation of opposing mixed convection hear transfer in the vertical flat channel in a laminar-turbulent transition region. *International Journal of Heat and Mass Transfer*, 54(1 - 3):662 – 668, 2011.

[65] Antonios Monokrousos, Luca Brandt, Philipp Schlatter, and Dan S. Henningson. DNS and LES of estimation and control of transition in boundary layers subject to free-stream turbulence. *International Journal of Heat and Fluid Flow*, 29(3):841 – 855, 2008.

[66] Wolfgang Rodi. DNS and LES of some engineering flows. *Fluid Dynamics Research*, 38(2-3):145 – 173, 2006.

[67] A.A. Dimas, B.M. Mowli, and U. Piomelli. Large-eddy simulation of subcritical transition in an attachment-line boundary layer. *Computers Mathematics with Applications*, 46(4):571 – 589, 2003. Turbulence Modelling and Simulation.

[68] S. Hickel and N.A. Adams. Implicit LES applied to zero-pressure-gradient and adverse-pressure-gradient boundary-layer turbulence. *International Journal of Heat and Fluid Flow*, 29(3):626 – 639, 2008.

[69] Ibrahim E Abdalla and Zhiyin Yang. Numerical study of the instability mechanism in transitional separating-reattaching flow. *International Journal of Heat and Fluid Flow*, 25(4):593 – 605, 2004.

[70] Hossam S. Aly, Khalid M. Saqr, Yehia A. Eldrainy, and Mohammad Nazri Jaafar. Can large eddy simulation(LES) predict laminar to turbulent flow transition? *International Journal of Mechanical and Material Engineering*, 4(1):42 – 48, 2009.

[71] X. Huai, R.D. Joslin, and U. Piomelli. Large-eddy simulation of transition to turbulence in boundary layers. *Theoretical and Computational Fluid Dynamics*, 9(2):149 – 163, 1997.

[72] Joon Sang Lee, Xiaofeng Xu, and Richard H. Pletcher. Large eddy simulation of heated vertical annular pipe flow in fully developed turbulent mixed convection. *International Journal of Heat and Mass Transfer*, 47(3):437 – 446, 2004.

[73] J.S. Lee and R.H. Pletcher. Large eddy simulations of variable property turbulent flow in horizontal and vertical channels with buoyancy and heat transfer effects. *Proceedings of the Institution of Mechanical Engineers, Part C: Journal of Mechanical Engineering Science*, 221(4):429 – 441, 2007.

[74] W.-P. Wang and R.H. Pletcher. On the large eddy simulation of a turbulent channel flow with significant heat transfer. *Physics of Fluids*, 8(12):3354 – 3366, 1996.

[75] Lyle D. Dailey, Ning Meng, and Richard H Pletcher. Large eddy simulation of constant heat flux turbulent channel flow with property variations: Quasi-developed model and mean flow results. *Journal of heat transfer*, 125:27–38, 2003.

[76] Jing Yin, Bing-Chen Wang, and Donald J. Bergstrom. Large-eddy simulation of combined forced and natural convection in a vertical plane channel. *International Journal of Heat and Mass Transfer*, 50(19 - 20):3848 – 3861, 2007.

[77] Amir Keshmiri, MarkA. Cotton, Yacine Addad, and Dominique Laurence. Turbulence models and large eddy simulations applied to ascending mixed convection flows. *Flow, Turbulence and Combustion*, 89(3):407–434, 2012.

[78] Bamdad Lessani and Miltiadis V. Papalexandris. Numerical study of turbulent channel flow with strong temperature gradients. *International Journal of Numerical Methods for Heat & Fluid Flow*, 18(3/4):545–556, 2008.

[79] E.L.M. Padilla and A. Silveira-Neto. Large-eddy simulation of transition to turbulence in natural convection in a horizontal annular cavity. *International Journal of Heat and Mass Transfer*, 51(13-14):3656 – 3668, 2008.

[80] D. G. Barhaghi and L. Davidson. Natural convection boundary layer in a 5:1 cavity. *Physics of Fluids (1994-present)*, 19(12), 2007.

[81] Darioush G.Barhaghi. *A Study of Turbulent Natural Convection Bounary Layers Using Large-Eddy Simulation.* PhD thesis, Chalmers University of Technology, 2007.

[82] A.M. Shehata and D.M. McEligot. Mean structure in the viscous layer of strongly-heated internal gas flows. measurements. *International Journal of Heat and Mass Transfer*, 41(24):4297–4313, 1998.

[83] Xiaofeng Xu, Joon Sang Lee, Richard H. Pletcher, A. Mohsen Shehata, and Donald M. McEligot. Large eddy simulation of turbulent forced gas flows in vertical pipes with high heat transfer rates. *International Journal of Heat and Mass Transfer*, 47(19-20):4113 – 4123, 2004.

[84] Adam Richards Michal Hradisky, Thomas Hauser and Robert Spall. Large eddy simulation of strongly heated internal gas flows. In *9th AIAA/ASME Joint Thermophysics and Heat Transfer Conference*, pages 974–984, San Francisco, June 2006.

[85] Shin ichi Satake, Tomoaki Kunugi, A. Mohsen Shehata, and Donald M. McEligot. Direct numerical simulation for laminarization of turbulent forced gas flows in circular tubes with strong heating. *International Journal of Heat and Fluid Flow*, 21(5):526 – 534, 2000.

[86] Joong Hun Bae, Jung Yul Yoo, Haecheon Choi, and Donald M. McEligot. Effects of large density variation on strongly heated internal air flows. *Physics of Fluids*, 18(7), 2006.

[87] W.S. Kim, C. Talbot, B.J. Chung, and J.D. Jackson. Variable property mixed convection heat transfer to air flowing through a vertical passage of annular cross section: Part 1. *Chemical Engineering Research and Design*, 80(3):239 – 245, 2002.

[88] W.J. Minkowycz, J.P. Abraham, and E.M. Sparrow. Numerical simulation of laminar breakdown and subsequent intermittent and turbulent flow in parallel-plate channels: Effects of inlet velocity profile and turbulence intensity. *International Journal of Heat and Mass Transfer*, 52(17 - 18):4040 – 4046, 2009.

[89] JP Abraham, EM Sparrow, and JCK Tong. Breakdown of laminar pipe flow into transitional intermittency and subsequent attainment of fully developed intermittent or turbulent flow. *Numerical Heat Transfer, Part B: Fundamentals*, 54(2):103–115, 2008.

[90] J.P. Abraham, E.M. Sparrow, J.C.K. Tong, and D.W. Bettenhausen. Internal flows which transist from turbulent through intermittent to laminar. *International Journal of Thermal Sciences*, 49(2):256 – 263, 2010.

[91] J.P. Abraham, E.M. Sparrow, and J.C.K. Tong. Heat transfer in all pipe flow regimes: laminar, transitional/intermittent, and turbulent. *International Journal of Heat and Mass Transfer*, 52(3 - 4):557 – 563, 2009.

[92] A. Behzadmehr, N. Galanis, and A. Laneville. Laminarturbulent transition for low reynolds number mixed convection in a uniformly heated vertical tube.

International Journal of Numerical Methods for Heat & Fluid Flow, 12(7):839–854, 2002.

[93] A. Behzadmehr, N. Galanis, and A. Laneville. Low reynolds number mixed convection in vertical tubes with uniform wall heat flux. *International Journal of Heat and Mass Transfer*, 46(25):4823 – 4833, 2003.

[94] A. Behzadmehr, N. Galanis, and C.T. Nguyen. Predicted effects of inlet turbulent intensity on mixed convection in vertical tubes with uniform wall heat flux. *International Journal of Thermal Sciences*, 45(5):433 – 442, 2006.

[95] A. Behzadmehr, A. Laneville, and N. Galanis. Experimental study of onset of laminar-turbulent transition in mixed convection in a vertical heated tube. *International Journal of Heat and Mass Transfer*, 51(25 - 26):5895 – 5905, 2008.

[96] JianKang. Li and J.D. Jackson. Buoyancy-influenced variable property turbulent heat tranfer to air flowing in a uniformaly heated vertical tube. In *2nd International Conference on Turbulent Heat Transfer*, Manchester, UK, 1998.

[97] Li JianKang. *Studies of Buoyancy-influenced convective heat transfer to air in a vertical pipe*. PhD thesis, Univeristy of Manchester, 1994.

[98] Biswadip Shome. Numerical study of turbulent flow in heated circular tube using transitional shear stress transport turbulence model. *International Journal of Thermal Sciences*, 79(0):90 – 102, 2014.

[99] FX Trias. Direct numerical simulation and regularization modelling of turbulent flows on loosely coupled parallel computers using symmnetry-preserving discretizations.

[100] FX Trias, M Soria, A Oliva, and CD Pérez-Segarra. Direct numerical simulations of two-and three-dimensional turbulent natural convection flows in a differentially heated cavity of aspect ratio 4. *Journal of Fluid Mechanics*, 586:259 – 293, 2007.

[101] Oriol Lehmkuhl Barba et al. Numerical resolution of turbulent flows on complex geometries. 2012.

[102] Ivette Rodriguez, Ricard Borell, Oriol Lehmkuhl, Carlos D Perez Segarra, and Assensi Oliva. Direct numerical simulation of the flow over a sphere at re= 3700. *Journal of Fluid Mechanics*, 679:263–287, 2011.

[103] O Lehmkuhl, I Rodríguez, A Baez, A Oliva, and CD Pérez-Segarra. On the large-eddy simulations for the flow around aerodynamic profiles using unstructured grids. *Computers & Fluids*, 84:176–189, 2013.

[104] R Capdevila, CD Perez-Segarra, O Lehmkuhl, and G Colomer. Numerical simulation of turbulent natural convection and gas radiation in differentially heated cavities using fvm, dom and les. *ICHMT DIGITAL LIBRARY ONLINE*, 2010.

[105] M.K. Groff, S.J. Ormiston, and H.M. Soliman. Numerical solution of film condensation from turbulent flow of vapor–gas mixtures in vertical tubes. *International Journal of Heat and Mass Transfer*, 50(19 - 20):3899 – 3912, 2007.

[106] Erh Chang Siow. Numerical solution of a two-phase model for laminar film condensation of vapour-gas mixtures in channels. 2001.

[107] Wei-Mon Yan. Effects of film vaporization on turbulent mixed convection heat and mass transfer in a vertical channel. *International Journal of Heat and Mass Transfer*, 38(4):713 – 722, 1995.

[108] Wei-Mon Yan. Evaporative cooling of liquid film in turbulent mixed convection channel flows. *International Journal of Heat and Mass Transfer*, 41(23):3719 – 3729, 1998.

[109] Jer-Huan Jang and Wei-Mon Yan. Thermal protection with liquid film in turbulent mixed convection channel flows. *International Journal of Heat and Mass Transfer*, 49(19 - 20):3645 – 3654, 2006.

[110] M Feddaoui, A Mir, and E Belahmidi. Cocurrent turbulent mixed convection heat and mass transfer in falling film of water inside a vertical heated tube. *International Journal of Heat and Mass Transfer*, 46(18):3497 – 3509, 2003.

[111] M. Feddaoui, H. Meftah, and A. Mir. The numerical computation of the evaporative cooling of falling water film in turbulent mixed convection inside a vertical tube. *International Communications in Heat and Mass Transfer*, 33(7):917 – 927, 2006.

[112] Jun-De Li. CFD simulation of water vapour condensation in the presence of non-condensable gas in vertical cylindrical condensers. *International Journal of Heat and Mass Transfer*, 57(2):708 – 721, 2013.

[113] Yu-Hong Dong, Xi-Yun Lu, and Li-Xian Zhuang. Large eddy simulation of turbulent channel flow with mass transfer at high-schmidt numbers. *International Journal of Heat and Mass Transfer*, 46(9):1529 – 1539, 2003.

[114] Isabelle Calmet and Jacques Magnaudet. Large-eddy simulation of high-schmidt number mass transfer in a turbulent channel flow. *Physics of Fluids (1994-present)*, 9(2):438–455, 1997.

[115] Isabelle Calmet and Jacques Magnaudet. High-schmidt number mass transfer through turbulent gas–liquid interfaces. *International Journal of Heat and Fluid Flow*, 19(5):522 – 532, 1998.

2

Numerical simulation of the two-fluid model with Fractional step method in two phase flow

The contents of this chapter have been published as:
Xiaofei Hou, Joaquim Rigola, Oriol Lehmkuhl, Assensi Oliva. Simulation of the two-fluid model on incompressible flow with Fractional step method for both resolved and unresolved scale interfaces. *International Journal of Heat and Fluid Flow*, Volume 52, 15-27, April 2015.

2.1 Abstract

In the present paper, the Fractional Step Method usually used in single fluid flow is here extended and applied for the Two-Fluid model resolution using the finite volume discretization. The use of a projection method resolution instead of the usual pressure-correction method for multi-fluid flow, successfully avoids iteration processes. On the other hand, the main weakness of the two fluid model used for simulations of free surface flows, which is the numerical diffusion of the interface, is also solved by means of the conservative Level Set method (interface sharpening) [1]. Moreover, the use of the algorithm proposed has allowed presenting different free-surface cases with

or without Level Set implementation even under coarse meshes under a wide range of density ratios. Thus, the numerical results presented, numerically verified, experimentally validated and converged under high density ratios, shows the capability and reliability of this resolution method for both mixed and unmixed flows.

2.2 Introduction

The primary goal of this section is focused on the detailed two-dimensional numerical simulation of gas-liquid flow with small or large length scale interface. The governing equations of two-fluid model for the incompressible interfacial flows are discretized while the drag force, the surface tension model and interface sharpening are described. Although the same model was implemented by Strublj et al. [1] with pressure-correction algorithm(SIMPLE) [2], which is a common solution in single fluid and has been widely extended to multiphase flow, the present paper is focused on Fractional Step algorithm [3, 4] being different from pressure-correction algorithm. Another objective of the present work is to validate the capability of the solution algorithm in multiphase flows and explore the possibility of two fluid model in free surface with and without interface sharpening method, which is not totally validated by Strublj et al. [1]. With the proposed algorithm, the validation of two-fluid model applied on dispersed flow and free surface is performed out under different cases with a wide range of density ratio and viscosity ratio: Rayleigh-Taylor instability case with low density ratio, dam break case with high density ratio and high viscosity; while the pressure jump over a droplet interface, an oscillating droplet and a rising bubble are also tested. Finally, sedimentation case is implemented for the dispersed flow.

2.3 Mathematical Model

2.3.1 Governing equations

The two-fluid model is an average numerical representation for multiphase flow, characterized by two independent velocity fields which specify the motions of each phase. The basic conservative governing equations consist of two continuity equations and two momentum equations including surface tension. They are derived by averaging the original ones for single phase fluid. Detailed derivation of the two-fluid model can be found in the book ([5]). Thus, two sets of mass and momentum conservation governing equations of each k phase are defined as:

$$\frac{\partial(\rho_k \alpha_k)}{\partial t} + \nabla\cdot(\rho_k \alpha_k \mathbf{u}_k) = 0 \tag{2.1}$$

$$\frac{\partial(\rho_k \alpha_k \mathbf{u}_k)}{\partial t} + \nabla\cdot(\rho_k \alpha_k \mathbf{u}_k \mathbf{u}_k) = -\alpha_k \nabla p + \nabla\cdot(\mu_k \alpha_k \nabla \mathbf{u}_k) + \rho_k \alpha_k \mathbf{g} + \mathbf{F}_{D,k} + \mathbf{F}_{S,k} \tag{2.2}$$

Assuming that the fluid is incompressible, and there is no phase change through the interface, a non-conservative mathematical formulation form of two-fluid model is written below:

$$\frac{\partial(\rho_k \alpha_k)}{\partial t} + \nabla\cdot(\rho_k \alpha_k \mathbf{u}_k) = 0 \tag{2.3}$$

$$\frac{\partial \mathbf{u}_k}{\partial t} + \nabla\cdot(\mathbf{u}_k \mathbf{u}_k) = -\frac{1}{\rho_k}\nabla p + R(\mathbf{u}_k) + \frac{\mathbf{F}_{D,k}}{\alpha_k \rho_k} \tag{2.4}$$

where $R(\mathbf{u}_k)$ is defined as

$$R(\mathbf{u}_k) = -\nabla\cdot(\mathbf{u}_k \mathbf{u}_k) + \frac{\mu_k}{\rho_k}\Delta \mathbf{u}_k + \mathbf{g} + \frac{\mathbf{F}_{S,k}}{\rho_k \alpha_k}$$

Both fluids share the same space and pressure having different velocity fields. In that sense, their both continuity equations are added and can be written in the following form

$$\nabla\cdot(\alpha_1 u_1 + \alpha_2 u_2) = 0 \tag{2.5}$$

2.3.2 Drag force

Drag force $\mathbf{F}_D$ describes interfacial forces in momentum equations (also called interfacial friction forces), referred to forces that oppose the relative motion of an object through a fluid (liquid or gas). Since drag force is dependent on the relative velocities between both phase flows, if interface tracking is implemented within two-fluid model, drag force term has to be taken into account. It is important to highlight that the sum of local drag forces of both phases must be zero: $\mathbf{F}_{D,2} = -\mathbf{F}_{D,1}$.

Different drag force formulations were employed in many references [6–10]. The drag force over k phase usually used by many researchers is $F_{D,k} = (\alpha_k \frac{c_D}{2})\rho_c A_c |\mathbf{u}_r|\mathbf{u}_r$ ([10]), where subscript c represents the continuous phase, ρ_c is the density of continuous phase, A_c is the volumetric interfacial area, $\mathbf{u}_r$ is the relative velocity and c_D is an empirical coefficient. Other variant of drag force is $F_{D,d} = -F_{D,c} = \frac{3}{4}\alpha_c \alpha_d \rho_c \frac{c_D}{d}|\mathbf{u}_r|\mathbf{u}_r$ [8], where subscript d, c represents dispersed and continuous phase respectively, and d is the diameter of dispersed flow instead of A_c although having the same unit.

In the present paper, the drag force equation for dispersed flow is $F_D = \alpha_1 \alpha_2 \rho_m \frac{C_D}{d}|\mathbf{u}_1 - \mathbf{u}_2|(\mathbf{u}_1 - \mathbf{u}_2)$ [11], where mixture density is ρ_m, drag coefficient c_D is usually a function of bubble or droplet, while the modeling of the interfacial length scale is imposed by the physics of the flow and is equal to the fluid equivalent diameter d. For free surface, drag force applied only to free surface flow is an empirical closure correlations [11]. The term depends on relative velocity $\mathbf{u}_2 - \mathbf{u}_1$, mixture density ρ_m, drag coefficient c_D and interfacial length scale d

$$\mathbf{F}_{D,1} = \alpha_1 \alpha_2 (\mathbf{u}_2 - \mathbf{u}_1)\rho_m \frac{c_D}{d} \tag{2.6}$$

$$\rho_m = \alpha_1\rho_1 + \alpha_2\rho_2 \tag{2.7}$$

where $c_D = 0.44$ and $d = \dfrac{c_D\Delta t}{100}$ is large enough for equalizing the velocities of both phases at interface.

2.3.3 Surface force

Surface force $\mathbf{F}_S$ is calculated as continuum surface force, based on curvature κ, as follows

$$\mathbf{F}_S = \sigma\kappa\nabla\alpha_1 \tag{2.8}$$

where σ is surface tension coefficient. The curvature is calculated as follows

$$\kappa = -\nabla\cdot\mathbf{n}, \qquad \mathbf{n} = \frac{\nabla\alpha_1}{|\nabla\alpha_1|} \tag{2.9}$$

Finally, surface tension force can be split between two phases occupying the cell, since two momentum equations are solved in the presented system

$$\mathbf{F}_{S,k} = \beta_k\mathbf{F}_S \tag{2.10}$$

where β_k is the averaged factor of k phase. To evaluate β_k value, Bartosiewicz et al. [12] proposed two models for averaged factor β_k: the first based on mass average $\beta_k = \alpha_k\rho_k/(\alpha_1\rho_1 + \alpha_2\rho_2)$, and the second one based on volume average in the cell $\beta_k = \alpha_k$ (the second model is being applied in this paper).

2.3.4 Interface sharpening algorithm

As free surface is smeared over several cells, and even if continuity equation is solved with the high resolution scheme, the smearing is still increasing with time. In the present paper conservative Level Set method is applied [13]. The method consists of two steps: in the first step, the continuity equation for the volume fraction equation (2.1) is solved with high resolution scheme; in the second step an equation that acts as an artificial compression is solved

$$\frac{\partial\alpha_1}{\partial\tau} + \nabla\cdot(\alpha_1(1-\alpha_1)\mathbf{n}) = \varepsilon\Delta\alpha_1 \tag{2.11}$$

where $\mathbf{n}$ stands for the normal at the interface, and is calculated only once at the beginning of the second step. τ is an artificial time, not equivalent to the actual time t. ε is a small amount of "viscosity", which is added to avoid discontinuities. Accuracy is assured when

$$\int |a^{n+1} - a^n| < \varepsilon_T\cdot\Delta\tau \tag{2.12}$$

for a specified total tolerance ε_T.

The volume fraction values obtained through the equation 2.11 may not satisfy the constraint $\alpha_1 + \alpha_2 = 1.0$, due to the numerical error. Afterwards, the new volume fraction can be handled further using an average

$$\alpha_1^{n+1} = \frac{\alpha_1^{n+1}}{\alpha_1^{n+1} + \alpha_2^{n+1}} \qquad \alpha_2^{n+1} = \frac{\alpha_2^{n+1}}{\alpha_1^{n+1} + \alpha_2^{n+1}} \tag{2.13}$$

2.4 Numerical Algorithm

Since each fluid in the two-fluid model has its own set of governing equations, the solution is further complicated by the couplings of different terms(interchange on mass, momentum and energy). The solution algorithm becomes more important and two principal classes of algorithms have been devised. The first class of approach is a coupled or semicoupled time-marching solution strategy [14–16], which deals principally with fast transients. When the interaction among the phases is very strong or the processes to be simulated have short time scales i.e. nuclear reactor, the governing equations are more tightly coupled. A fully implicit method or semi-implicit approach, which is derived from Implicit Continuous Eulerian(ICE) [17] method, is preferred. Its advantages is robustness, efficiency, generality and simplicity due to solving the velocity, pressure and volume fraction equations simultaneously, while the principal drawback is high storage requirements [18].

The second one consists of segregated algorithms derived from the pressure-based schemes widely used in single-phase flow. Among the solution algorithms, pressure-correction technique caters for implicit-type algorithms of steady or unsteady solutions. In the same way, pressure-correction technique is centered on the basic philosophy of effectively coupling between the pressure and the velocity of which the pressure is linked to the velocity via the construction of a pressure field to guarantee the conservation of mass [19]. SIMPLE [2], IPSA [20, 21] and PISO [22] are common approaches employed for multifluid flow, and have been investigated by many researchers. A common aspect of these pressure-correction procedures is the adoption of pressure correction iteration solution, which is usually most time-consuming during the process, especially in the fine mesh.

Although the widespread information is available on the single-phase solution algorithm, much less information is available on the multifluid algorithm. Many algorithms and techniques developed for single-fluid flow have neither been fully extended nor applied to the simulation of multifluid flow. Fraction step method [3, 4] being a popular method in a single fluid flow, is also a pressure-based segregated approach and can reduce the calculation quantity greatly in single time level by solving the pressure directly. Considering the weakness of the pressure-correction solution, an incompressible Fractional step method widely employed in single fluid is extended to

multifluid field.

2.4.1 The application of Fractional Step method

The numerical resolution algorithm applied is the classical Fractional Step projection method. The temporal discretization is based on a central difference scheme for the time derivative term in the momentum equation (2.4)

$$\frac{\partial \phi_k}{\partial t}|^{n+1/2} \approx \frac{\phi_k^{n+1} - \phi_k^n}{\Delta t} + O(\Delta t^2) \tag{2.14}$$

A fully explicit second-order Adams-Bashforth scheme is used for $R(\phi_k)$ without drag force term is

$$R^{n+1/2}(\phi_k) \approx \frac{3}{2}R^n(\phi_k) - \frac{1}{2}R^{n-1}(\phi_k) + O(\Delta t^2, \Delta x^m) \tag{2.15}$$

And a first-order backward Euler scheme is considered for the pressure-gradient term. Incompressibility constraint is treated implicitly. Thus, the semi-discretized momentum equation (2.4) is computed to obtain an intermediate predictor as

$$\phi_k^* = \phi_k^n + \Delta t[\frac{3}{2}R^n(\phi_k) - \frac{1}{2}R^{n-1}(\phi_k)] \tag{2.16}$$

Regarding source equation (2.4) terms, the interfacial forces near the interface in two phase flow are usually large, making the system of equation stiff. Therefore, governing equations become an hyperbolic system with stiff source terms, which have been widely studied in the past years [23, 24].

A successful numerical method to overcome the previous method limitation is the operator splitting method (OSM), which splits stiff source term from others terms in equation (2.4). These other terms are integrated with explicit scheme and the stiff part (interfacial forces) is integrated with implicit scheme. The system is then analytically solved and a new predictor is calculated as:

$$\phi_1^p = \frac{\phi_1^*(1 + \Delta t\frac{C_D}{d}\frac{\rho_m}{\rho_2}\alpha_1) + \phi_2^*(\Delta t\frac{C_D}{d}\frac{\rho_m}{\rho_1}\alpha_2)}{1 + \Delta t\frac{C_D}{d}\frac{\rho_m}{\rho_2}\alpha_1 + \Delta t\frac{C_D}{d}\frac{\rho_m}{\rho_1}\alpha_2} \tag{2.17}$$

$$\phi_2^p = \frac{\phi_1^*(\Delta t\frac{C_D}{d}\frac{\rho_m}{\rho_2}\alpha_1) + \phi_2^*(1 + \Delta t\frac{C_D}{d}\frac{\rho_m}{\rho_1}\alpha_2)}{1 + \Delta t\frac{C_D}{d}\frac{\rho_m}{\rho_2}\alpha_1 + \Delta t\frac{C_D}{d}\frac{\rho_m}{\rho_1}\alpha_2} \tag{2.18}$$

Defining pseudo-pressure as $\tilde{p} = \Delta t p^{n+1}$, variables at $n+1$ can be calculated as

$$\phi_k^{n+1} = \phi_k^p - \frac{1}{\rho_k}\nabla\tilde{p} \tag{2.19}$$

In fact,the above momentum equation just holds where its phase exists. In order to make the equation hold in all the domain, both sides of the equation are multiplied by α_k^{n+1}

$$\alpha_k^{n+1}(\mathbf{u}_k^{n+1}) = \alpha_k^{n+1}(\mathbf{u}_k^p - \frac{1}{\rho_k}\Delta t \nabla p^{n+1}) \tag{2.20}$$

The sum of the two fluid equations yields the combined momentum equation

$$(\alpha_1\phi_1)^{n+1} + (\alpha_2\phi_2)^{n+1} = (\alpha_1^{n+1}\phi_1^p + \alpha_2^{n+1}\phi_2^p) - (\frac{\alpha_1^{n+1}}{\rho_1} + \frac{\alpha_2^{n+1}}{\rho_2})\nabla\tilde{p} \tag{2.21}$$

Taking the divergence of the above equation yields a Poisson equation for $\tilde{p}$ and substituting the equation (2.5), equation (2.22) is obtained

$$\nabla \cdot (\frac{\alpha_1^{n+1}}{\rho_1} + \frac{\alpha_2^{n+1}}{\rho_2})\nabla\tilde{p} = \nabla \cdot (\alpha_1^{n+1}\phi_1^p + \alpha_2^{n+1}\phi_2^p) \tag{2.22}$$

The above Poisson equation is solved with SLU solver package developed by Davis [25]. In order to close equation (2.22), the Neumann boundary condition is imposed. Once the Poisson equation is solved, the new velocity can be calculated as follows:

$$\begin{aligned} &\mathbf{u}_k^{n+1} = \mathbf{u}_k^p - \frac{1}{\rho_k}\tilde{p}^{n+1}, && if \quad \alpha_k > 0 \\ &\mathbf{u}_k^{n+1} = 0, && if \quad \alpha_k <= 0 \end{aligned}$$

Since an explicit time integration scheme is applied, the time-step Δt is bounded by the CFL condition [26],

$$(\Delta t)_k(\frac{|\mathbf{u}_k|}{\Delta x_i})_{max} \leq C_{conv} = 0.35, \qquad (\Delta t)_k(\frac{|\nu_k|}{\Delta x_i^2})_{max} \leq C_{visc} = 0.2$$
$$\Delta t = min(\Delta t_1, \Delta t_2)$$

2.4.2 Convective Numerical Scheme

In governing equations, convection term based on low order scheme usually leads to strongly diffused solutions, particularly for long integration times. As the two fluid is separated by one interface, and the flux is a discontinuous function, numerical diffusion caused will quickly mix the two phases and the interface will lose its sharpness and disappear. It is, therefore, of considerable interest to employ flux limiter. It can avoid the spurious oscillations (wiggles), which would otherwise occur with high order spatial discretization schemes due to shocks, discontinuities or sharp changes in the solution domain.

Using the flux limiter, the flux F at face in convective term is calculated as $F_{i,j} = F^L_{i,j} + \varphi_{i,j}(F^H_{i,j} - F^L_{i,j})$, where F^H is a high-order flux calculated with Lax-Wendroff scheme [27], F^L is a low-order flux with upwind scheme and φ is the flux limiter. Vanleer flux limiter [28] is applied in the work. It is defined as follows:

$$\varphi_{i,j} = \frac{|r_{i,j}| + r_{i,j}}{1 + |r_{i,j}|} \tag{2.23}$$

r is smoothness parameter, which is defined by:

$$r_{i,j} = \frac{\beta_P - \beta_D}{\beta_U - \beta_P} = \frac{1}{\beta_{i+1,j} - \beta_{i,j}} \begin{cases} \beta_{i,j} - \beta_{i-1,j} & \text{when } u_{i,j} > 0 \\ \beta_{i+2,j} - \beta_{i+1,j} & \text{when } u_{i,j} < 0 \end{cases} \tag{2.24}$$

where variable β stands for variables that is being calculated. The notations 'U' ,'D' and 'P' denote respectively the upstream, downstream points and the point being calculated.

2.4.3 Numerical procedure

The main strategy for solving the system as Fractional Step Method is summarized as:

Step 1. Input relative parameters (geometry, physical properties, boundary condition).

Step 2. Calculate the time step.

Step 3. Evaluate the predictor $R(\mathbf{u}_k)$ and intermediate predictor with the equation (2.16).

Step 4. Substituting the intermediate predictor into the equations (2.17) and (2.18) to get the final predictor u^p.

Step 5. Solve Poisson equation (2.22) and the new velocities are obtained.

Step 6. Solve the continuity equation (2.1) and interface sharpening equation 2.11 to obtain the new volume fraction field.

2.5 Test cases

To validate and explore the capabilities of Fractional Step method in the two-fluid model with and without Level Set method, different multiphase flow problems with small or large length scale are solved, while the results obtained are compared with the existing experimental, analytical and numerical data. Two free surface cases: Rayleigh-Taylor instability and Dam Break are presented without considering the surface tension, while three different cases: pressure jump over a droplet, an oscillating droplet and a rising bubble are carried out taking into account surface tension. Finally, a dispersed case-sedimentation is simulated considering only gravity effects.

2.5.1 Rayleigh-Taylor instability

Rayleigh-Taylor instability has attracted the attention of physicists due to its important role in inertially confined nuclear fusion. At the initial state of the Rayleigh-Taylor instability, a horizontal interface separates two fluids of different densities, when higher density fluid is at the top and lower density fluid is at the bottom. As this configuration is unstable, once a small perturbation is introduced, the heavy fluid falls into the light fluid as a spike, and the light fluid rises into the heavy fluid as a bubble.

2.5.1.1 Initial and boundary conditions

The relative parameters and conditions are exactly the same as in references [7, 11]. All simulations are performed in a two dimensional closed box (Length $L = 1m$, Height $H = 5.0m$) containing two immersible fluids (see Fig. 2.1). The interface between two fluids has a shape of weak cosine wave

$$\delta = H - \delta(cos(\frac{2\pi x}{L} - \pi) + 1) \qquad 0 \leq x \leq L \tag{2.25}$$

where $\delta_0 = 0.001m$. The properties of higher density fluid are density $\rho_1 = 3kg/m^3$, dynamic viscosity $\mu_1 = 0.03Pa \cdot s$ and the properties of lighter density fluid are density $\rho_2 = 1kg/m^3$, dynamic viscosity $\mu_2 = 0.01Pa \cdot s$. The gravity is considered as $g = -10m/s^2$ and is downward vertically.

Non-slip boundary condition and the Neumann condition for velocity $\mathbf{u}$ are respectively prescribed at the top, bottom and side wall, while a symmetry boundary condition for pressure equation ($\mathbf{n}_{wall} \cdot \nabla p = 0$) is imposed at all the walls. Although there is no surface tension considered, the wetting angle is taken as $\theta = 90°$ since it is needed by interface sharpening. Results are presented in terms of dimensionless time $\tau = t/\beta$. The deformation and its amplitude time development is exponential

$$y(\tau) = \delta_{\tau=0} e^{\beta\tau} \qquad \beta^2 = gkAt \qquad At = \frac{\rho_1 - \rho_2}{\rho_1 + \rho_2} \tag{2.26}$$

Where $\delta_{\tau=0} = 0.002m$. $k = \pi/L$ is the smallest wave number and At is Atwood number.

2.5.1.2 Results

Rayleigh-Taylor instability has been carried out considering different numerical schemes. Table 2.1 details 6 different groups considering continuity and momentum equations with or without interface sharpening. Fig. 2.2 (a) shows the amplitude growth in the evolution process of Rayleigh-Taylor instability under different meshes considering

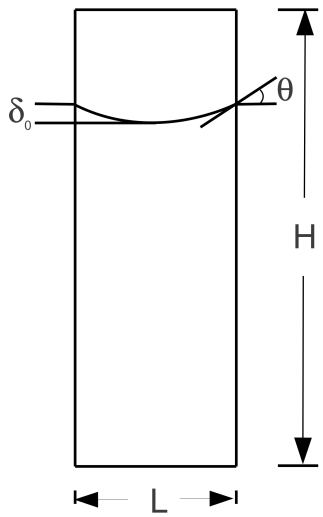

Figure 2.1: Rayleigh-Taylor instability case.

scheme f. It can be observed that at the beginning period ($\tau < 0.15$) the numerical results present a slight disagreement with the analytical data. This effect is due to, the volume fraction near interface is always discontinuous or nonlinear, but the linear interpolation is applied to track the greatest sunken point in the simulation. The problem is specially important at the beginning period where the initial disturbance is very thin, and the relative error is significant. The maximum discrepancy between mesh 32×160 and 64×320 is 17% while the maximum discrepancy between mesh 64×320 and 128×640 is 4.5%, which is clearly reduced with mesh density increasing. The amplitude difference between the numerical and analytical data at $\tau = 0.07$ is 0.002 and at $\tau = 0.3$ is 0.0338 on mesh 64×320.

Fig. 2.2(b) demonstrates the amplitude growth between the analytical result and simulation data in the evolution process of Rayleigh-Taylor instability at mesh 64×320. The numerical results show all the schemes present a very similar result. The discrepancy between analytical and numerical data at $\tau = 0.05$ is 0.0014 and at $\tau = 0.3$ is 0.05 . In order to further illustrate the influence of the convective term discretization schemes in momentum, continuity equations and interface sharpening, the different discretized schemes with or without interface sharpening are depicted in Fig. 2.3.

Table 2.1: The detailed numerical schemes being applied

	Scheme-a	Scheme-b	Scheme-c	Scheme-d	Scheme-e	Scheme-f
momentum equation	upwind	upwind	upwind	upwind	Vanleer	Vanleer
continuity equation	upwind	upwind	Vanleer	Vanleer	Vanleer	Vanleer
interface sharpening	without	with	without	with	without	with

Furthermore, it can be seen from Fig. 2.3 that the diffusion of scheme-a is significant, while others schemes show good agreement of overcoming diffusion. Both Level Set interface sharpening and Vanleer flux limiter can reduce the diffusion significantly.

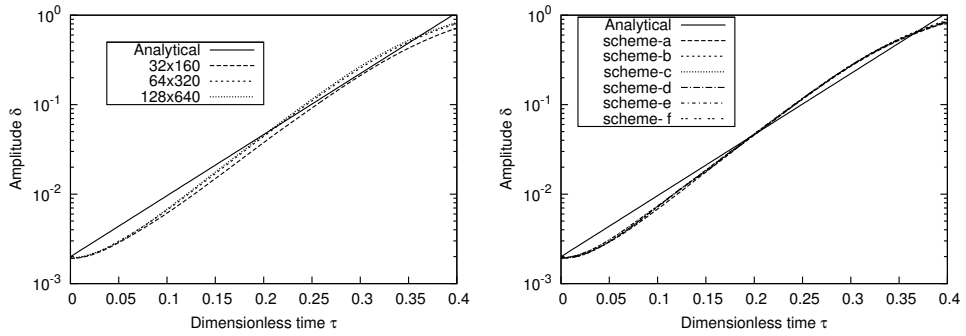

(a) Amplitude of different meshes at scheme f (b) Amplitude of different schemes on mesh 64 × 320

Figure 2.2: Rayleigh-Taylor instability

2.5.2 Dam break

Due to the wide application of dam break in engineering, such as designing offshore and coast structure, it has been widely studied in the literature by many different experimental, theoretical and numerical methods [29, 30]. This problem was adopted by several researchers as a benchmark test to validate the numerical performance of the proposed formulations for solving two-liquid interfaces or free-surface flows.

Cruchaga et al. [31]) performed a set of dam break experiments using a reservoir with shampoo and water for two different initial column aspect ratios with the cor-

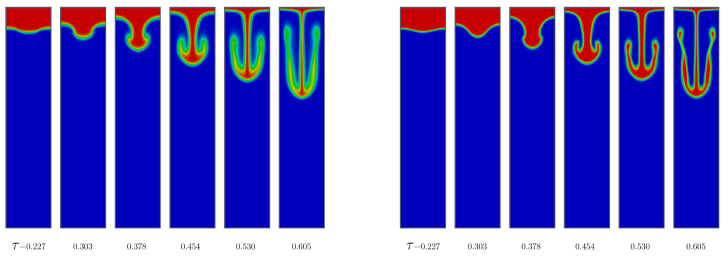

(a) scheme-a

(b) scheme-b

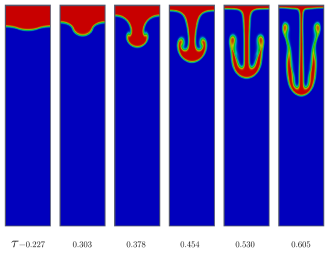

(c) scheme-c

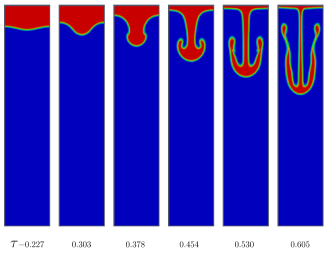

(d) scheme-d

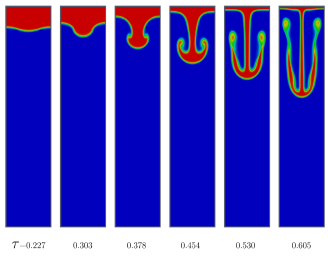

(e) scheme-e

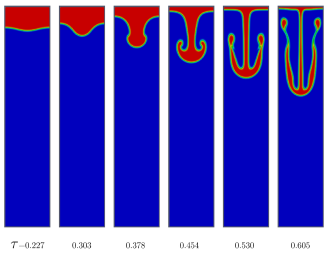

(f) scheme-f

Figure 2.3: Volume fraction field at different instants for different schemes. (a) scheme-a. (b) scheme-b. (c) scheme-c. (d) scheme-d. (e) scheme-e. (f) scheme-f

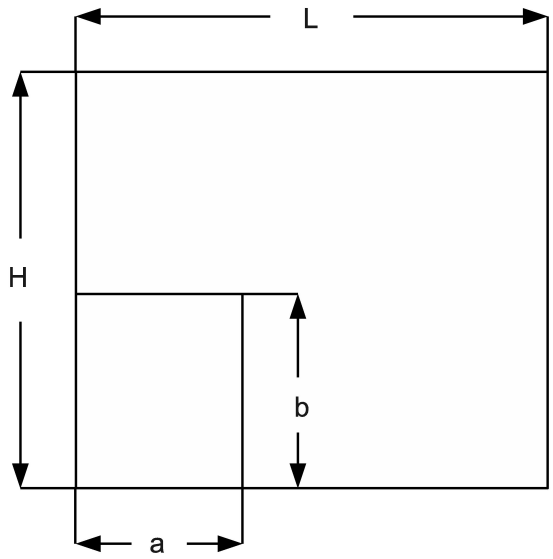

Figure 2.4: Dam break case.

responding numerical predictions. In their simulation, the formulation–edge-tracked interface locater technique (ETILT) is used, while wall friction and turbulence effects are also included. In order to validate the capability of two-fluid model at high density ratio and high viscosity, the same set of dam break is simulated. The length and height of the whole container is $L = 0.42m$ and $H = 0.44m$ respectively (see Fig. 2.4). The initial width of the column a is $0.114m$ while the liquid aspects ratio is defined as

$$A_r = \frac{b}{a} \tag{2.27}$$

All the simulations were done on the same mesh size as Cruchaga et al. ([31]): 100×75 for water and 60×45 for shampoo with and without additional Level Set method(LSM) in order to validate capability of Fractional Step method under high density and viscosity ratios. The upwind scheme is applied in the discretization of momentum equation while Van leer flux limiter is used in continuity equation. The spread of the water along the floor, the height of the water along the left vertical wall, and the height of the water along the right vertical wall are compared. Since the later

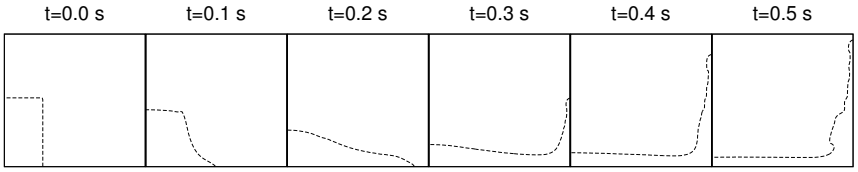

h!

Figure 2.5: Evolution process of a water column with aspect ratio $A_r = 2$.

period of flow is mixed with turbulent flow, only the early stage of result is compared against the experimental data. In reference, the simulation with and without wall friction effects were simulated, respectively. In the present paper, M.A.Cruchaga-1 represents M.A.Cruchaga numerical results without wall friction, M.A.Cruchaga-2 is numerical results with wall friction and dimensionless position is defined $H(L)/a$, Present-with and without LSM stands for algorithm with and without additional Level Set method, respectively.

2.5.2.1 Collapse of a water column

The first case is a water column collapse. The fluid properties are: $\rho_1 = 1000kg/m^3$ and $\mu_1 = 0.001kg/m \cdot s$ for the water, and $\rho_2 = 1kg/m^3$ and $\mu_2 = 1.983 \cdot 10^{-5}kg/m \cdot s$ for the air. Fig. 2.5 illustrates the collapsing process of a water column with aspect ratio $A_r = 2$ with interface sharpening method(due to the space limitation, the evolution process without Level Set method is not presented). Since the turbulent flow is involved in the later stage of water collapse, only the first $0.5s$ was simulated. It can be observed that the column begins to move due to the sudden drawing of the baffle. Afterward the water flows along the bottom of the container until reaches the right wall. The water column starts to climb along the right wall because of the existing inertia.

Fig. 2.6 shows the numerical result performance of the water column collapse against the reference's experimental data and numerical results [31]. The numerical results obtained with and without Level Set method show good agreement. They are both very similar with the referred experimental and numerical data on the horizontal position with a maximum time advance of $0.02s$. The left vertical position almost coincides with the experimental and their numerical data, with a time delay of $0.03s$ compared to the experimental data, which confirms good performance of the present model in the case. The right vertical position is more similar with the experimental result compared to the referred numerical data. The maximum peak value discrepancy between the experimental data and the present numerical result is 3.5%. The mass

conservation performs very well in the case with a range of deviation ±1%. The good consistency with and without Level Set method shows the capability of the present Fractional Step method in high density ratio.

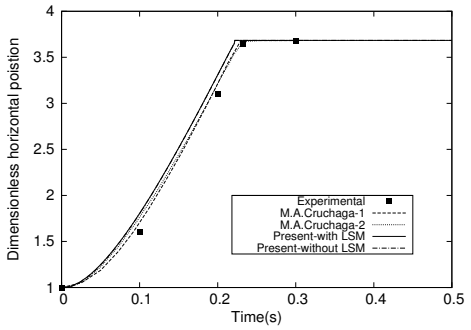

(a) Horizontal point

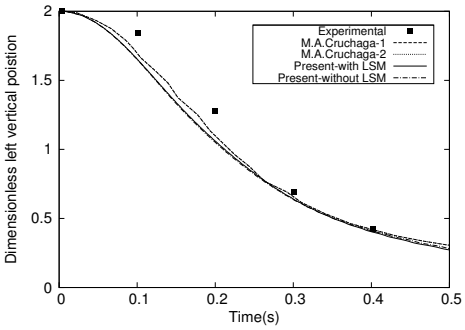

(b) Left vertical point

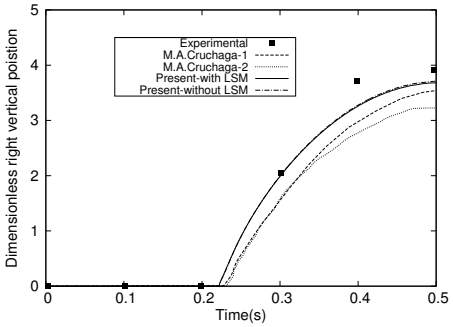

(c) Right vertical point

Figure 2.6: Collapse of a water column with aspect ratio $A_r = 2$

2.5.2.2 Collapse of a shampoo column

The collapse of shampoo column is dam break with high density and viscosity ratios. Shampoo properties are $\rho_1 = 1042kg/m^3$ and $\mu_1 = 8kg/m \cdot s$ and air properties are $\rho_2 = 1kg/m^3$ and $\mu_2 = 1.983 \cdot 10^{-5}kg/m \cdot s$.

Fig. 2.7 shows the evolution process and predicts the interface behaviour of a shampoo column collapse with aspect ratio $A_r = 2$ with Level Set method(the evolution process without Level Set method is not shown because of lack of space). It

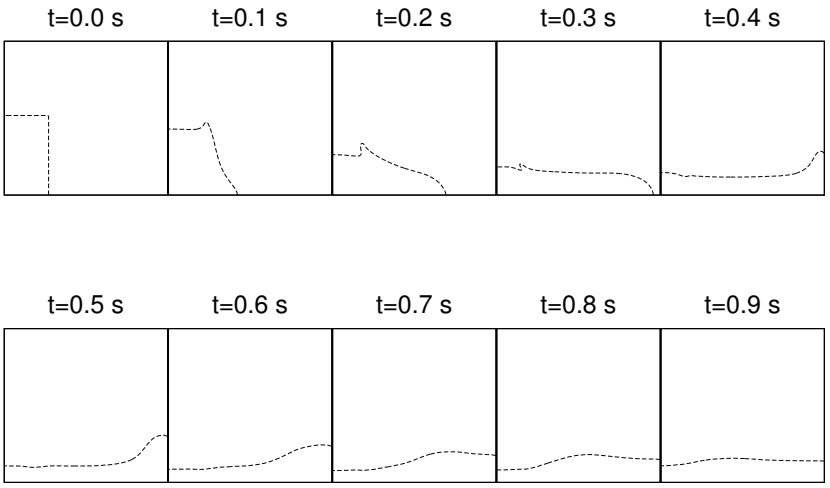

Figure 2.7: Evolution process of a shampoo column with aspect ratio $A_r = 2$.

can be seen from the evolution of Fig. 2.7 that there is a tiny bulge at $t = 0.1s$ and $t = 0.2s$, which is not consistent with the experimental phenomenon. One possible reason is that the drag force parameter being applied in the present model maybe not completely suitable for the flow with high viscosity and there is lack of surface tension force. Fig. 2.8 exhibits the interface positions at different walls during the evolution of shampoo collapse with and without Level Set method. On the horizontal position comparison, there is a time advance of $0.015s$ at beginning and a time delay of $0.025s$ at the late stage ($t > 0.3s$). The left vertical position shows a good agreement with the numerical data of Cruchaga while all the four results present significant deviations with the experimental data. Different from the horizontal position and right vertical position comparison, the left vertical position with and without Level Set method are not highly coincident while they present a discrepancy from $0.3s$ to $0.9s$. In the comparison of the right vertical position, a clear distinction between the present data and experimental data is presented with an average error of $0.3s$ before $0.7s$. In the simulation, the shampoo was considered a Newtonian fluid, but actually the shampoo is not a pure Newtonian fluid with a variable viscosity, which is a significant aspect resulting in all the inconsistency observed. The good consistency with and without Level Set method at high viscosity ratio are confirmed further through the shampoo collapsing case.

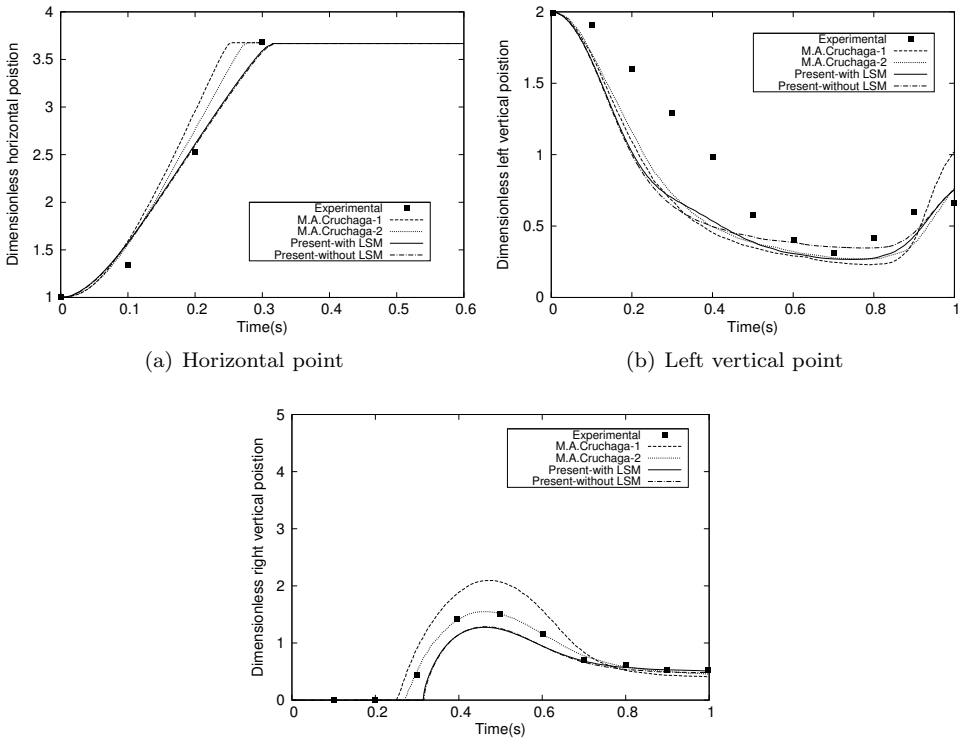

(a) Horizontal point

(b) Left vertical point

(c) Right vertical point

Figure 2.8: Collapse of a shampoo column with aspect ratio $A_r = 2$

2.5.3 Pressure jump over a droplet interface

The static drop in equilibrium without gravity has been tested to validate our surface tension force model, which has been studied as a validation case in many literatures [32–35]. The theoretical jump in pressure across drop in this case is given by $\Delta p = \sigma/R$, where σ is surface tension coefficient and R is radius of a droplet

The computational domain considered is a two-dimensional square cavity having a side length of $L = 7.5mm$. An ethanol droplet is initially located at the center of the domain with a radius $R = 2mm$. The whole domain full of air is in zero gravity and the surface tension coefficient between the ethanol and air is taken to be $\sigma = 0.02361N/m$. The fluid properties are $\rho_1 = 787.88kg/m^3$, $\mu_1 = 1.2 \cdot 10^{-3}Pa \cdot s$ for ethanol and $\rho_2 = 1.1768kg/m^3$, $\mu_2 = 1.0 \cdot 10^{-5}Pa \cdot s$ for the air. The real physical properties of air and ethanol are employed in the present paper, which are different

Table 2.2: Pressure jump over a droplet and numerically induced velocities in the ethanol on different meshes

	32×32	64×64	128×128
Δp[Pa]	12.32	11.7359	11.7803
Δp error[/%]	4.36	0.59	0.21
C_p	1.11e-3	7.93e-4	4.54e-04

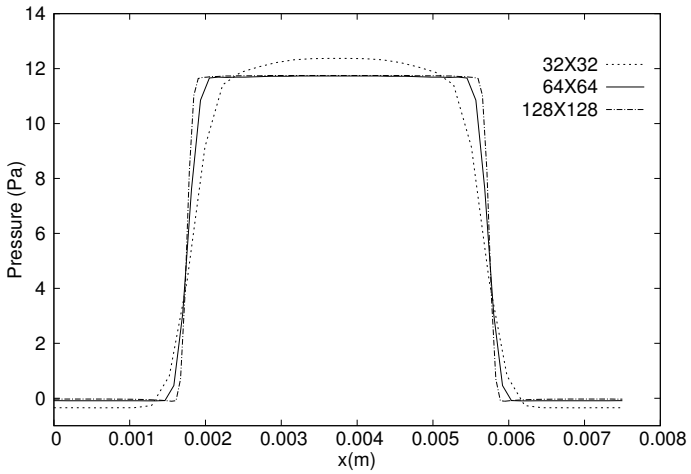

Figure 2.9: Pressure cut-line (y = 0.00375) for different mesh sizes

from Tiselj's test case [1].

Initially the velocity and pressure are fixed to zero. The exact pressure difference Δp is $11.8050 Pa$. In the computational results that follow, the error in the pressure jump and in the maximum velocity is investigated. The relative pressure jump error is evaluated as

$$\varepsilon(\Delta p) = \frac{|\Delta p_{numerical} - \Delta p_{analytical}|}{\Delta p_{analytical}} \tag{2.28}$$

where $\Delta p_{simulation}$ denotes the averaged pressure difference between inside and outside the drop. To avoid considering the transition region, inside means the cell of volume fraction $\alpha >= 0.999$.

Spurious currents near the interface are best illustrated in the static drop in equilibrium. The reason of its appearance are numerical errors. The order of magnitude

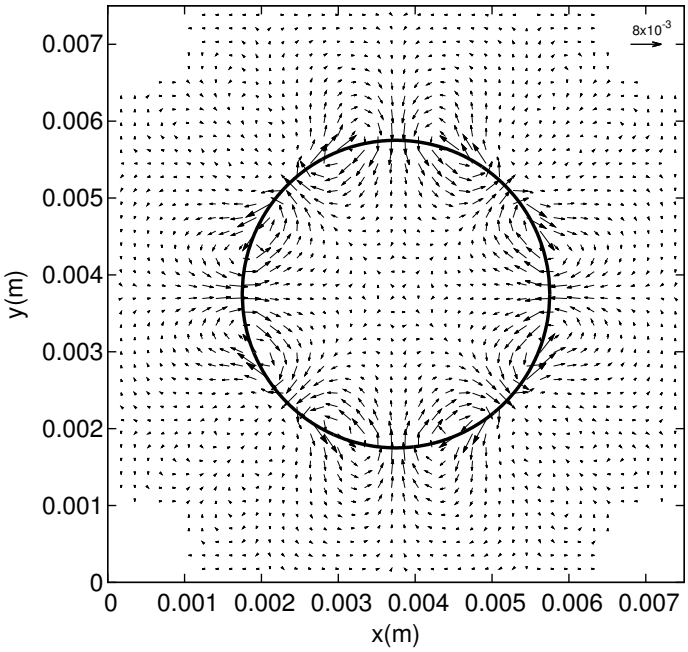

Figure 2.10: Spurious velocity at $t = 0.2s$

of parasitic velocities can be estimated according to the surface tension and dynamic viscosity of the drop ([35])

$$u_p = \frac{C_p \sigma}{\mu_1} \tag{2.29}$$

where C_p is a numerical constant characteristic of the quality of the numerical modeling of surface tension forces(a non-dimensional number similar to a capillary number).

A pressure jump over a droplet interface is presented at different meshes, while the results are depicted at 0.2s when U_{max} tends to asymptotic value. Fig. 2.9 presents the pressure cut-lines at y = 0.00375 for various levels of grid refinement and as can be seen the pressure approximation become sharper with the finer grids. The pressure jump and velocities induced by numerical error are given in Table 2.2. The relative error decreases as the mesh increases. Typical C_p is found between 10^{-3} and 10^{-10}. The minimum C_p for VOF-PLIC approach is $5 \cdot 10^{-5}$ and $5 \cdot 10^{-7}$ for the front tracking method [35], the present parasitic velocities are in a reasonable range. Fig. 2.10 show the spurious velocity field at 0.2s, for the finest mesh 128×128 with a reference vector of $8 \cdot 10^{-3}$. It can been observed from the figure that the spurious

velocity is concentrated near the interface region, even if the light spurious velocity exists in other regions.

2.5.4 Oscillating droplet

Table 2.3: Oscillation period of droplet in simulation with different numbers cells and time steps

Mode($n = 2$)	Analytical	64×64	128×128
$\tau[s]$	1.5888	1.565	1.5978
τ error[%]	–	-1.498	0.057
Mode($n = 4$)	Analytical	64×64	128×128
$\tau[s]$	0.5024	0.5147	0.515
τ error[%]	–	2.45	2.508

Oscillating droplet has been employed to illustrate the dynamic case of surface tension force [32, 36, 37]. The same test case as [1, 35] was considered. The ethanol ellipsoid drop or square drop is located in a computational domain of square cavity full of air with zero gravity. The size of the domain is $75mm \times 75mm$. The shape of ellipse drop is given by the equation $(x/0.02856)^2 + (y/0.01782)^2 = 1$. The side length of square drop is $40mm$. The fluid properties are the same as the previous test case. The initial velocity field is set to zero in the whole domain and the Neumann boundary condition was imposed. The theoretical oscillation period is obtained by

$$\omega_0^2 = \frac{(n^3 - n)\sigma}{(\rho_1 + \rho_2)R^3}, \qquad \tau_0 = \frac{2\pi}{\omega_0} \tag{2.30}$$

where ω_0 is oscillation frequency and τ_0 is oscillating time period.

Due to the surface tension, the droplet begins to oscillate. A mesh refinement assessment has been carried out. Fig. 2.11(a) shows the evolution process of north pole of ellipse drop on mesh size 64×64 and 128×128. It can be observed that the oscillation damping of mesh size 64×64 is larger than the results on mesh size 128×128, which is consistent with the previous observation [1]. The observed oscillation damping is caused by the larger numerical viscosity (discretization error in the convective part, which acts as a diffusive term) in the momentum equation. The oscillation period on fine mesh is more accurate than on the coarse mesh, but both are in the range of $\pm2\%$. The maximum deviation of mass conservation is 0.02% through the whole process.

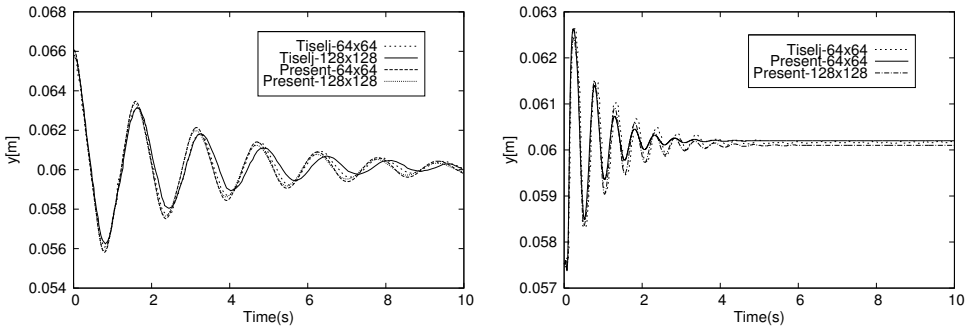

(a) North point of ellipse (b) North point of square drop

Figure 2.11: Performance of a drop

The simulation of square drop was also done (Fig. 2.11(b)). It was found that there is maximum oscillation period discrepancy of ±3% on different mesh sizes, and the drop hardly oscillated any more in the simulation of initially square droplet after $6s$. The mass conserve exactly during the whole process.

In order to illustrate the exact error among different mesh size and time step, Table 2.3 is given. At smaller time step on the same mesh, oscillation period agree well with the analytical data.

2.5.5 Rising bubble

The rise of an air bubble in water by buoyancy forces was proposed by [38] as benchmark case to validate the code's capability. Results obtained are compared with Tiselj's data [1] and Hysing's data [38]. The gas bubble of density $\rho_1 = 100kg/m^3$, viscosity $\mu_1 = 1Pa \cdot s$ and $R_0 = 25cm$ is initially imposed in the liquid with properties $\rho_2 = 1000kg/m^3$, viscosity $\mu_2 = 10Pa \cdot s$. The chosen fluids are non-realistic and the purpose is to compare the results obtained with different numerical methods. The gravity in the system is $g = -0.98m/s^2$ and the surface tension between fluids is $\sigma = 24.5N/m$. The corresponding dimensionless numbers are $Re = \rho_1\sqrt{g}(2R_0)^{3/2}/\mu_1 = 35$ and $Eo = 4\rho_1 g R_0^2/\sigma = 10$. The initial fluids are both at rest initially. The computational domain for the test problem is chosen to be $[0,1]\times[0,2]$. The geometry is shown in Fig. 2.12(a).

Several parameters were analyzed and compared to the results of Tiselj [1] and Hysing [38]: the position of bubble mass center, the rise velocity, mass conservation of the bubble and the circularity. The numerical simulation were implemented respectively on mesh size 80×160, 160×320 and 320×640. Vanleer flux limiter was applied to both continuity equation and momentum equation. With and without Level Set

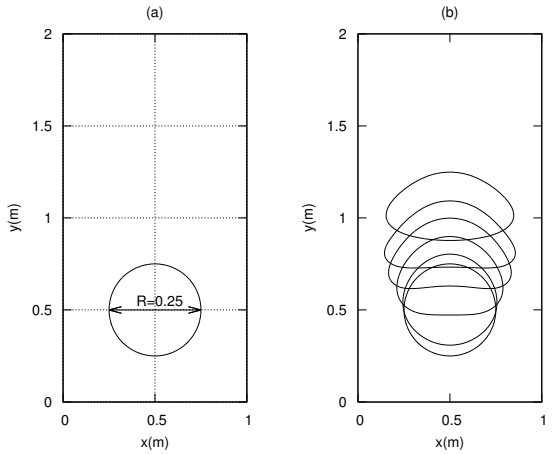

Figure 2.12: Initial bubble position.

method algorithm were respectively performed in this case for verifying the capability in this moving situation.

Fig. 2.13 presents the performance of rising bubble with Level Set method in the present simulation. The numerical result were compared with the Tiselj data and Hysing data [38]. Seeing that the curve on different meshes are very close in reference [1], only the result on mesh size 80×160 is employed as the reference in the case. In Fig. 2.13(a), the results on different mesh size are almost the same, and their mass center curves coincide within the first $2s$. Afterward the difference among them starts to increase but still is not great. It can be observed from Fig. 2.13(b) that, the results is closer to the Tiselj data than the Hysing curve, which is obtained with Level Set method, but the result move slowly toward the Hysing curve with the increasing mesh. Fig. 2.13(c) presents the rising velocity of the bubble at mass center. The similar phenomenon as Fig. 2.13(b) appears, but the difference among different mesh sizes is quite small and can be neglected. The bubble evolution with time can be seen in Fig. 2.12(b).

Fig. 2.14 gives the result of a rising bubble without Level Set method at different grids. It shows the similar performance as with Level Set method on bubble mass center position and bubble circularity, while the pronounced difference between them appears on bubble rise velocity. With level Set method, the data with a coarse mesh

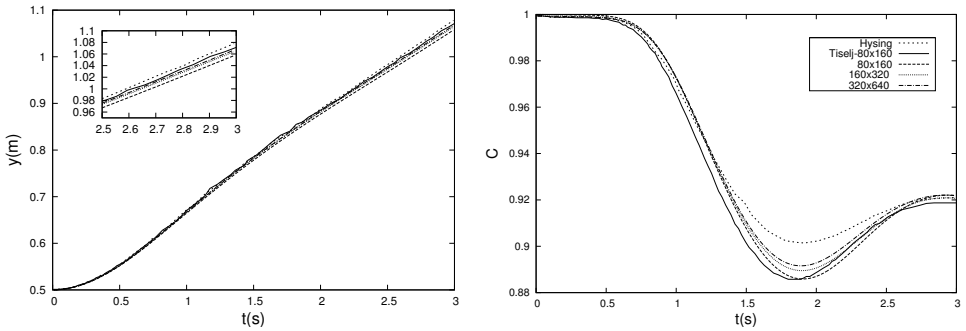

(a) Mass center (b) Circularity

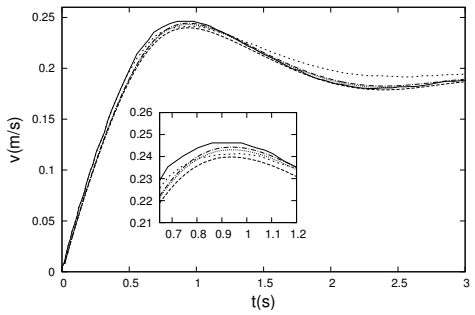

(c) Rise velocity

Figure 2.13: Performance of rising bubble with LSM

is closer to a Tiselj curve between $1.5s$ and $2.5s$, and the result is far from the Tiselj curve, and towards the Hysing curve as the mesh size increases. On the contrary, without the Level Set method, the data in coarse mesh is closer to a Hysing curve between $1.5s$ and $2.5s$ and the curve goes close to the Tiselj curve as the mesh become finer. Meanwhile, the clear disagreement was observed after $2.5s$, especially in the coarse mesh.

All the results show the good consistency with the Tiselj result. The total mass in all the simulations is conserved very well, and the maximum error is less than 0.1%.

In order to compare the key parameters quantitatively, Table 2.4 was given. In the table, the position of center mass at $t = 3s$, the maximum rising velocity and its appearing time, the minimum circularity and its appearing time are listed and compared with the Hysing result and Tiselj result. It can be summarized from the

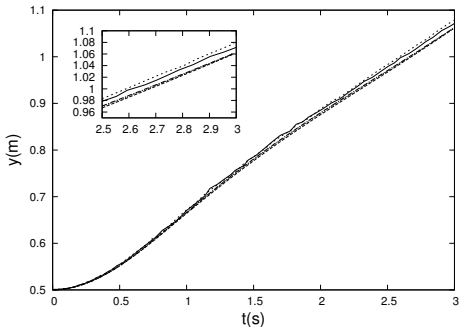

(a) Mass center

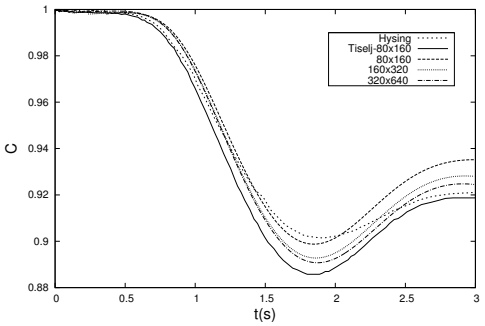

(b) Circularity

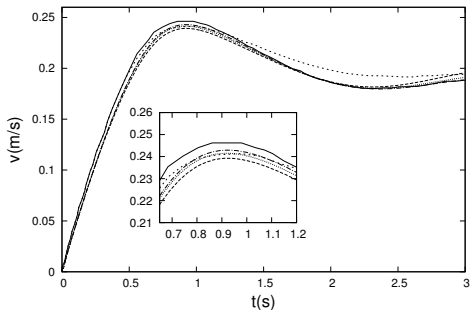

(c) Rise velocity

Figure 2.14: Performance of rising bubble without LSM

table that the results of the two fluid model with and without Level Set method using Fractional Step method are very similar to the results of Hysing and Tiselj.

Table 2.4: Parameter comparison of bubble development

			with level set method			without level set method		
Parameter	Hysing	Tiselj	80×160	160×320	320×640	80×160	160×320	320×640
Mass center($t = 3s$)	1.0817	1.0679	1.0569	1.064	1.066	1.060	1.061	1.061
Max velocity(m/s)	0.2418	0.2457	0.2398	0.2431	0.2443	0.2392	0.2415	0.2429
time(s)	0.9214	0.9235	0.9301	0.9301	0.9301	0.9251	0.9201	0.9251
Min circularity(m)	0.9012	0.8876	0.8859	0.8895	0.8916	0.8987	0.8928	0.8907
time(s)	1.8830	1.8915	1.9001	1.9001	1.8901	1.8501	1.8601	1.8701

2.5.6 Sedimentation

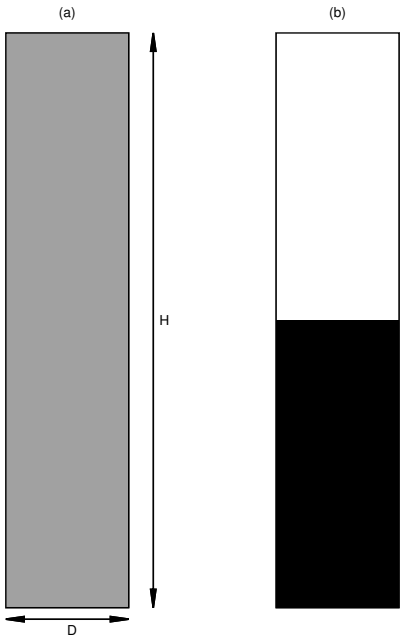

Figure 2.15: Sedimentation case. (a) Initial state (b) Final state

Sedimentation is a classical dispersed flow case, in which the interface characteristic length scale of fluids are usually smaller than the grid cell. This problem is a simplified physical phenomena proposed by Coquel et al. [39], based on a separation of air and water by gravity. It consists of a vertical tube of $H = 7.5$m length and $D = 1$m diameter, where the gravity is the only source term, any others terms including drag forces are not taken into account. At the initial condition of zero gravity, the tube is filled with stagnant liquid and gas with a homogeneous volume fraction of 0.5 and a uniform pressure of $p_0 = 0.1MPa$ (Fig. 2.15(a)). The tube is closed at both ends and, thus, the velocities of the two fluids are forced to equal zero at both ends. The Neumann boundary condition is imposed on lateral walls in velocity and volume fraction. At one instant, the gravity is suddenly imposed on the whole system. Due to the gravity effect, the liquid falls downwards to the bottom of the tube, while the gas come up to the top of the tube (Fig. 2.15(b)). The objective of this problem is to check the capability of the model in the dispersed flow with small scale interface

describing countercurrent flow conditions with strong void gradients typical of many situations where phase separation are dominating.

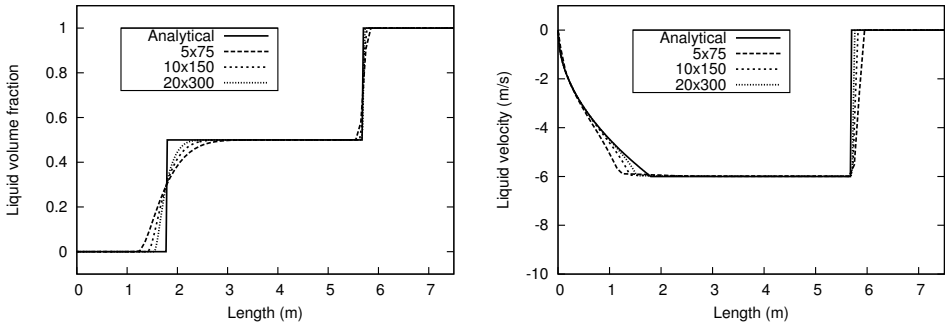

(a) Volume fraction (b) Liquid velocity

Figure 2.16: Comparison between numerical and analytical results at t=0.6s

The physical properties for water are: $\rho_1 = 1000kg/m^3$ and $\mu_1 = 0.798\times10^{-3}Pa{\cdot}s$ and for air: $\rho_2 = 1kg/m^3$ and $\mu_1 = 1.983 \times 10^{-5}Pa \cdot s$. In order to check the mesh independence, the simulations are respectively implemented using 5×75, 10×150 and 20×300 control volumes. Since it is a dispersed flow, interface sharpening equation in step 6 (section 3.3) is not implemented in the case. Vanleer flux limiter is applied on continuity and momentum equations, and the obtained results are compared with the analytical solution from literature [40]. The liquid volume fraction distribution

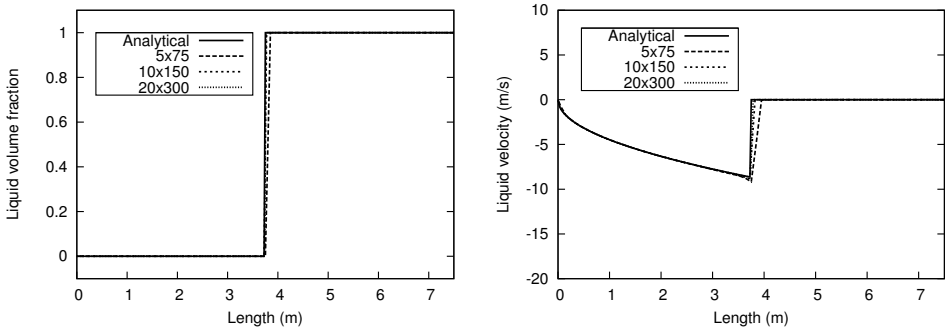

(a) Volume fraction (b) Liquid velocity

Figure 2.17: Comparison between numerical and analytical results at t=1.0s

along the vertical height at different times is shown in Fig. 2.16 and Fig. 2.17. The comparisons show that the present numerical results are in good agreement with the analytical ones. Separation point between mixture phase and liquid phase at $t = 0.6s$ (Fig. 2.16(a)) presents a slight delay in comparison with the analytical prediction with a maximum deviation of 0.1m. The differences measured by 1-norm $\|E\| = \sum_j \Delta x |\alpha_j - \alpha_j^{analytical}|$ are 0.2466, 0.1458, 0.0906 at $t = 0.6s$ for three different refined meshes respectively, and 0.1997, 0.1001, 0.0500 at $t = 1s$ for the same mesh sizes. The slight delay of separation point between gas and liquid phase still exists with the same discrepancy of 0.1m (Fig. 2.17(a)).

2.6 Conclusions

In the present work, the two-fluid model has been solved by means of the explicit Fractional Step method avoiding the problem of implicit formulation under pressure-based iteration method. Surface tension is also solved, while diffusion effects have been reduced, considering high resolution schemes and implementing interface sharpening method. Verification tests of mesh density and numerical schemes are carried out in order to confirm the influence of discretization scheme.

The capability of the two-fluid model with Fractional Step method in flow with small or large scale length interface has been assured by means of different numerical and experimental cases with and without interface sharpening method. In order to highlight the capability of the two fluid model in flow with large scale length, Rayleigh-Taylor instability, Dam break, droplet and rising bubble have respectively been implemented. The results obtained are all consistent with the referred data. The case of Rayleigh-Taylor instability illustrates clearly the advantages of Vanleer flux limiter and interface sharpening on controlling the diffusion. Dam break cases shows the good performance in the flow with high density ratio and high viscosity. Through the simulation of pressure jump over droplet interface, oscillating droplet and rising bubble, the capability of the two-fluid model where surface tension dominated was validated. The capability of the two-fluid model in the flow with small scale length interface is presented in the case of sedimentation.

Overall, the present simulations and results conclude that, the two fluid model with small or large characteristic scales can be solved successfully to obtain the accurate results through Fractional Step Method algorithm, and it can also be applied to simulate the free surface flow if appropriate formulations and parameters are used. The fractional step method is able to solve the large characteristics scale problems without interface sharpening even with coarse meshes, reducing the diffusion and sharp the interface in all situations.

References

[1] L. Strubelj, I. Tiselj, and B. Mavko. Simulations of free surface flows with implementation of surface tension and interface sharpening in the two-fluid model. *International Journal of Heat and Fluid Flow*, 30(4):741–750, 2009.

[2] S. V. Patankar. *Numerical heat transfer and fluid flow.* Hemisphere, 1980.

[3] N.N.Yanenko. *The Method of Fractional Steps.* Springer-verlag, 1971.

[4] Alexandre Joel Chorin. Numerical solution of the Navier-Stokes Equations. *Mathematics of Computation*, 22(104):745–762, 1968.

[5] M Ishii and T Hibiki. *Thermo-fluid Dynamics of Two-phase flow.* Springer:New York/Berlin, 2006.

[6] R.S Oey, R.F Mudde, L.M Portela, and H.E.A van den Akker. Simulation of a slurry airlift using a two-fluid model. *Chemical Engineering Science*, 56(2):673 – 681, 2001.

[7] Gregor Cerne and Stojan. Petelin. Coupling of the interface tracking and the two-fluid models for the simulation of incompressible two-phase flow. *Journal of Computational Physics*, 171(2):776–804(29), 2001.

[8] Vivek V. Buwa and Vivek V. Ranade. Dynamics of gas–liquid flow in a rectangular bubble column: experiments and single/multi-group CFD simulations. *Chemical Engineering Science*, 57(22–23):4715 – 4736, 2002.

[9] Kai Yan and Defu Che. A coupled model for simulation of the gas-liquid two phase flow with complex flow patterns. *International Journal of Multiphase flow*, 36(4):333–348, 2010.

[10] M. Ishii and K. Mishima. Two-fluid model and hydrodynamic constitutive relations. *Nuclear Engineering and Design*, 82(2–3):107 – 126, 1984.

[11] L. Strubelj and I. Tiselj. Two-fluid model with interface sharpening. *International Journal for Numerical Methods in Engineering*, 85(5):575–590, 2011.

[12] Yann Bartosiewicz, Jérôme Lavieville, and Jean-Marie Seynhaeve. A first assessment of the NEPTUNE-CFD code: Instabilities in a stratified flow comparison between the VOF method and a two-field approach. *International Journal of Heat and Fluid Flow*, 29(2):460–478, 2008.

[13] Elin Olsson and Gunilla Kreiss. A conservative level set method for two phase flow. *Journal of Computational Physics*, 210(1):225–246, 2005.

[14] D.R Liles and Wm.H Reed. A semi-implicit method for two-phase fluid dynamics. *Journal of Computational Physics*, 26(3):390 – 407, 1978.

[15] John H Mahaffy. A stability-enhancing two-step method for fluid flow calculations. *Journal of Computational Physics*, 46(3):329 – 341, 1982.

[16] H Bruce Stewart and Burton Wendroff. Two-phase flow: Models and methods. *Journal of Computational Physics*, 56(3):363 – 409, 1984.

[17] Francis H Harlow and Anthony A Amsden. A numerical fluid dynamics calculation method for all flow speeds. *Journal of Computational Physics*, 8(2):197 – 213, 1971.

[18] Andrea.P and Gretar.T. *Computational Methods for Multiphase flow.* Cambrige University Press, 2007.

[19] Guan Heng Yeoh and Jiyuan Tu. *Computational techniques for multiphase flow.* Butterworth-Heinemann, 2009.

[20] D. B. Spalding. *Calculation of two-dimensional two-phase flows.* Hemisphere, 1979.

[21] D. B. Spalding. Developments in the ipsa procedure for numerical computation of multiphase flow phenomena. In *In T. M. Shi, editor, Proceedings of the Second National Symposium on Numerical Methodologies in Heat Transfer*, pages 421–436. Hemisphere, 1983.

[22] R.I Issa. Solution of the implicitly discretised fluid flow equations by operator-splitting. *Journal of Computational Physics*, 62(1):40 – 65, 1986.

[23] L.A.Monthe. A study of splitting scheme for hyperbolic conservation laws with source terms. *Journal of Computational and Applied Mathematics*, 137(1):1–12, 2001.

[24] Iztok Tiselj and Andrej Horvat. Accuracy of the operator splitting technique for two-phase flow with stiff source terms. *In: Proceedings of the 2002 ASME Joint US-European Fluids Engineering Conference. Montreal, Que, Canada*, 1:1165–1171, 2002.

[25] T. A. Davis. Suitesparse, 2013.

[26] R. Courant, K. Friedrichs, and H. Lewy. Über die partiellen differenzengleichungen der mathematischen physik. *Mathematische Annalen*, 100(1):32–74, 1928.

[27] Peter Lax and Burton Wendroff. Systems of conservation laws. *Communications on Pure and Applied Mathematics*, 13(2), 1960.

[28] Bram Van Leer. Towards the ultimate conservative difference scheme. IV. A new approach to numerical convection. *Journal of Computational Physics*, 23(3):276 – 299, 1977.

[29] Stephen Hugh. Garrioch. *A Volume Tracking Method for the Simulation of Two-Fluid Flows.* PhD thesis, McGill Univeristy, 2000.

[30] K.P.Thiagarajan K.Abdolmaleki and M.T.Morris-Thomas. Simulation of the Dam Break problem and impact flows using a Navier-Stokes solver. *15th Australasian Fluid Mechanics Conference*, pages 13–17, 2004.

[31] Marcela A. Cruchaga, Diego J. Celentano, and Tayfun E. Tezduyar. Collapse of a liquid column: numerical simulation and experimental validation. *Computational Mechanics*, 39(4):453–476, 2007.

[32] Marianne M. Francois, Sharen J. Cummins, Edward D. Dendy, Douglas B. Kothe, James M. Sicilian, and Matthew W. Williams. A balanced-force algorithm for continuous and sharp interfacial surface tension models within a volume tracking framework. *Journal of Computational Physics*, 213(1):141–173, 2006.

[33] M. Seifollahi, E. Shirani, and N. Ashgriz. An improved method for calculation of interface pressure force in PLIC-VOF methods. *European Journal of Mechanics-B/Fluids*, 27(1):1–23, 2008.

[34] Takashi Yabe, Feng Xiao, and Takayuki Utsumi. The constrained interpolation profile method for multiphase analysis. *Journal of Computational Physics*, 169(2):556–593, 2001.

[35] S.Vincent and J.P.Caltagirone. Test-case no 10: parasitic currents induced by surface tension(PC). *Multiphase Science and Technology*, 16(1-3):69–74, 2004.

[36] D.J. Torres and J.U. Brackbill. The Point-Set Method: Front-tracking without connectivity. *Journal of Computational Physics*, 165(2):620–644, 2000.

[37] B. Stuckrad, W. J. Hiller, and T. A. Kowalewski. Measurement of dynamic surface tension by the oscillating droplet method. *Experiments in Fluids*, 15(4-5):332–340, 1993.

[38] S. Hysing, S. Turek, D. Kuzmin, N. Parolini, E. Burman, S. Ganesan, and L. Tobiska. Quantitative benchmark computations of two-dimensional bubble dynamics. *International Journal for Numerical Methods in Fluids*, 60(11):1259–1288, 2009.

[39] F. Coquel, K. El Amine, E. Godlewski, B. Perthame, and P. Rascle. A numerical method using upwind schemes for the resolution of two-phase Flows. *Journal of Computational Physics*, 136(2):272 – 288, 1997.

[40] Steinar Evje and Tore Flåtten. Hybrid flux-splitting schemes for a common two-fluid model. *Journal of Computational Physics*, 192(1):175 – 210, 2003.

3

Numerical study of heat and mass transfer in laminar flow

The part contents of this chapter have been published as:
Xiaofei Hou, Rigola Joaquim, Lehmkuhl Oriol, Oliet Carles and Pérez-Segarra Carlos D. Numerical modeling of simultaneous heat and moisture transfer under complex geometry for refrigeration purposes. *Journal of Physics: Conference Series*, Vol. 395, No.1, 2012

3.1 Abstract

In this chapter, the mixture model is introduced and used to solve the problem of evaporation/condensation in the multicomponent flow. Three cases are chosen to investigate the effect of different parameters on the evaporation and flow. A hydrodynamically fully developed laminar flow over the surface of a water tray is firstly simulated in a horizontal 3D rectangular duct. Its goal is to validate the evaporation model with constant physical property in our simulation. The obtained results are compared with the published numerical and experimental results. The contour of temperature and vapor density of air at a cross section is provided and analyzed. In order to validate the falling film model, the heat and mass transfer with the evaporation of a falling film in a cavity was studied numerically. A simplified model for the falling film was adopted, which can avoid the solution of the momentum and energy governing equations in the liquid film. Meanwhile the governing equation with variable physical property is used to further test the accuracy of the property computation. The numerical results are analyzed and compared with the existing numerical

and experimental data. It is helpful to predict the evaporation and condensation rates under the natural convection condition. In the third case, a mixed convection flow with a falling film is tested. The affecting factors are also analyzed and compared to the existing data.

3.2 Introduction

In multicomponent flows, evaporation and condensation on surface are widely encountered as a consequence of the interaction of humid air and cold surface or for heat transfer augmentation. Notable examples include cooling towers, evaporator in domestic refrigerator and air conditioner and so on. The primary goal of the present chapter is to model the behaviour of surface evaporation and condensation in different cases and to validate the capability of the homogeneous mixture model in the multicomponent flow. The major investigations are focused on laminar mixed flow.

In these test cases, the governing equation with constant physical properties has been tested firstly and the same case as reference [1] is performed. The results obtained - outlet air and water temperature, outlet relative humidity, average Sherwood number, local Nusselt and Sherwood number, temperature and concentration field of different cross sections are compared with the reference experimental and numerical ones for validation of the presented model.

The simultaneous heat and mass transfer with a falling liquid film is important since it can enhance heat transfer greatly. Thus it is also a focus of the present study. Regarding to the falling film, its full governing equation is not solved. Instead, in order to simplify the computation, the energy balance equation is employed as a boundary condition considering the uniform temperature inside the falling liquid film. The one-dimensional velocity is assumed and it is only dependent on the film flow rate. The simplified film model is validated in a natural convection case of Ben Jabrallah et al. [2]. With the validated model of liquid film, a mixed convection flow case proposed by Cherif et al. [3] is also implemented. In the two cases, the effects of heat flux, feed temperature and liquid flow rate on evaporation are analyzed as well.

3.3 Mathematical model of the mixture

The movement of the air-vapor fluid mixturre inside the channel are governed by the following equations of conservation of mass, momentum, energy and concentration. They are expressed in 3D Cartesian coordinate: Mass conservation equation is

$$\frac{\partial \rho}{\partial t} + \frac{\partial (\rho u_j)}{\partial x_j} = 0 \tag{3.1}$$

Momentum equation

$$\frac{\partial(\rho u_i)}{\partial t} + \frac{\partial(\rho u_j u_i)}{\partial x_j} = -\frac{\partial p}{\partial x_i} + \frac{\partial^2(\mu u_i)}{\partial x_j^2} + f_i \tag{3.2}$$

Energy equation

$$\frac{\partial(\rho T)}{\partial t} + \frac{\partial(\rho u_j T)}{\partial x_j} = \frac{\partial}{\partial x_j}(\frac{\kappa}{c_p}\frac{\partial T}{\partial x_j}) \tag{3.3}$$

Concentration equation is

$$\frac{\partial(\rho c)}{\partial t} + \frac{\partial(\rho u_j c)}{\partial x_j} = \frac{\partial^2(\rho D c)}{\partial x_j^2} \tag{3.4}$$

u_j is the velocity components in the x, y and z directions, respectively. p, T and c are the pressure, temperature and vapor mass fraction. ρ, g, κ and c_p are density, gravity, thermal conductivity and specific heat at constant pressure. Buoyancy forces created by both temperature and concentration gradient are considered and are included in the y-momentum equation. In the constant physical property condition, $f = \rho\beta g(T - T_0) + \rho\beta^* g(c - c_0)$. The volumetric coefficient of thermal expansion β and the specified expansion coefficient β^* for air are taken approximately as $\beta = 1/T_0$ and $\beta^* = (M_a/M_v - 1)$ based on reference temperature T_0 and concentration c_0. They are the inlet temperature and vapor specific density of air, respectively.

In the variable property condition, $f = (\rho - \rho_0)g$. The quantities per unit volume are averaged by their respective volume fraction. The detailed calculation of mixture physical property is referred to Appendix A.

The above governing equation is solved by using the CFD&HT code–Termofluids [4] which is an intrinsic 3D parallel CFD object-oriented code applied to unstructured/structured meshes, which can handle the thermal and fluid dynamic problems in complex geometries. Fully conservative second-order schemes for spatial discretization [5] and second order explicit time integration are used [6]. The pressure-velocity linkage is solved by means of an explicit finite volume fractional step procedure.

3.4 Model of liquid film

Compared to the heat transfer without evaporation, heat transfer through a falling liquid film could be augmented clearly since it not only involves the evaporation heat transfer on the liquid surface but also convection heat transfer inside the liquid film. Therefore it is widely applied in the industrial fields. As the thickness of the falling liquid film is by far less than the characteristic dimension(tube diameter and channel width), taking into account the two-dimensional character of the governing equations

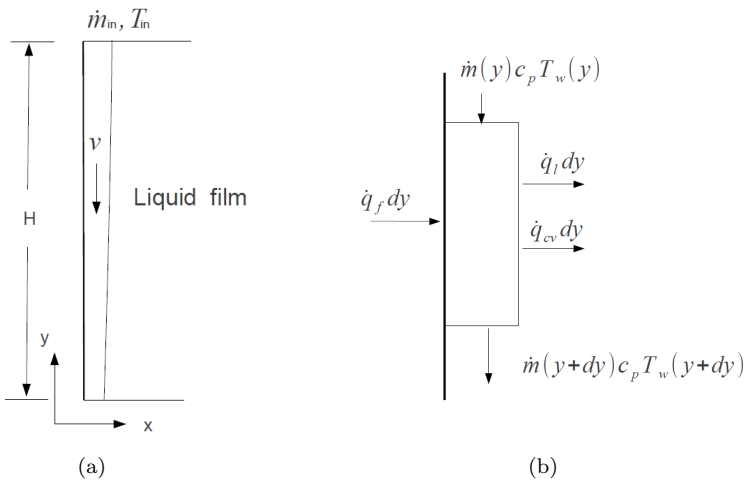

Figure 3.1: Schematic of liquid film

in the liquid film poses several problems and induces heavy computation. In order to simplify the computation, the flow can be assumed to be laminar if its Re number is less than 1500 [7]. With the above assumption, inertial terms in the momentum equation are negligible. The momentum and energy balance equations for the liquid film can be expressed with the following form [8]:
Momentum equation

$$\frac{\partial}{\partial x}(\mu_w \frac{\partial v}{\partial x}) + \rho_w g = 0 \tag{3.5}$$

Energy equation is

$$\rho_w c_p v_w \frac{\partial T_w}{\partial y} = \frac{\partial}{\partial x}(\lambda_w \frac{\partial T_w}{\partial x}) \tag{3.6}$$

where the right member expresses the conductive transport. In the two above momentum and energy equations, the film being vertical, the convective transport in energy equation is reduced to the term with respect to y direction.

At the phase interface, the following assumption is often applied,

$$v_I = v_{G,I} = v_{L,I}, \quad T_I = T_{G,I} = T_{L,I} \tag{3.7}$$

$$\tau_I = [\mu \frac{\partial v}{\partial x}]_{L,I} = [\mu \frac{\partial v}{\partial x}]_{G,I} \tag{3.8}$$

The velocity profile in liquid film is obtained by integrating the equation (3.5) using the boundary conditions given by equations (3.7) and (3.8)

$$v_y(x) = -\frac{\rho_w g}{2\mu_w}x^2 + [\frac{\mu_g}{\mu_w}(\frac{\partial v}{\partial x})_g|_{x=\delta} + \frac{\rho_w g}{\mu_w}]x \tag{3.9}$$

The mass flow rate per unit perimeter of the liquid film at each y level, $\dot{m}_y$ can be obtained from the following equation:

$$\dot{m}_y = \int_{x=0}^{x=\delta} \rho_w v_w(x)\,\mathrm{d}x \tag{3.10}$$

The integral in the above equation is evaluated using the velocity profile equation (3.9), and the following equation is obtained for mass flow rate of the falling liquid film

$$\dot{m}_y = \frac{\rho_w^2 g}{3\mu_w}\delta^3 + \frac{\rho_w \delta^2}{2}\frac{\mu_g}{\mu_w}(\frac{\partial v}{\partial x})_g|_{x=\delta} \tag{3.11}$$

The liquid film rate at each y level can also be obtained in terms of the evaporation and inlet liquid film flow rate. The overall mass balance in the gas and liquid film should be satisfied:

$$\dot{m}_y = \dot{m}_{in} - \int_y^H \dot{m}_{evp}\mathrm{d}y \tag{3.12}$$

With a known film flow rate, the equation (3.11) is a polynomial function for liquid film thickness δ. It can be solved by various methods to obtain the film thickness δ. Neglecting the shear stress at gas-liquid interface, the thickness of the liquid film can be calculated as,

$$\delta = (\frac{3\dot{m}\nu}{\pi d\rho g})^{1/3} \tag{3.13}$$

The velocity at interface is

$$U = \frac{\rho g}{\mu}(\delta y - y^2) = \frac{\rho g}{\mu}\frac{\delta^2}{2} \tag{3.14}$$

In two-dimensional model of energy equation the temperature profile is assumed to vary along x direction. With the two-dimensional energy equation, the computation cost is also expensive. Feddaoui et al. [9] have conducted the simulation of falling liquid film along an insulated vertical channel. The above governing equations (3.5) and (3.6) were employed to solve the falling liquid film. In his study, the film flow rate was equal to $10^{-2} kg \cdot m^{-1} \cdot s^{-1}$. The wall temperature were compared against the interfacial temperature. It was found that the temperature difference between them is very small and can be neglected. In addition, in experiment of An et al. [10] they

also thought the wall temperature was equal to film temperature with the film flow rate of $1.3 * 10^{-2} kg \cdot m^{-1} \cdot s^{-1}$ and $2.7 * 10^{-2} kg \cdot m^{-1} \cdot s^{-1}$. In this chapter, the film flow rate has a maximum value of $1.74 * 10^{-3} kg \cdot m^{-1} \cdot s^{-1}$. Therefore, for simplifying the computation, the temperature in the liquid film is assumed to vary little with respect to the x coordinate and one-dimensional model was employed in the present numerical study. In any vertical zone of the falling film, a simplified method for the film temperature - energy balance for a section of width dy (Fig. 3.1(b)) is performed in term of the energy balance in this study,

$$\dot{q}_f \mathrm{d}y = \dot{m} c_p \mathrm{d}T_w + \dot{q}_l \mathrm{d}y + \dot{q}_s \mathrm{d}y \tag{3.15}$$

where $\dot{q}_l = \dot{m}_v L_v$, q_f is the heat flux imposed on wall and $\dot{q}_s = -\lambda_g \frac{\partial T}{\partial x}|_{x=\delta}$ are the heat fluxes corresponding respectively to evaporation and convection between liquid film and air-vapor mixture flow.

3.5 Boundary and interfacial conditions

3.5.1 For the liquid film

The liquid water enters the heated plates with a uniform profile of mass flow rate $\dot{m}_{in}$ and temperature T_{in} at the top of geometry as shown in Fig.3.1(a)

$$\dot{m} = \dot{m}_{in}, \quad T_w = T_{in} \qquad at \quad y = H \tag{3.16}$$

where T_w represents the mean temperature of the water film at the considered height. At steady state, it is assumed that the heat flux absorbed by the external face is totally transmitted to the liquid film which flows on its internal face, giving the condition

$$-\lambda_w \frac{\partial T_w}{\partial x} = \dot{q}_f \qquad at \quad x = 0 \tag{3.17}$$

The following condition of adherence of the liquid at the internal face of the plate is

$$v_w = 0 \qquad at \quad x = 0 \tag{3.18}$$

3.5.2 At the liquid-gas interface

The hypothesis of continuity and velocity and temperature at the interface($x = \delta$) allows us to write

$$v_w(\delta) = v(\delta), \qquad T_w(\delta) = T(\delta) \tag{3.19}$$

The transverse velocity of the air-vapor mixture can be expressed as Tsay and Lin [8] and Eckert [11]

$$u(\delta) = -\frac{D}{1 - c_\delta} (\frac{\partial c}{\partial x})_\delta \tag{3.20}$$

The continuity of the heat flux at the interface is given by

$$-\lambda_w(\frac{\partial T_w}{\partial x})_\delta = -\lambda_g(\frac{\partial T}{\partial x})_\delta + L_v\dot{m}_v \tag{3.21}$$

If the liquid film does not appear (e.g. is still the wet wall), the term of the left side is the heat flux $\dot{q}_f$ imposed on the wall and the convection and evaporation will be at the equilibrium state. The mass flux $\dot{m}_v$ exchanged at the interface is given by applying Fick's law [11] [12], and supposing that the interface is impermeable to dry air, resulting in

$$\dot{m}_v = -\frac{\rho_g D}{1-c_\delta}(\frac{\partial c}{\partial x})_\delta \tag{3.22}$$

where D is the binary diffusion coefficient of water vapor in air.

The thermodynamic equilibrium is assumed during the change of phase, the concentration at liquid-gas interface is,

$$c(\delta) = c_{sat}(T_\delta) \qquad at \quad x = \delta \tag{3.23}$$

It is calculated according to Dalton law, assuming that the air-vapor mixture is an ideal gas mixture [10]

$$c_{sat} = \frac{p_{v,sat}M_v}{p_{v,sat}M_v + (p - p_{v,sat})M_a} \tag{3.24}$$

where p is the total pressure and $p_{v,sat}$ is the vapour pressure at the interface temperature at saturated conditions.

3.6 Characteristic parameters

The local total heat transfer coefficient h_g at the interface is defined as given below

$$\dot{q}_s = -\lambda_w(\frac{\partial T_w}{\partial x})|_{x=\delta} = h_g(T_I - T_m) \tag{3.25}$$

where T_m is the local bulk temperature of the gas-vapor mixture in the channel and T_I is the temperature at the interface. T_m is defined as an integrated average of the local fluid temperature at a specified cross section

$$T_m = \frac{\int_{A_L}\rho v T \mathrm{d}A_L}{\int_{A_L}\rho v \mathrm{d}A_L} \tag{3.26}$$

As seen in the equation (3.21), the heat transfer $\dot{q}_I$ at interface include two parts: convection $\dot{q}_s$ and evaporation heat transfer $\dot{q}_l$, which correspond to the two heat

transfer coefficients: h_s and h_l. The local Nusselt number along the interface of gas-liquid is defined as:

$$Nu_y = \frac{h_g \Phi}{\lambda_g} = \frac{\dot{q}\Phi}{\lambda_g(T_I - T_m)} = \frac{(\dot{q}_s + \dot{q}_l)\Phi}{\lambda_g(T_I - T_m)} = Nu_{y,s} + Nu_{y,l} \tag{3.27}$$

where Φ is the characteristic length. $Nu_{y,s}$ and $Nu_{y,l}$ are the local Nusselt number for sensible and latent heat transfer, respectively. The mean Nusselt number is defined as

$$Nu_m = \frac{1}{A_L} \int_{A_L} Nu_y \mathrm{d}A_L \tag{3.28}$$

Similar for the mass transfer, the local Sherwood number is defined by

$$Sh_y = \frac{h_m \Phi}{D} = \frac{\dot{m}_v \Phi}{(c_x - c_m)D}, \quad c_m = \frac{\int_{A_L} \rho v c \mathrm{d}A_L}{\int_{A_L} \rho v \mathrm{d}A_L} \tag{3.29}$$

and the mean Sherwood number is

$$Sh_m = \frac{1}{A_L} \int_{A_L} Sh_y \mathrm{d}A_L \tag{3.30}$$

The mean specific mass flow rate of evaporation is defined by

$$\overline{\dot{m}}_v = \frac{1}{A_L} \int_{A_L} \dot{m}_y \mathrm{d}A_L \tag{3.31}$$

To better understand the efficiency of a system, a dimensionless ratio M_r representing the evaporated mass fraction is defined by

$$M_r = \frac{\int_{A_L} \dot{m}_y \mathrm{d}A_L}{\dot{m}_{in}} \tag{3.32}$$

The thermal efficiencies of evaporation are defined as

$$\eta_l = \frac{\dot{q}_l}{\dot{q}_f}, \quad \eta_s = \frac{\dot{q}_s}{\dot{q}_f}, \quad \eta_m = \frac{\dot{q}_m}{\dot{q}_f} \tag{3.33}$$

where η_l, η_s and η_m represents the ratio of heat flux for evaporation, convection and the heat flux carried out by liquid film versus the wall heat flux.

3.7 Numerical tests

In order to address the ability of our code and study the effect of different parameters on heat and mass transfer, three cases are chosen to conduct the simulation. In

the first case, a hydrodynamically fully developed flow of moist air flowing over the surface of water tray is conducted. It is used to validate the capability of the homogeneous mixture model with constant physical property. The second case is used to validate the simplified liquid film model. The natural convection with a liquid film is conducted and the effect of heat flux, film flow rate and inlet temperature on the evaporation are studied considering the variable physical properties. The final case is used to study the mixed convection with a falling liquid film and variable physical properties.

3.7.1 Test case 1

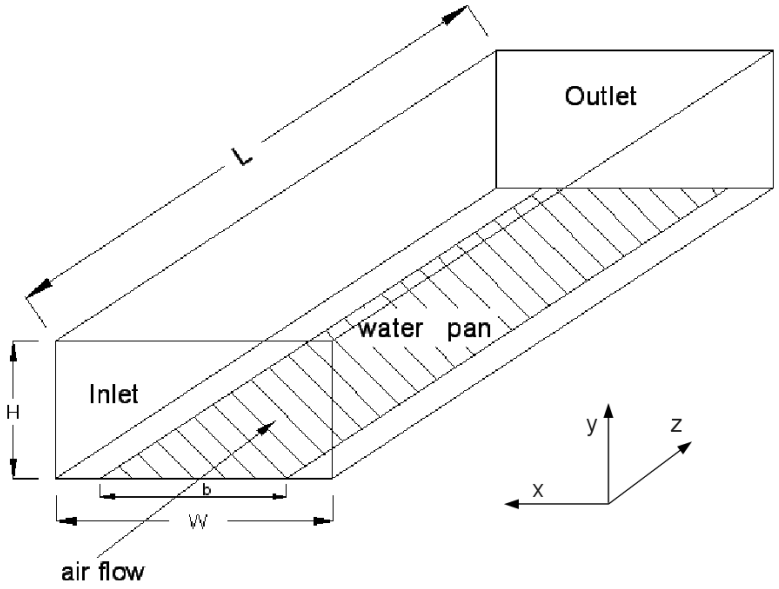

Figure 3.2: Geometry of the rectangular duct

Talukdar et al. [1] and Iskra et al. [13] performed the experiment and numerical simulation of laminar flow of moist air in a duct. The experimental data and simulation results were compared and analyzed in detail. The same case is chosen to validate our code in simultaneous heat and mass transfer with an evaporating wall and constant property.

The geometry of the system is a horizontal 3D rectangular duct with a dimension of $298mm(W) \times 20.5mm(H) \times 600mm(L)$ (refer to [1] for details). There is a water

pan of $280mm$ in width centered in the duct bottom wall with a $9mm$ insulation layer in each side of bottom boundary. The other walls are well insulated and considered adiabatic. A fully-developed axial velocity profile is imposed at the entrance $z = 0$ (Equation (3.34) [14]) with a constant temperature T_0 and relative humidity RH_0. The flow is assumed to be steady, laminar and has constant thermal physical properties except the density which is allowed to vary in the buoyancy term of the y momentum equation. Viscous dissipation and compressibility effects in the energy equation are also neglected. To facilitate the analysis, the secondary effects of concentration gradient on thermal diffusion and of thermal diffusion on mass transfer have been neglected. The simulation was carried out on $25 \times 25 \times 50$ and $50 \times 50 \times 100$ control volumes respectively in the present work and the maximum deviation of 3% for water outlet temperature was observed. $50 \times 50 \times 100$ control volumes was chosen to discuss the final result. The velocity profile is given in Equation (3.34),

$$\frac{w}{w_{av}} = (\frac{m+1}{m})(\frac{n+1}{n})[1-(\frac{y}{H/2})^n][1-(\frac{x}{W/2})^m] \tag{3.34}$$

The average velocity w_{av} is calculated from the specified Reynolds numbers, and parameters m and n are detailed by:

$$w_{av} = \frac{Re\mu}{\rho D_h} \tag{3.35}$$

$$m = 1.7 + 0.5(\gamma)^{-1.4}$$

$$\begin{cases} n = 2 & for \quad \gamma <= 1/3 \\ n = 2 + 0.3(\gamma - 1/3) & for \quad \gamma > 1/3 \end{cases}$$

where $\gamma(= W/H = 14.54)$ is the aspect ratio of the duct.

In the case, constant property is assumed and buoyancy force in momentum equation is $f = \rho\beta g(T - T_0) + \rho\beta^* g(\rho c - \rho c_0)$, where the volumetric coefficient of thermal expansion β and the specified expansion coefficient β^* for air are taken approximately as $0.00343(1/K)$ and $0.513(m^3/kg)$ based on reference temperature T_0 and concentration c_0. They are the inlet temperature and vapor specific density of air, respectively.

At bottom wall($y = 0$), the water is static and the vapor water is saturated at local temperature. In the equation (3.21), the left side term is zero and the amount of heat of phase change required for the evaporation of water is equal to the sensible heat transfer from the air to the water surface. This gives a boundary condition at the bottom surface as:

$$-\lambda \frac{\partial T}{\partial y}|_{y=0} = \frac{\rho L_v D}{1-c} \frac{\partial c}{\partial y}|_{y=0} \tag{3.36}$$

Table 3.1: Inlet parameters and outlet results in simulation cases

Case	Re	$T_0(°C)$	$RH_0(\%)$
1	2079	22.9	17.9
2	1863	23.1	25.4
3	1583	22.7	19.7
4	1340	22.8	23.0
5	796	22.3	17.2
6	1303	22.1	35.2
7	2059	22.3	34.5
8	699	21.9	33.6
9	844	22.4	53.1
10	1531	22.0	54.7

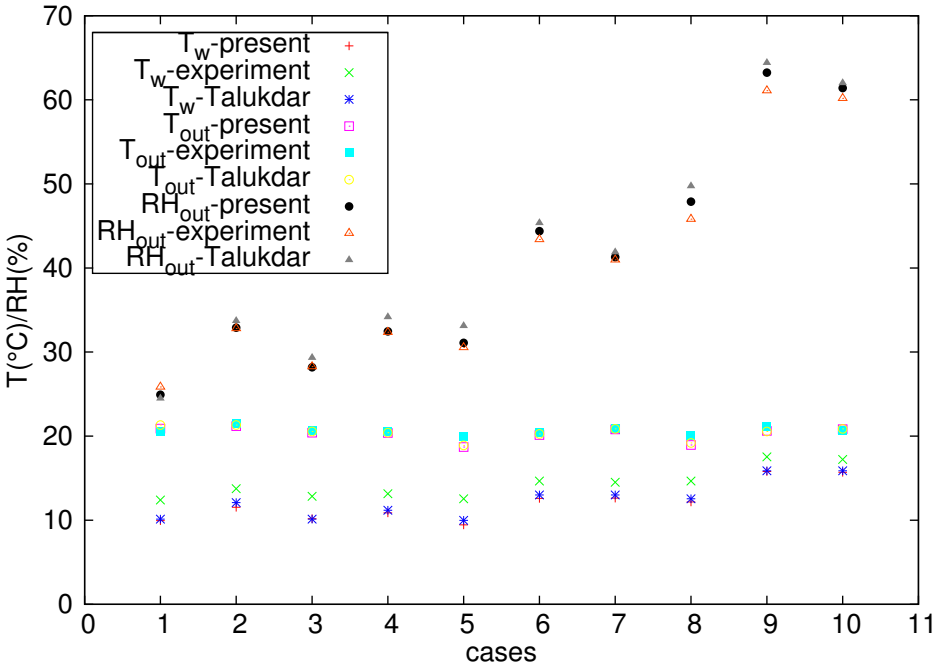

Figure 3.3: Outlet parameters

Table 3.1 provides the specific inlet parameters of different cases. Fig. 3.3 shows the comparison of the present numerical results, experimental data and reference numerical data [1] at outlet. The present results show a good agreement with the reference numerical data, but both present deviations with the experimental result, especially on the pan water temperature of outlet. The average errors of all the 10 cases between the present results and reference numerical data are 0.13°C on air outlet temperature, 1.04% on relative humidity and 0.29°C on water outlet temperature. The average errors between the present results and experimental data are −0.36°C on air outlet temperature, 0.66% on relative humidity and −2.2°C on water outlet temperature. The air outlet temperature presents a slight reduction because of the effect of cold water at bottom and its evaporation. Within the narrow range of inlet temperature from 21.9°C to 23.1°C, the outlet water temperature and air temperature are more influenced by the inlet relative humidity. The higher RH means less evaporation and less heat loss to water, and the outlet air temperature is higher.

Fig. 3.4(a) shows the Sherwood number and the comparison with the experimental and numerical results of Talukdar et al. [1] for case 9. The present numerical results show good agreement with the data of Talukdar et al. [1]. However the difference at the entrance of the duct is greater since the uncertainty and mesh size have a great influence at the beginning. As the flow goes forward, the difference decreases and their profiles are closer. The experimental results are shown with a ±10% error bar considering the uncertainty of the experiment data. Compared to the experimental data, the present results show the same behaviour as the reference numerical data. Case 9 and case 10 which have a higher inlet RH are outside the experiment error bars but the present profile are closer to the experiment data. As the flow develops, Sh value approaches an asymptotic value.

Fig. 3.5 shows the air temperature fields at $z = 0.05m$ and $z = 0.45m$ cross sections for case 9. At the bottom of Fig. 3.5(b), the temperature is lower due to the effect of water evaporation and cold water. Its influence is more obvious at $z = 0.45m$ cross section as the flow approaches the fully hydrodynamically and thermally developed state. It illustrates a curved profile along the x direction. The air temperature field next to two sides of the water pan shows slightly lower temperature than central part. It was not observed by Talukdar et al. [1] since the transverse velocity was not considered in their study.

Fig. 3.6 illustrates the velocity field at the section of z=0.45m. Because of the influence of the additional mass flow transferred through the wall, there exist the density and concentration gradients between the core and wall area, and a secondary flow (low velocity compared to the streamwise direction velocity) is detected from the core to the walls. It causes the non-uniform distribution of temperature across x direction. Since the remaining edge of 9mm in bottom boundary is insulated in each side, the secondary flow generates also a vortex near the wall. Fig. 3.7 illustrates the

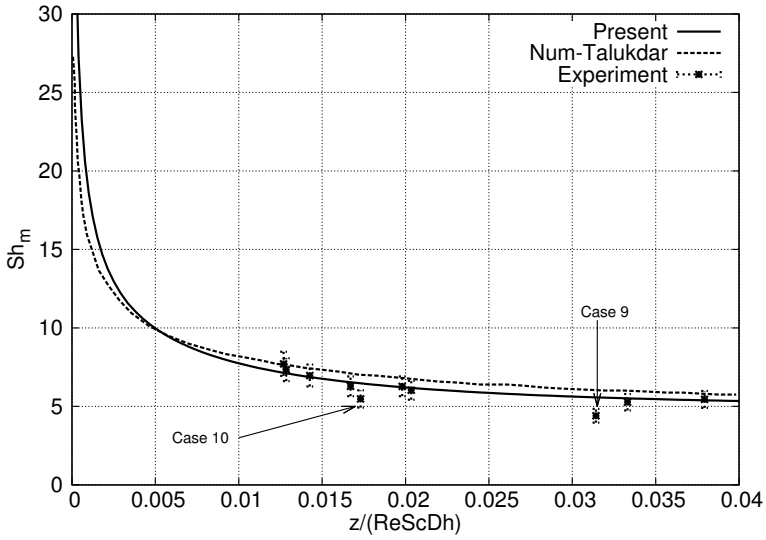

(a) Average Sh number

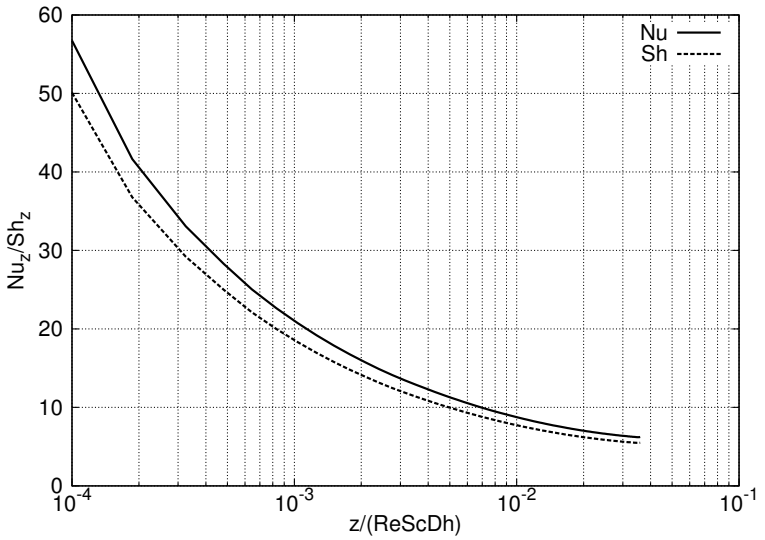

(b) Local Nu and Sh number for case 9

Figure 3.4: The Nusselt and Sherwood number distribution along z direction

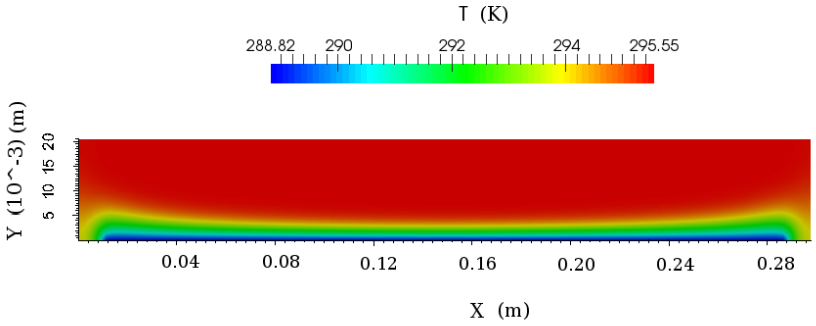

(a) z=0.05m

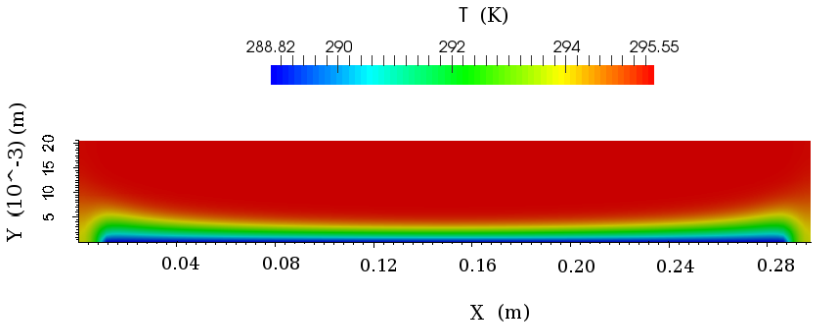

(b) z=0.05m

Figure 3.5: Isotherms at different z location for case 9

boundary layer development of temperature and concentration. The general development shows a good agreement with the boundary layer theory. The temperature and concentration contour are concentrated near the bottom. Both temperature and concentration have great variations within the thin layer, because the water evaporates and heat is transferred to water. The air temperature decreases and water vapor density increases as thermal boundary layer and concentration boundary layer are developed along z direction. According to the heat transfer book [14], the fully developed length of laminar thermal boundary layer for case 9 is more than 1m while the concentration boundary is also longer than the duct length. Therefore, Fig. 3.7

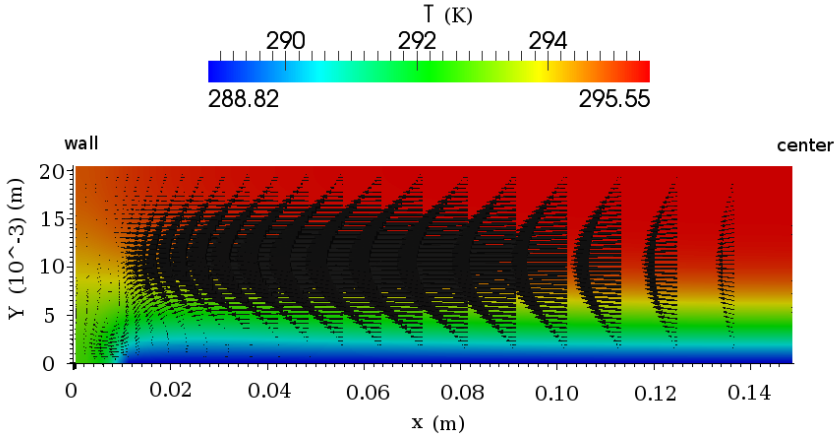

Figure 3.6: Velocity field near left wall for case 9 at the section of z=0.45m

only presents the developing process of temperature and concentration fields. Based on the definition of Pr and Sc number (Pr=0.71, Sc=0.59), the higher Pr means that the thermal boundary develops more slowly than the concentration boundary layer. Fig. 3.4(b) gives the local Nu and Sh number, it can be seen that the Nu number is higher than Sh number along the whole duct. As explained in the reference [1], there exists a relation between the latent heat of evaporation of water and the sensible heat transfer from the air to water under the condition of all the boundaries of the duct insulated,

$$-\lambda\frac{\partial T}{\partial y}|_{y=0} = \frac{\rho_g L_v D}{1-c}(\frac{\partial c}{\partial y})|_{y=0} \Rightarrow \frac{-\Phi\frac{\partial T}{\partial y}|_0}{\Delta T} = -\frac{-\Phi\frac{\partial c}{\partial y}|_0}{\Delta c}\cdot(-\frac{L_v D\Delta c}{\lambda\Delta T(1-c)})$$
$$\Rightarrow Nu_z = Sh_z\cdot(-S)$$

where Φ is characteristic length. S is a dimensionless parameter which shows the ratio between Nu and Sh number. Its value depends on the properties of the fluid. In the simulation of Talukdar et al., the value of S is in a range of -1.06 and -1.08 while the value is -1.13 in the present calculation.

3.7.2 Test case 2

In order to validate the simplified liquid film model - the equation (3.15), the simulation on the distillation experiment [2] in a cavity is conducted considering variable physical properties. At the same time, the effect of variable parameters on

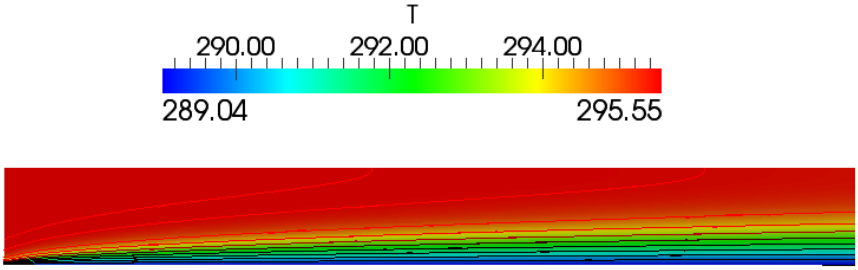

(a) Temperature

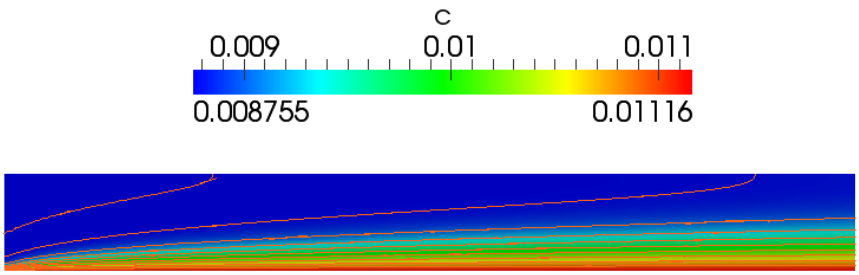

(b) Concentration

Figure 3.7: Contours of temperature and vapor density of air for case 9

the evaporation efficiency is also studied. Fig. 3.8 shows the geometric parameters in the cavity. The cavity is a paralleled channel of low width $b = 0.04m$, formed by a frame of height $h = 0.4m$, length $l = 0.4m$. The whole channel is closed on both sides. On the outer face of the left plate heated by a constant heat flux, a very thin water film flows downwards along the plate. The water film enters with a mass flow rate $\dot{m}_{in}$ and leaves the cell with a mass flow rate $\dot{m}_{out}$. The opposite plate is maintained at constant temperature T_c and a part of water vapor condensates on its surface. Due to the constant heat flux imposed on the plate, the temperature of

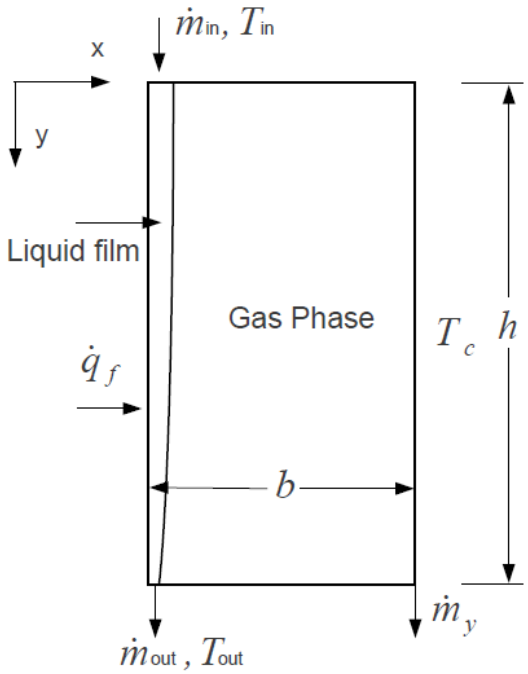

Figure 3.8: Scheme of the distillation cell

liquid film increases as the liquid film flow downwards. The difference in temperature and concentration causes the natural convection flow inside the cavity. Its Rayleigh number is calculated in terms of $Ra = (Gr_t + Gr_c) * Pr$ (the characteristic length is the height of cavity). For the working conditions of current study, Ra is in a range of 0.85×10^8 to 3.12×10^8. A fully steady without instabilities is observed in the present simulations. Therefore the cases under the study can be considered to be laminar flow, as also assumed in the study of Ben Jabrallah et al. [2]. The numerical calculations are performed using different mesh sizes $25 \times 50 \times 50$ and $50 \times 100 \times 100$. Their results are very close with a negligible error in liquid film. Since the calculation is performed on cluster and the converged time is rather small, a high density mesh

of $50 \times 100 \times 100$ is used in the present study.

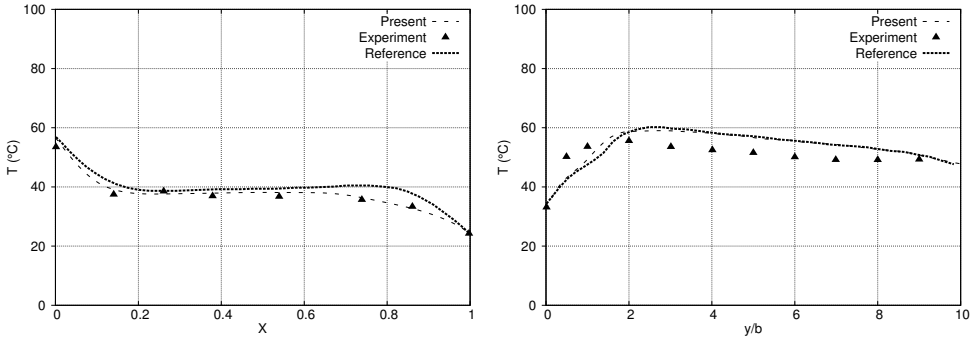

(a) Temperature at y=h/2 (b) Wall Temperature

Figure 3.9: Comparison of the present numerical results, the experimental and calculated results in reference (Condition:$T_c = 24.3\,^{\circ}\mathrm{C}$, $T_{in} = 33.7\,^{\circ}\mathrm{C}$, $\dot{m}_{in} = 0.811 \times 10^{-3} kg \cdot s^{-1} \cdot m^{-1}$, $\dot{q}_f = 700W \cdot m^{-2}$)

Fig. 3.9 presents the comparison between the numerical results, the experimental and calculated results of reference. The wall temperature and the air-vapor mixture temperature at $y = h/2$ are given. Both profiles show that the numerical results are consistent with the reference result. It can be observed from the comparison that the present simulation using the variable properties is closer to the experimental results than the calculated results with constant physical properties in the reference, in particular near the condensation wall zone. The thermal gradient is large at the zone next to both walls due to the heating on the left wall and cooling on the right wall while the variation in the middle part is not clear. However our simulation results presents a more gradual trend than the reference calculation near the condensation wall. The present trend is more consistent with the experiment data. Probably the reason is that the Boussinesq correlation was used in the reference by Ben Jabrallah et al. [2]. The calculation on the physical properties in the present work is more similar to the actual value under the condition of significant property variation due to the strong evaporation.

Concerning the wall temperature, the present profile is almost identical with the calculated profile of the reference and both lines have the same trend with the experimental result. The temperature firstly increases at the entrance of liquid film due to the heating and less evaporation, then the liquid film temperature decreases gradually with the increasing of the evaporation. However the deviation between them still exists. The present numerical simulation and the reference numerical data overestimated on the majority of the film at the bottom section of the cavity while

it underpredicted the temperature at the top section. There could be two factors resulting in the phenomenon. The deviation at the inlet of the liquid film could be caused by the instability of the liquid flow due to the sudden rejection of the water. In the simulation the heat flux applied to the wall is assumed to transmitted to the film completely without considering the heat loss. It may overpredict the film temperature at the bottom section of the cavity.

3.7.2.1 Influence of the heat flux

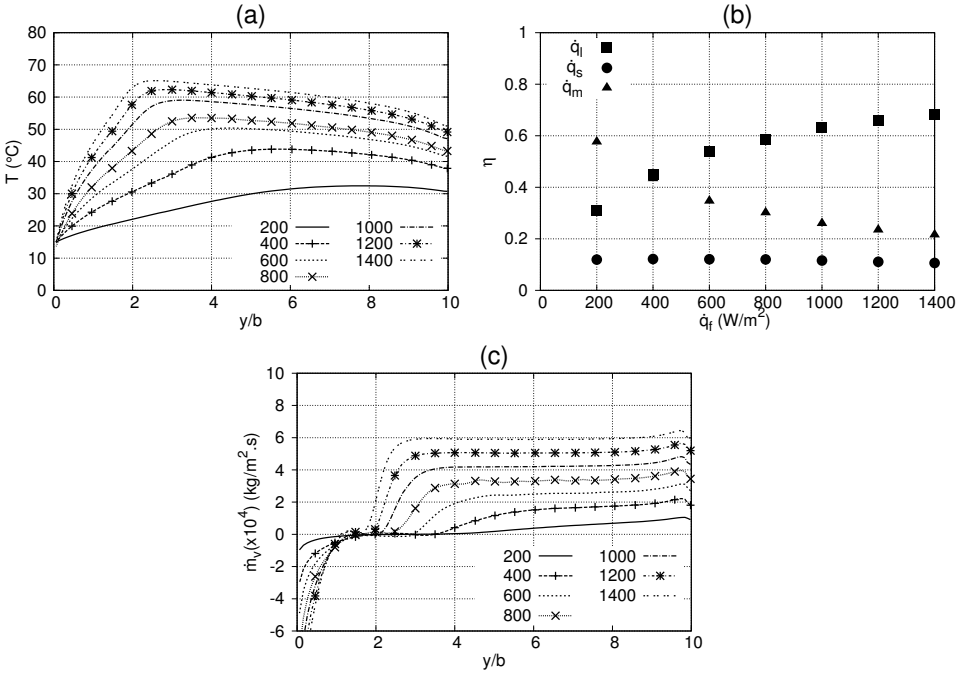

Figure 3.10: Influence of the heat flux (Condition:$T_c = 16\,^{\circ}\mathrm{C}$, $T_{in} = 15\,^{\circ}\mathrm{C}$, $\dot{m}_{in} = 0.833 \times 10^{-3} kg \cdot s^{-1} \cdot m^{-1}$)

The heat flux $\dot{q}_f$ imposed on the heated wall is from 200 $W \cdot m^{-2}$ to 1400 $W \cdot m^{-2}$ with a step of 200 $W \cdot m^{-2}$. Fig. 3.10 describes the influence of the heat flux $\dot{q}_f$ applied to the heated wall on the wall temperature, thermal efficiency and evaporation rate. It is needed to note that at the top of cavity the condensation happens on the surface of the liquid film with the negative evaporation rate. There is more condensation with the higher heat flux. It is because under the high heat flux, the temperature of liquid

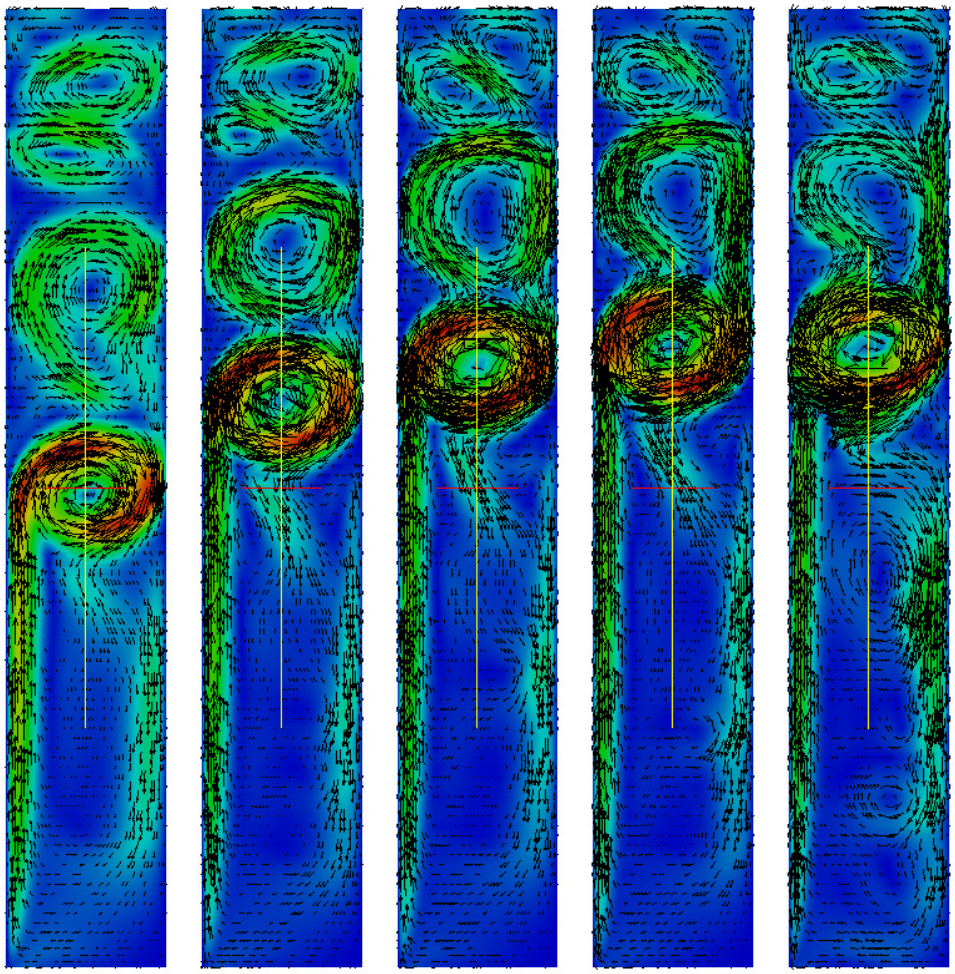

(a) 200 (b) 600 (c) 1000 (d) 1200 (e) 1400

Figure 3.11: The velocity field with the different heat flux (W/m^2)

film is higher and the concentration inside the cavity is also high at its equilibrium state. Meanwhile the inlet temperature of liquid film are same and are lower than the air temperature. As a result, the bigger gradient of concentration exists at the top of the cavity with high heat flux and the strong condensation appears. The temperature of the film increases with the heat flux and the peak point moves toward the top of the cavity, which is same as the observation of Ben Jabrallah et al. [2]. It can be explained that under the high heat flux, the stronger condensation exists and it absorbs more energy from the air side. With the fixed liquid film and inlet film temperature, less area is needed to reach its peak value. As explained in the energy balance equation of the falling film, the heat flux $\dot{q}_f$ applied on the wall can be divided into three contributions, the heat flux $\dot{q}_l$ as latent heat by evaporation of the film due to the concentration gradient, the heat flux $\dot{q}_s$ exchanged by pure convection due to the thermal gradient along the normal direction and the heat flux $\dot{q}_m$ carried out by the water film flow to increase its temperature. In the distillation application, it is desirable to increase the portion of evaporation latent heat and reduce the heat carried out by liquid film. It is significant to analyze the thermal efficiency under different heat flux. It can clearly be seen from Fig. 3.10 that latent heat efficiency increases clearly with the heat flux while the thermal efficiency of the carrying heat by water film decreases quickly with a nearly linear slope and the convection heat efficiency reduces slightly. It is worthy to note that once the heat flux is over 1000 $W \cdot m^{-2}$, the increase slope of thermal efficiency is gradually reduced with the rise of heat flux. It illustrates a method of increasing the distillation efficiency.

Fig. 3.11 illustrates the velocity vector field under the condition of the different heat flux. Due to the heating and evaporation, the vapor-gas mixture flows upwards near the hot wall. It separates from the hot wall at the middle of the cavity and creates a clear vortex. Meanwhile a weak reverse vortex appears at the top of the cavity. With the increase of heat flux (from 200 to 1000 W/m^2), the vortex location moves towards the top of the cavity. From 1000 to 1400 W/m^2, the variation of the velocity field is not significant and the location of the vortex is fixed.

3.7.2.2 Influence of the temperature of the feed water

As a boundary condition, the inlet temperature of the feed water T_{in} has a significant influence on the evaporation, which is shown in Fig. 3.12. At the heating zone, the slope of the temperature increase keeps constant under the different feed water temperature. It is because the water temperature is lower at the entrance zone and the evaporation is very weak. All the heat flux imposed on the wall is used to increase the water temperature and the temperature variation shows a nearly linear trend. The small difference on the slope is caused by the condensation rate at the initial stage. Different length shows the portion used to heat the water film. The lower feed water temperature covers more area to approach the peak points. After the

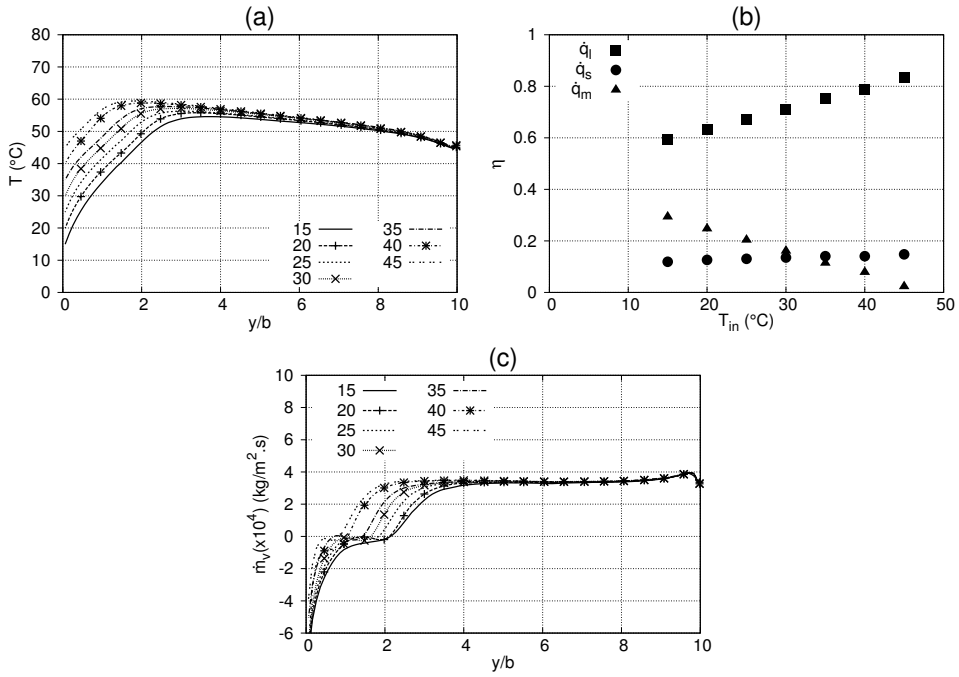

Figure 3.12: Influence of the temperature of water feed (Condition:$T_c = 15\,^{\circ}\mathrm{C}$, $\dot{m}_{in} = 0.808 \times 10^{-3} kg \cdot s^{-1} \cdot m^{-1}$, $\dot{q}_f = 800W \cdot m^{-2}$)

maximum temperature, all the temperature curves move closer and finally merge near the bottom of the cavity. As the temperature increase, the latent heat efficiency η_l increases linearly while the thermal efficiency of the carrying heat by water film reduce linearly. It can be easily explained that the lower temperature requires more heat flux for liquid film heating. With higher inlet water temperature, the film temperature arrives its peak point earlier and with higher temperature. As a consequence, the evaporation zone is extended and enhanced in the peak region, resulting in a stronger evaporation.

3.7.2.3 Influence of the temperature of the condensation wall

The influence of the temperature of the condensation wall T_c is shown in Fig. 3.13. In the observation of Ben Jabrallah et al. [2], the wall temperature profiles at different condensation temperature coincided at the top of the cavity cell. However, the profiles at different T_c show rising deviations in the present simulation. In the simulation of

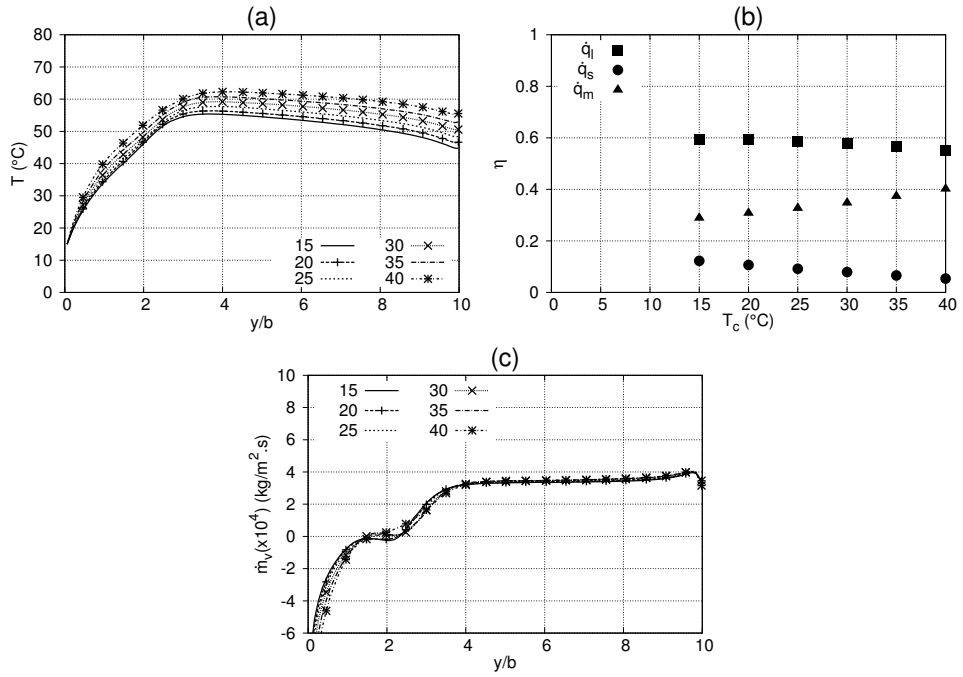

Figure 3.13: Influence of the temperature of the condensation wall (Condition:$T_{in} = 15\,^{\circ}\mathrm{C}$, $\dot{m}_{in} = 0.808 \times 10^{-3} kg \cdot s^{-1} \cdot m^{-1}$, $\dot{q}_f = 800W \cdot m^{-2}$)

Ben Jabrallah et al. [2], the condensation at the side of liquid film was neglected. In that way, the heat flux imposed on the wall was completely converted into the internal energy of the water film. Due to the fixed heat flux and water flow rate, the temperature of liquid film at different condensation temperature showed a linear increase in their simulation and all the profiles merged till the evaporation appeared. However in the present simulations the deviation appears at the beginning of the liquid film and become more obvious as it falls downward. The main reason is that the condensation at the beginning is considered in the present simulation since the condensations at the top cell actually exist. At the bottom of the cavity, the liquid film profile shows higher temperature with high condensation temperature. From the thermal efficiency analysis, it can be found that the influence of cold wall temperature on the thermal efficiency is not significant even it decreases with the increase of condensation temperature. It can be explained from the thermodynamic equilibrium state. With the lower condensation temperature, the temperature of liquid film is

lower with lower evaporation and the concentration on the air side is also lower with higher evaporation. The actual result of this combined effect is that the evaporation on the film side is slightly enhanced. It can be confirmed by the profiles of evaporation rate. The evaporation rate at different T_c is almost same.

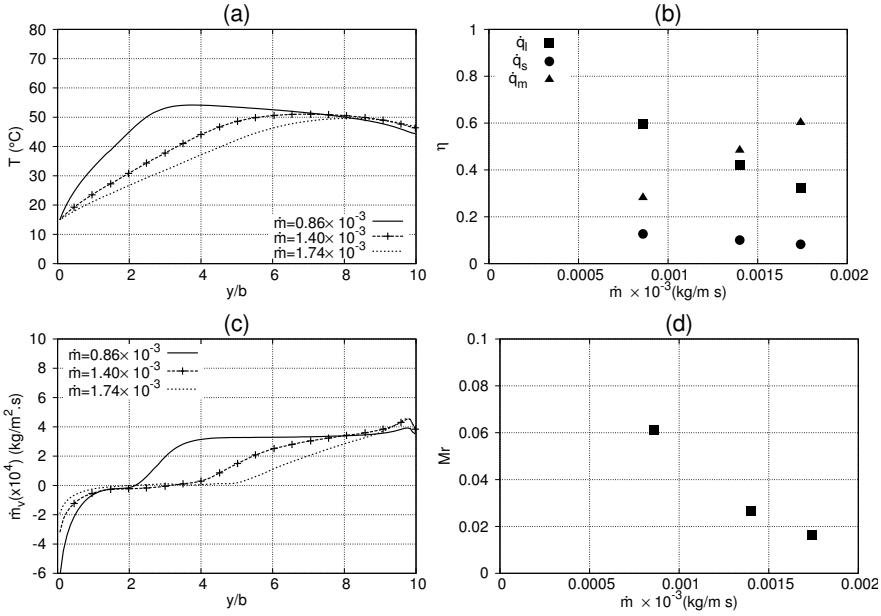

Figure 3.14: Influence of the flow rate (Condition:$T_c = 16\,^{\circ}\mathrm{C}$, $T_{in} = 15\,^{\circ}\mathrm{C}$, $\dot{q}_f = 800W \cdot m^{-2}$)

3.7.2.4 Influence of the flow rate of feed water

The influence of the mass flow rate of feed water $\dot{m}_{in}$ on the evaporation of the film is presented on Fig. 3.14. With the fixed inlet water temperature and heat flux imposed on the wall, the evaporation efficiency and evaporation ratio M_r decrease significantly as the water flow rate increases. The sensible heat carried out by the falling liquid is enhanced greatly while the convection heat transfer between the liquid film and gas changes little. It can be reflected by the liquid film temperature. With lower flow rate, the water temperature increases greatly at the top of the cavity cell, which enhances the evaporation rate. At the bottom of the cavity, the liquid film temperature profiles of different flow rates merge again. That is because the higher temperature increase evaporation and the film temperature is cooled accordingly. It can be concluded from

the figure that the lower flow rate should be employed to improve the latent heat efficiency and evaporation ratio. The profiles of evaporation ratio M_r show a very low value even for the lowest film flow rate. Under these conditions a good wettability of the whole plate is expected. However, the extrapolation of these conclusions to much lower film flow rates should consider the possible film breakup into rivulets or even the drying of the film.

3.7.3 Test case 3

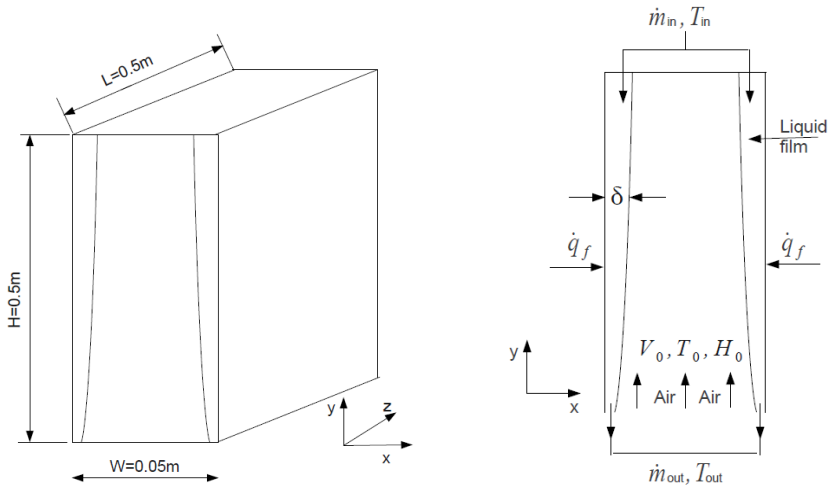

Figure 3.15: Schematic of system under study

In the second case, a natural convection case with a falling film is studied and the simplified film model was validated. Based on the validated film model, a series of mixed convection upward flows with the falling liquid film are to be studied in this case. The case was firstly conducted by Cherif et al. [3] through the experiment and numerical test. The geometry is given in Fig. 3.15. The channel is comprised of two paralleled plates, spaced by a distance 0.05m. The plates are square with a height and length of 0.5m. The bilateral plates are heated by a constant heat flux. The experimental case with lowest air velocity (0.27m/s) has been selected for simulation considering variable physical properties, as the one being in laminar flow (Re=1620). After a mesh refinement study, the same size as test case 2 of $50 \times 100 \times 100$ is used in case 3. The results obtained were compared with the relate experimental results. Different parameters affecting the flow were analyzed to investigate the performance

of our model in the mixed convection flow.

3.7.3.1 Liquid film temperature

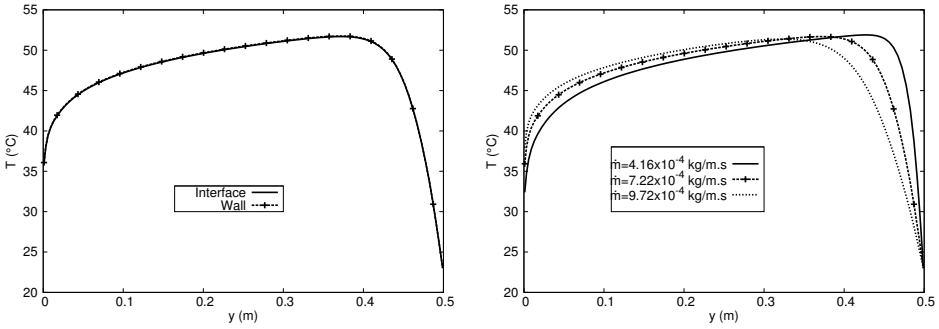

(a) $\dot{m}_{in} = 7.22 \times 10^{-4} kg \cdot s^{-1} \cdot m^{-1}$ (b) Different feed flow rate

Figure 3.16: Evolution of the temperature of liquid film along the plate:$V_0 = 0.27m/s$, $RH_0 = 76.5\%$, $T_0 = 27\,^{\circ}\mathrm{C}$, $T_w = 23\,^{\circ}\mathrm{C}$, $\dot{q} = 750\,W/m^2$

In order to study the temperature drop in the liquid film, the two-dimensional film energy model (equations 3.5, 3.6) is used to compute the liquid film temperature. Fig. 3.16(a) presents the axial profiles of the liquid film temperature. Interface represents the temperature at the liquid-air phase interface and wall is the temperature at the liquid-wall face. It can be observed from the comparison of the two curves that the temperature difference between them is very tiny and can be neglected, which has been confirmed by Li [15]. Therefore, the simplified equation 3.15 is used to solve the liquid film in the following study. The variation of the liquid film temperature with height can be decomposed into three zones. The first zone($y > 0.4m$) is located close to the inlet of the liquid film and the outlet of the air flow. Seeing that the relative humidity of the air-vapor mixture near the wall is high at the zone, the concentration at the interface is relatively low due to the low film temperature. The concentration gradient is small near the wall and the film hardly evaporates. Hence most of the heat flux has been conducted to the liquid. The direct consequence is that the heat flux from plates is converted into the sensible heat of liquid film and its temperature increases rapidly as the liquid film falls along the heated plate. During the second zone($0.05m < y < 0.4m$), the falling film temperature decreases slightly because the evaporation prevails and the major part of the heat provided is converted into latent heat. The third zone where the film temperature declines very fast is near the air inlet. In this zone, the inlet air is far away from saturated state and is at the developing regime. Its Nu number and Sh number is high, thus the heat transfer and

evaporation is strong. The part of internal energy in the liquid film is released for the latent heat of evaporation.

The influence of the feed flow rate on liquid film temperature is illustrated in Fig. 3.16(b). When the water feed flow rate increases, the peak location of liquid film temperature moves downwards because more area is needed to heat the liquid film under the condition of the constant heat flux. Furthermore the maximum temperature of the minimum feed flow rate $\dot{m}_{in} = 4.16 \times 10^{-4} kg \cdot s^{-1} \cdot m^{-1}$ is slightly larger than that of the other feed flow rates. With the reducing feed flow rate, the temperature curve declines more rapidly after the peak points. Under the condition that the heat evaporated is over than the heat flux, the sensible heat of liquid film is additionally needed and a smaller feed flow rate results in a larger temperature drop under a certain quantity of heat flux.

3.7.3.2 Temperature profiles in the gas phase

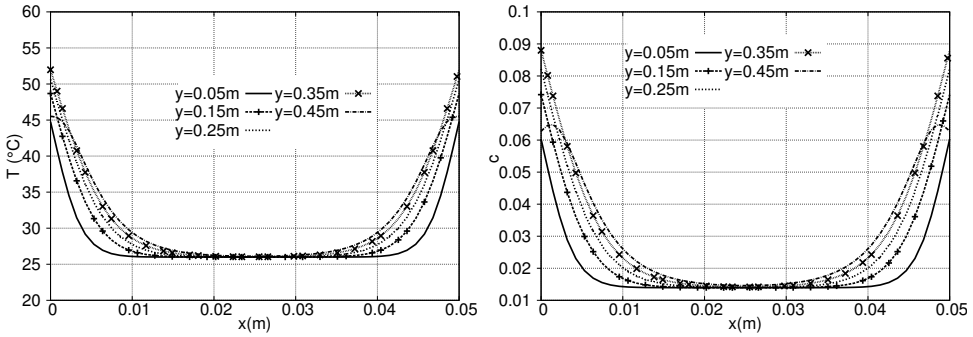

(a) Temperature (b) Concentration

Figure 3.17: Thermal and concentration field in the gas phase at various heights of the channel:$V_0 = 0.27 m/s$, $RH_0 = 76.5\%$, $T_0 = 27\,^{\circ}\mathrm{C}$, $T_w = 23\,^{\circ}\mathrm{C}$, $\dot{q} = 750\,W/m^2$, $\dot{m}_{in} = 7.22 \times 10^{-4} kg \cdot s^{-1} \cdot m^{-1}$

The exploration of the thermal and concentration field in the moist air helps us to understand the phenomena occurring in this case. The temperature and concentration of the gas mixture air-water stream according to the spacing of the two walls is given in Fig. 3.17 at various height of the channel. It can be seen that the air at the center of the channel is not influenced by the evaporation of film, its temperature and concentration remain constant. As the flow develops, the thermal and moist boundary layer increase along the channel. The temperature and concentration next to the wall do not show a monotonical trend due to the heat and mass transfer with

liquid film. The moist air is heated before y=0.35m, but it is cooled from y=0.35m till outlet by liquid film. The influence is only limited the very thin layer next to the wall, instead of the whole temperature and moist boundary layer.

3.7.3.3 Influence of heat flux

The influence of heat flux is analyzed in this section and the comparison against experiment results is given in Table 3.2. The present numerical data are highly close to the experimental results with a maximum deviation of 8.09% in $\dot{q} = 500W/m^2$ case.

Table 3.2: Comparison of evaporated flow rate(Unit:$kg/m^2 \cdot s$):$V_0 = 0.27m/s$, $RH_0 = 76.5\%$, $T_0 = 27\,^{\circ}\mathrm{C}$, $T_w = 23\,^{\circ}\mathrm{C}$, $\dot{m}_{in} = 7.22 \times 10^{-4} kg \cdot s^{-1} \cdot m^{-1}$

$\dot{q}(W/m^2)$	Reference	Experiment	Present data
500	0.981×10^{-4}	1.100×10^{-4}	1.189×10^{-4}
650	1.349×10^{-4}	1.500×10^{-4}	1.564×10^{-4}
750	1.630×10^{-4}	1.800×10^{-4}	1.808×10^{-4}
850	1.981×10^{-4}	2.130×10^{-4}	2.065×10^{-4}

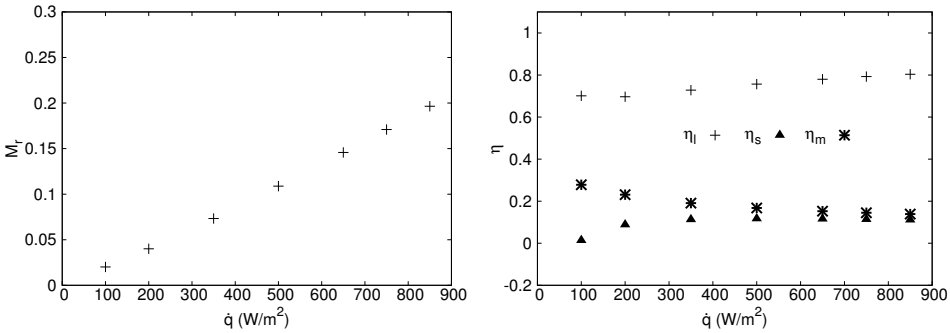

(a) Evaporated ratio M_r (b) Thermal efficiency of evaporation η_l

Figure 3.18: Influence of heat flux: $RH_0 = 67\%$, $T_0 = 27\,^{\circ}\mathrm{C}$, $T_w = 23\,^{\circ}\mathrm{C}$, $\dot{m}_{in} = 7.22 \times 10^{-4} kg/s$

To better understand the efficiency of the system, the influences of heat flux on evaporated ratio M_r and thermal efficiency are studied in Fig. 3.18. M_r increases quasi

linearly with the heat flux. Fig. 3.19(b) shows that the evaporation rate increases with heat flux except for the top zone (film inlet zone). At the top zone, strong condensation is observed for $\dot{q} = 750W/m^2$. It is because liquid film temperature for $\dot{q} = 750W/m^2$ (see Fig.3.19(a)) is higher and it reaches the peak earlier, strong heat and mass transfer is generated inside the channel. Therefore the temperature and concentration of mixture inside the channel for $\dot{q} = 750W/m^2$ are higher than those at lower heat flux $\dot{q} = 100, 350W/m^2$, in particular at the air outlet zone for the accumulated consequence. With the same inlet film temperature, the concentration at interface are also same, velocity and concentration gradient (negative) is bigger with high heat flux. Even strong condensation exists for $\dot{q} = 750W/m^2$, its evaporation rate is higher in the majority of the channel area. M_r shows a linearly increasing trend.

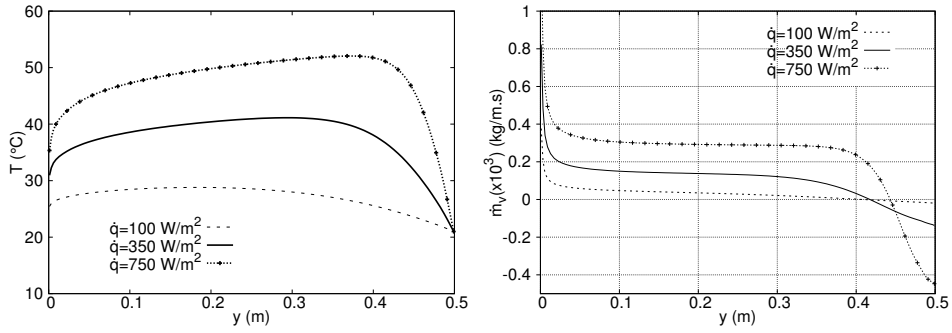

(a) Film temperature

(b) Evaporation rate

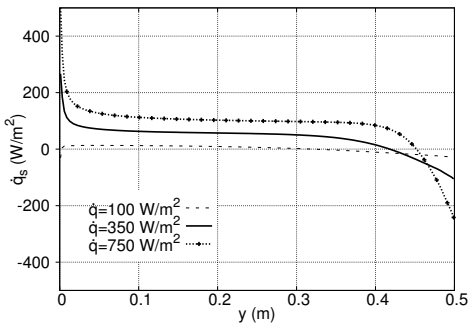

(c) Convection heat transfer $\dot{q}_s$

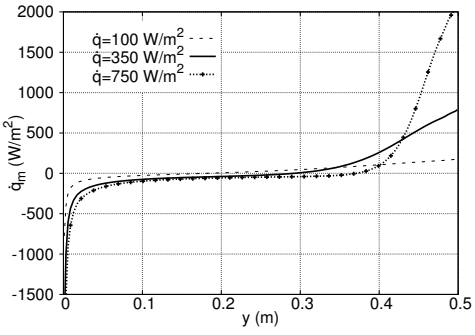

(d) Heat transfer by film $\dot{q}_m$

Figure 3.19: Flow parameters at $v_0 = 0.27m/s$

The thermal efficiency η_l and η_s in Fig 3.18(b) show a slight increase trend while η_m decreases slowly with heat flux. The sensible heat transfer $\dot{q}_s$ in Fig. 3.19(c) shows that in the zone (0.45-0.5m), convective heat transfer $\dot{q}_s$ for high heat flux gives a greater negative value due to the higher mixture temperature. However $\dot{q}_s$ increases with heat flux in the majority of the wall (positive). From $\dot{q} = 100W/m^2$ to $350W/m^2$, its magnified scale is slightly more than the increase of heat flux. Therefore η_s illustrates a slow increase trend. For $\dot{q}_m$ shown in Fig. 3.19(d), the clear difference appears only in the zone of 0.4-0.5m. Within this zone, strong condensation occurs for $\dot{q} = 750W/m^2$. Moreover high heat flux is absorbed by the liquid film. As a result, the film temperature shows a quick increase process and $\dot{q}_m$ is clearly greater. In the majority of wall, $\dot{q}_m$ does not show an obvious increase with heat flux. Thus its thermal efficiency η_m shows a minor reduction trend. In general, it can be observed from the heat transfer distribution that, although their quantities increase with heat flux, the total heat flux also increases. The final result is that their efficiency do not change significantly, in particular after $\dot{q} = 500W/m^2$.

3.8 Conclusion

The present study concerned the numerical study of simultaneous heat and mass transfer in laminar flow. During the present study, three cases are chosen: a horizontal flow with constant physical properties, natural convection with variable properties and mixed convection with variable properties. In the first case, a static wet boundary condition is applied while liquid film boundary condition is imposed in the last two cases. During the work, a method of solving liquid film equations has been applied which takes into account of the transfer in liquid film and also between the film and the flowing air-vapor mixture. The method employs integration of conservation equation at a level y to establish the local heat and mass balances. Through the solution of the balances in the liquid film coupled with the conservation equations in the gas phase allows us to track the dynamic characteristics of the liquid film including temperature and evaporated rate of each level.

The mixture model and simplified liquid film model are validated in the laminar flow. The influence of heat flux and liquid feed rate on film temperature, air temperature, evaporated ratio and thermal efficiency have been studied in detail. Brief summaries of the major results are listed in the following:

- In the first case, the mixture model can accurately predict the laminar flow with constant physical properties. A spanwise boundary layer is also observed, which results in the non-uniform temperature field along spanwise direction. Meanwhile a small vortex has been seen near the corner to bottom wall due to the imposed transverse velocity and evaporation.
- In the second case, the simplified model from energy balance is developed to

calculate the boundary condition and it gives good results compared to the experimental ones. The mixture model with variable physical properties provides more accurate than the one with constant properties. Meanwhile the condensation in the film side is also considered and it could have an impact on the heat flux profiles and the detailed values. Multiple vortex have been observed in the natural cavity flow and they move upwards with heat flux.

- In the third case, the mixed convection has been studied. It is found that the evaporation thermal efficiency at low inlet velocity does not change greatly with heat flux. The behavior is different to the one in natural convection. The thermal efficiency is influenced by the forced convection through the imposed inlet velocity. The temperature drop across the liquid film is very small and can be neglected.

References

[1] Prabal Talukdar, Conrad R Iskra, and Carey J Simonson. Combined heat and mass transfer for laminar flow of moist air in a 3d rectangular duct: Cfd simulation and validation with experimental data. *International Journal of Heat and Mass Transfer*, 51(11):3091–3102, 2008.

[2] S Ben Jabrallah, A Belghith, and JP Corriou. Convective heat and mass transfer with evaporation of a falling film in a cavity. *International journal of thermal sciences*, 45(1):16–28, 2006.

[3] AS Cherif, MA Kassim, B Benhamou, S Harmand, JP Corriou, and S Ben Jabrallah. Experimental and numerical study of mixed convection heat and mass transfer in a vertical channel with film evaporation. *International Journal of Thermal Sciences*, 50(6):942–953, 2011.

[4] O. [et al.] Lehmkuhl. Termofluids: A new parallel unstructured cfd code for the simulation of turbulent industrial problems on low cost pc cluster. In *Proceedings of the Parallel CFD 2007 Conference*, pages 1–8, Ismail H. Tuncer, 2007.

[5] Ivette Rodriguez, Ricard Borell, Oriol Lehmkuhl, Carlos D. Pérez Segarra, and Assensi Oliva. Direct numerical simulation of the flow over a sphere at Re = 3700. *Journal of Fluid Mechanics*, 679(25):263–287, JULY 2011.

[6] F. X. Trias and O. Lehmkuhl. A Self-Adaptive Strategy for the Time Integration of Navier-Stokes Equations. *Numerical Heat Transfer, Part B: Fundamentals*, 60(2):116–134, JULY 2011.

[7] T Ueda and H Tanaka. Measurements of velocity, temperature and velocity fluctuation distributions in falling liquid films. *International Journal of Multiphase Flow*, 2(3):261 – 272, 1975.

[8] YL Tsay and TF Lin. Evaporation of a heated falling liquid film into a laminar gas stream. *Experimental thermal and fluid science*, 11(1):61–71, 1995.

[9] M'barek Feddaoui, El Mustapha Belahmidi, Ahmed Mir, and Abdelaziz Bendou. Numerical study of the evaporative cooling of liquid film in laminar mixed convection tube flows. *International Journal of Thermal Sciences*, 40(11):1011 – 1020, 2001.

[10] P An, J Li, and JD Jackson. Study of the cooling of a uniformly heated vertical tube by an ascending flow of air and a falling water film. *International journal of heat and fluid flow*, 20(3):268–279, 1999.

[11] Ernst Rudolf Georg Eckert and Robert M Drake Jr. Analysis of heat and mass transfer. 1987.

[12] Frank P Incropera. *Fundamentals of heat and mass transfer*. John Wiley & Sons, 2011.

[13] Conrad R. Iskra and Carey J. Simonson. Convective mass transfer coefficient for a hydrodynamically developed airflow in a short rectangular duct. *International Journal of Heat and Mass Transfer*, 50(11-12):2376–2393, JUNE 2007.

[14] R.K. Shah. *Laminar Flow Forced Convection in Ducts, Advances in Heat Transfer*. Academic Press, 1978.

[15] Cheng LI and Junming LI. Laminar forced convection heat and mass transfer of humid air across a vertical plate with condensation. *Chinese Journal of Chemical Engineering*, 19(6):944–954, 2011.

4

Large eddy simulation of transitional flow with buoyancy force

4.1 Abstract

A forced and natural mixed convection flow in a uniformly heated vertical pipe is studied using large eddy simulation. A series of experimental conditions are considered by applying different heat flux boundary condition to the pipe wall and adjusting the mass flow rate. The subgrid scale model (SGS) -Wall Adapting Local Eddy- viscosity model (WALE) is employed in the paper. The mode of heat transfer ranges from forced convection with negligible influence of buoyancy to mixed convection with very strong influences of buoyancy. In one case, complete laminarization phenomenon appears during the flow process. The obtained results are compared to the existing DNS and experimental simulation with a relative coarse mesh in a detail. The simulation result yields good prediction with a significant reduction computation cost. In second case, the flows in a very long tube are tested, in which the flow proceeds the two transition process: turbulent-laminar transition, laminar-turbulent transition. Moreover the flow process from turbulence recovery to fully developed state is as well illustrated. The results obtained are compared with the existing experimental data. The aim of the paper is to examine the capability of the present large eddy simulation approach for predicting in the transition flow and to study the flow structure variation in the spatially-developing flow of very long tube with strong heating.

4.2 Introduction

In the chapter 3, the evaporation and condensation in the laminar flow has been studied. However, most evaporations and condensations in industrial equipments and surroundings are in turbulent regime. In a large number of flow phenomenons, the forced and natural mixed convective flow are included. The large physical property variation caused by heat and mass transfer may change the flow regime and cause the transitional flow. The transition process is a kind of flow that initially laminar becomes turbulent (laminarization) or inverse (turbulization). On the one side, the process is very complicated and is not fully understood at present. On the other side, it is very significant for evaluating the efficiency of heat and mass transfer in the cooling applications.

In the turbulent evaporation or condensation, it involves the phase change at the interface, diffusion equation of vapor and the physical properties of multicomponent mixture. All the factors make the computation more difficult. Before the implementation of turbulent or transitional evaporation or condensation simulation, it is necessary to study the transitional flow with the pure air as the flow fluid. With the studying, the capability of the WALE model in the turbulent or transitional flow can be validated. It can provide a fundamental for the turbulent evaporation or condensation simulation.

As mentioned in the introduction, although there are several investigations on the mixed flows including laminar, transitional and turbulence, periodic boundary condition in streamwise and fixed temperature on wall was imposed in the majority of the literatures. The large eddy simulation for flows in vertical circular and annular tubes are very sparse, especially with constant heat flux boundary condition and spatial developing flow. It is needed to explain that, in the upward flow where buoyancy aids the motion and turbulence is inhibited, the process of flow development is slowed down and a fully development is hard to reach. It is only approached with very long tubes and only well downstream [1]. To the best knowledge of the author, there is no study on the complex spatial developing flow with buoyancy-influenced flow for the difficulty. During the long development flow, the flow regime is very complicated depending on the specified flow situations, boundary conditions and geometry. The whole flow could proceed laminarization, turbulence reduction and enhancement, deterioration and local enhancement in turbulent heat transfer.

The main objectives in this chapter is to address the capability of the compressible LES formulation to simulate transitional flow in a vertical pipe with significant variable properties and constant heat flux boundary condition based on TermoFluid computer code. It is also to study the flow process in a long vertical tube at the matching experimental conditions of Li [2] and to explore the buoyancy effect on the related important parameters in the strongly heated air flows. In the present chapter, the sub-grid scale models -WALE- is applied with system-conserving scheme. With their

combination, it is capable of predicting the location of the transition from laminar to turbulent flow correctly.

4.3 Mathematical model

4.3.1 Governing equation

The fundamental equations of fluid dynamics are based on the conservation laws for mass, momentum, and energy. The fully compressible Navier-Stokes equation in Cartesian coordinates are written as:

$$\frac{\partial \rho}{\partial t} + \frac{\partial}{\partial x_j}(\rho u_j) = 0 \tag{4.1}$$

$$\frac{\partial \rho u_i}{\partial t} + \frac{\partial}{\partial x_j}(\rho u_j u_i) = -\frac{\partial p}{\partial x_i} + \frac{\partial \tau_{ij}}{\partial x_j} + \rho g \tag{4.2}$$

$$\frac{\partial \rho E}{\partial t} + \frac{\partial}{\partial x_j}(\rho E u_j) = -\frac{\partial p u_j}{\partial x_j} - \frac{\partial \dot{q}_j}{\partial x_j} + \frac{\partial \tau_{ij} u_i}{\partial x_j} \tag{4.3}$$

Where the total energy(per unit mass) is $E = e + u_j u_j/2$(internal energy + kinetic energy), the viscous stress tensor $\tau_{ij} = \mu(\frac{\partial u_i}{\partial x_j} + \frac{\partial u_j}{\partial x_i} - \frac{2}{3}\delta_{ij}\frac{\partial u_k}{\partial x_k})$. where δ_{ij} is the Kronecker delta function. p is the hydrodynamic pressure and μ is the dynamic viscosity. According to the Fourier's law of heat conduction, the heat flux is expressed as $\dot{q} = -\lambda\frac{\partial T}{\partial x_j}$. The equation of state of the ideal gas is applied to close the system of fluid dynamic equations, the detailed formulation for the thermodynamic variables is shown in Appendix A.

In the large eddy simulation, only the large scale of turbulent motion is solved while the small ones are modeled. It is needed to separate the large scale motion and the small one with a filter which can be written in terms of a convolution integral as

$$\overline{f}(\overrightarrow{f}, t) = \int_D G(\overrightarrow{x}, \xi) f(\overrightarrow{\xi}, t) d\overrightarrow{\xi} \tag{4.4}$$

where G is a filter function that determines the size and structure of the small scales. The variables can be decomposed into two components $f = \overline{f} + f^{'}$. Where $\overline{f}$ represents for the large scale or resolved component and $f^{'}$ is the subgrid scale or modeled component.

Substracting the mechanical energy to the energy equation, the above compressible equations are filtered to obtain the governing equation for large eddy simulation.

$$\frac{\partial \overline{\rho}}{\partial t} + \frac{\partial \overline{\rho u_j}}{\partial x_j} = 0 \tag{4.5}$$

$$\frac{\partial \overline{\rho u_i}}{\partial t} + \frac{\partial \overline{\rho u_j u_i}}{\partial x_j} = -\frac{\partial \overline{p}}{\partial x_i} + \frac{\partial \overline{\tau}_{ij}}{\partial x_j} + \overline{\rho} g \tag{4.6}$$

$$\frac{\partial \overline{\rho h}}{\partial t} + \frac{\partial}{\partial x_j}(\overline{\partial \rho h u_j}) = -\overline{p\frac{\partial u_j}{\partial x_j}} - \frac{\partial \overline{\dot{q}_j}}{\partial x_j} + \overline{\tau_{ij}\frac{\partial u_i}{\partial x_j}} \tag{4.7}$$

where $\overline{\tau}_{ij} = \overline{2\mu(S_{ij} - \frac{1}{3}S_{kk}\delta_{ij})}$. In the above filtered equation, the SGS Reynolds stress becomes $\overline{\rho' u' v'}$, which is a triple product of the unknown variables. As a result, tremendous complexities would be introduced into the SGS modeling if the above filter operation is used. Favre filtering is introduced to simplify the filtered equations and they are

$$\tilde{f} = \frac{\overline{\rho f}}{\overline{\rho}}, \qquad \overline{\rho f} = \overline{\rho}\tilde{f} \tag{4.8}$$

where f is a general variable such as the velocity and temperature but not the density and pressure. The variables can be decomposed in two ways,

$$f = \overline{f} + f', \qquad f = \tilde{f} + f'' \tag{4.9}$$

where f' and f'' are both the unresolved components. The related Favre filtering variables are,

$$\overline{\rho u} = \overline{\rho}\tilde{u}, \quad \overline{\rho u_i u_j} = \overline{\rho}\widetilde{u_i u_j}, \quad \overline{\rho h} = \overline{\rho}\tilde{h}, \quad \overline{\rho u h} = \overline{\rho}\widetilde{u h} \tag{4.10}$$

The decomposition term is

$$\overline{\rho u_i u_j} = \overline{\rho}\tilde{u}_i\tilde{u}_j + (\overline{\rho u_i u_j} - \overline{\rho}\tilde{u}_i\tilde{u}_j) = \overline{\rho}\tilde{u}_i\tilde{u}_j + \overline{\rho u_i'' u_j''}$$
$$\overline{\rho u_i h} = \overline{\rho}\tilde{u}_i\tilde{h} + (\overline{\rho u_i h} - \overline{\rho}\tilde{u}_i\tilde{h}) = \overline{\rho}\tilde{u}_i\tilde{h} + \overline{\rho u_i'' h''}$$

where the first term is resolved and the second term is the corresponding SGS contribution.

In order to obtain the low-Mach number formulation, the compressibility effects and the acoustic interactions are filtered out. The viscous heating term $\overline{\tau_{ij}\frac{\partial u_i}{\partial x_j}}$, the term $-\overline{p\frac{\partial u_j}{\partial x_j}}$ and the term $-\frac{2}{3}\delta_{ij}\frac{\partial u_k}{\partial x_k}$ are considered to be negligible in the low speed flows. Finally, the Low-Mach governing equations are obtained by the Favre filtering

$$\frac{\partial \overline{\rho}}{\partial t} + \frac{\partial \overline{\rho}\tilde{u}_j}{\partial x_j} = 0 \tag{4.11}$$

$$\frac{\partial \overline{\rho}\tilde{u}_i}{\partial t} + \frac{\partial \overline{\rho}\tilde{u}_j\tilde{u}_i}{\partial x_j} = -\frac{\partial \overline{p}}{\partial x_i} + \frac{\partial(\overline{\tau}_{ij} + \overline{\tau}^t_{ij})}{\partial x_j} + \overline{\rho}g \tag{4.12}$$

$$\frac{\partial \overline{\rho}\tilde{h}}{\partial t} + \frac{\partial \overline{\rho}\tilde{u}_j\tilde{h}}{\partial x_j} = -\frac{\partial(\overline{\dot{q}_j} + \overline{\dot{q}}^t_j)}{\partial x_j} \tag{4.13}$$

where the filtered diffusion term is laminar filtered stress tensor

$$\overline{\tau}_{ij} = \overline{\mu(\frac{\partial u_i}{\partial x_j} + \frac{\partial u_j}{\partial x_i} - \frac{2}{3}\delta_{ij}\frac{\partial u_k}{\partial x_k})} \approx \tilde{\mu}(\frac{\partial \tilde{u}_i}{\partial x_j} + \frac{\partial \tilde{u}_j}{\partial x_i} - \frac{2}{3}\delta_{ij}\frac{\partial \tilde{u}_k}{\partial x_k}) \tag{4.14}$$

The Reynolds stress tensor (subgrid scale tensor) is:

$$\overline{\tau}^t_{ij} = -\overline{\rho}(\widetilde{u_i u_j} - \tilde{u}_i\tilde{u}_j) \tag{4.15}$$

and it is modeled as:

$$\overline{\tau}^t_{ij} = 2\overline{\rho}\nu_t(\tilde{S}_{ij} - \frac{1}{3}\delta_{ij}\tilde{S}_{kk}), \quad \tilde{S}_{ij} = \frac{1}{2}(\frac{\partial \tilde{u}_i}{\partial x_j} + \frac{\partial \tilde{u}_j}{\partial x_i}) \tag{4.16}$$

The filtered heat flux is:

$$\overline{\dot{q}}_i = -\frac{\lambda}{c_p}\frac{\partial \tilde{h}}{\partial x_j} \tag{4.17}$$

The subgrid scale heat flux is:

$$\overline{\dot{q}}^t_i = \overline{\rho}(\widetilde{u_i h} - \tilde{u}_i\tilde{h}) \tag{4.18}$$

and the modelization for $\tilde{q}^t$ is written as:

$$\overline{\dot{q}}^t_i \approx \tilde{\dot{q}}^{sgs}_i = -\lambda_t\frac{\partial \tilde{T}}{\partial x_i}, \qquad \lambda_t = \frac{\mu_t C_p}{Pr^t} \tag{4.19}$$

The turbulent Prandtl number is fixed at $Pr^t = 0.4$.

The properties of dry air are calculated by using the equations of Appendix A.

4.3.2 SGS-WALE model

A subgrid scale viscosity model is introduced to close the formulation in the present study, namely WALE model. The wall-adapting eddy viscosity model(WALE) was proposed by Nicaud and Ducros [3] and the model is based on the square of the velocity gradient tensor. In its formulation the SGS viscosity accounts for the effects of both the strain and the rotation rate of the smallest resolved turbulent fluctuations. It is particularly suited for the wall-bounded flows, which is a challenging task for LES.

In addition, the proportionality of the eddy viscosity near walls is recovered without any dynamic procedure,

$$\begin{aligned}
\nu_t &= (C_w\Delta)^2 \frac{(\tilde{V}_{ij}\tilde{V}_{ij})^{\frac{3}{2}}}{(\tilde{S}_{ij}\tilde{S}_{ij})^{\frac{5}{2}} + (\tilde{V}_{ij}\tilde{V}_{ij})^{\frac{5}{4}}} \\
\tilde{S}_{ij} &= \frac{1}{2}[\mathrm{G}_{ij}(\tilde{u}) + \mathrm{G}_{ji}(\tilde{u})] = \frac{1}{2}(\frac{\partial\tilde{u}_i}{\partial x_j} + \frac{\partial\tilde{u}_j}{\partial x_i}) \\
\tilde{V}_{ij} &= \frac{1}{2}[\mathrm{G}^2_{ij}(\tilde{u}) + \mathrm{G}^2_{ji}(\tilde{u})] - \frac{1}{3}[\mathrm{G}^2_{kk}(\tilde{u})\delta_{ij}] = \frac{1}{2}(\frac{\partial\tilde{u}_i}{\partial x_j} + \frac{\partial\tilde{u}_j}{\partial x_i}) - \frac{1}{3}\delta_{ij}\frac{\partial\tilde{u}_k}{\partial x_k}
\end{aligned} \tag{4.20}$$

where Δ is the characteristic filter length. In the present study a constant value of $\mathcal{C}_w = 0.325$ is used. G_{ij} are the velocity gradients of the resolved scales and $\tilde{V}_{ij}$ being the traceless symmetric part of the square of the velocity gradient tensor.

Numerical results are carried out by using the CFD&HT code–Termofluids [4] which is an intrinsic 3D parallel CFD object-oriented code applied to unstructured /structured meshes, which can handle the thermal and fluid dynamic problems in complex geometries. The governing equations are discretized on a collocated mesh in Cartesian coordinates. The numerical integration is performed by a finite volume method.

In problems with very Low Mach numbers and where acoustic phenomena are not of interest, the common strategy is to use a variant of the Predictor-Corrector scheme shown by Najm et al. [5]. The pressure-velocity coupling is solved by a fractional step as described by Nicoud [6] where a constant coefficient Poisson results. In the Predictor step a second-order Adams-Bashforth time integration scheme is used to calculate the intermediate scalar fields and the velocity and it incorporates a pressure correction step to satisfy the continuity equation. The Corrector step uses a Crank-Nicolson integration to advance the scalar fields, and it also involves a pressure correction step. The specific algorithm scheme can be referred as Appendix B.

4.4 Problem description

We choose two cases to address the capability of our LES model to simulate complete transitional flows in mixed convection. The experiment of Shehata et al. [7] with the detailed information in the field was chosen as the first case. In the case, complete laminarization is covered and DNS has also been implemented by Bae et al. [8]. Due to the detailed parameters obtained from the experiment and DNS in the whole flow field, it is very suitable for a benchmark reference result and for validation of the laminarization. In the second case a hydrodynamically and thermally fully developed flow is finally approached in a very long tube. It provides global and detailed results for a wide range of Buoyancy force in both upwards and downwards

flow. The Nusselt ratio can be accessed by the comparison with the forced flow. It is used to test the capability of the transitional flow. Meanwhile the flow structure is studied in the whole field.

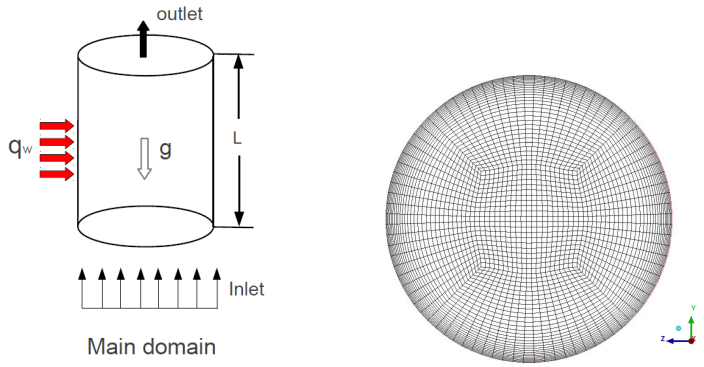

(a) Geometry (b) mesh

Figure 4.1: Schematic diagram of flow region and mesh distribution

Fig. 4.1 gives a sketch of the flow regions with the boundary conditions and mesh distribution for the present study. In both cases of our present simulation, the hydrodynamic fully developed flow condition is required at the inlet to the main heated domain. We adopted a separate computer program called inflow generator to obtain a inlet condition for the present simulation. The inflow generator needs to be run before the main code. The instantaneous data at one section is saved at each fixed time step for a long-enough period. The instantaneous velocity at inlet of main domain is imposed through the interpolation of the saved data in terms of time and node position. This is different with that of DNS [8] in which inflow generator code and main code were running simultaneously. For the inflow simulation, a periodic boundary condition in the streamwise direction was used while non-slip condition was imposed on the wall. Different from the Low Mach numerical model in main code, the incompressible LES-WALE model without energy equation is employed to obtain the hydrodynamically fully developed turbulent flow.

As for thermal boundary condition, we assumed that the entering fluid has a uniform temperature distribution at the inlet and constant heat flux condition is imposed at the wall as follows:

$$\dot{q} = -\lambda \frac{\partial T}{\partial r} \tag{4.21}$$

where $\dot{q}$ is the heat flux imposed on the wall. Neumann boundary condition is considered at the exit of the main computational domain.

To the author's knowledge, the majority of the finite volume methods in the circular pipe simulations, the governing equation were discretized in cylindrical coordinates. With cylindrical coordinate the mesh is more uniform and it is easier to process the result, however the singularity may occur at the center line of the pipe. In order to avoid the problem, the governing equation is discretized in the Cartesian coordinate and O-grid (hexahedral) mesh are built in the present study using the software ANSYS ICEMCFD. In order to facilitate the comparison and analysis, it is necessary to convert the parameters in Cartesian coordinate to the ones in cylindrical coordinate according to the coordinate transformations.

The distance to the center axis of the tube is,

$$r = \sqrt{y^2 + z^2} \tag{4.22}$$

The normal wall velocity and the circumferential velocity is given as,

$$\mathrm{u}_r = \mathrm{u}_y \sin\theta + \mathrm{u}_z \cos\theta, \quad \mathrm{u}_\theta = \mathrm{u}_y \cos\theta + \mathrm{u}_z \sin\theta \tag{4.23}$$

where u_y and u_z is the velocity at y and z direction, respectively. θ is the angle between y axis and radius direction. In the following analysis, only parameters on axial and normal wall direction are provided.

Owing to the low velocity of the present flow, this simulation case is nearly incompressible and isothermal and the density fluctuations are assumed to be small enough, therefore the Reynolds and Favre average are essentially equivalent. The Reynolds averaging variable $\langle\phi\rangle$ or $\overline{\phi}$ is equal to the density-weighted Favre averaging variable $\tilde{\phi}$. The fluctuation about Reynolds-averaged mean $\phi^{'}$ is equal to the one on Favre-averaged mean $\phi^{''}$.

4.5 Laminarization case

The experiment conducted by Shehata et al. [7] is used to address the capability of the present model in the laminarization simulation at lower cost than DNS and higher generality than RANS. In his experiment, the main heated zone has a length of 30D. The internal diameter of the test tube is 0.0274m. DNS mesh size in reference [8] is about 7 millions, which imposes a severe demand for the computer capability. In the present work two different grid resolutions, namely $400 \times 15 \times 30$ (1.5M) and $250 \times 13 \times 20$ (0.5M), were used to study the grid independence. The results are very similar and the mesh of 1.5M is used in the present paper. In the successful simulation of turbulent flow using LES, spatial resolution is a critical factor. The resolution of the inner layer (viscous sublayer) is much more challenging and the mesh is required fine. At the outer flow (buffer zone or turbulent zone), larger spacing can be used. Criteria often applied to indicate the adequacy of LES, are mesh spacing in wall units.

Usual values are [9]:

$$50 \leq \Delta x^+ \leq 150, \qquad \Delta y^+_{wall} < 1, \qquad 15 \leq \Delta z^+ \leq 40 \text{ for LES} \tag{4.24}$$

$$10 \leq \Delta x^+ \leq 20, \qquad \Delta y^+_{wall} < 1, \qquad 5 \leq \Delta z^+ \leq 10 \text{ for DNS} \tag{4.25}$$

where x is streamwise, y is wall normal and z is streamwise direction. Table. 4.1 lists the grid information corresponding to each entry Reynolds number and comparison is made with the existing DNS data [8]. According to the above criteria, the present mesh completely obeys it.

In the detailed flow conditions given in Table. 4.2, all the heat flux on the wall is exactly same as DNS. The two Reynolds number were chosen, namely Re=4300 and 6000. In the DNS simulation for run445, 5% higher heat flux than the nominal value was employed to better match the experimental data for wall temperature distribution. In the present simulation, the same heat flux value is employed for the same reason.

Table 4.1: Parameters of the grid resolution

	Run445		Run618 and Run635	
Re	4300		6000	
	Present	DNS	Present	DNS
$(\Delta y)^+$	28.6	11.8	37.4	16.0
$(\Delta r)^+_{min}$	0.60	0.14	0.75	0.19
$(R\Delta\theta)^+$	9.38	7.42	12.25	10.3

Table 4.2: Simulation condition for strongly heated air flows in a vertical tube

case	Re	U_0(m/s)	q^+	q_w(kW/m^2)	$Gr_0(\times 10^{-7})$	$Bo(\times 10^6)$	Gr_0/Re_0^2
Run 618	6000	3.31	0.0018	2.11	0.678	1.023	0.188
Run 635	6000	3.31	0.0035	4.11	1.318	1.989	0.366
Run 445	4300	2.37	0.0047	3.98	1.277	6.033	0.691

4.5.1 Bulk parameters

The bulk temperature and velocity in the simulation are compared with the references. Their definitions are,

$$T_b = \frac{1}{A}\int_A \overline{\rho u}\,\overline{T}\,\mathrm{d}A, \qquad U_b = \frac{1}{A}\int_A \overline{\rho u}\,\mathrm{d}A \tag{4.26}$$

The heating could increase the mean flow velocity due to the reduction of the fluid

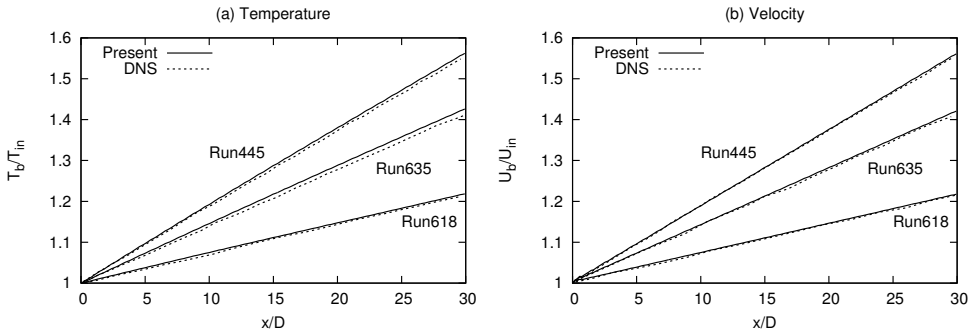

Figure 4.2: Bulk variables

density. The flow acceleration in axial direction decreases the turbulence in the flow. Therefore, the turbulent flow can be laminarized and the heat transfer decreases drastically. The acceleration effect is represented by the parameter, K_v, which is defined with dimensional variables as

$$K_v = \frac{u}{U_b^2}\frac{dU_b}{dx}. \tag{4.27}$$

Applying energy balance and continuity equation with perfect gas to the equation above, an alternative non dimensional definition of acceleration parameter K_v can be derived [10]:

$$K_v = \frac{4q^+}{Re_b}\frac{1}{C_{pb}T_b} \tag{4.28}$$

Fig. 4.2 presents the bulk flow parameters. The present data for all the parameters are in excellent agreement with that of DNS solution. As shown in the figures, the rate of increase in T_b and U_b become more significant as the heat flux imposed on the wall increase and they are nearly linear. The flow acceleration in axial direction decreases the turbulence in the flow. Therefore, the turbulent flow can be laminarized and the heat transfer decreases drastically. According to the K_v critical value of 3.6×10^{-6} given by Kline et al. [11], the value in the present simulation reaches to 3.7×10^{-6}, which is very close the data ($K_v = 3.65 \times 10^{v}$) predicted by DNS [8]. The nearly complete laminarization is confirmed again in the present LES.

4.5.2 Parameters on the walls

Fig. 4.3 shows the predicted distributions of wall temperature along the tube compared with those measured in the experiments and those in the DNS. In the figure, the symbols present the experimental data. As shown in the figure, the profiles of wall

temperature are very close to DNS ones. Both are in agreement with the experimental data for all conditions although there exist some deviations. The obtained wall temperature was underpredicted in the present simulation. The discrepancy reason is probably the heat flux difference on boundary condition between the simulation and experiment. In the present simulation, constant heat flux is applied on the wall, without considering the heat losses and heating instability existing in the experiment, the conduction along the tube wall and radiation effects. In another hand, since the electrical resistance increases with the temperature, the actual heating rate could be larger than the nominal average value, especially in the two highest heating rate cases. A higher temperature could appear in the experiment while such effect is not considered in the simulation. Local Nusselt number along axial direction for the different

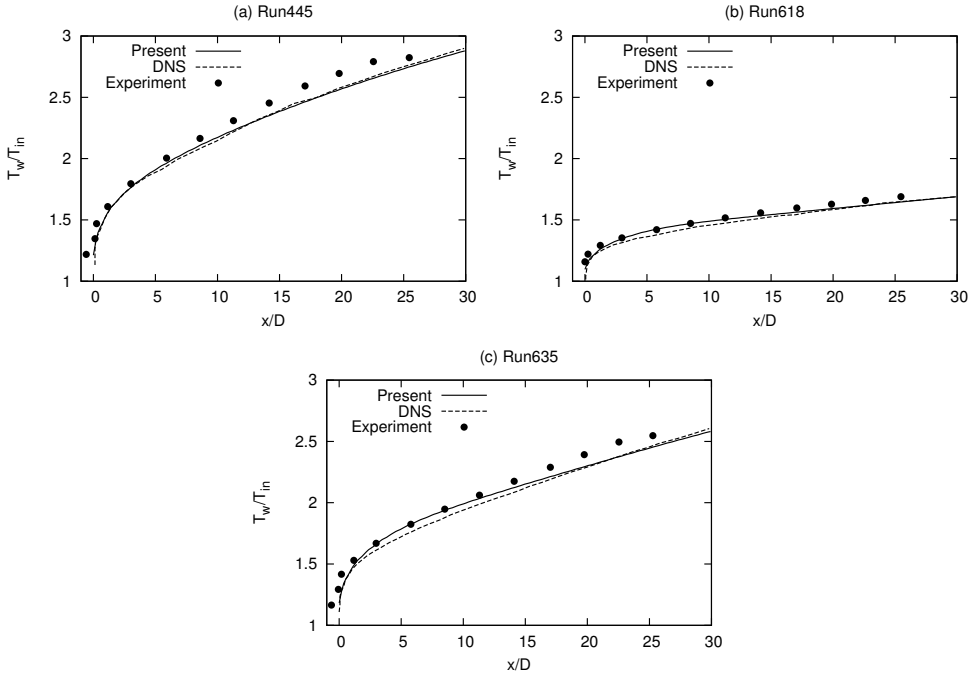

Figure 4.3: Wall temperature

cases are compared to the experimental and DNS data in Fig. 4.4. As can be seen from the figures, the present result shows the consistent Nusselt number as DNS results in Run445 case. Both present a clear deviation in the first few diameters in thermal entry region while the predicted Nusselt number agrees well with the experimental

data in others regions. In Run618 and Run635 cases, the present simulations give a better result than the experiment and DNS data in the entrance region, and remain the same good results in the downstream region. Compared to the correlations used by Bae et al. [8], a more accurate correlation was employed to calculate the physical properties. This is probably a reason that the wall temperature and Nusselt number is closer to the experiment than DNS.

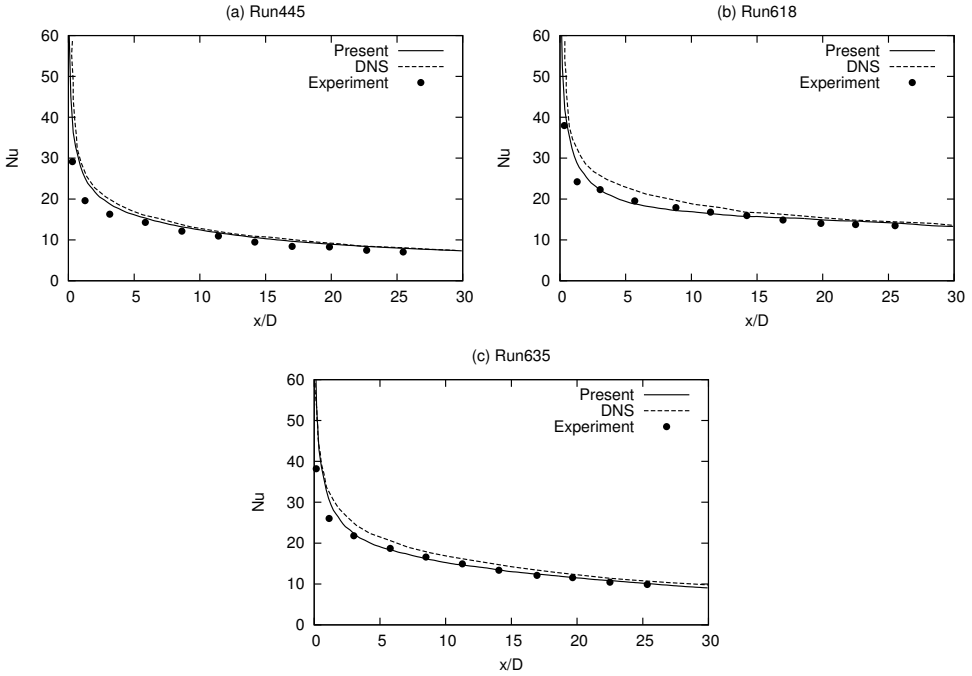

Figure 4.4: Nusselt number. (a)Run445 (b)Run618 (c) Run635

The local skin friction coefficient is defined as:

$$C_f = \frac{2\tau_w}{\rho_b U_b^2}, \quad \tau_w = \mu \frac{\partial u}{\partial r}|_{wall} \tag{4.29}$$

Fig. 4.5 illustrates the local skin friction coefficient variation along the axial direction. The predicted result are compared with DNS data and the existing correlation of McEligot [12]. As seen in the figure, the present simulation gives a fairly consistent result with DNS for case Run445. Both results present a pronounced deviation from the correlation, which is for heated turbulent gas flows in dominant forced convection,

since the flow is laminarized under the intense heating on the wall with the low Reynolds. For Run618 and Run635 with small buoyancy number, C_f presents clear different with DNS data in the initial regions and their difference decrease along the axial direction. The probable reason is that DNS has higher level of spatial discretization since denser mesh in cylindrical coordinate is used and mesh distribution is more uniform. However O-grid mesh in Cartesian coordinate is employed in the present LES. As the inlet velocity is low and the distance from the wall to its neighbour control volume is low, the error in velocity gradient could be magnified. It may contribute a part of the deviation. The figures also illustrate the buoyancy influence on C_f that local skin coefficient increases with heat flux.

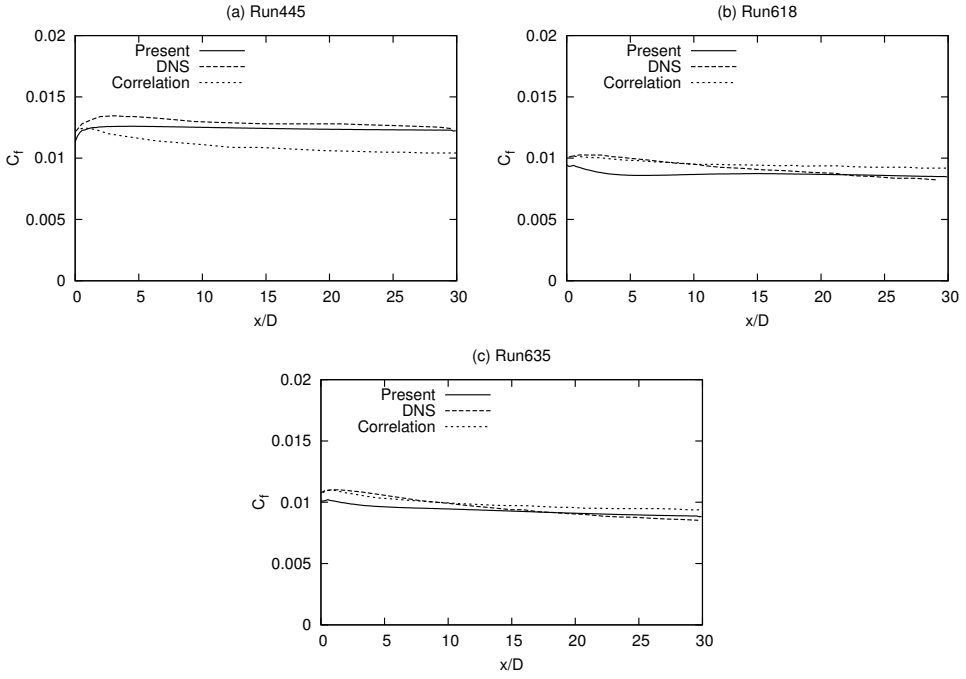

Figure 4.5: Local skin friction coefficient

4.5.3 Mean parameters fields

Figs. 4.6-4.8 provide the development of the predicted normalised velocity and temperature profiles along the tube for various conditions. The comparisons are made at three representative locations $3.2D$, $14.2D$ and $24.5D$. Although the bulk velocity

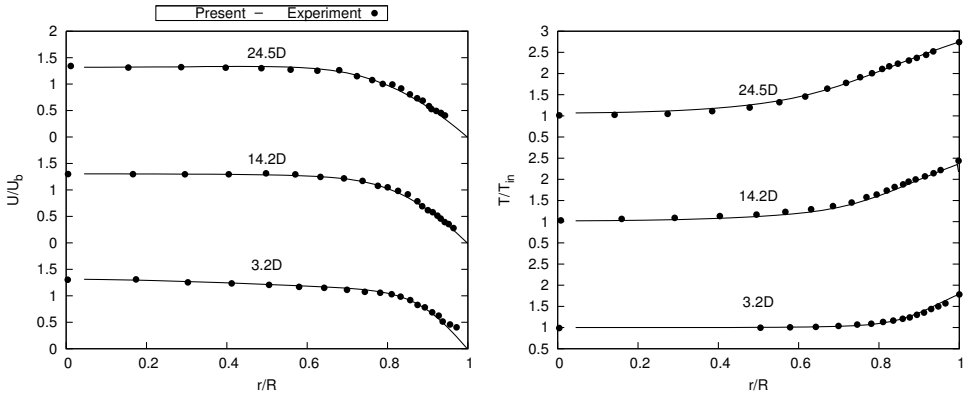

Figure 4.6: Mean temperature and velocity profiles for Run445

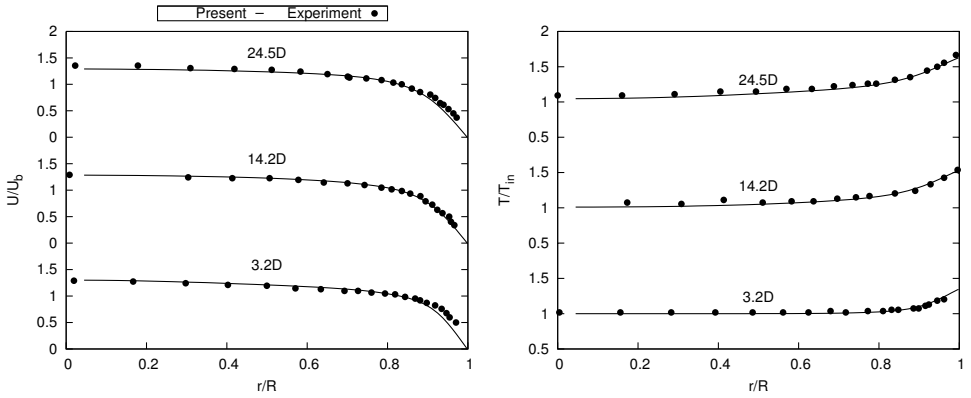

Figure 4.7: Mean temperature and velocity profiles for Run618

and temperature may vary considerably according to the experimental conditions, the normalized velocity and temperature profiles are rather similar for all the cases. The mean velocity and temperature profiles show mostly agreement with the experimental data for all the test conditions, with the exception of a few points near the wall at the first station. The region near the all is the most difficult measuring one [7] since the variations of the parameters are large within the region. The uncertainty eg., the distance to wall, could result in a clear deviation.

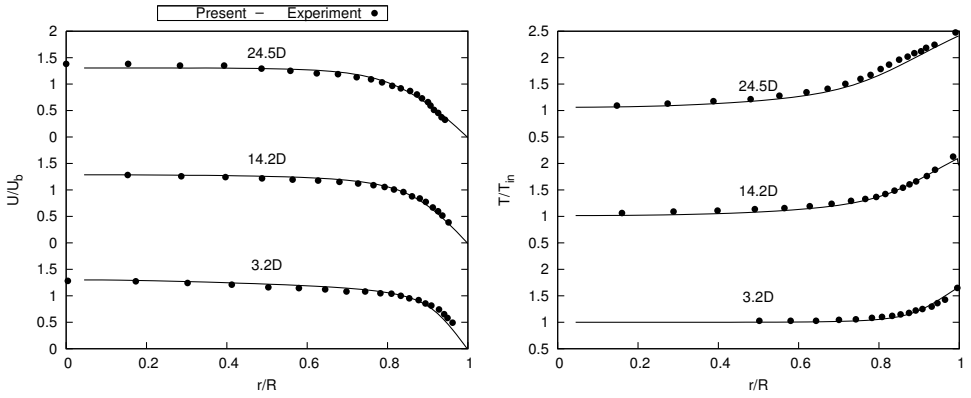

Figure 4.8: Mean temperature and velocity profiles for Run635

In order to validate the present simulation further, the mean streamwise velocity and temperature distributions are presented in wall coordinates and are compared to the experimental results and DNS results in Fig. 4.9-4.11. The definition of wall velocity is,

$$u^+ = \frac{u}{u_\tau}, \qquad u_\tau = \sqrt{\frac{\tau_w}{\rho_w}}, \qquad y^+ = \frac{(R-r)u_\tau}{\nu_w} \tag{4.30}$$

The definition of temperature difference in wall coordinates is given as,

$$\theta^+ = \frac{T_w - T}{T_\tau}, \qquad T_\tau = \frac{\dot{q}_w}{\rho_w c_p u_\tau} \tag{4.31}$$

As seen in Fig. 4.6 and Fig. 4.9, the obtained results show good agreements between the experiment on the velocity distributions in Run445 case. However in the temperature comparison, it shows a clear difference with experiment at the core of $x = 24.5D$ section while it appears better agreement with DNS result. The main reason is, that the temperature difference between the simulation and experiment increases as the flow downstream due to the strong heating rate and the uncertainties, eg., heat flux, friction coefficient. The temperature difference was magnified in wall coordinates because of the small friction velocity unit u_τ. In Fig. 4.10 and 4.11, the obtained data keeps excellent consistency with the reference results, especially with the DNS data. The existing slight difference is because the simulation conditions, such as heat flux and velocity uncertainty in the experiment, are not exactly same as the experiment. Meanwhile it is impossible to directly measure the local wall shear stress in the conditions of the experiment due to the thin thickness of viscous sublayer.

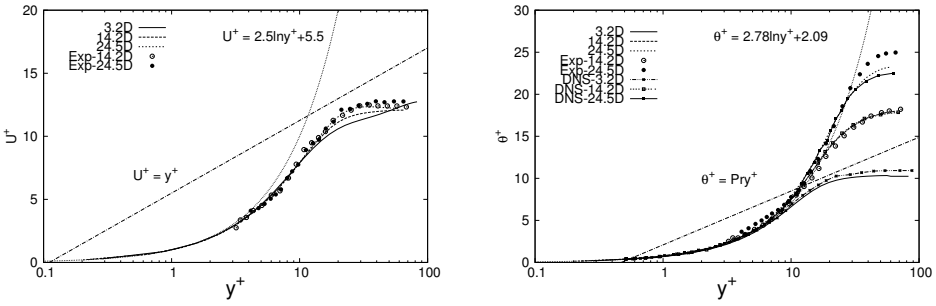

Figure 4.9: Local mean velocity and temperature profiles in wall coordinates for Run445

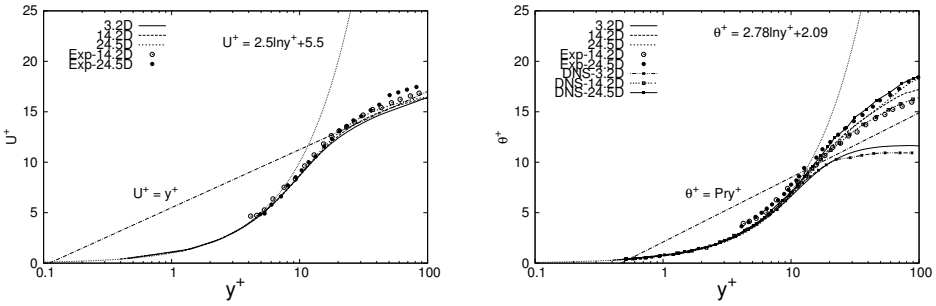

Figure 4.10: Local mean velocity and temperature profiles in wall coordinates for Run618

In his experiment a turbulence model was adjusted to match the measured data along the tube. Once the simple model was validated, $u_{\tau,w}$ was deduced in terms of the combination of the numerical predictions and experimental data. In their experiment, a simple modified van Driest model [13] was finally chosen to predict internal flow. The $u_{\tau,w}$ difference may exist between the present simulation and the experiment. The most noticeable point is that the variation range of temperature difference at each axial location is increasing significantly as the heat flux increases. The temperature profile for Run445 is seen to move close to laminar profile and the semi-logarithmic region is becoming smaller as the fluid flows downstream. Likewise, the velocity profiles fall farther to the fully developed turbulent flow as q^+ increases from Run618 to Run445. In Run618, the predicted velocity profiles u^+ coincide mostly with the

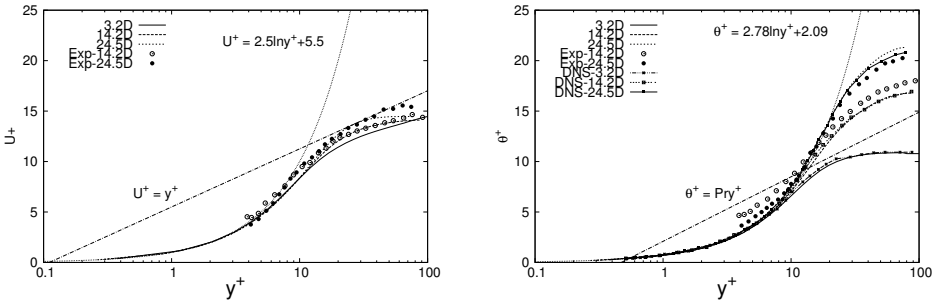

Figure 4.11: Local mean velocity and temperature profiles in wall coordinates for Run635

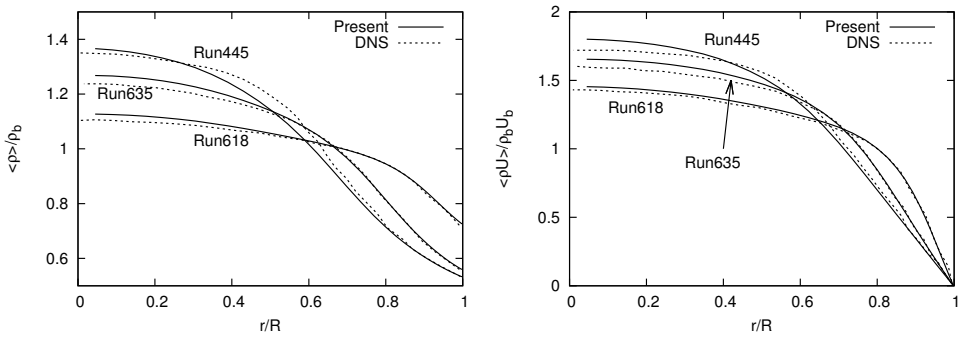

Figure 4.12: Local mean density and mass flux profiles

fully developed turbulence flow at each locations, which reflects the little influence of buoyancy force. On the other hand, the velocity profiles in Run445 deviate severely from the fully developed velocity profile. The successive profiles illustrate the growth of the thermal boundary layer towards the core of the pipe.

Fig. 4.12 provides the local mean density and mass flux profiles against the DNS results. Our results show a excellent agreement with DNS data. The mass flux profile is fairly flat with the small heat flux while the mass flow moves toward the center of the tube with strong heating due to the density variation. The mass flux profile exhibits a rather clear trend of laminarization as q^+ increase progressively from Run 618 to Run 445 [8], so that the normalized mass flux profile becomes more parabolic like the one for laminar velocity with constant properties.

4.5.4 Velocity and temperature fluctuations

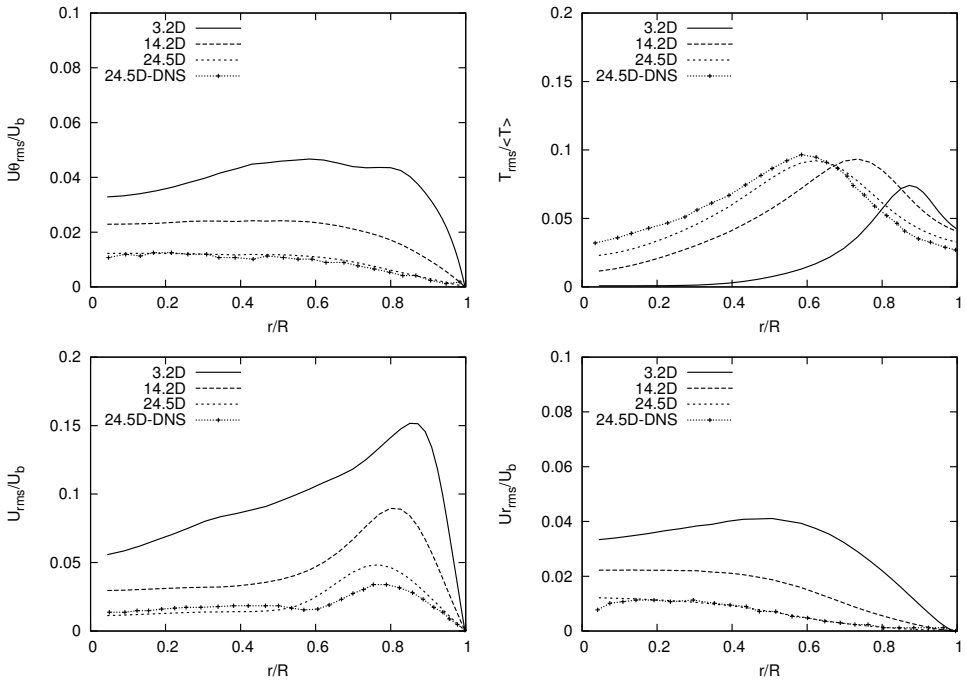

Figure 4.13: Velocity and temperature fluctuation for Run445

The velocity fluctuation in the axial, radial and circumferential direction normalized by bulk velocity and the temperature fluctuation normalized by bulk temperature are shown in Figs. 4.13, 4.14, 4.15 by root-mean-square values. The fluctuations are compared with the DNS data at 24.5D and good agreement is obtained. It can also be seen from the comparison of the fluctuation that the trend is quite different in different cases. The turbulence intensities decrease as the nondimensional heating is increasing. For Run445 shown in Fig. 4.13, the velocity fluctuations decay significantly along the streamwise direction. Meanwhile the turbulence in the near wall region responds to the wall boundary condition. This response propagates towards the core of the tube as we proceed downstream. The strongest turbulence intensity moves towards the centre of the tube. The fluctuation reaches to a low level at the exit and the flow is predicted to be effectively laminarized.

For Run618 with the weakest heating, it can be observed from Fig. 4.14 that turbulence intensity is almost the same at different locations with a slight reduction

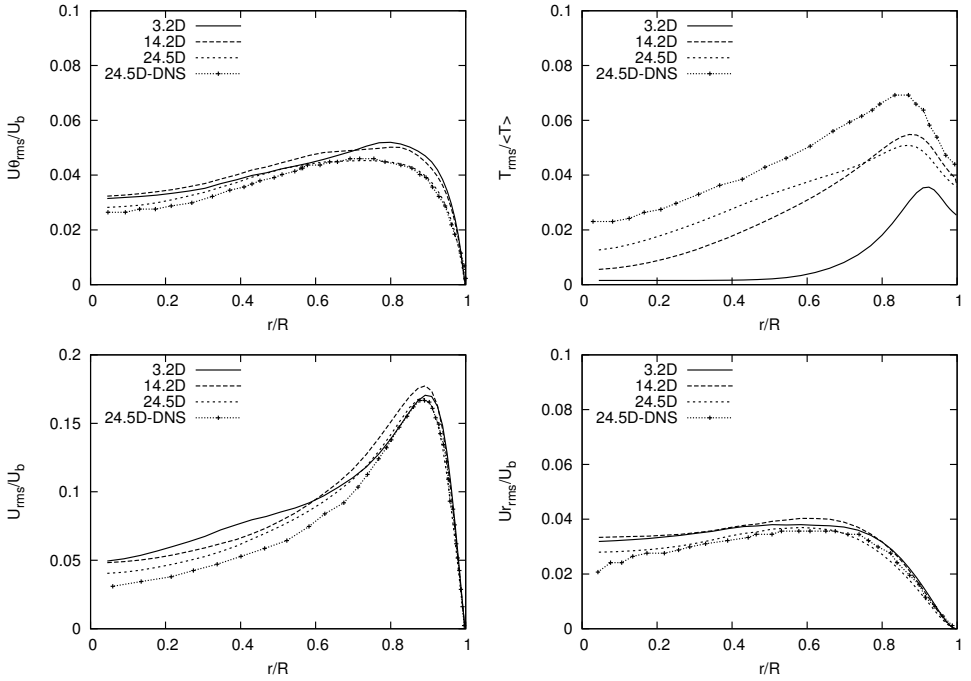

Figure 4.14: Velocity and temperature fluctuation for Run618

in the core region of the tube while its evolution along the axial direction change slightly. It mostly maintains the fully developed turbulent flow characteristics during the whole tube. Run635 case is between Run445 and Run618, its heating is not the same strong as Run445, but higher than Run 618. Its behaviour in the flow is also between them. The velocity fluctuation appears a reduction trend along the downstream flow, however, its laminarization is not clear as the Run445.

The temperature fluctuation evolutions along the axial direction show the effect of heating on the different regions in the tube. The regions close to the wall is more intensely influenced by the wall. The temperature fluctuation peaks move toward the centerline of the tube as the fluid flows downstream in the radial distribution profiles. The temperature fluctuation shows a relative independence of heat flux. The temperature fluctuations are in good agreement with DNS results for Run445 and Run635 while it presents a higher difference at 24.5D for Run618. In general, the temperature fluctuation distributions reflect the thermal boundary layer variation. The present LES model present a excellent performance as DNS on the turbulent-

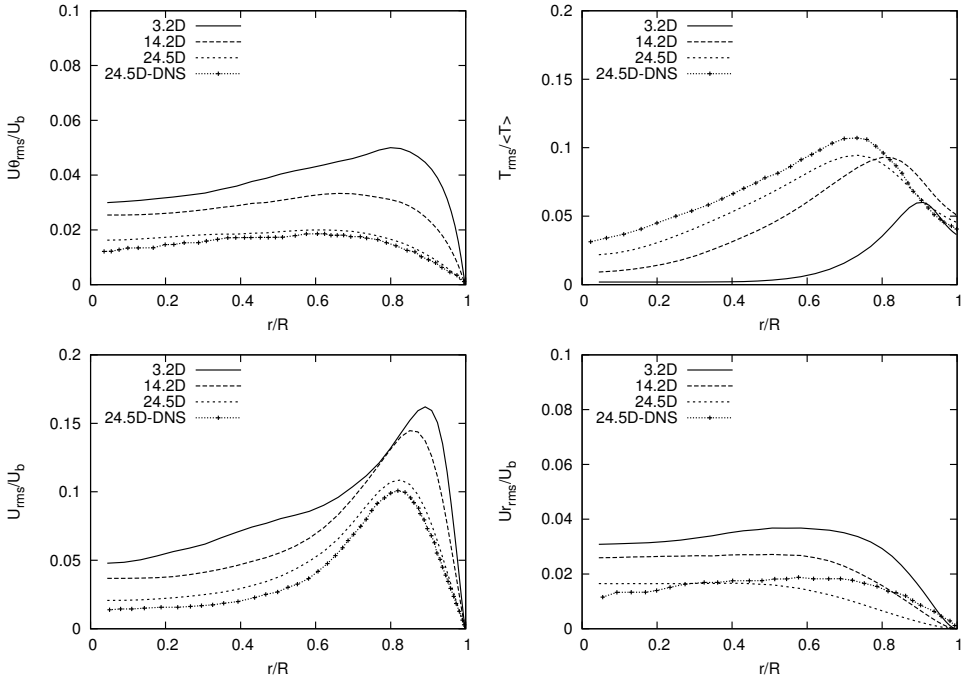

Figure 4.15: Velocity and temperature fluctuation for Run635

laminar transition flow.

4.5.5 Reynolds shear stress

In the turbulent flow, the total shear stress $\tau = \mu\frac{d\overline{u}}{dr} - \rho\overline{u^{'}u_r^{'}} = \tau_{lam} + \tau_{turb}$. If the flow is laminar, $u^{'} = u_r^{'} = 0, \overline{u^{'}u_r^{'}} = 0$, so the resolved Reynolds shear stress could directly present the turbulence intensity. Thus, we compared the Reynolds shear stress with DNS data(Fig. 4.16) at x=24.5D. It decreases dramatically from 3.2D to 24.5D in run 445 with a very low level of Reynolds shear stress, again illustrates us the effect of laminarization. Meanwhile in Run618, Reynolds shear stress shows a weak change along the tube which is similar as the behaviour of the velocity fluctuation. Through all the comparison with DNS, it show a very good agreement at 24.5D, which can validate the capability of the present model in laminarization case at lower cost.

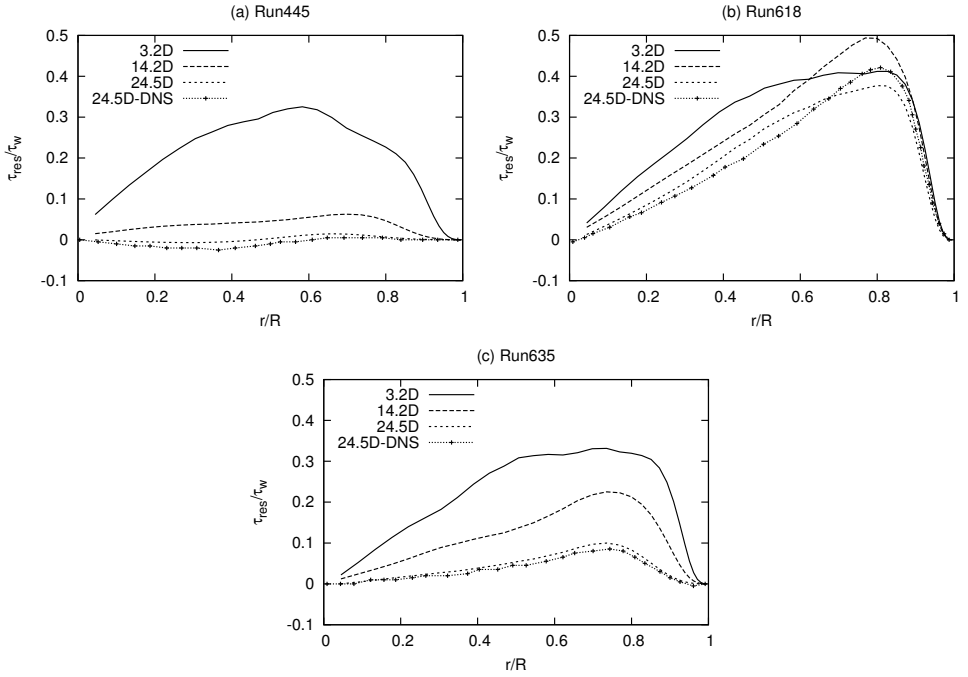

Figure 4.16: Reynolds shear stress normalized by the wall shear stress

4.6 Fully-developed case

Although the complete laminarization was covered in the first case, the hydrodynamically and thermally fully developed flow was not reached because of the short tube. It is very significant to study the variation of the flow developing process. However in the mixed upward flow the development length is much longer than for constant property cases, especially with the buoyancy force and so few experiments and simulations were performed on it. Fortunately Li and Jackson [2, 14] did a series of experiment for air flow upward and downward in a vertical circular tube with constant heat flux. In their experiment, a very long tube was used to approach the fully hydrodynamically and thermally developed flow. It was comprised of two sections: an unheated hydrodynamic development section to generate the fully developed flow which is length of 3.926m. Followed the unheated section was the test section of 7.874m, which was heated in a uniform manner along the whole of its length by passing electrical current through it. A forced upward or downward flow of air was created in the tube by supplying air from the laboratory by a blower to a settling

Table 4.3: Simulation condition for strongly heated air flows in a vertical tube

case	Direction	Re_0	Gr_0^*	Bo_0	T_{in}	U_0(m/s)	q_w(W/m^2)	q^+
1	up	3049	1.039e8	12.71	17.2	0.59	516	0.00244
2	up	3773	8.105e7	4.786	22.3	0.76	442	0.00164
3	up	7220	1.145e8	0.732	17.6	1.41	571	0.00114
4	up	9486	1.190e8	0.299	22.0	1.91	646	0.00096
5	up	16465	2.225e8	0.0845	21.1	3.29	1243	0.00102
6	down	2918	9.427e6	1.342	21.2	0.59	50	0.00024
7	down	9776	2.657e8	0.602	23.3	1.98	1477	0.00210

box at the bottom or top of the tube. The air flowed from the entry box into the bellmouth intake where a uniform inlet velocity profile was generated. The flow then developed in the long unheated hydrodynamic development section to a fully developed condition at the inlet to the heated section. The detailed experiment could be found in Li [2].

In their experiment, different conditions were employed to consider the forced flow with negligible influences of buoyancy to mixed convection with dominant influence of buoyancy. The complete experiment was done by adjusting the inlet mass flow rate and the heat flux imposed on the wall. The inlet Grashof and Reynolds numbers covered $4 \times 10^6 - 6 \times 10^8$ and $1000 - 35,000$, respectively. Since there were plenty of experimental data, only several classical conditions were chosen to perform in the present paper for covering the enough wide flow regimes. The detailed parameters are shown in Table. 4.3. The hydrodynamically fully developed state is imposed at the inlet of the tube and it is generated according to the above description in section 4.4.

In the case the simulations are performed with the grid resolution 3.5M for lower Reynolds number ($Re < 9000$) and 7M for higher Reynolds number ($Re > 9000$). To represent accurately the structures in the near-wall region, the first grid point must be located at $y^+ < 1$, and the grid spacing must be of order $\Delta x^+ = 50 - 150$, $\Delta y^+ = 15 - 40$ for LES. Table 4.4 lists the grid information corresponding to each entry Reynold number.

Table 4.4: Parameters of the grid resolution

case	1	2	3	4	5	6	7
Re	3049	3773	7220	9486	16465	2918	9776
$(\Delta y)^+$	16.22	22.06	36.85	14.72	73.04	16.78	39.62
$(\Delta r)^+_{min}$	0.24	0.29	0.47	0.23	0.66	0.21	0.43
$(R\Delta\theta)^+$	4.90	6.75	12.30	4.37	21.65	5.21	11.63

4.6.1 Assessment of development state

The buoyancy aids the motion in the upward heated flow and turbulence production is inhibited, thus the process of flow development is slowed down and a fully development is only approached in a very long tube. Although the hydrodynamically and thermally fully developed condition was achieved in the experiment according to the statement by Kim et al. [15], the detailed explanation was not given. It is necessary to decide the state using the specific parameters. In the circular tube subject to constant heat flux, after the turbulent flow is hydrodynamically and thermally fully developed, the time-averaged temperature profile is no longer a function of axial distance from the inlet [16], i.e.,

$$\frac{\partial}{\partial x}\left(\frac{T_w - \overline{T}}{T_w - \overline{T}_c}\right) = 0 \rightarrow \frac{T_w - \overline{T}}{T_w - \overline{T}_c} = f(r) \tag{4.32}$$

where $\overline{T}_c$ is the time-averaged temperature at the centerline of tube and T_w is the wall temperature. If the turbulent flow is thermally fully developed, the nondimensional temperature is a function of r only and it is independent of axial location x.

For fully developed state, the nondimensional velocity should also be a function of r,

$$\frac{\overline{u}}{\overline{u}_c} = f(r) \tag{4.33}$$

where $\overline{u}$ is the velocity and $\overline{u}_c$ is the time-averaged velocity at the centerline of the tube.

The above two parameters at $r = 0.3R$ and $r = 0.6R$ are given in Fig. 4.17 to study the development state of the turbulent flow along the tube. It can be seen in Fig. 4.17(a) that at the $r = 0.3R$ the profiles of the nondimensional velocity and temperature for all the cases almost keep constant near the outlet of the tube and they are not dependent of axial distance. In Fig. 4.17(b) for $r = 0.6R$, the profiles of the nondimensional velocity vary little while the ones of the nondimensional temperature remain changing in case 1, 2, 3 and 4, but their variation is not so obvious. For the flow with strong heating, no truly fully hydrodynamically and thermally developed conditions can be reached because the temperature increases lead to continuous axial and radial property variations, in particular for the upward flow with strong buoyancy force. Only the approximately fully developed state (quasi-developed state) can be obtained. Therefore, even the weak variation exists near the outlet of the tube, it is reasonable to consider it as a fully developed state near the outlet.

4.6.2 Comparison with the experiment

In the present study, only the mixed flow are simulated. In order to quantify the extent to which buoyancy forces influence the heat transfer process, it is necessary to establish a reliable buoyancy-free, forced convection base for comparison. Petukhov

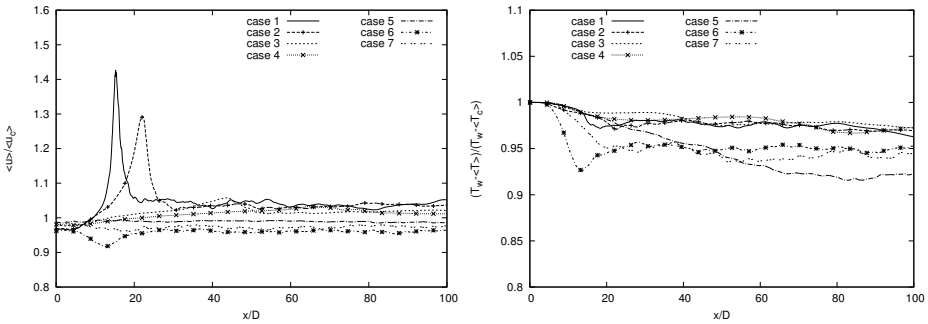

(a) r = 0.3R

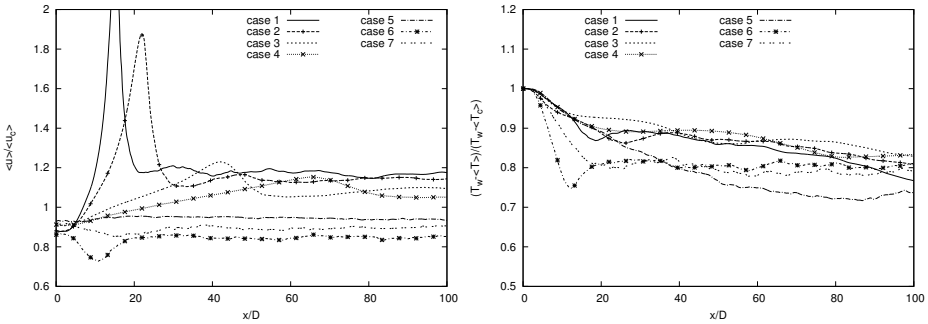

(b) r = 0.6R

Figure 4.17: Nondimensional velocity and temperature along the tube

correlation [17] has been adopted by Li [14]. It is available for variable property forced convection heat transfer to gases in smooth uniformly heated tubes with hydrodynamically developed turbulent flow at entry but developing thermal conditions. The equation showed good agreement with a wide range of experimental data. It consists of three parts.

A main part which is proposed by Petukhov et al. [17]:

$$Nu_{pkp} = \frac{RePr(f/8)}{1.07 + 900/Re - [0.63/(1 + 10Pr)] + 12.7\sqrt{f/8}(Pr^{2/3} - 1)} \tag{4.34}$$

where

$$f = (1.82log_{10}Re - 1.64)^{-2}, \qquad Re > 10,000 \text{(Filonenko formula)} \tag{4.35}$$

$$f = 0.3164/Re^{-0.25}, \qquad 10000 > Re > 4000 \text{(Blaisius formula)} \tag{4.36}$$

A coefficient to take account of the thermal entry effects:

$$C_{thermal} = 1.0 + 0.48(1.0 + \frac{3600}{Re\sqrt{x/D}} \frac{e^{-0.17x/D}}{(x/D)^{0.25}}) \tag{4.37}$$

The property variation needs to be considered because of the important temperature difference. In the present study, the coefficient of the property variation proposed by Rohsenow et al. [18] has been adopted, as the original modifier reported by Li [2] has produced in inaccurate results.

$$C_{prop} = (\frac{T_w}{T_m})^n \tag{4.38}$$

where subscript w and m stands for the wall and bulk mean temperature. The value of exponents $n = -[log_{10}(T_w/T_m)]^{1/4} + 0.3$ for gas heating in turbulent flow.

In the reference [17], the used correlation overpredicted the experimental Nu numbers. A modification factor Mod_h was employed, which was calculated based on the Reynolds number and location x/D

$$\begin{aligned}
\text{Mod}_h &= 0.995 + 1.0 \times 10^{-7} \times \text{Re}, \quad \text{x/D} = 12.1 \\
\text{Mod}_h &= 0.988 + 4.0 \times 10^{-7} \times \text{Re}, \quad \text{x/D} = 26.8 \\
\text{Mod}_h &= 0.978 + 9.0 \times 10^{-7} \times \text{Re}, \quad \text{x/D} = 41.5 \\
\text{Mod}_h &= 0.962 + 1.6 \times 10^{-6} \times \text{Re}, \quad \text{x/D} = 56.2 \\
\text{Mod}_h &= 0.946 + 2.3 \times 10^{-6} \times \text{Re}, \quad \text{x/D} = 70.9 \\
\text{Mod}_h &= 0.926 + 3.1 \times 10^{-6} \times \text{Re}, \quad \text{x/D} = 90.5
\end{aligned} \tag{4.39}$$

The location between them was obtained by the method of interpolation. Therefore, the final forced convection Nusselt number can be written as

$$Nu_f = \text{Mod}_h \times C_{thermal} \times C_{prop} \times Nu_{pkp} \tag{4.40}$$

Figs. 4.18-4.20 provide Nu, Nu ratio and wall temperature for the all cases and comparison with the existing experimental results. Nusselt number of case 1, 2, 3 and 4 in the upward flow are in good agreement with the measurements while case 5 with large Reynolds number presents a bigger difference and case 6 in downward flow also shows a relatively clear difference. Regarding to the Nusselt ratio, the large difference appears at the entrance region and downstream region for case 1 and case 6. One reason could be that the forced flow correlation used in the Li's literature are different with the one in the present study. In order to the compare the Nu ratio difference caused by the correlation, the Nusselt number of the forced flow in Li's thesis [2] are compared with the calculated one using the modified equation, which are shown in

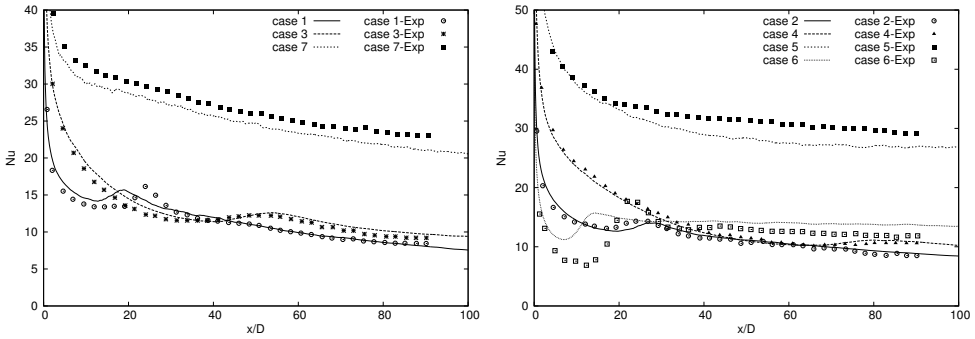

(a) case 1, 3 and 7 (b) case 2, 4, 5,and 6

Figure 4.18: Comparison between the prediction and experimental data on Nu

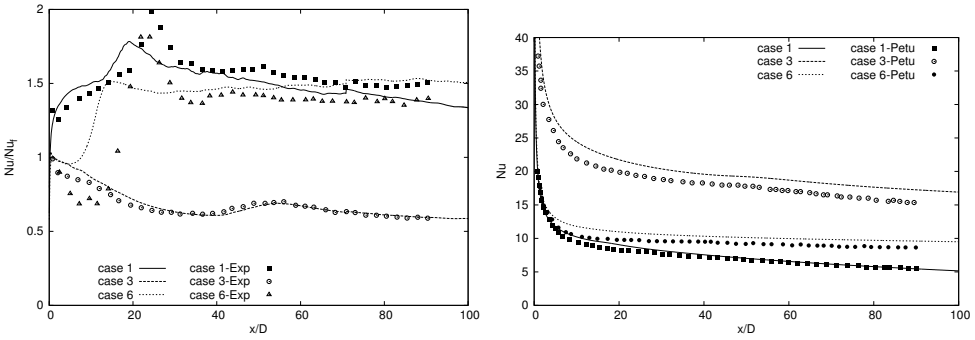

(a) Nu ratio (b) Forced Nu

Figure 4.19: Comparison between the prediction and experimental data on Nu ratio

Fig. 4.19(b). Although they illustrates the consistent results in the three cases, the difference in case 1 can not be neglected with a 5% error at 90D. With the present correlation, Nu ratio is 1.38 at 90D while it is 1.46 with the forced Nu number in Li's thesis. Therefore, the correlation adopted is one of the reasons that cause the Nu ratio difference in the downstream region for case 1. Nu ratio deviation in case 6 is mostly caused by the Nu difference. The wall temperature in case 6 are compared against the measured one(Fig. 4.20(b)). It can be observed that a clear difference appears near the entrance region, causing the corresponding deviation in Nu and Nu ratio. Meanwhile, the temperature profile of case 6 also presents a certain error in

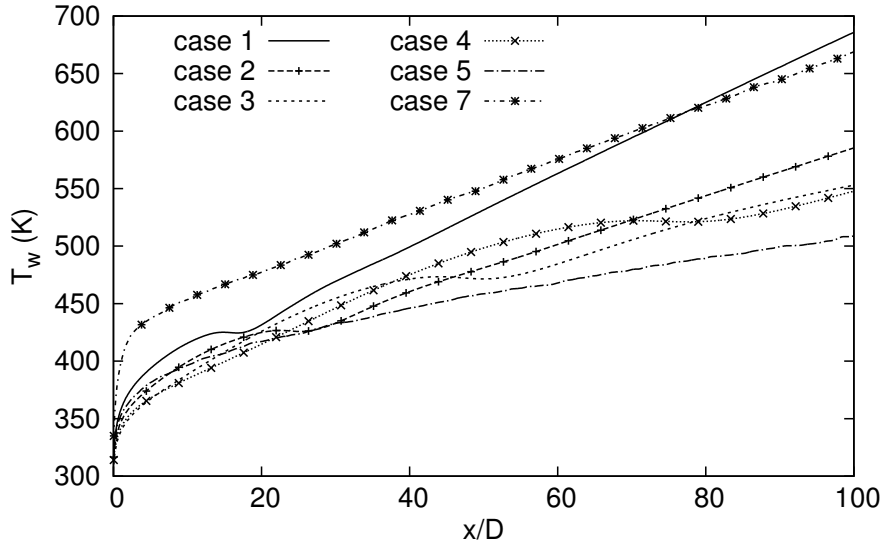

(a) case 1-5 and 7

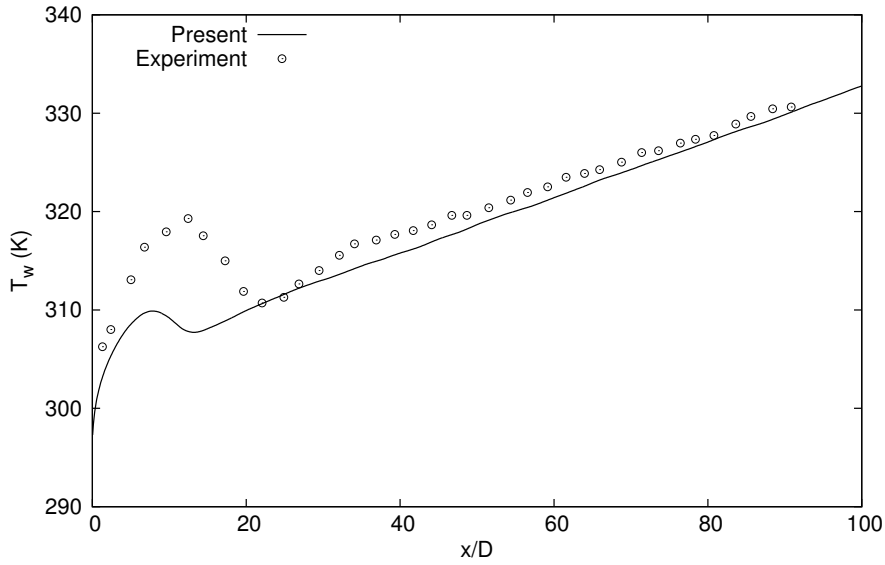

(b) case 6

Figure 4.20: Wall temperature

the downstream region. The reason could due to at several aspects: inlet condition, heat loss and heat flux uniformity. The velocity characteristic at inlet could not be completely same with the fully developed turbulence state even with a long unheated tube because the uncertainties such as the conduction and skin friction could probably influence its developing. As a result, the turbulence intensity could be enhanced or reduced compared to the simulation result. The axial conduction along the tube wall was not considered in the simulation but it could actually exist in the experiment. Meanwhile the heat loss to the surrounding is not small and could have a significant impact on the imposed heat flux. Electrical resistance variation with the temperature could also result in the non-uniformity of the heat flux imposed on the wall.

Fig. 4.20 shows the distribution of wall temperature T_w along the streamwise direction for all the cases. There is a fluctuation of the wall temperature in all the cases except case 5 and case 7. The wall temperature begins to decrease along the axial direction after reaching a peak. After proceeding the reduction, the wall temperature begins to increase gradually from the dip point again. Its fluctuation is caused by the reduced or enhanced turbulence, which will be explained later. Different from others cases, the wall temperature in case 5 and case 7 show a monotonical increasing trend. Due to the weak buoyancy force, the convection flow is very similar to the forced flow and the caused temperature reduction at the entry region is very small and is not apparent. Meanwhile those findings were obtained: the wall temperature has a rapid increase at the beginning of the flow; in the upward flow, the peak moves downstream with the decreasing buoyancy force parameter; the wall temperature distribution in downward flow is lower than that of the corresponding upwards flow (case 4 vs 7). In general, the obtained results in the present simulations are qualitatively in good agreement with the experiment, especially in the downstream zone.

A semi-empirical model for the influence of buoyancy force was developed by Jackson [19] based on the experimental data. The correlation is available for the hydrodynamically and thermally fully developed turbulent mixed convection and its form is

$$\frac{Nu}{Nu_f} = [|1 \pm 2.5 \times 10^5 \frac{Gr^*}{Re^{3.425} Pr^{0.8}} (\frac{Nu}{Nu_f})^{-2}|]^{0.46} \tag{4.41}$$

where the positive sign refers to the buoyancy-opposed flow and the negative sign to the buoyancy-aided flow. The correlation is most likely to be successful in predicting mixed convection in the downstream region, where fully developed conditions are being approached.

Fig. 4.21 gives the comparison for 26.5D and 90D respectively in terms of Nusselt number ratio plotted against buoyancy parameter. Also shown in the figure are the experimental results of Li [2] and the profiles predicted by the semi-empirical correlation (Equation. 4.41). At 26.5D (Fig. 4.21(a)), the predicted values are located in the range of the experimental data. For the upward flow, the experimental Nu ratio profile deviates from the semi-empirical correlation while the agreement in the

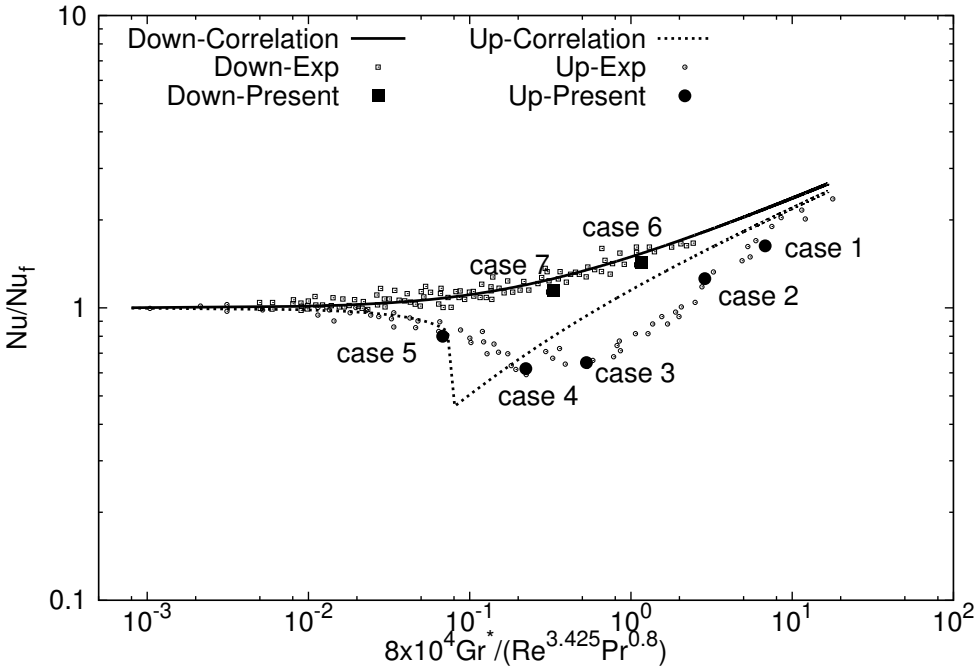

(a) x=26.5D

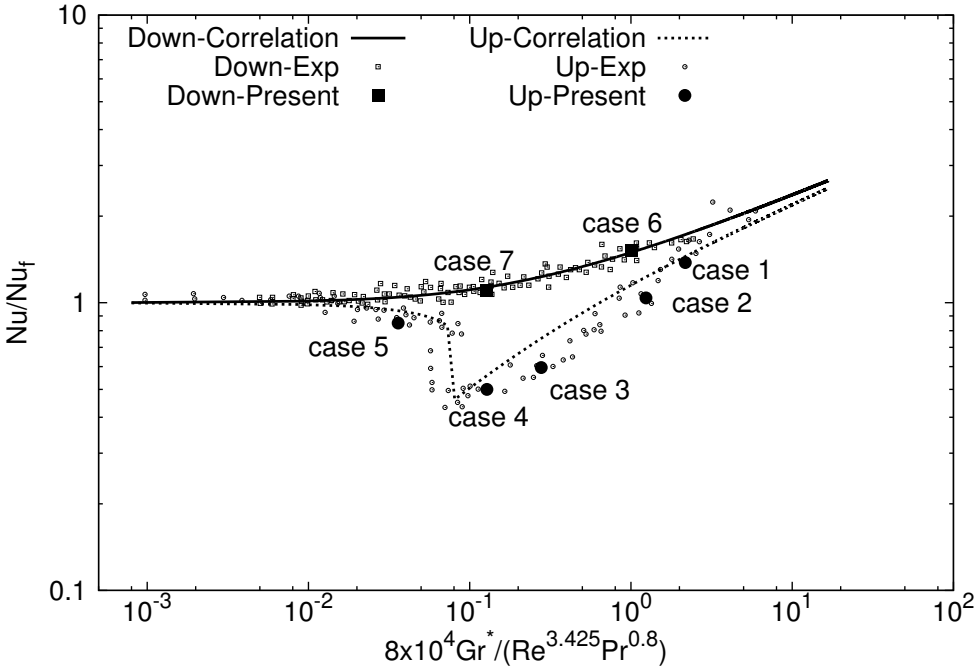

(b) x=90D

Figure 4.21: Nu ratio distribution for the mixed flow

downward flow is good. It need to be noted that the semi-empirical model is only available for the hydrodynamically and thermally fully developed flow. In the upward flow, the flow is far from the fully developed flow owing to the aiding effect of buoyancy force at this location while the flow quickly approaches the fully developed state in the downward flow. From Fig. 4.21(b) of at x/D=90, it can be seen both that the experimental data and the predicted data are consistent with the model profiles, which confirms that the flow has approached the hydrodynamically and thermally fully developed state. Meanwhile the Nu ratio for downward flow varies little compared to the one at 26.5D since it reaches the fully developed flow both at 26.5D and 90D. From the observation for the whole Nu ratio profile, it can be seen that Nu ratio for the upward flow decreases gradually in the non-fully developed region with buoyancy force then it recovers slowly. For the hydrodynamically and thermally fully developed profile, Nu ratio has a sudden reduction followed by a steady recovery enhancement with the further increase of buoyancy force parameter.

4.6.3 Reynolds and buoyancy parameters

Fig. 4.22 shows the variation of the bulk Reynolds and Buoyancy parameter along the tube for the different cases. As the fluid flows downstream, the air temperature increases and the dynamic viscosity increases more quickly than the velocity. As a result, both the bulk Re number and buoyancy parameter decrease gradually along the tube from inlet to outlet. Both parameters are only dependent of the heat flux and mass flow rate, regardless of the flow direction.

Distribution of the local skin friction coefficient is shown in Fig. 4.23. It varies significantly with the buoyancy force. In the upward flow of case 1, C_f increases initially near the inlet with a steep slope and then it quickly falls to a low value from where it decreases slowly to the end. From the definition, skin friction is dependent on the velocity gradient at wall. The reason of the fierce variation is on the steep reduction or increase of the velocity gradient near the wall due to the buoyancy-induced flow acceleration which occurs in the streamwise direction. The peak-velocity location shifts from the tube center toward the wall from inlet to 20D and the velocity gradient near the wall become steeper (see Fig. 4.24 and Fig. 4.25). Afterward, the velocity peak is diminished slowly. For the same reason, similar phenomenas were observed in case 2, 3, 4 and 5. The fluctuation extents are reduced due to the decreasing buoyancy force.

On contrast, in the downward heated flow, the velocity decreases near the wall and increases in the core region with the strong heating in the entrance zone. The velocity near the wall is retarded and thus the skin friction decreases which is reflected in case 6. The skin friction coefficient begin to increase from the deepest point due to the recovery of the velocity. In case 7, similar phenomenon also exists although it is not apparent due to the weak buoyancy effects.

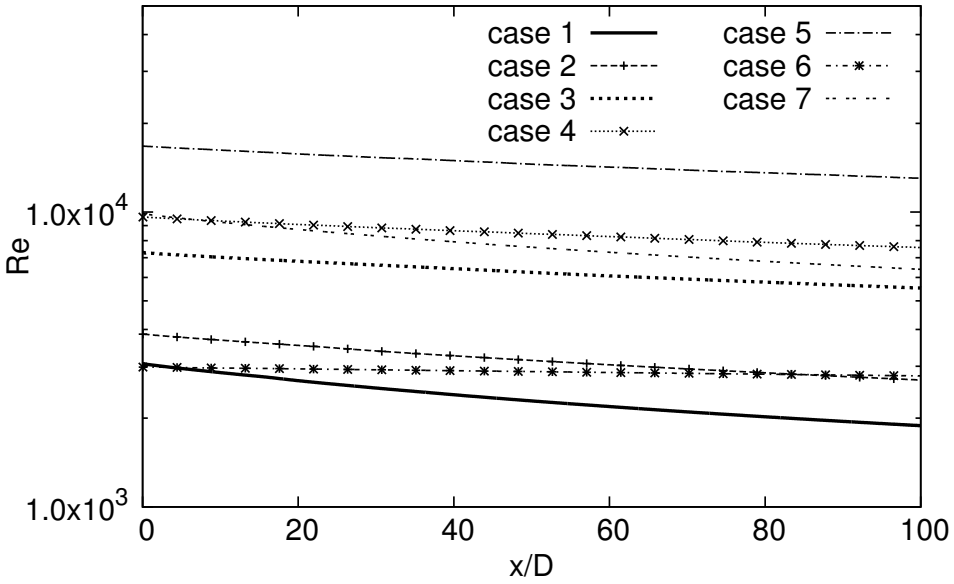

(a) Reynolds number

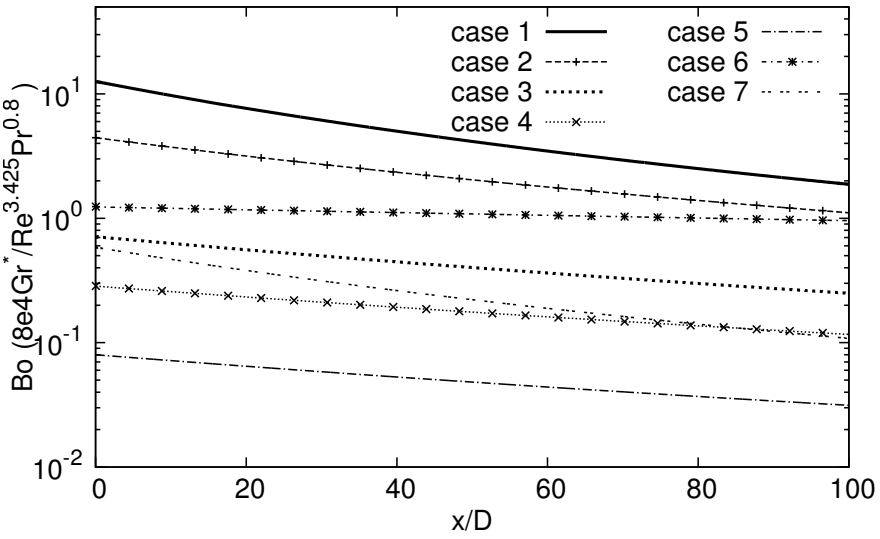

(b) Buoyancy force

Figure 4.22: Streamwise distributions of Reynolds and buoyancy force

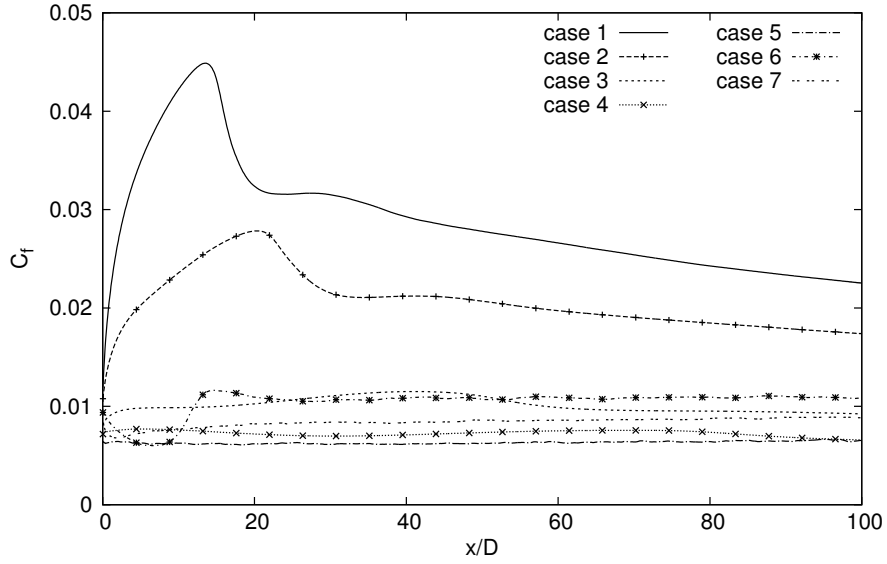

Figure 4.23: Streamwise distributions of skin friction coefficient

4.6.4 Mean resolved parameters profiles

Although the simulation on seven cases are conducted in our work, only four typical cases are chosen to study in details due to the space limitations. Case 1, 4, 6 and 7 are selected and they represent for the four typical flow states with the strong heating. In case 1, the buoyancy force is enough strong that it can enhance the heat transfer compared the forced convection while in case 4, the heat flux is impaired greatly. Correspondingly, the downward flow with the same buoyancy force parameters are chosen for the comparison study.

The predicted mean temperature and velocity profiles normalized with the corresponding local bulk parameters are given in Fig. 4.24 and Fig. 4.25. It can be seen from the temperature profiles that the thermal boundary layer becomes thicker as the flow develops. Owing to the heat flux imposed on the wall, the temperature near the wall is higher than bulk fluid and the density near the wall becomes smaller, so that the velocity near the wall accelerates relatively than the core region because of the fixed mass flow rate. The velocity field characteristic departs from the forced convection theory(the profile at inlet) and develops a dip at the tube center and thus shows an M-shape. Similar results were also obtained by Carr et al. [20] and

Polyakov [21]. However, the core flow is more accelerated than in the near-wall region in the downstream and the M-shape profile vanishes again since the temperature difference between near the wall and in the core decrease. The difference between case 1 and 2 is that the distortion of field in case 1 appears earlier and more clear than case 2 due to the stronger buoyancy force. As the velocity near the wall increase, the non-dimensionalized temperature gradient near the wall also increase, resulting in the increase in Nusselt number as shown in Figs. 4.18 and 4.19.

As Petukhov and Polyakov explained [22], the heating for upward flow can cause two effects. One is the external effect and the other is the structural effect. The external effect is defined as the mean velocity field change due to the buoyancy force, which is reflected by the M-shape profile in the present study. The structural effect is defined as an additional work for the turbulence to overcome the stabilized density

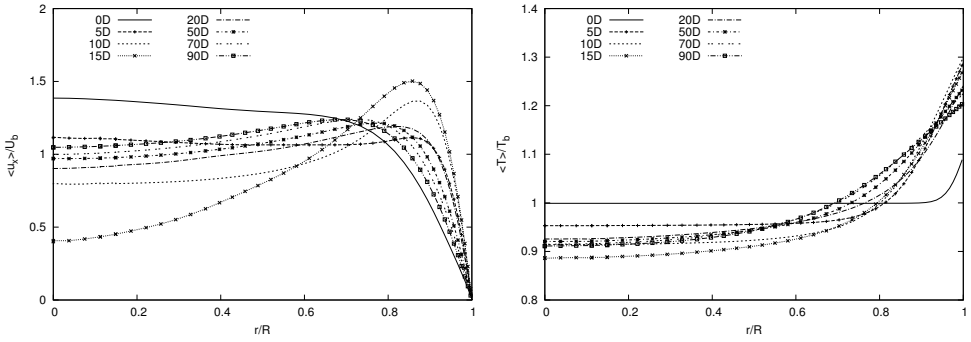

(a) Case 1

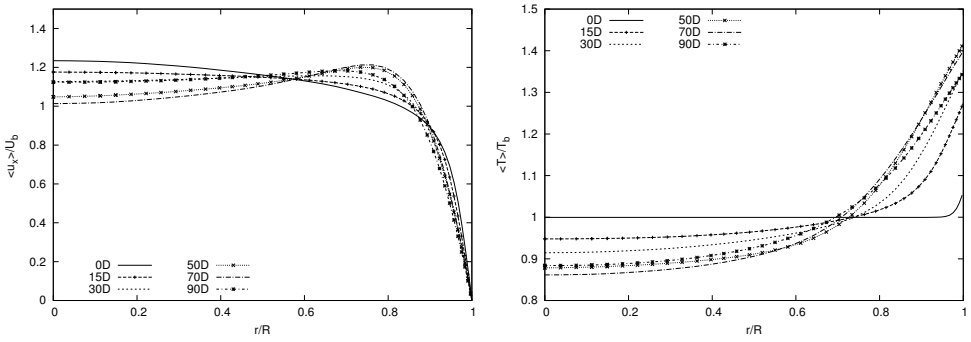

(b) Case 4

Figure 4.24: Mean velocity and temperature for case 1 and case 4

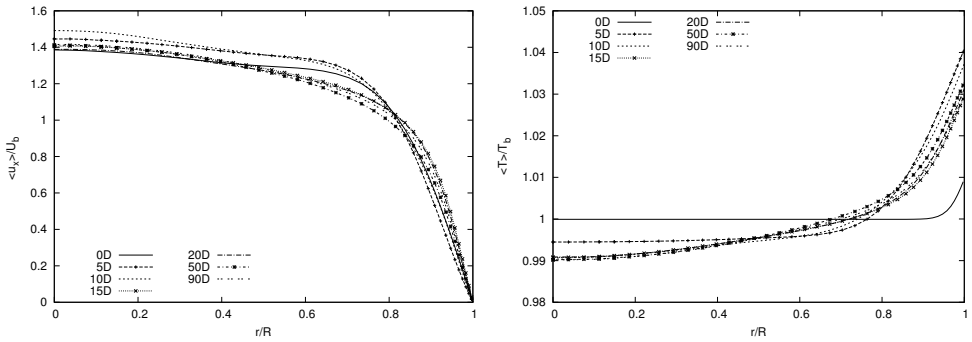

(a) Case 6

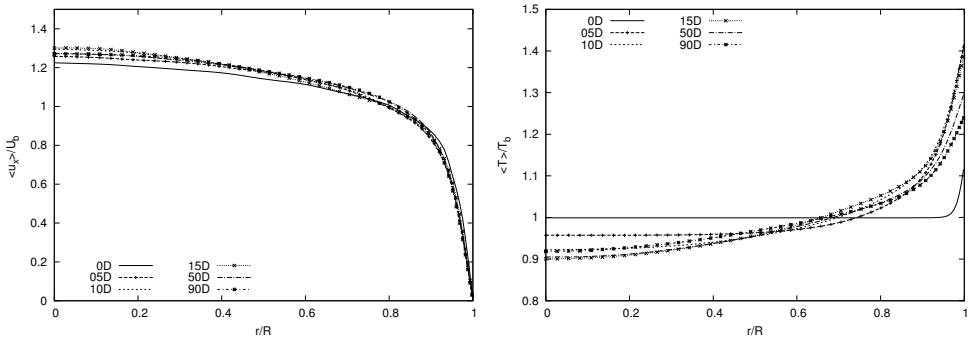

(b) Case 7

Figure 4.25: Mean velocity and temperature for case 6 and case 7

gradient for upward heated flow. For the intermediate heating power, the structural effect is much stronger than the external effect, which leads to decrease in the turbulent intensity due to the additional energy loss of the turbulence to work against the stabilized density distribution. As heating power increases further, the external effect starts to induce steeper velocity gradient and, as a result, more turbulence is generated near the wall. This phenomenon in the spatially-developing flow is striking and more details on structural effects will be explained later.

Compared to the clear M-shape distortion phenomenon in the case 1 and case 2, the distortion also exist in case 3, 4 and 5, but the deviation from the fully developed velocity field are less important due to the smaller buoyancy force. In the upward heating flow the buoyancy can cause the acceleration near the hot wall, and the effect of buoyancy force on the velocity is opposite in the downward flow. Therefore in case

6, the velocity gradient at 5D and 10D is less steep than the one at inlet while the reduced velocity near the wall result in a increased velocity at the center of tube. After the entrance zone(10D), the velocity profile becomes more like the forced flow again. This behaviour could be explained from the shear stress variation along the tube. The sudden increase in shear stress near the wall causes the velocity reduction in the wall region. At downstream, the maximum shear stress begins to move toward the center part which cause the velocity profile go back to the forced flow.

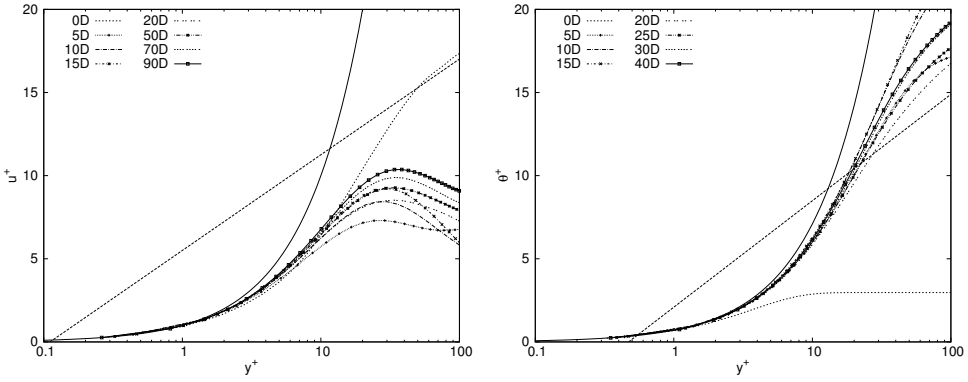

(a) Case 1

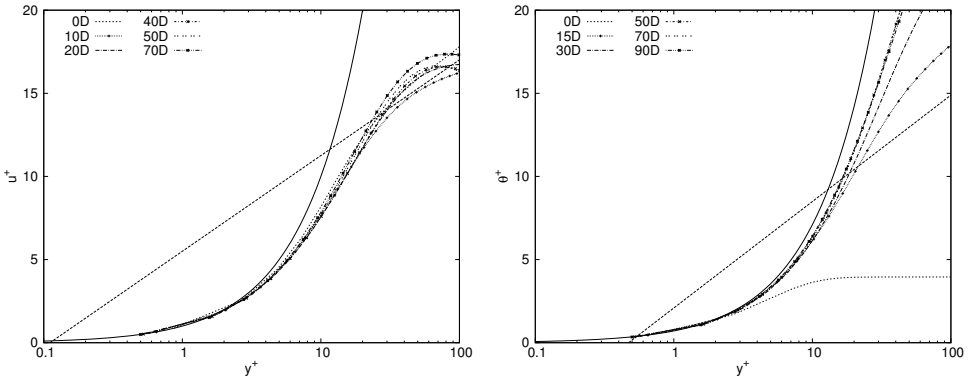

(b) Case 4

Figure 4.26: Mean velocity and temperature in wall coordinate for case 1 and case 4

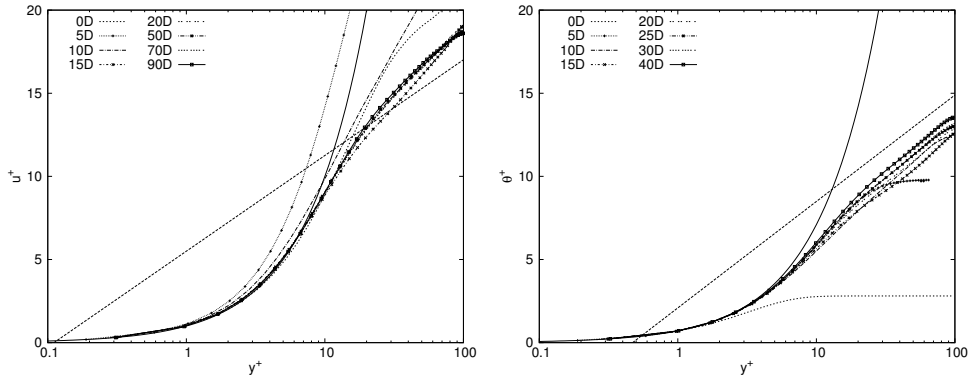

(a) Case 6

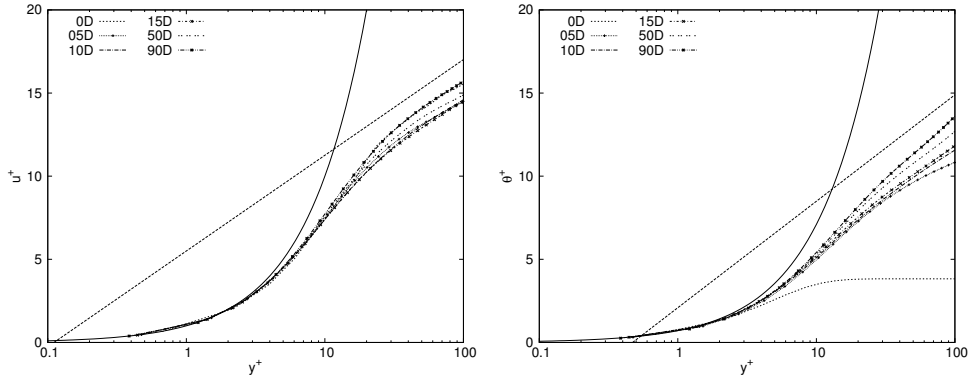

(b) Case 7

Figure 4.27: Mean velocity and temperature in wall coordinate for case 6 and case 7

In order to investigate the effects of heating on the mean velocity and temperature profiles more closely, the mean velocity and temperature profiles using wall coordinates are presented in Fig. 4.26 and Fig. 4.27 for case 1, 4, 6 and 7. Compared with the fully developed turbulent flow, the mean resolved velocity profiles deviate very quickly from the conventional logarithmic law in case 1 for response to the buoyancy force. After 5D from the entrance, its curve change little even though the turbulence intensity is suddenly enhanced around 15D. In case 4, the variation of velocity is

apparently slow due to the weak buoyancy force. In the downward flow, the predicted u^+ and θ^+ are shown to be in much better agreement with the corresponding universal profiles. This indicates that the stabilizing effect of streamwise flow acceleration induced by heating is canceled out by the destabilizing effect of buoyancy in downward heated flows [10] so that the flow remains as fully turbulent. However for case 6, there is a clear deviation of velocity at 5D corresponding the distortion of velocity. Afterwards it is recovered to the universal profile. For case 1 and 4, the predicted θ^+ shows a clear trend of laminarization from the wall with heat flux so that it is more closely matched to the laminar profile. Quite unlikely θ^+, however, the predicted u^+ does not show the expected trend of laminarization as shown in the θ^+, which is an interesting feature of the strongly heated internal air flows with large density variation. As a matter of fact, the specified difference was first identified by Bae et al. [8]. The effect of significant density variation on the mean velocity profile is different from that on the mean temperature profile. The nondimensional mass flux, instead of the mean velocity, was considered to be similar to the nondimensional temperature because both profiles bear a distinctive character of the laminar-like flows under the high heating conditions. He also suspect that the dissimilarity is because the existence of the gravitational force term makes the momentum equations different from the energy equation. The detailed reason of dissimilarity could referred to [8]. The divergence from the representative laminar profile does not indicate that the turbulent momentum is actually enhanced.

4.6.5 Velocity and temperature fluctuations

In order to investigate the influence of strong heating on the turbulence fluctuation, we have looked into the various turbulent statistics in this study. Figs. 4.28 and Fig. 4.29 show the root-mean-square values of the fluctuating velocities and temperature along the tube for case 1, 4, 6 and 7. They are normalized by the local bulk velocity or temperature. It can be seen from Fig. 4.28(a) that the maximum velocity fluctuations for case 1 are located around 15D or 20D while the minimum values are around 5D or 10D. The velocity fluctuations in all the three directions proceed a process of sudden reduction, increase and slow decrease. The maximum point moves towards the core along the tube. In case 4, the similar trend was observed but the maximum velocity fluctuation location are different depending on the buoyancy force. It is needed to notice in the downward flow that the velocity fluctuation has a quick increase process in the entrance region. After that they decrease gradually and remain a higher level than at inlet. The maximum point does not move towards the core of the tube very clearly.

The temperature fluctuations do not show the consistent trend with the velocity fluctuations in the upward flow. They monotonically increase with the commencement of the flow and heating. After a certain of excursion, the temperature fluctuation reaches to the maximum point and then changes little at downstream. The distance

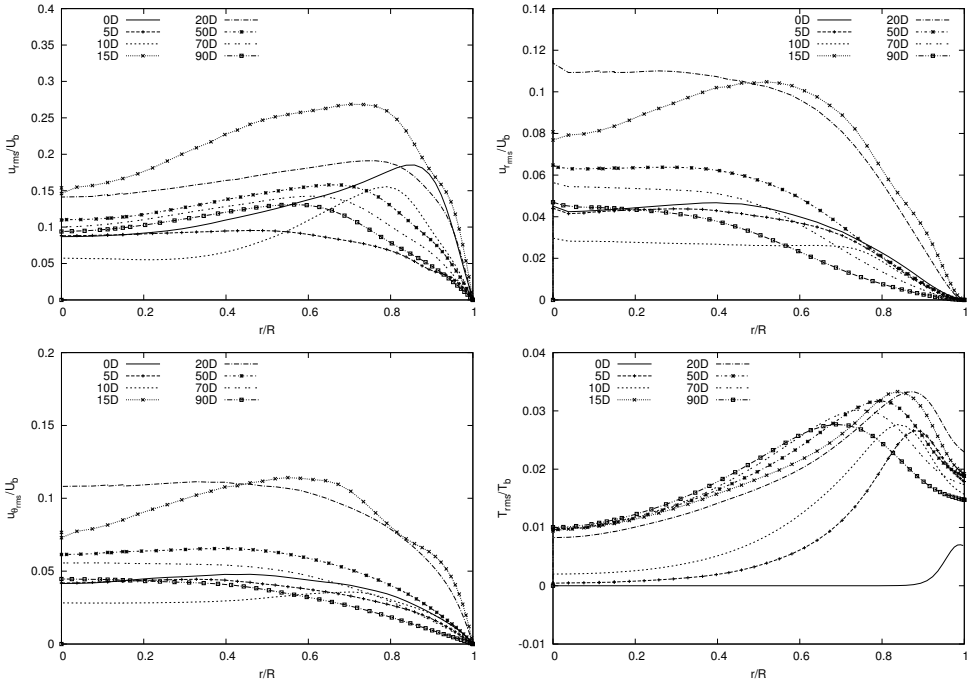

(a) Case 1

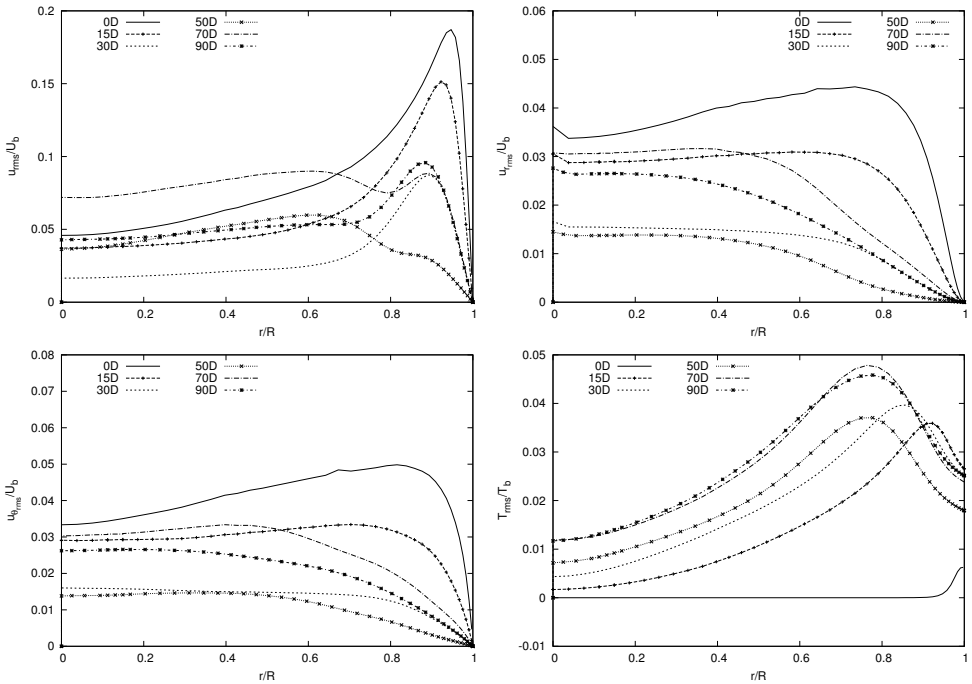

(b) Case 4

Figure 4.28: Velocity and temperature fluctuations for case 1 and case 4

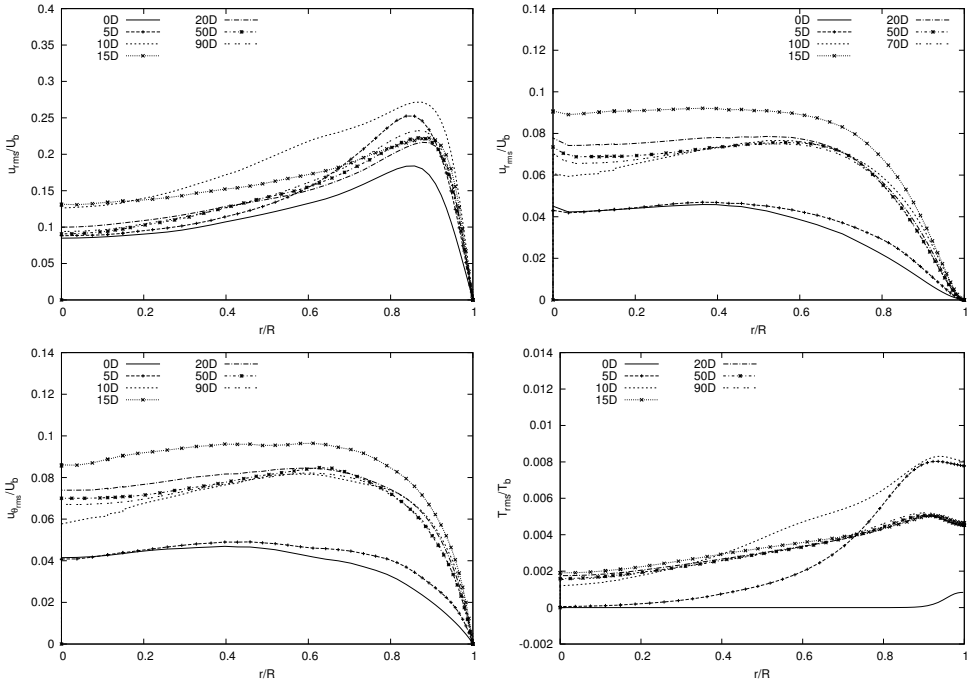

(a) Case 6

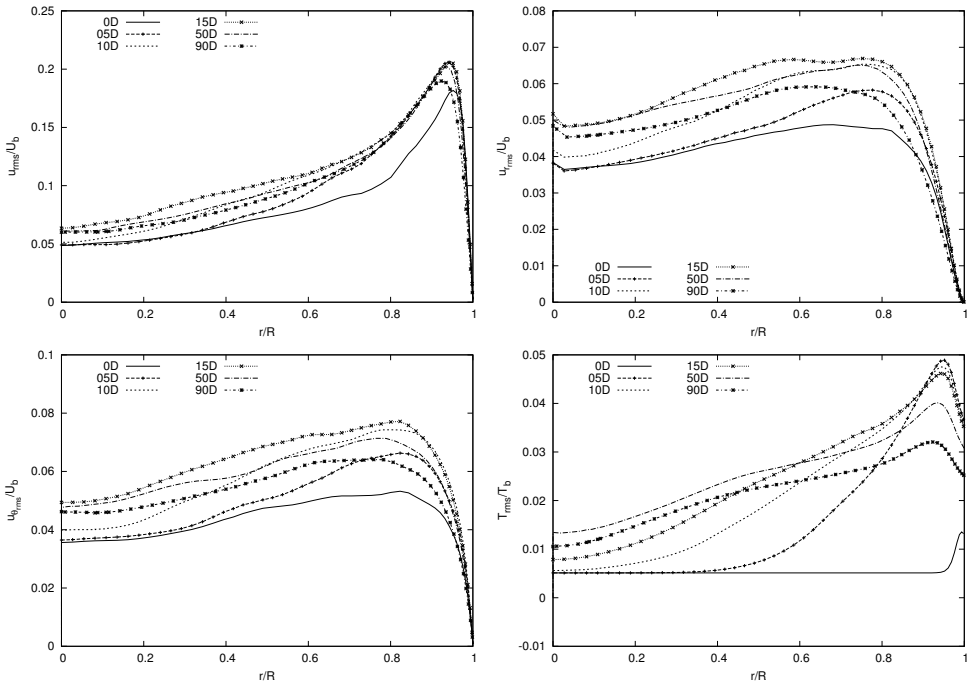

(b) Case 7

Figure 4.29: Velocity and temperature fluctuations for case 6 and case 7

of excursion depends on the buoyancy force. The maximum point has a general trend of deviation from wall. Case 4 illustrates the similar phenomenon.

In the downward flow, the temperature fluctuations increase to the maximum point much more quickly than in the upward flow with the same buoyancy force. Its variation is small after peak point. It is noticeable that there is a rapid jump and reduction in case 6. It could be explained from the turbulent heat flux. The turbulent heat flux proceeds a sudden increase and reduction near the entrance region. As a direct influence, the temperature fluctuation presents a rapid fluctuation. One significant characteristic is that the peak of the temperature fluctuation does not change clearly as in the upward flow except in the entry region.

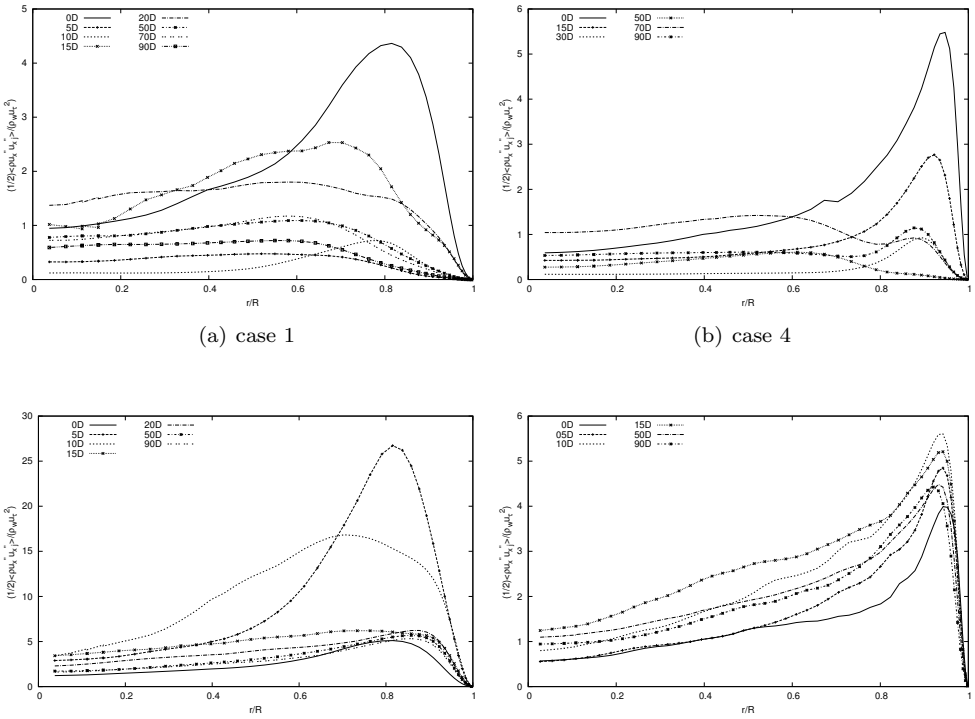

(a) case 1

(b) case 4

(c) case 6

(d) case 7

Figure 4.30: Turbulent kinetic energy

The turbulence kinetic energy(TKE) distributions for case 1, 4, 6 and 7 are given in Fig. 4.30. This figure illustrates the effects of strong heating on turbulence intensity

very nicely because it includes the velocity fluctuations on three directions. In the all cases of upward flow, turbulence kinetic energy shows non-monotonic behaviours. In case 1 where the strongest heating exists, the turbulence intensity is high at inlet with the hydrodynamically fully turbulent developed state. According to the TKE equation given by Lele [23] for compressible turbulent flow, the buoyancy production term $\mp(gR/U_0^2\overline{\rho' u_x'})$ (see Fig. 4.35) is included in it, which imply the direct relation between them. The initial tendency of TKE follows the variation of the negative buoyancy force production term and it decreases rapidly from inlet to 5D. The very low value of TKE represents the effective laminarization of a strongly heated air flow. After that, TKE is enhanced to a peak point at a quick speed due to the positive negative effect of the buoyancy force production. The recovery of turbulence intensity shows the reverse of laminarization process(laminar-turbulence transition). After the maximum point, the turbulence intensity begins to decrease slowly again due to the subordinate effect of buoyancy force production in the TKE transport equation, but remains a intermediate level of turbulence intensity, which means that the flow does not be laminarized completely. Finally the hydrodynamically and thermally fully developed turbulent flow are approached in the vertical tube. In the downward flow, for instance case 6, the turbulence intensity is enhanced to a very high level at the entry region due to the rapid increase of buoyancy force production term $\mp(gR/U_0^2\overline{\rho' u_x'})$, which is dominated initially in the TKE transport equation at the entrance region. After that, the turbulence intensity is reduced gradually to the same level as the inlet. In case 7, a similar behaviour is observed, but it is not that clear due to the small buoyancy force. The turbulence intensity varies little along the whole field.

4.6.6 Turbulent shear stress

The shear stress contributions were calculated by

$$\tau_{res} = - < \rho u'' u_r'' > \tag{4.42}$$

$$\tau_{vis} = - < \mu \frac{\partial u}{\partial r} > \tag{4.43}$$

$$\tau_{sgs} = \overline{\tau}^t = - < \mu_t \frac{\partial u}{\partial r} > \tag{4.44}$$

$$\tau_{total} = \tau_{res} + \tau_{vis} + \tau_{sgs} \tag{4.45}$$

where the four equations represent the resolved Reynolds shear stress, resolved viscous shear stress and the modeled SGS shear stress, respectively. Fig. 4.31 and Fig. 4.32 present the distributions of the four shear stresses normalized by the wall shear stress

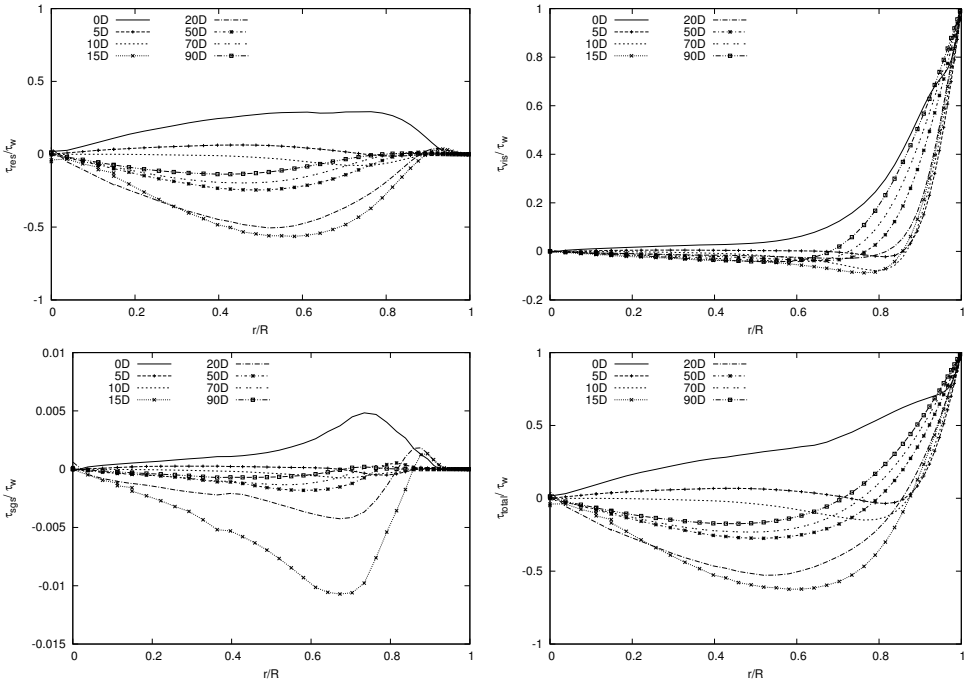

(a) Case 1

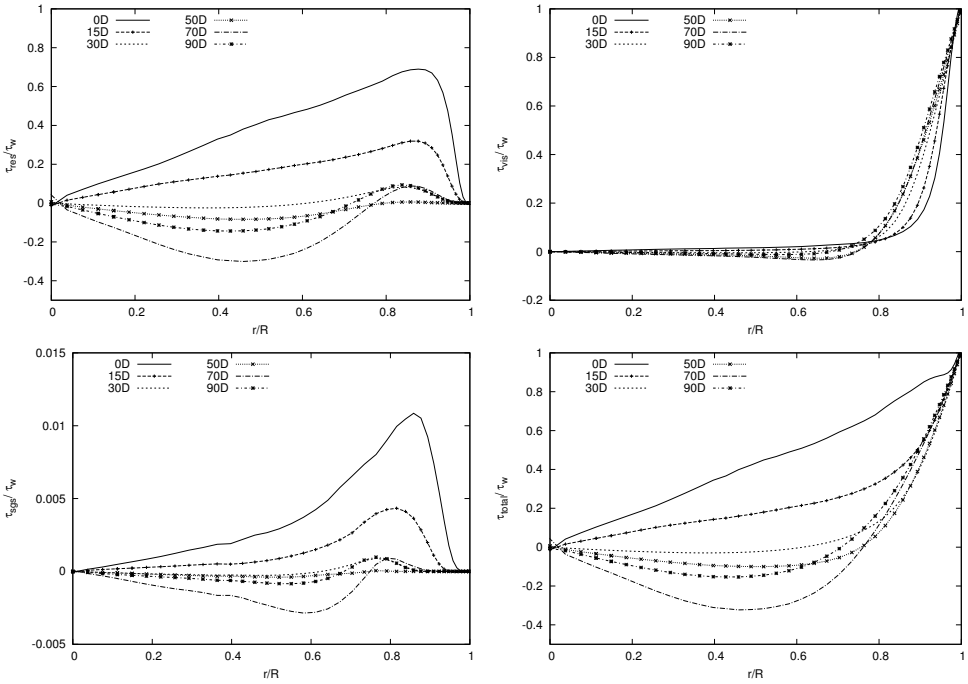

(b) Case 4

Figure 4.31: Shear stress distribution normalized by wall shear stress for case 1 and case 4

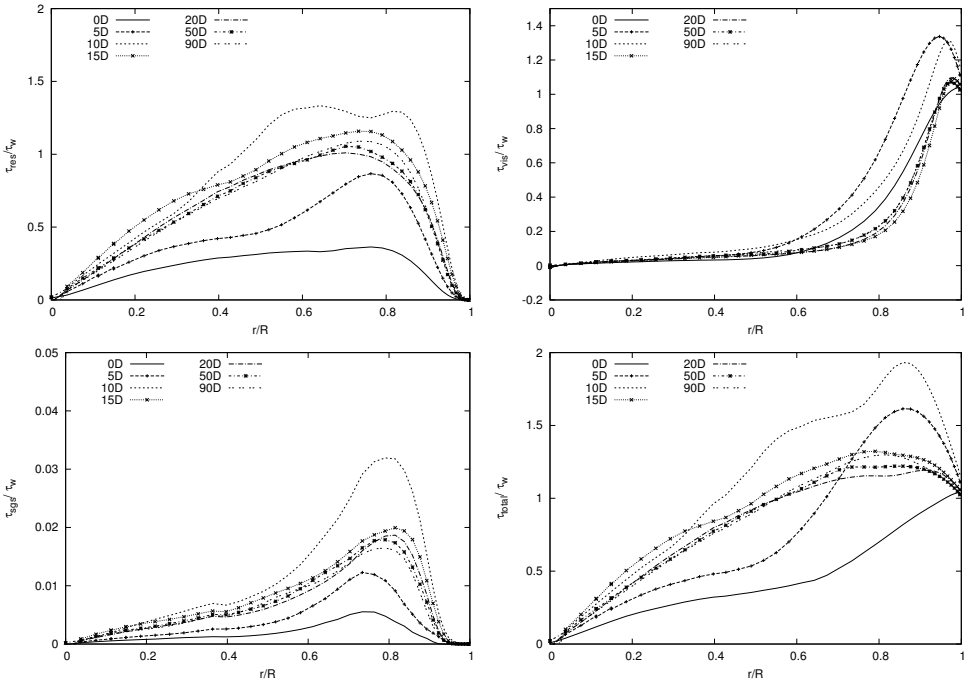

(a) Case 6

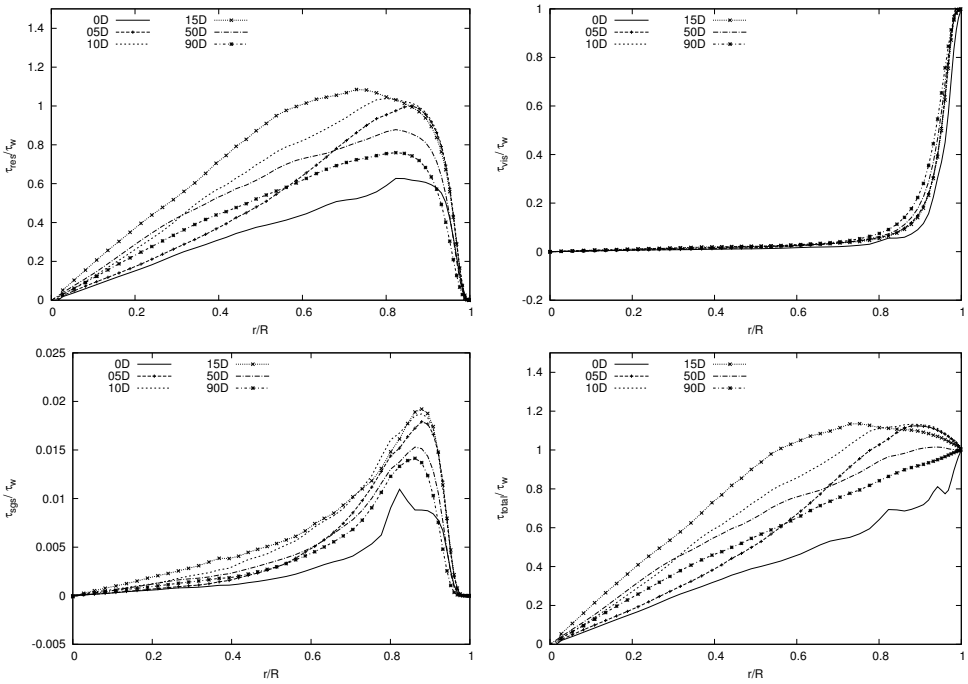

(b) Case 7

Figure 4.32: Shear stress distribution normalized by wall shear stress for case 6 and case 7

for case 1, case 4, case 6 and case 7. For case 1, the resolved Reynolds shear stress at the inlet corresponding to the hydrodynamically fully developed flow is reduced rapidly to a low level from 0D to 5D with buoyancy-aiding the flow. As a result, the flow starts to stabilize and heat transport begins to reduce, which implies the change from turbulent flow to laminar flow. The maximum turbulent Reynolds shear stress at the entrance zone is located in the region close to the wall. However as the flow develops, the Reynolds shear stress becomes negative (but is still quite small) further out since the maximum velocity point moves to near the heated wall and steeper velocity gradient is achieved. Negative Reynolds shear stress of considerable magnitude are suddenly present around 15D while the fiercest fluctuation is shifted toward the core of the tube radius because in the near-wall region the buoyancy force and the force driving forced convection act in the same direction. Therefore, after a certain point the buoyancy effect will start to destabilize the flow and enhance the turbulent heat transfer. The same phenomenon was observed by Axcell and Hall [24]. Afterwards, the Reynolds shear stress decreases gradually but a small negative turbulence exists.

In the condition of the hydrodynamically fully developed flow and a statistically steady state, the total shear stress must be linear and the normal-to-the-wall gradient of total shear stress must balance the pressure gradient [25, 26]. Hence in a sense the total shear stress can illustrate the deviation extent from the hydrodynamially fully developed flow. For case 1, the resolved Reynolds shear stress and SGS shear stress are very small near the wall region while the viscous shear stress is very large. In the core region, the viscous shear stress is very low. The total shear stress is nearly linear at the inlet and quickly shows a deep bend at 15D. At x=10D, the resolved and modeled SGS shear stress is almost zero and the total shear stress is mainly determined by the viscous stress. Meanwhile the distribution of the three shear stresses could reflect the thickness of viscous layer. The viscous shear stress increases near the wall along the streamwise direction, which is more clear in case 4. In large eddy simulation, the large scale motions contribute the most the resolved fields and are calculated directly, while the modeled SGS shear stress is one or two order smaller than the other two terms. The variation characteristics of the shear stress in the others cases of the upward flow are similar with the case 1, but is more pronounced in the latter.

For the downward flow, for instance, case 6, the resolve Reynolds shear stress is enhanced in the entrance region due to the opposed buoyancy force effect. It reaches to the peak value at 10D and after that, it decreases gradually untill 20D. From 20D, its variation is not significant and the Reynolds shear stress is higher than at the inlet. The variation of the Reynolds shear stress is consistent with the one of turbulent kinetic energy in case 6 and case 7. The behaviour of the viscous shear stress and modeled SGS shear stress in the downward flow are significantly different from the upward flow. Accompanying by the increase of resolved Reynolds shear stress, the

viscous shear stress has a rapid jump at 5D and it quickly returns to the constant level again at x=15D. The normalized viscous shear stress is always less than one in the upward flow. However it is more than one near the wall region in the downward flow. Due to the opposed buoyancy effect, the flow is retarded at the wall, which results in a lower velocity gradient and a smaller wall shear stress. Following the conservation of the flow rate, the velocity near the wall presents a trend of acceleration. With the great velocity, the viscous shear stress is more than one while it remains a low level in the core of the tube. Since the resolved Reynolds shear stress is enhanced compared to the forced flow, the total shear stress shows a reverse bend. In case 7, the similar phenomenon exists but is not clear because of the weak buoyancy effect.

The streamwise shear stress normalized by wall shear stress is illustrated in Fig. **??** for the following discussion on buoyancy force effect. The variation profiles of the streamwise shear stress are consistent with the turbulent kinetic energy(TKE).

4.6.7 Turbulent heat fluxes

Corresponding to the shear stress components, the turbulent heat flux contributions are calculated as,

$$\dot{q}_{res} = \bar{\dot{q}}^{t} = - < \rho u_r^{''} h^{''} > \tag{4.46}$$

$$\dot{q}_{con} = - < \frac{\mu c_p}{Pr} \frac{\partial T}{\partial r} > \tag{4.47}$$

$$\dot{q}_{sgs} = - < \frac{\mu_t c_p}{Pr_t} \frac{\partial T}{\partial r} > \tag{4.48}$$

$$\dot{q}_{total} = \dot{q}_{res} + \dot{q}_{con} + \dot{q}_{sgs} \tag{4.49}$$

Where the three heat flux components represent the resolved heat flux, heat conduction and modeled SGS heat flux, respectively. The sum of the three heat flux is the total heat flux. The four heat flux distributions normalized by the wall heat flux are shown in Fig. 4.33 and Fig. 4.34. Unlike to the rapid reduction of the resolved Reynolds shear stress in case 1 from inlet to 5D where the Reynolds stress is very small, the turbulent heat flux variation presents a slight increase in the radial direction and nearly remains unchanged at a somewhat from 5D to 10D. It is readily understood that the resolved turbulent heat flux depends on both the velocity and enthalpy(temperature) variation. The imposed temperature at inlet is uniform and the enthalpy fluctuation at the inlet is near zero. As the flow and thermal layer develop, the velocity fluctuation is reduced due to the buoyancy force and the temperature fluctuation is increasing due to the heating. The overall result depends on the variations of the two parameters. The maximum value appears at 20D where both the radial velocity and temperature fluctuation are at high level.

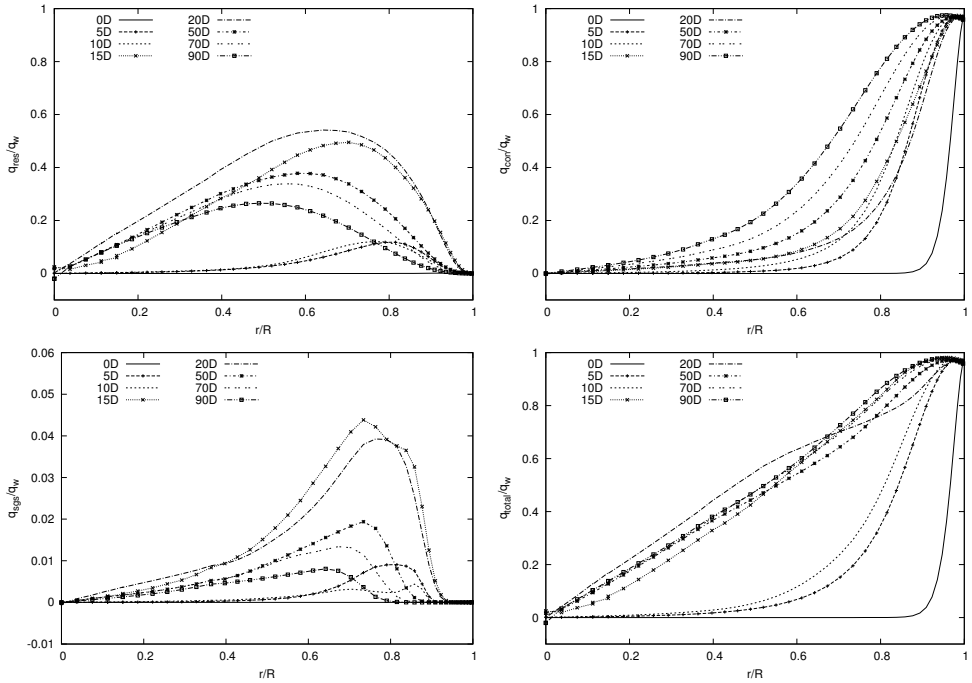

(a) Case 1

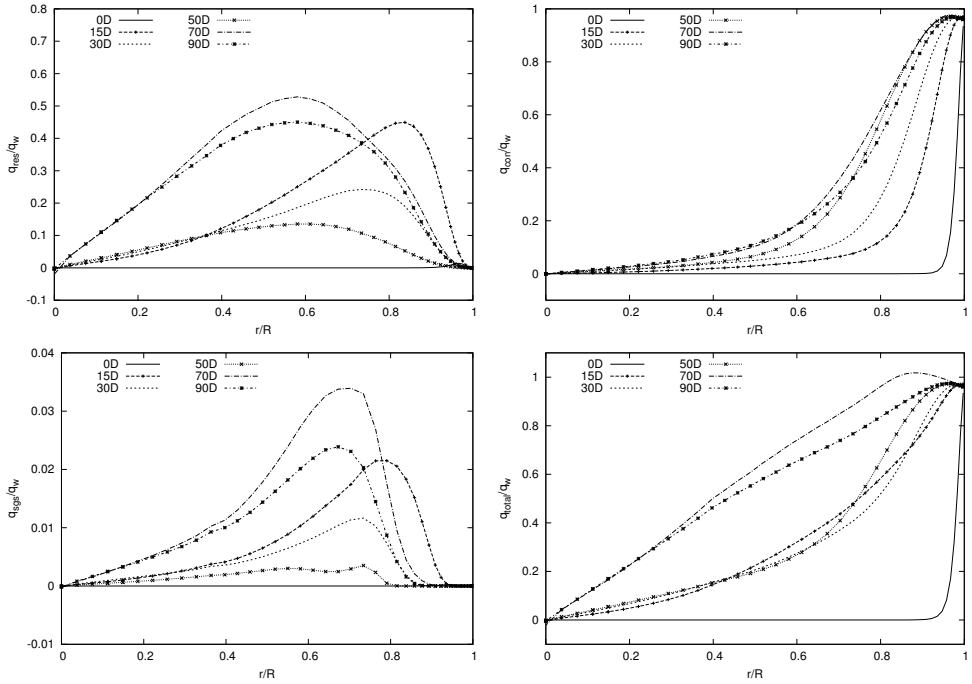

(b) Case 4

Figure 4.33: Heat flux distributions normalized by wall heat flux for case 1 and case 4

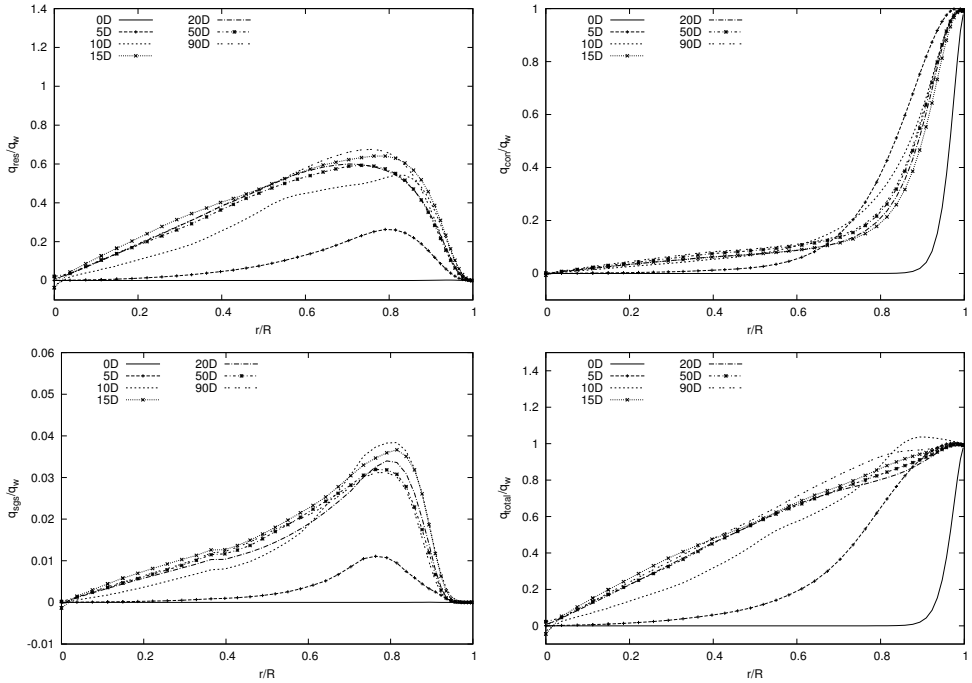

(a) Case 6

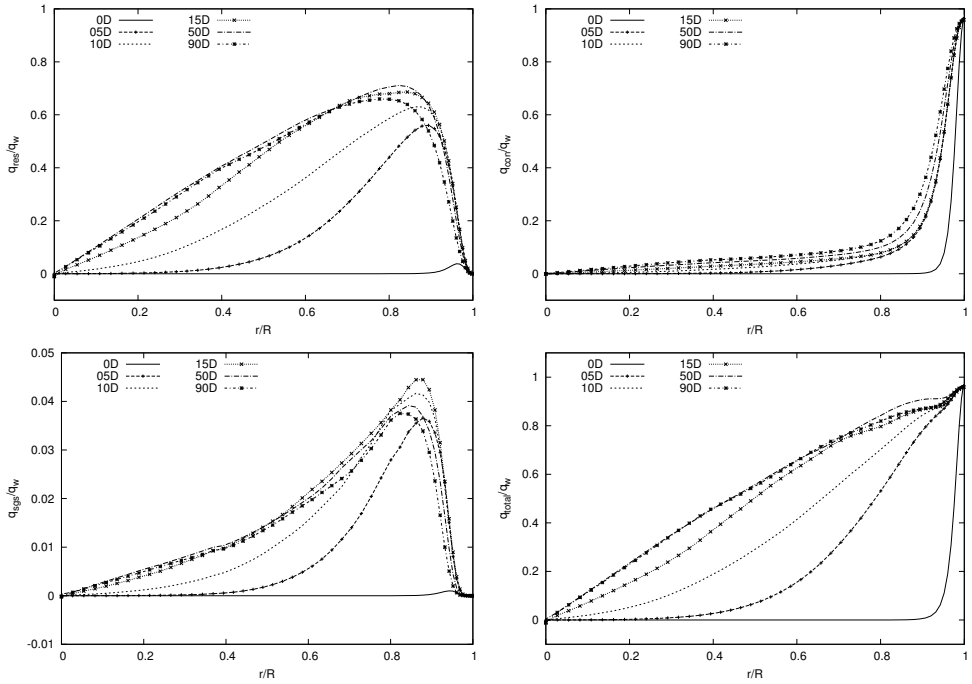

(b) Case 7

Figure 4.34: Heat flux distributions normalized by wall heat flux for case 6 and case 7

According to Prandtl's model [27], heat transfer to turbulent flows is controlled by two mechanisms in series, i.e. heat conduction through the viscous layer and diffusive energy transport from the border of the viscous layer to the core of the turbulent flow. Heat conduction is significant in the viscous sublayer. In case 1, the dominated region of heat conduction begins to thicken as the fluid flows downstream, which clearly illustrates the increase of viscous sublayer.

Like the total shear stress, the total heat flux should be nearly linear distribution in the hydrodynamically and thermally fully developed flow. The maximum deviation from the linear distribution is observed at the inlet of the tube because it is far from the fully developed state. The total heat flux is only comprised of heat conduction at the inlet. With the development of the flow, the total heat flux profile has a tendency of approaching the fully developed flow. Thus the profile at 70D is approximately linear, which confirms that the fully developed flow has been reached. Meanwhile the total heat flux shows a reverse bend around 20D, which is over the linear profile and is caused by the large resolved turbulent heat flux. The sudden increase of the total heat flux and streamwise turbulent heat flux explain why the wall temperature distribution is nonmonotonical. After the maximum value, the maximum total heat flux and streamwise heat flux begin to decrease slowly in the downstream region, so the wall temperature shows a increase trend again.

A similar behaviour also happens in case 2, 3 and 4. The magnitude of resolved turbulent heat flux also varies clearly at the initial region with high Reynolds number but the location of maximum is further downstream with the decreasing buoyancy force. Meanwhile in the buoyancy-opposed flow, the three heat flux components show a consistent profile with the corresponding shear stress except at the inlet region. It is because the shear stress and temperature profiles change little after the entrance region while the temperature is relatively uniform in the entrance region-thermally developing region. In the flow of both directions, the similar behaviour except the initial region shows that Reynolds normal stress and Reynolds shear stress are directly connected with the streamwise and radial turbulent heat flux, respectively. The linkage between them was also observed by You et al. [28] via the buoyancy production terms. It will be discussed in the following section.

In the turbulent heat transfer mechanisms, the diffusive energy transport from the viscous layer to the core is dominated beyond the viscous layer. It is proportional to the turbulence production in the area close to the rim of the viscous layer. The turbulence production depends on the difference between the velocity at the rim of the viscous layer to that in the core of the flow. The absolute difference of the velocity at the inlet of the tube is large since the state at inlet is fully developed turbulent flow (the velocity at the rim of the viscous layer is lower than in the core). The difference begins to decrease and becomes zero when increasing the impact of natural convection on the pure forced convection due to the increase of the velocity in the viscous

layer(near the wall). Further increase of the buoyancy forces enhances this difference because the velocity at the rim of the viscous layer could be higher than that in the core. Since the velocity difference determines the turbulence production, turbulence intensity shows its characteristic decline, when the influence of natural convection is augmented, before it rebounds with further increase of buoyancy force. The reduced turbulence production for small buoyancy influence in aiding flow causes a laminarization of turbulent flows. The axial wall temperature distribution in Fig. 4.20 for uniform heat flux thermal boundary conditions shows that local temperature maxima occur which indicate minima in heat transfer caused by the laminarization of the flow [21,29]. Laminarization after a certain entrance length, reaches full strength, yielding the minimum heat transfer rate(see Fig. 4.18), and is overridden by increasing strength of buoyancy force. The similar phenomenons were observed in the upward flow, i.e. case 2, 3 and 4. The difference among them is that the negative turbulent shear stress location is delayed and the extent that turbulence recovery is weak due to the weak buoyancy force.

For the opposed mixed convection on the other hand, the overall difference between the velocity at the rim of the viscous layer and the core increases with increasing buoyancy force and yields a higher heat transfer. But the behaviour are different along the different regions. In the entrance region, the imposed heat flux has only influence on the layer near the wall, so the velocity increases at core and decrease near the wall due to the buoyancy-opposed effect and the conservation of mass flow rate. The difference between the velocity at the rim of the viscous layer and the core increases compared to the inlet value. Therefore the turbulent shear stress presents a increase trend at the entrance zone. The increased shear stress causes the heat transfer enhanced. The enhanced heat transfer implies the influence of the boundary heat flux move towards the core and the velocity difference decreased. As a result, the shear stress is reduced gradually but still is greater than the inlet level due to the buoyancy force.

4.6.8 Effect of Buoyancy force on TKE

The transport equation for turbulent kinetic energy can be written as

$$\frac{\partial k}{\partial t}+\overline{u}_j\frac{\partial k}{\partial x_j}=-\frac{1}{\rho}\overline{\frac{\partial u_i^{''}p^{''}}{\partial x_i}}-\frac{1}{2}\overline{\frac{\partial u_j^{''}u_j^{''}u_i^{''}}{\partial x_i}}+\nu\frac{\partial^2 k}{\partial x_j^2}-\overline{u_i^{''}u_j^{''}}\frac{\partial \overline{u}_i}{\partial x_j}-\nu\overline{\frac{\partial u_i^{''}}{\partial x_j}\frac{\partial u_i^{''}}{\partial x_j}}-\frac{1}{\rho}\overline{\rho^{''}u_i^{''}} \tag{4.50}$$

In the equation above, convection, pressure diffusion, turbulent transport, viscous transport, production, dissipation buoyancy force term are included. The buoyancy force production term play an important role and it is our focus. The influence of buoyancy force on turbulence can be viewed as resulting from two distinct mechanisms [15,22], namely, the direct effect and indirect effect. The indirect effect is essentially the response of turbulence to the distortion of the mean flow field resulting from

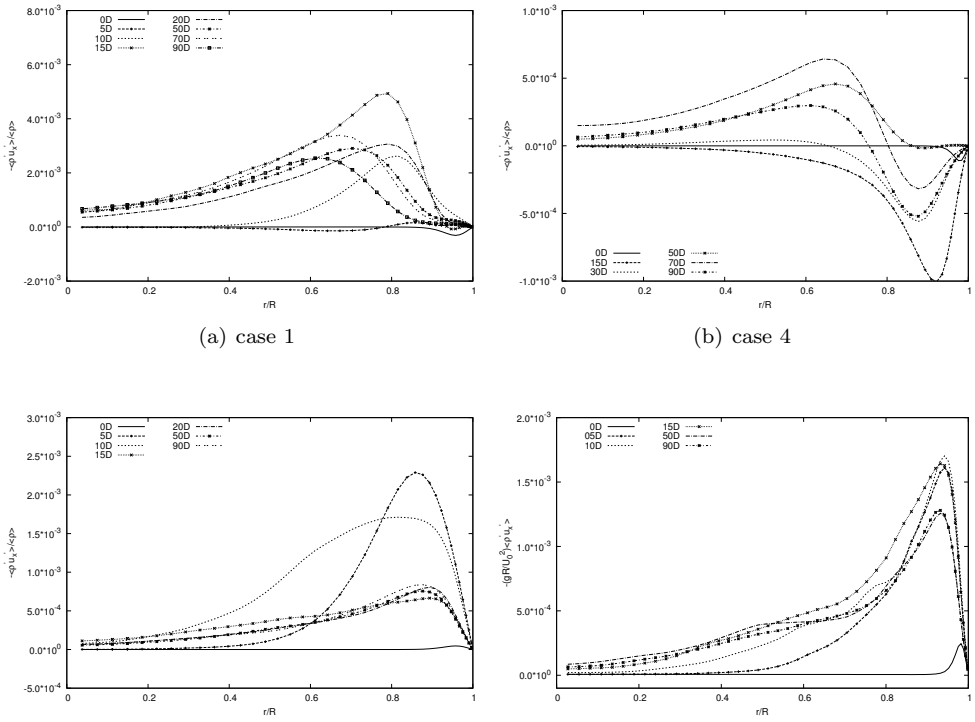

(a) case 1

(b) case 4

(c) case 6

(d) case 7

Figure 4.35: Buoyancy production term

the influence of buoyancy, which has been discussed earlier in the mean parameter section. For the turbulent mixed convection flow in a vertical tube, this is the principal mechanism responsible for the impairment or enhancement of heat transfer. The direct effect refers to turbulent energy production/destruction arising as a result of density fluctuations in a buoyancy-influenced flow. This is accounted for by the buoyancy production terms, which will focus on the following discussion.

Fig. 4.35 presents the distributions of the above buoyancy production terms for the four cases chosen. The buoyancy force term is slightly negative initially at $x < 5D$ for case 1, and the initial TKE decays greatly. It implies that although the effect of buoyancy force term on TKE is negative initially, it is not dominant. After 10D, the buoyancy force production becomes positive and reaches to the maximum. Therefore the TKE is expected to increase from the 10D and become more pronounced at around

15D with the peak of buoyancy production. At further downstream, buoyancy force term is still positive which means the positive effect on TKE. However, TKE deviates from the buoyancy production theory and shows a slight reduction trend. It can be explained that the M-shape velocity at 15D vanishes gradually and the buoyancy force production effect is not prevalent in the downstream region at $x > 20D$. TKE is not only determined by its buoyancy production term. In the downward flow, although buoyancy force term is always positive in all the field, the behaviour of TKE closely follows the characteristics of buoyancy force term only at the initial region as well. Similarly, the effect of the buoyancy production term is weak at the downstream region.

4.6.9 Laminarization assessment

Laminarization of the turbulent flow in a heated upward tube is caused by acceleration, buoyancy force and thermophysical property variation effects. As explained before, the heating could arise the increase of the mean flow velocity due to the reduction the fluid density. The flow acceleration in axial direction decreases the turbulence in the flow. Meanwhile the variation of fluid density caused by heating leads to the buoyancy force. The buoyancy force is large near the wall due to the strong heating, as a result, the turbulence is suppressed within the boundary layer. The variation of the physical property caused by the heating will result in the reduction of Reynolds number with high viscosity, which also causes the reduction of turbulence.

The laminarization criterion is significant to assess whether the flow is laminarized or not, but the criterion for the transitional condition for "laminarization" is ambiguous. The acceleration variable K_v is usually used as a parameter to measure the extent of laminarization. Fig. 4.36(a) presents the acceleration variation along the tube. Kline et al. [11] proposed a critical value of 3.6×10^{-6} as a threshold of complete laminarization. Coon et al. [30, 31] proposed the condition of transition as $K_v > 1.5 \times 10^{-6}$. In terms of the threshold, it suggests that the transitional state may exist for case 1 and case 2 due to the high heating but the flow may remain turbulent for others cases.

The acceleration parameter as a approach of address the laminarization has a disadvantage. In the method, only the acceleration is taken into account, which could be caused by heating or converge area. The others aspects such as buoyancy force and thermal physical property effect are not included in it. The most direct indicator of the turbulence is the resolved Reynolds shear stress. Shome [32] has proposed a laminarization criteria which is based on the reduction of in the level of Reynolds shear stress. He considered the flow as laminarization, when the maximum value of the Reynolds shear stress to viscous wall shear stress ratio reduced to 5% of the constant property value corresponding to the same value of inlet Reynolds number. Fig. 4.36(b) illustrates the maximum ratio variation of the Reynolds shear stress to the local viscous wall shear stress along the tube. Based on the criterion, the maximum

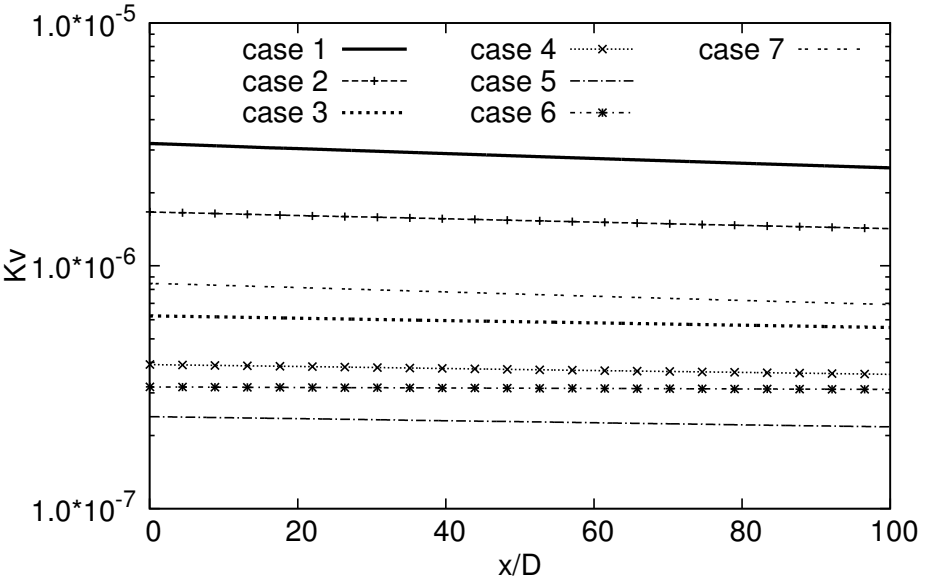

(a) Acceleration number

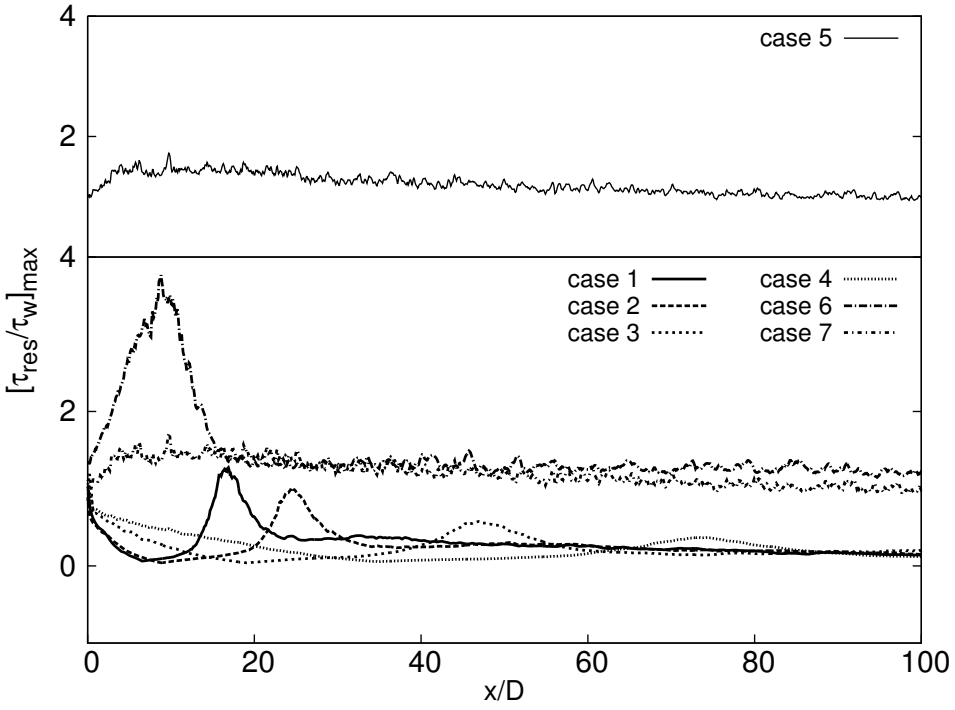

(b) Maximum Reynolds shear stress

Figure 4.36: Streamwise distributions of acceleration number and maximum Reynolds Shear stress

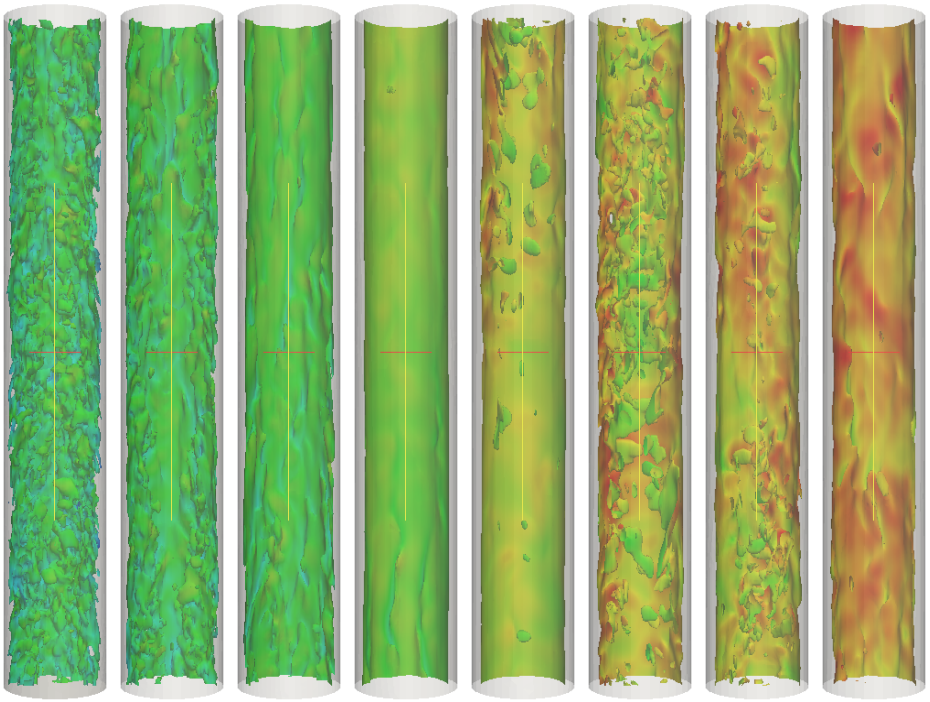

(a) 0-1m (b) 1-2m (c) 2-3m (d) 3-4m (e) 4-5m (f) 5-6m (g) 6-7m (h) 7-8m

Figure 4.37: Instantaneous isovorticity surfaces colored by velocity for case 4

ratio reduced to 9.5% of the inlet ratio in case 1, which indicates that it does not be completely laminarized but the turbulence is effectively reduced. The maximum ratio reduce to 4.3%, 3.4%, 5.3% in case 2, 3 and 4, respectively. The results show the flow proceed the process of complete laminarization in these cases. In the case 5 where the buoyancy is very weak, the Reynolds shear stress remain the same level along the tube. It illustrates that the flow during the whole process is turbulent.

In the downward flow of case 6 and case 7, the maximum ratio of the Reynolds shear stress to viscous wall shear stress is reduced, which shows the enhancement of the turbulence.

4.6.10 Instantaneous velocity field

The changes in characteristic of the flow field of case 4 are illustrated in Figs. 4.37 and 4.38 where instantaneous isovorticity surface and velocity vector at cross section

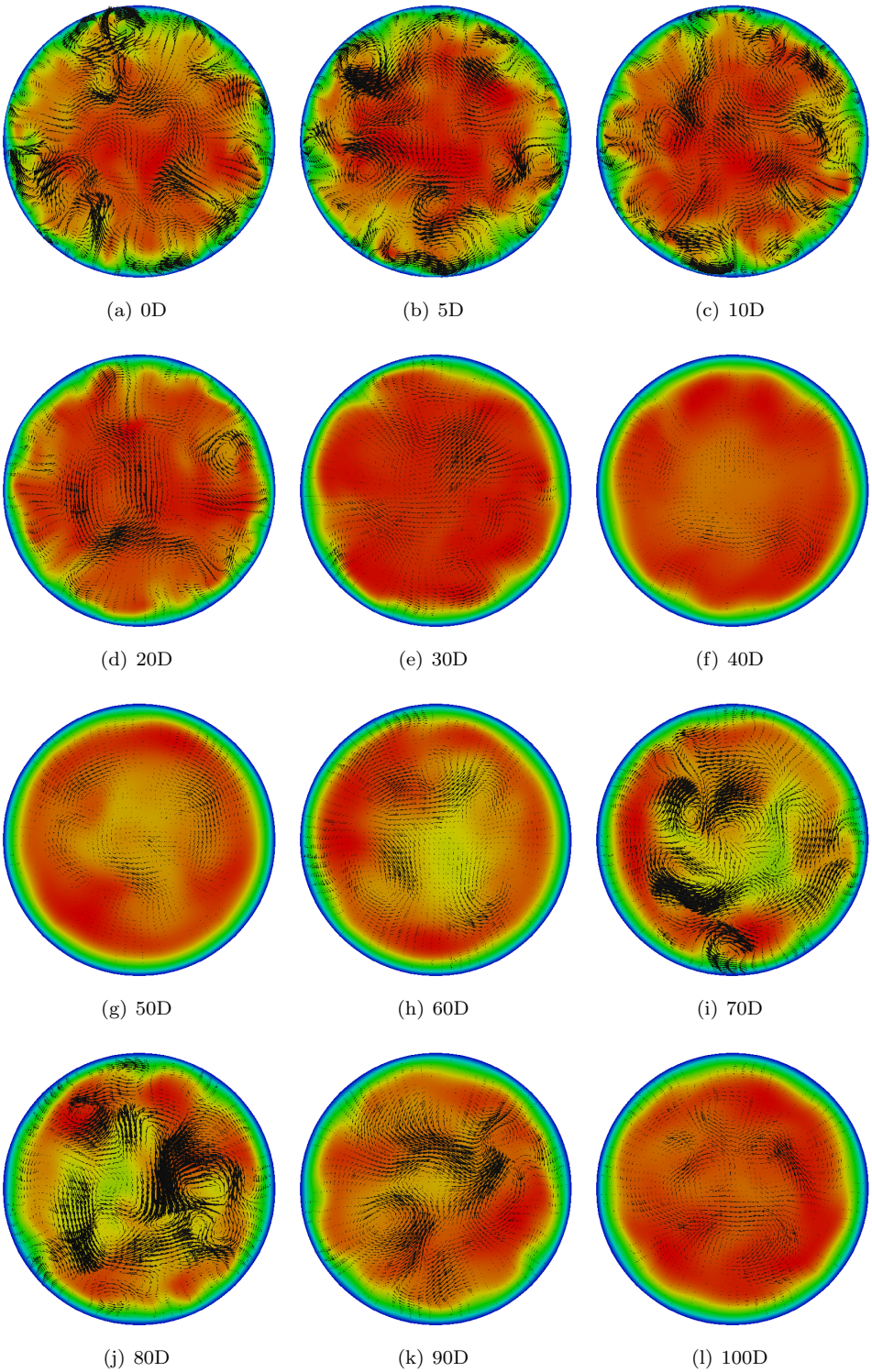

(a) 0D (b) 5D (c) 10D

(d) 20D (e) 30D (f) 40D

(g) 50D (h) 60D (i) 70D

(j) 80D (k) 90D (l) 100D

Figure 4.38: Instantaneous velocity field and vector in cross section for case 4

are shown. In the axial sectional views, the vorticity variation can be clearly seen. For 0-1m (0-13D), the characteristic of turbulent flow is apparent and the fluid vorticity is large. The fluid vorticity decreases progressively in the flow direction as the flow is laminarized. The minimum vorticity in case 4 appears in the region of 3-4m. Afterwards the vorticity presents a recovered trend till around 5.5m where the second peak is arrived. This phenomenon corresponds to the reverse shear stress induced by the buoyancy force. Compared to the vorticity at inlet, the second peak is clearly weak. After the second peak, it proceeds a process of slow reduction to the end of the tube.

In the illustration of the velocity vector field at the cross section, the voritcal motion is intense at the entrance region (0D and 5D). The large scale eddies are successfully captured in the region next to the wall. The average spacing between near-wall low-speed streaks is about 100 wall units at the inlet x=0D (hydrodynamically fully developed state). In the core region of the tube, the flow structure shows more isotropic than the wall region. As the flow develops, the large scale eddies is weakened and it almost vanishes at x=40D. From 30D to 50D, the resolved shear stress approaches to a very low level where the flow is effectively laminarized. At x=60D, the large scale motion appears again but it is mainly located in the core of the tube, which reflects the thickening of the viscous layer. It can again be explained by the resolved shear stress. After x=50D, the resolved shear stress shows a negative value and it further decreases toward the downstream. The rising negative shear stress induces turbulence production and its peak also moves towards the core of the tube. It can be seen that the vortical structure is obvious at 70D and 80D and the vortex moves towards the wall region again. The streaky is enhanced both in the core and viscous sublayer. Near the outlet, the large scale eddies are reduced and they move to the center again. It is because the resolved shear stress in Fig. 4.31(b) is enhanced in the core region and near the wall region. Two peaks appear with a negative one and positive one. The enhance turbulence induces large scale motion both in the core and near the wall. However the turbulence intensity is reduced again at x=90-100D, where the flow is close to being completely laminarized again. Only the weak large scale motions exist in the core of tube at x=90D.

4.7 Conclusion

Large-eddy simulation of heated vertical air flows in the turbulent mixed convection have been performed for the experimental conditions of Shehata [7] and Li [14] in the present study. WALE model is used as the SGS model and symmetry-preserving scheme discretization were adapted, with which a relative coarse mesh could be chosen. In the simulation for Shehata case, the detailed data in the whole field were compared with experiment and DNS results. It covered the complete laminarization

transition. Good agreement shows that the present model can be successfully applied to the turbulence-laminar transitional flow with high heating.

Based to the verification of the model in turbulence-laminar transitional flow, a flow in a very long tube which proceed turbulence-laminar and reverse transition was simulated. Furthermore, the change after the reverse transition to the fully developed state were obtained. Meanwhile the downward flow under the same conditions were compared. The obtained Nu or Nu ratios agree well with the experimental results. The variable parameters in the whole tube were studied. In general, the present model could be successfully applied to the transition flow with the heating, capturing the transition and accurately predicting the heat transfer and flow structure.

References

[1] W.S. Kim, C. Talbot, B.J. Chung, and J.D. Jackson. Variable property mixed convection heat transfer to air flowing through a vertical passage of annular cross section: Part 1. *Chemical Engineering Research and Design*, 80(3):239 – 245, 2002.

[2] Li JianKang. *Studies of Buoyancy-influenced convective heat transfer to air in a vertical pipe*. PhD thesis, Univeristy of Manchester, 1994.

[3] F. Nicoud and F. Ducros. Subgrid-scale stress modelling based on the square of the velocity gradient tensor. *Flow, Turbulence and Combustion*, 62(3):183–200, 1999.

[4] O. [et al.] Lehmkuhl. Termofluids: A new parallel unstructured cfd code for the simulation of turbulent industrial problems on low cost pc cluster. In *Proceedings of the Parallel CFD 2007 Conference*, pages 1–8, Ismail H. Tuncer, 2007.

[5] Habib N. Najm, Peter S. Wyckoff, and Omar M. Knio. A semi-implicit numerical scheme for reacting flow: I. stiff chemistry. *Journal of Computational Physics*, 143(2):381 – 402, 1998.

[6] F. Nicoud. Conservative high-order finite-difference schemes for low-mach number flows. *Journal of Computational Physics*, 158(1):71 – 97, 2000.

[7] A.M. Shehata and D.M. McEligot. Mean structure in the viscous layer of strongly-heated internal gas flows. measurements. *International Journal of Heat and Mass Transfer*, 41(24):4297–4313, 1998.

[8] Joong Hun Bae, Jung Yul Yoo, Haecheon Choi, and Donald M. McEligot. Effects of large density variation on strongly heated internal air flows. *Physics of Fluids*, 18(7), 2006.

[9] Ugo Piomelli and Elias Balaras. Wall-layer models for large-eddy simulations. *Annual review of fluid mechanics*, 34(1):349–374, 2002.

[10] Joong Hun Bae, Jung Yul Yoo, and Haecheon Choi. Direct numerical simulation of turbulent supercritical flows with heat transfer. *Physics of Fluids (1994-present)*, 17(10):–, 2005.

[11] F. A. Schraub S. J. Kline, W. C. Reynolds and P. W. Runstadler. The structure of turbulent boundary layers. *Journal of Fluid Mechanics*, 30:741–773, 1967.

[12] D. M. McEligot. Convective heat transfer in internal gas flows with temperature-dependent properties. Technical report, 1982.

[13] DM McEligot and CA Bankston. Turbulent predictions for circular tube laminarization by heating. *ASME paper*, 1969.

[14] JianKang. Li and J.D. Jackson. Buoyancy-influenced variable property turbulent heat tranfer to air flowing in a uniformaly heated vertical tube. In *2nd International Conference on Turbulent Heat Transfer*, Manchester, UK, 1998.

[15] W.S. Kim, S. He, and J.D. Jackson. Assessment by comparison with DNS data of turbulence models used in simulations of mixed convection. *International Journal of Heat and Mass Transfer*, 51(5-6):1293 – 1312, 2008.

[16] Amir Faghri, Yuwen Zhang, and John R Howell. *Advanced heat and mass transfer*. Global Digital Press, 2010.

[17] Petukhov B.S, Kurganov V.A, and Gladuntsov A.I. Heat transfer in turbulent pipe flow of gases with variable physical properties. *Heat Transfer Soviet Research*, 5(4):109 – 116, July-August 1973.

[18] Warren M Rohsenow, James P Hartnett, and Young I Cho. *Handbook of heat transfer*, volume 1. 1997.

[19] O. Buyukalaca. *Studies of convective heat transfer to water in steady and unsteady pipe flow*. PhD thesis, Univeristy of Manchester, 1993.

[20] A. D Carr, M. A. Connor, and H.O Buhr. Velocity, temperature, and turbulence measurements in air for pipe flow with combined free and forced convection. *Journal of Heat Transfer*, 95(4):445–452, 1973.

[21] A.F. Polyakov and S.A. Shindin. Development of turbulent heat transfer over the length of vertical tubes in the presence of mixed air convection. *International Journal of Heat and Mass Transfer*, 31(5):987 – 992, 1988.

[22] Petukhov B.S and Polyakov A.F. *Heat transfer in turbulent mixed convection*. Hemisphere Publishing Corporation, 1988.

[23] Sanjiva K. Lele. Compressibility effects on turbulence. *Annual Review of Fluid Mechanics*, 26:211–254, 1994.

[24] BP Axcell and WB Hall. Mixed convection to air in a vertical pipe. In *Proceedings of the 6th International Heat Transfer Conference*, pages 37–42, 1978.

[25] Xu. Xiaofeng. *Large eddy simulation of turbulent pipe flow with property variations*. PhD thesis, Iowa State University, 2002.

[26] Stephen B Pope. *Turbulent flows*. Cambridge university press, 2000.

[27] Prandtl L. *Fuhrer durch die stromunslehre*. Vieweg, Braunschweig, 1942.

[28] Jongwoo You, Jung Y. Yoo, and Haecheon Choi. Direct numerical simulation of heated vertical air flows in fully developed turbulent mixed convection. *International Journal of Heat and Mass Transfer*, 46(9):1613 – 1627, 2003.

[29] J.D. Jackson, M.A. Cotton, and B.P. Axcell. Studies of mixed convection in vertical tubes. *International Journal of Heat and Fluid Flow*, 10(1):2 – 15, 1989.

[30] FW Chambers, HD Murphy, and DM McEligot. Laterally converging flow. part 2. temporal wall shear stress. *Journal of Fluid Mechanics*, 127:403–428, 1983.

[31] Carlos Weldon Coon and HC Perkins. Transition from the turbulent to the laminar regime for internal convective flow with large property variations. *Journal of Heat Transfer*, 92(3):506–512, 1970.

[32] Biswadip Shome. Numerical study of turbulent flow in heated circular tube using transitional shear stress transport turbulence model. *International Journal of Thermal Sciences*, 79(0):90 – 102, 2014.

5

Numerical study of heat and mass transfer in turbulent flow inside a vertical tube with falling film

5.1 Abstract

This chapter presents a detailed numerical investigation of an air and water vapour mixed turbulent flow with liquid falling film in a vertical circular channel using large eddy simulation. Different cases are considered by imposing different heat flux boundary condition to wall while the feed water flow rate is adjusted as well. In this study, the inlet Reynolds number based on the inlet velocity and pipe diameter covers from 4600 to 13800 as in the experiments by An et al. [1]. Low-Mach number equation is employed to consider the large property variations along the tube and WALE model accounts for the subgrid-scale turbulence. The liquid film is assumed to occupy a negligible volume and its effect on the evaporation/condensation of the water vapour has been taken into account by imposing a set of boundary conditions. The effects of gas-liquid phase coupling, variable thermophysical properties and film vaporization are considered in the analysis. Due to the strong evaporation of the liquid film, large density variation arises and the flow structure changes greatly along the tube. With

the different conditions, the flow may proceed laminar, transitional and turbulent regimes. The obtained wall temperature are compared with the experimental data and in general agree well with the measured quantities.

5.2 Introduction

In Chapter 4, the capability of LES in the turbulent or transitional mixed convection flow has been validated without evaporation or condensation. It has confirmed that WALE model can accurately predict the transitional flow. Meanwhile the liquid film model has also been validated in Chapter 3. Based on the previous validation, in this chapter, the WALE and liquid film model are combined together to solve the turbulent and transitional flow combined with evaporation or condensation. The present existing study on the turbulent evaporation in similar cases [2–6] is mainly focused on the application of RANS models. For a detailed bibliographic study, please see section 1.3.3. Since the empirical coefficient employed in RANS model is dependent on many factors, such as geometry, flow condition, it can be accurate in some flow situations while being very inaccurate in others. Moreover, the time-averaging value are used in RANS model, the transient flow structure can not be simulated using RANS. The poor generality of RANS model limits its application in the complex geometry and in unsteady situations.

To our best knowledge, there is no LES of turbulent heat and mass transfer in pipe upward flows, in which the flow is considerably complicated. It could process laminar-turbulent transitional or reverse flow. In this chapter, large eddy simulations of turbulent heat and mass transfer in pipe flow, under isoflux wall condition, Reynolds numbers up to 13800 and with falling liquid film, are conducted. The aim of the present research is to investigate the characteristic of heat and mass transfer and the effects of Reynolds number, heat flux and water flow rate on evaporating in a circular pipe flow. The study is also intended to advance our understanding of evaporation mechanism in transitional flow. For a detailed bibliography study, please see section 1.3.

5.3 Mathematical model

5.3.1 Governing equation

Due to the large property variations caused by the strong evaporation, the low-Mach number equation used in the chapter 4 is applied to the turbulent flow with evaporation and condensation. The derivation is same as the one in Chapter 4. An additional governing equation for the diffusion is applied to solve the evaporation and

condensation. The whole low-Mach number governing equation are as following:

$$\frac{\partial \overline{\rho}}{\partial t} + \frac{\partial \overline{\rho}\tilde{u}_j}{\partial x_j} = 0 \tag{5.1}$$

$$\frac{\partial \overline{\rho}\tilde{u}_i}{\partial t} + \frac{\partial \overline{\rho}\tilde{u}_j\tilde{u}_i}{\partial x_j} = -\frac{\partial \overline{p}}{\partial x_i} + \frac{\partial(\overline{\tau}_{ij} + \overline{\tau}^t_{ij})}{\partial x_j} + \overline{\rho}g \tag{5.2}$$

$$\frac{\partial \overline{\rho}\tilde{h}}{\partial t} + \frac{\partial \overline{\rho}\tilde{u}_j\tilde{h}}{\partial x_j} = -\frac{\partial(\overline{\dot{q}_j} + \overline{\dot{q}}^t_j)}{\partial x_j} \tag{5.3}$$

$$\frac{\partial \overline{\rho}\tilde{c}}{\partial t} + \frac{\partial \overline{\rho}\tilde{u}_j\tilde{c}}{\partial x_j} = -\frac{\partial(\overline{J_j} + \overline{J}^t_j)}{\partial x_j} \tag{5.4}$$

where the filtered diffusion terms is laminar filtered stress tensor

$$\tau_{ij} = \overline{\mu(\frac{\partial u_i}{\partial x_j} + \frac{\partial u_j}{\partial x_i} - \frac{2}{3}\delta_{ij}\frac{\partial u_k}{\partial x_k})} \approx \tilde{\mu}(\frac{\partial \tilde{u}_i}{\partial x_j} + \frac{\partial \tilde{u}_j}{\partial x_i} - \frac{2}{3}\delta_{ij}\frac{\partial \tilde{u}_k}{\partial x_k}) \tag{5.5}$$

The Reynolds stress tensor (subgrid scale tensor) is:

$$\overline{\tau}^t_{ij} = -\overline{\rho}(\widetilde{u_i u_j} - \tilde{u}_i\tilde{u}_j) \tag{5.6}$$

and it is modeled as:

$$\overline{\tau}^t_{ij} = 2\overline{\rho}\nu_t(\tilde{S} - \frac{1}{3}\delta_{ij}\tilde{S}_{kk}) \tag{5.7}$$

The filtered heat flux is:

$$\overline{\dot{q}}_i = -\frac{\lambda}{c_p}\frac{\partial \tilde{h}}{\partial x_j} \tag{5.8}$$

The subgrid scale heat flux is:

$$\overline{\dot{q}}^t_i = \overline{\rho}(\widetilde{u_i h} - \tilde{u}_i\tilde{h}) \tag{5.9}$$

and the modelization for $\tilde{\dot{q}}^t$ is written as:

$$\overline{\dot{q}}^t_i \approx \tilde{\dot{q}}^{sgs}_i = -\frac{\lambda_t}{c_p}\frac{\tilde{h}}{\partial x_i}, \qquad \lambda_t = \frac{\mu_t c_p}{Pr^t} \tag{5.10}$$

The turbulent Prandtl number is fixed at $Pr^t = 0.4$. The filtered mass transfer diffusive component flux is:

$$\overline{\dot{J}}_i = -\overline{\rho}\overline{D}\frac{\partial \tilde{c}}{\partial x_j} \tag{5.11}$$

The subgrid scale diffusive component flux is:

$$\overline{J}_i^t = \overline{\rho}(\widetilde{u_i c} - \tilde{u}_i \tilde{c}) \tag{5.12}$$

and the modelization for $\overline{J}^t$ is written as:

$$\overline{J}_i^t \approx \tilde{J}_i^{sgs} = -\rho D_t \frac{\partial \tilde{c}}{\partial x_i}, \qquad D_t = \frac{\mu_t}{\rho Sc^t} \tag{5.13}$$

The turbulent Schmidt number is fixed at $Sc^t = 0.4$.

5.3.2 SGS-WALE model

A subgrid scale viscosity model is introduced to close the formulation in the present study, namely WALE model. The wall-adapting eddy viscosity model(WALE) was proposed by Nicaud and Ducros [7] and the model is based on the square of the velocity gradient tensor. In its formulation the SGS viscosity accounts for the effects of both the strain and the rotation rate of the smallest resolved turbulent fluctuations. It is particularly suited for the wall-bounded flows, which is a challenging task for LES. In addition, the proportionality of the eddy viscosity near walls is recovered without any dynamic procedure,

$$\begin{aligned}
\nu_{sgs} &= (\mathcal{C}_w \Delta)^2 \frac{(\tilde{V}_{ij}\tilde{V}_{ij})^{\frac{3}{2}}}{(\tilde{S}_{ij}\tilde{S}_{ij})^{\frac{5}{2}} + (\tilde{V}_{ij}\tilde{V}_{ij})^{\frac{5}{4}}} \\
\tilde{S}_{ij} &= \frac{1}{2}[\mathrm{G}_{ij}(\tilde{u}) + \mathrm{G}_{ji}(\tilde{u})] = \frac{1}{2}(\frac{\partial \tilde{u}_i}{\partial x_j} + \frac{\partial \tilde{u}_j}{\partial x_i}) \\
\tilde{V}_{ij} &= \frac{1}{2}[\mathrm{G}_{ij}^2(\tilde{u}) + \mathrm{G}_{ji}^2(\tilde{u})] - \frac{1}{3}[\mathrm{G}_{kk}^2(\tilde{u})\delta_{ij}] = \frac{1}{2}(\frac{\partial \tilde{u}_i}{\partial x_j} + \frac{\partial \tilde{u}_j}{\partial x_i}) - \frac{1}{3}\delta_{ij}\frac{\partial \tilde{u}_k}{\partial x_k}
\end{aligned}$$

where Δ is the characteristic filter length. In the present study a constant value of $\mathcal{C}_w = 0.325$ is used. G_{ij} are the velocity gradients of the resolved scales and $\tilde{V}_{ij}$ being the traceless symmetric part of the square of the velocity gradient tensor.

Numerical results are carried out by using the CFD&HT code–Termofluids [8] which is an intrinsic 3D parallel CFD object-oriented code applied to unstructured /structured meshes, which can handle the thermal and fluid dynamic problems in complex geometries. The governing equations are discretized on a collocated mesh in Cartesian coordinates. The numerical integration is performed by a finite volume method.

In problems with very low Mach numbers and where acoustic phenomena are not of interest, the common strategy is to use a variant of the Predictor-Corrector

scheme shown by Najm et al. [9]. The pressure-velocity coupling is solved by a fractional step as described by Nicoud [10] where a constant coefficient Poisson results. In the Predictor step a second-order Adams-Bashforth time integration scheme is used to calculate the intermediate scalar fields and the velocity and it incorporates a pressure correction step to satisfy the continuity equation. The Corrector step uses a Crank-Nicolson integration to advance the scalar fields, and it also involves a pressure correction step. The specific algorithm scheme can be referred as Appendix B.

5.4 Problem description

In the experiment [1], a circular tube was used, which is made of stainless steel. The test section has a length of $8m$, a internal diameter of $76mm$ and a thickness of $1.9mm$. The tube was vertically mounted with bellmouth inlet. At the top of the tube, water was sprayed in a symmetrical manner onto the inside surface of the tube from a centrally positioned multi-jet nozzle so as to produce a uniform film. The injection water could be adjusted through a specified temperature and flow rate. The forming thin film of water rans down the inside surface while air flowed upward within the tube. The physical model under description is illustrated schematically in Fig. 5.1.

The water feed enters into the tube at top with a mass flow rate $\dot{m}_{in}$ and leaves the tube at bottom with a mass flow rate $\dot{m}_{out}$ due to the gravity. The constant heating of the plate enables to first increase the temperature of the falling water film, then to evaporate part of it. The air-vapor mixture entering into the channel from the bottom has a uniform axial velocity V_0, temperature T_0 and relative humidity RH_0.

In the experiment, different conditions were employed to consider from the forced flow with negligible buoyancy influences to mixed convection with dominant influence of buoyancy force. The complete experiment was done by adjusting the inlet air mass flow rate, water flow rate and the heat flux imposed on the wall. The Reynolds number of moisture air flow at inlet covers $4600 - 13800$ corresponding to the rates of 0.005, 0.010 and 0.015 kg/s, respectively. The water was supplied at rates of 0.013 and 0.027 kg/s. The detailed parameters are shown in the Table. 5.1.

Fig. 5.1(b) gives a sketch of mesh distribution for the present study. The mesh distribution is same as the one in chapter 4. They are all based on the O-grid (hexahedral) mesh. Three different grid resolutions are tested, which include the mesh sizes (3.5M and 7M) used in the chapter 4. In addition, mesh size 14M is also tested to validate the mesh independence. Since the maximum effective Reynolds number is around 17000 which is close to case 5 in chapter 4, $7M$ mesh is employed in the present work for better efficiency.

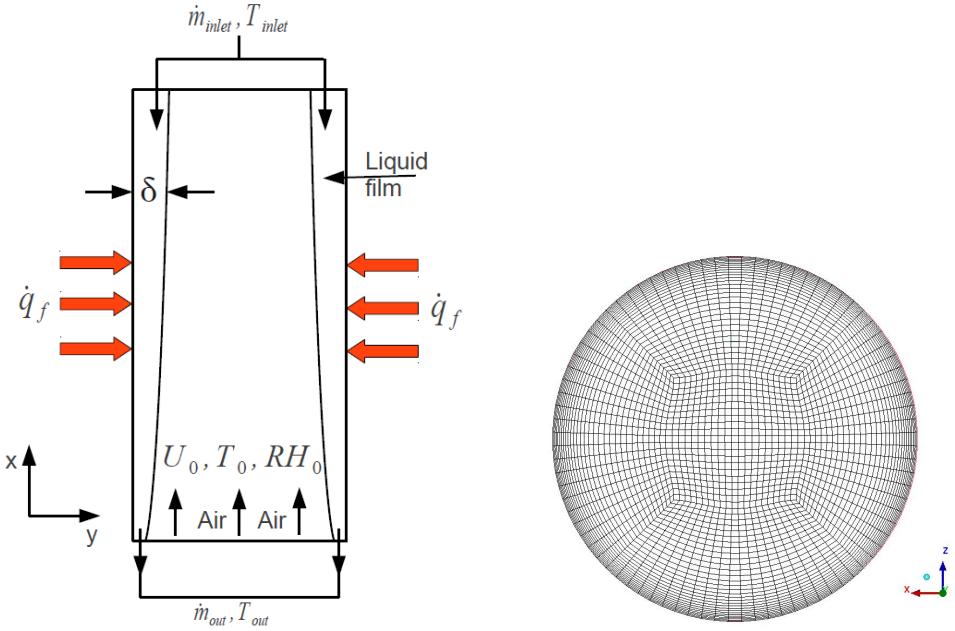

(a) (b)

Figure 5.1: Schematic of test section and mesh distribution

Table 5.1: Simulation conditions

Case	Direction	Power(W)	Re_0	T_a(°C)	Bo_0	$\dot{m}_l$(kg/s)	T_l(°C)
2	upward	1350	13800	30	0.84	0.027	70
3	upward	3000	13800	30	1.23	0.027	70
4	upward	3000	13800	30	1.34	0.013	66
5	upward	1350	13800	30	1.36	0.013	66
9	upward	1350	13800	30	0.55	0.027	40
10	upward	1350	13800	30	0.74	0.027	53
11	upward	1350	9200	30	2.63	0.027	71
12	upward	1350	4800	30	12.0	0.027	73
14	upward	3000	4800	30	15.8	0.027	76

5.4.1 Inflow turbulence

A bellmouth is set up at the bottom of the tube for the intake of the air in the experiment to obtain a uniform velocity. According to the simulation of He et

al. [11], a specified turbulence intensity of 6% is given. However the inlet condition for LES is not an easy problem. A inlet flow must include a stochastically-varying component: Reynolds average mean quantities, Reynold stress and turbulent length scale, etc. Moreover the selected conditions could have a strong influence in many situations. Klein et al. [12,13] developed a synthetic turbulence inflow generator based on the use of digital filters. The method is based on the reproduction of known or estimated statistical data and contain no other physical information. In the original formulation of the method turbulence correlation functions are described in terms of single turbulence length and time scales. This method is simple, flexible and more accurate than most of the existing methods. The algorithm for generating inflow data is implemented in the present study:

- Choose for each coordinate direction corresponding to the inflow plane, a length scale $L_y = n_y \Delta y$, $L_z = n_z \Delta z$ and also a time scale L_x(or, again by Taylors hypothesis, a length scale). Choose also a filter width according to the condition $N_\alpha \geq 2n_\alpha$, $\alpha = x, y, z$.

- Initialize and store three random fields $R_\alpha, \alpha = x, y, z$ of dimensions $[-N_x : N_x, (-N_y + 1) : (M_y + N_y), (-N_z + 1) : (M_z + N_z)]$, where $M_y \times M_z$ denotes the dimensions of the computational grid in the inflow plane.

- Calculate the filter coefficient $b(i, j, k)$ according to the following equation

$$b_{ijk} = b_i \cdot b_j \cdot b_k, \quad b_k = \tilde{b}_k / (\sum_{j=-N_\alpha}^{N_\alpha} b_j^2)^{1/2} \quad \text{and} \quad \tilde{b}_k = \exp(-\frac{\pi k^2}{2n^2}) \tag{5.14}$$

- Create the two-dimensional arrays of spatially correlated data $U_\alpha(j, k), \alpha = x, y, z$

$$U_\alpha(j,k) = \sum_{i'=-N_x}^{N_x} \sum_{j'=-N_y}^{N_y} \sum_{k'=-N_z}^{N_z} b(i', j', k') R_i(i', j + j', k + k') \tag{5.15}$$

- Perform the coordinate transformation using the given equation

$$(a_{ij}) = \begin{pmatrix} (R_{11})^{1/2} & 0 & 0 \\ R_{21}/a_{11} & (R_{22} - a_{21}^2)^{1/2} & 0 \\ R_{31//}/a_{11} & (R_{32} - a_{21}a_{31})/a_{22} & (R_{33} - a_{31}^2 - a_{32}^2)^{1/2} \end{pmatrix} \tag{5.16}$$

- With the method proposed by Lund et al. [14], the velocity at a specified time is calculated as: $u_i = \overline{u}_i + a_{ij} U_j$

- Discard the first y,z plane of R_α and shift the whole data: $R_\alpha(i,j,k) = R_\alpha(i+1,j,k)$. Fill the plane $R_\alpha(N_x,j,k)$ with new random numbers. Then repeat the step above for each time step.

Once the velocity at a plane are stored for a period, the inlet velocity of the tube could be obtained in terms of the time and position based on the interpolation.

5.4.2 Boundary and interfacial conditions

The detailed solution of liquid film has been explained in Chapter 3. In this chapter, the same solution is applied.

The transverse velocity of the air-vapor mixture can be expressed as Tsay and Lin [15] and Eckert [16]

$$v(\delta) = -\frac{D}{1-c_\delta}(\frac{\partial c}{\partial x})_\delta \tag{5.17}$$

where c is the mass fraction of vapor. The water film flows downward only under the action of gravity and the effect of air vapor mixture on it can be assumed negligible for this flow regimes [15]. Under the simplifying condition, the velocity at interface can be calculated as,

$$U = \frac{\rho g}{\mu}(\delta y - y^2) = \frac{\rho g}{\mu}\frac{\delta^2}{2}, \qquad \delta = (\frac{3\dot{m}\nu}{\pi d\rho g})^{1/3} \tag{5.18}$$

The continuity of the heat flux at the interface is given by

$$-\lambda_w(\frac{\partial T_w}{\partial x})_\delta = -\lambda_g(\frac{\partial T}{\partial x})_\delta + L_v\dot{m}_v \tag{5.19}$$

At steady state, it is assumed that the heat flux absorbed by the external face is totally transmitted to the liquid film which flows on its internal face, giving the condition

$$-\lambda_w\frac{\partial T_w}{\partial x} = \dot{q}_f \qquad at \quad y = R \tag{5.20}$$

Neumann boundary condition is considered at the exit of the main computational domain.

5.5 Result analysis

5.5.1 Comparison on the wall temperature

Fig. 5.2 gives the comparison between the present results and the reference results in which both the experimental results [1] and the numerical results of RANS model [11] are included. Fig. 5.2(a) explains the effects of air flow rate on the liquid film temperature along the tube; the air flow rate is varied with a Re range of

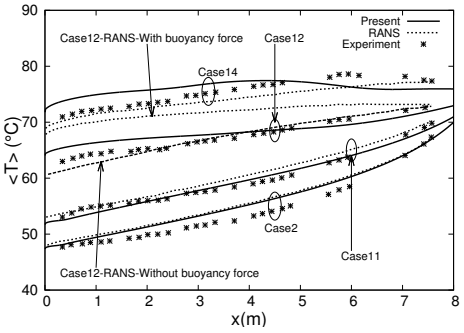

(a) Effect of air flow rate

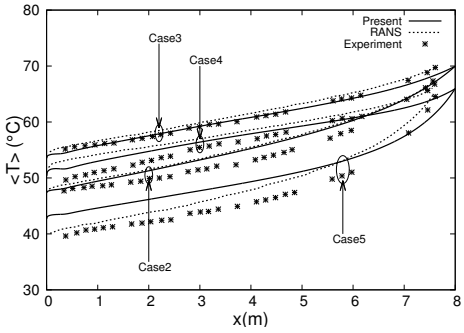

(b) Effect of water flow rate and heat flux

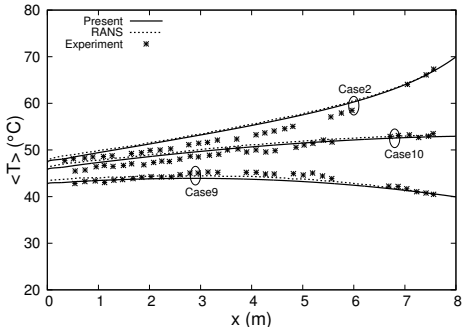

(c) Effect of water inlet temperature

Figure 5.2: Variation of wall temperature

4600-13800 while other conditions change little (except for case 14). The larger temperature drop is observed for a flow with a higher Reynolds number. This performance is consistent with the general concept that the heat and mass transfer is larger for a higher Reynolds number in the convective heat transfer. The present LES results agree well with the numerical one in the reference for case 2 and case 11. Both present a close trend with the measured data. For case 12, RANS model overpredicted the wall temperature clearly, and a simulation under the condition of free buoyancy force was also implemented by He et al. [11]. RANS model without buoyancy force predicted accurately the wall temperature. They thought that RANS model induced the flow to be almost completely laminarized and as a result, the predicted effectiveness of the heat and mass transfer was significantly decreased. In the present LES, only the result with buoyancy force is given, which is more similar to the actual experimental condition than RANS prediction. The obtained result overpredicts the wall

temperature for 1-4m but underpredicts it for 4-8m. In order to explain the over-prediction of buoyancy force effect in case 12, case 14 of the similar condition apart from power input was simulated by He et al. [11]. They thought that in case 14 the flow was actually laminarized due to the strong buoyancy force. However the result obtained by LES for case 14 is similar with case 12 on the turbulence development and temperature distribution. Compared to the experimental data, both results show a slightly higher wall temperature on the left side and lower temperature on the right side. They are not completely laminarized during the whole pipe. This conclusion can be drawn from the turbulent kinetic energy variation along the tube (Fig. 5.13) in the following discussion.

The effects of heat flux and water mass flow rate on the wall temperature are given in Fig.5.2(b). In case 2 and 3, the results obtained by LES show good agreement with both RANS model and experiment. In case 5, LES shows a clear difference with the experimental data while RANS model gives a better prediction. Through the comparisons of case 2&3 and case 4&5, it can be seen that under the condition of the fixed inlet water temperature and water flow rate, the wall temperature is higher with stronger heat flux imposed on the wall. This is readily understood that, with the higher heat flux on the wall, the energy contribution for evaporation is mostly from the heat flux imposed on the wall and the lost internal energy contribution in the liquid film for evaporation is small. Through the comparisons of case 2&5 and case 3&4, they have similar inlet film temperature but different water flow rate, the temperature drop of liquid film are close ($\Delta T = 22.6°$C for case 2, $\Delta T = 23.2°$C for case 5. $\Delta T = 16.4°$C for case 3, $\Delta T = 15.6°$C for case 4). Therefore it can be concluded that the influence of water flow rate on the cooling is not apparent under the high inlet liquid temperature ($T_{in} = 66 - 70°$C).

Fig. 5.2(c) illustrates the wall temperature under the condition of different inlet water temperature ($T_{in} = 70°$C for case 2, $T_{in} = 53°$C for case 10 and $T_{in} = 40°$C for case 9). With the higher inlet water temperature (case 2), the temperature profile decreases monotonically from the water inlet to outlet. The trend indicates that the imposed heat flux $\dot{q}_f$ on the wall is less than the energy $\dot{q}_l$ required for the evaporation. The part of the required energy comes from the internal energy stored in the liquid film. With the intermediate inlet temperature (case 10), although its film temperature decreases along the tube, the reduction slope is very small and the temperature drop is only $\Delta T = 7.2°$C. With lower inlet temperature (case 9), the liquid film temperature shows a increase trend at the beginning and then decreases slightly. It indicates that at the initial stage (top of the tube) the energy $\dot{q}_l$ for evaporation is less than the heat flux $\dot{q}_f$ and a part of heat flux imposed on the wall is stored in the liquid film. It is clearly illustrated in Fig. 5.9(c). As the temperature increases at the interface, the corresponding mass fraction of water vapor also increases and the evaporation begins to enhance. The enhanced evaporation requires more energy and the temperature

begins to fall again. Hence, $\dot{q}_l$ shows a trend of increase from the top to the bottom of the tube. The more detailed energy distributions will be discussed in the section 5.5.4.

5.5.2 Reynolds number and buoyancy parameter

In the present simulation, the velocity is negative at the wall since a thin liquid film falls downwards along the wall. The conventional Reynolds number $Re = \rho U D/\mu$ is suggested to be modified to take account of the negative velocity at the wall. The effective Reynolds number based on a modified characteristic velocity was adopted by He et al. [11], which was defined as,

$$Re_e = \frac{\rho_b (U_b - U_i) D}{\mu_b} \tag{5.21}$$

where ρ_b and μ_b are mass weighted density and dynamic viscosity of the moisture mixture, respectively. U_b and U_i are bulk velocity of the moisture mixture and the velocity of interface between the falling liquid film and the air-vapor mixture.

The effective Reynolds number of mixture flow along the tube is presented in Fig. 5.3. It can be seen that the Reynolds number increases in all the cases except case 9 where it presents a reduction trend. The same phenomenon was also observed in the simulation of He et al. [11]. This variation of Reynolds number in evaporation/condensation flow is different with the pure air flow in the heated tube. The Reynolds number formulation in a circular tube could be written as $Re = 4\dot{m}_{mix}/\pi D\mu$, where $\dot{m}_{mix}$ is the mass flow rate of fluid. In the pure air flow, due to the fixed mass flow rate and the increased dynamic viscosity caused by heating, the Reynolds number always decreases along the heated tube in pure air flow. However in the evaporation flow, the mass flow rate of the mixture may increase or decrease along the tube depending on the experimental conditions. Thus the effective Reynolds number can increase or decrease. The variation of Reynolds number is also decided by the dynamic viscosity which is based on the temperature and mass fraction. Hence the variation of effective Reynolds depends on the dynamic balance of the mass flow rate and dynamic viscosity. Unlike others cases, case 9 has the lowest evaporation rate due to the low liquid inlet temperature, therefore Reynolds number behaves more like dry air case.

Similarly, the conventional buoyancy force parameter $Bo = \dfrac{8 \times 10^4 Gr}{Re^{3.425} Pr^{0.8}}$ is also needed to be modified. A slightly modified formulation is employed in reference [17]

$$Bo = \frac{8 \times 10^4 Gr'}{Re_e^{2.625} Pr^{0.8}} \tag{5.22}$$

where $Gr' = \dfrac{(\rho_b - \rho_i)}{\rho_b} \dfrac{g D^3}{\nu^2}$. In the modified buoyancy definition which includes

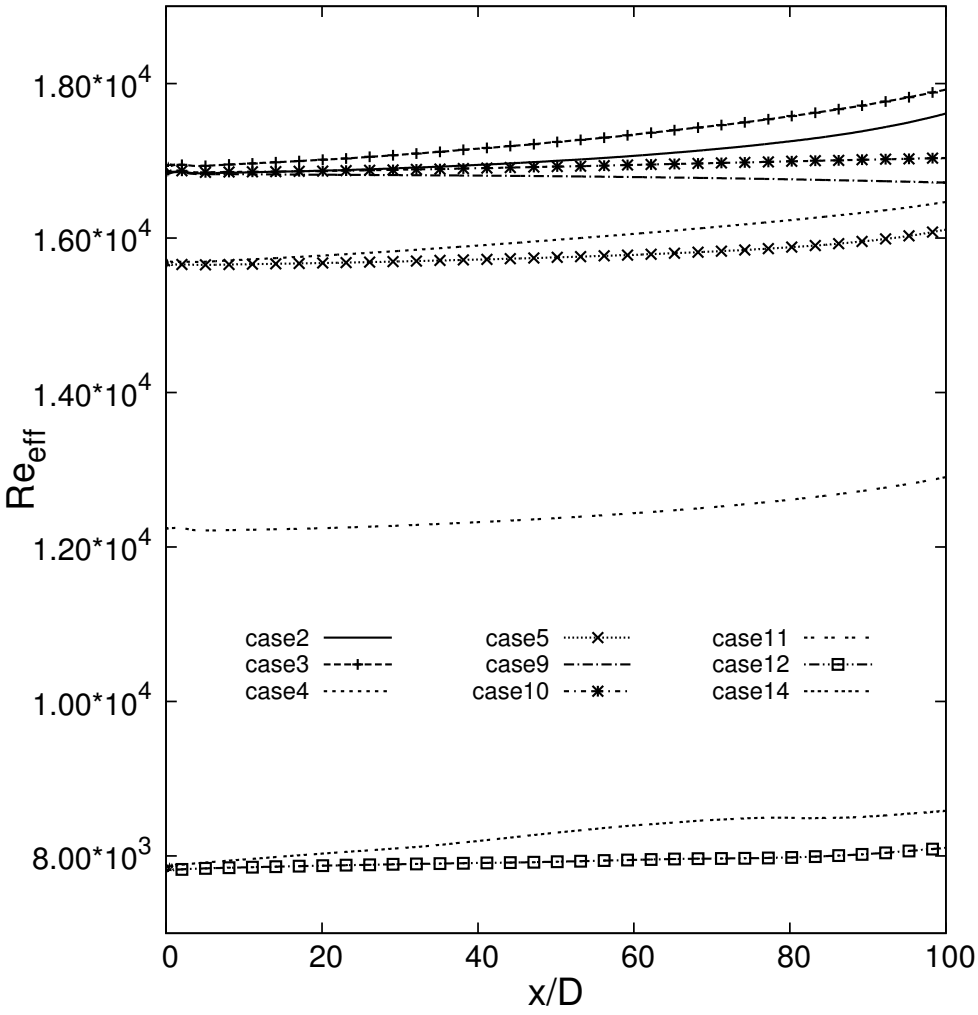

Figure 5.3: The effective Reynolds number along the tube

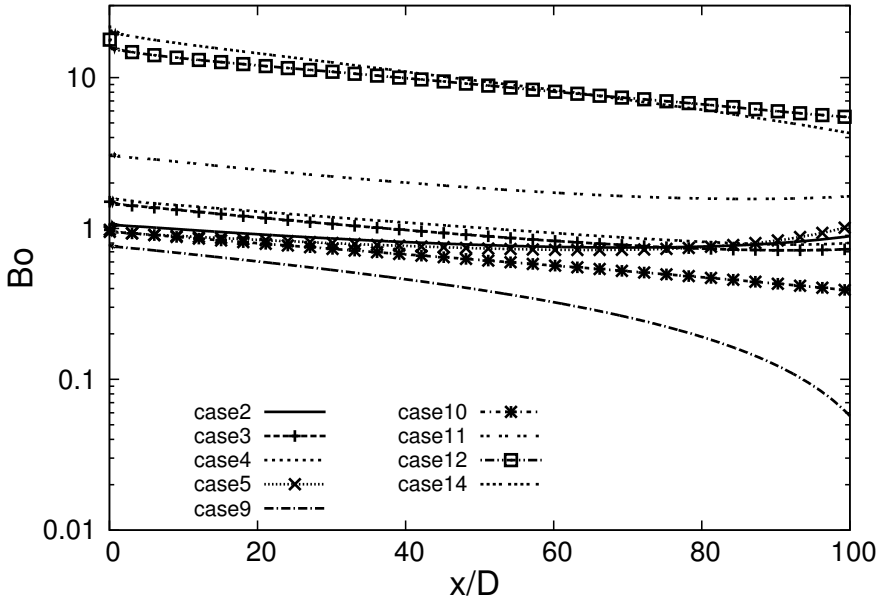

Figure 5.4: The buoyancy parameter along the tube

vapor density at the interface, the density difference caused by the temperature and the vapor concentration was considered.

Fig. 5.4 presents the variation of buoyancy force along the tube. In the pure air heated flow, the buoyancy force shows a linear monotonical reduction trend while the bulk temperature increases linearly. In the evaporation situation, the variation of buoyancy force is more complicated. According to its definition, it is influenced by the effective Reynolds number, bulk density and liquid-gas interface density. Under the condition of the fixed inlet Reynolds number and inlet water temperature, the film temperature increases with a rising heat flux. Usually, the higher film temperature may increase buoyancy force. The buoyancy force in case 3 is higher than the one in case 2 except the top region of the tube. In the top region, the buoyancy force in case 3 is lower than the one in case 2 even its film temperature is higher. The main reason is that the effective Reynolds number increases quickly at the top section of the tube in case 3 due to the stronger evaporation.

5.5.3 Mean parameters

The mean velocity fields normalized by the bulk velocity are shown in Fig. 5.5 for six typical cases. Cases 2, 3 and 9 are the high-Reynolds flow with different heat flux

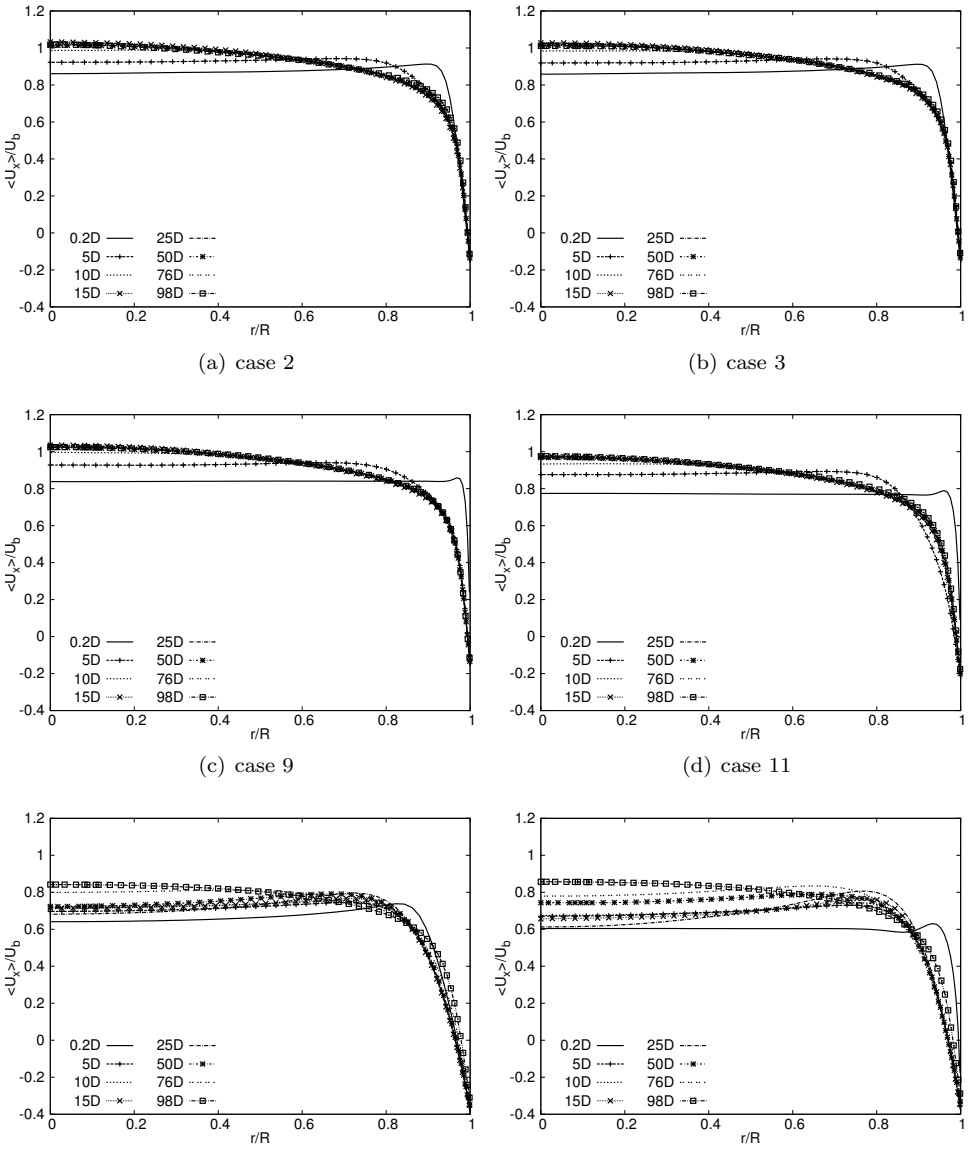

(a) case 2 (b) case 3

(c) case 9 (d) case 11

(e) case 12 (f) case 14

Figure 5.5: The mean velocity profile normalized by the effective bulk velocity

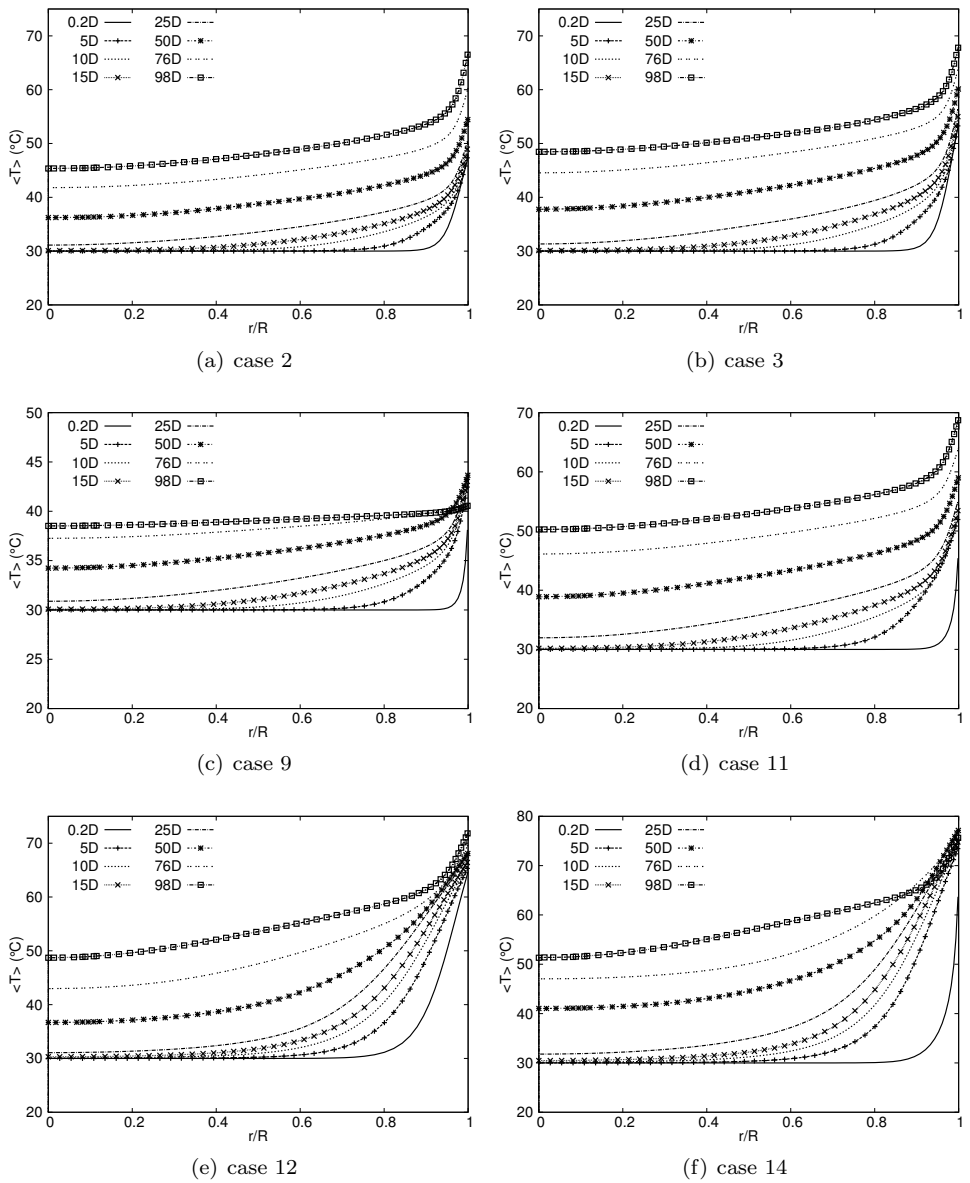

(a) case 2

(b) case 3

(c) case 9

(d) case 11

(e) case 12

(f) case 14

Figure 5.6: The mean temperature profile

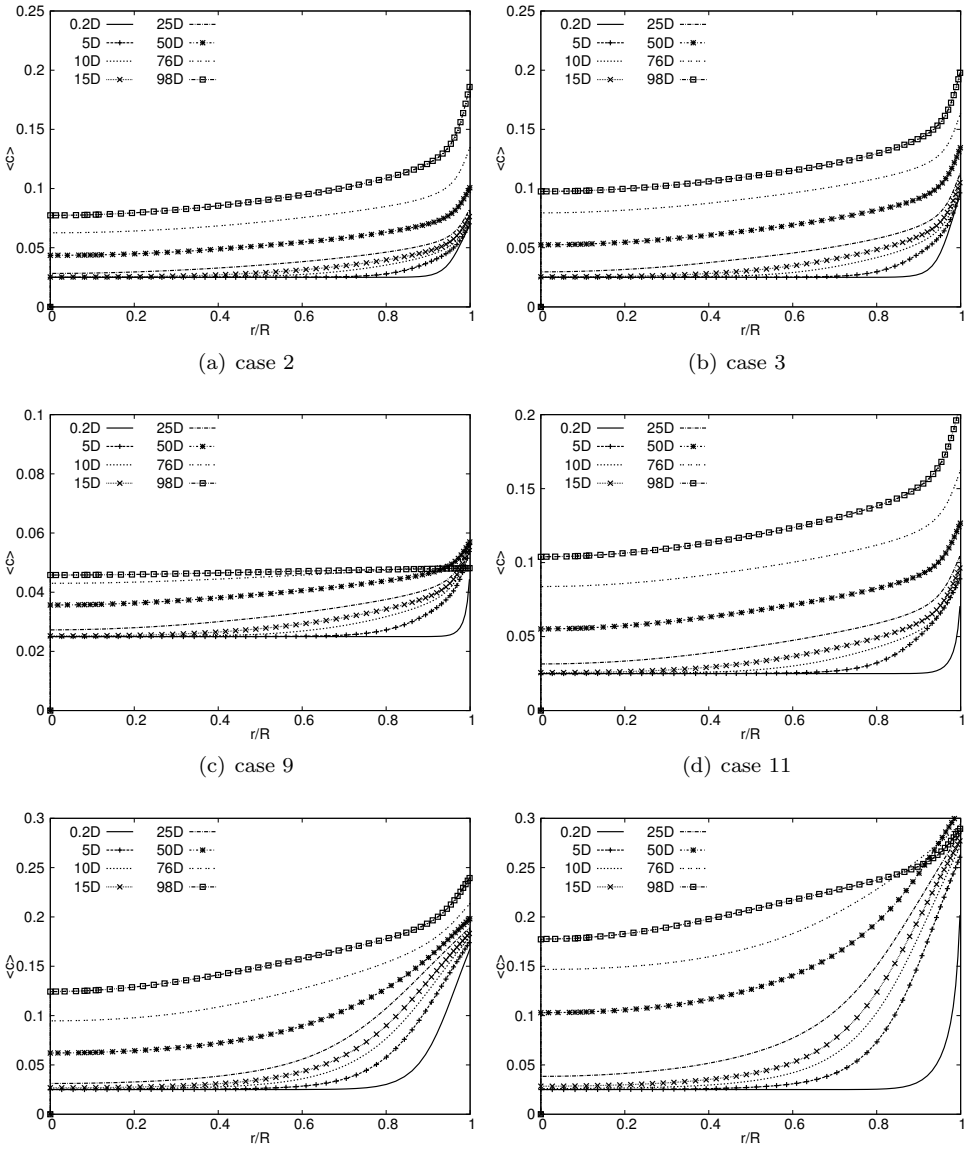

Figure 5.7: The mean mass fraction profile

and inlet temperature, case 11 is the flow with intermediate Reynolds number, and cases 12, 14 have the lower Reynolds number with different heat flux.

In the velocity development, the velocity profiles in case 2, 3, 9 and 11 are extremely similar. Their variation are very clear from uniform velocity at inlet to 15D and the variations show the hydrodynamically developing process. The velocity profiles are very similar from 15D which reflects the hydrodynamically fully developed state. However the development of the velocity field in case 12 and case 14 are different from that of the high Reynolds flow: they develop very slowly and keep changing along the whole tube. The velocity profile is relatively flat at the inlet. As the density is greatly reduced by the higher temperature and strong evaporation at the interface of the falling film, the flow velocity is clearly accelerated near the wall and a M-shape velocity profile is generated from 5D to 50D. At x=76D, the M-shape profile gradually vanishes. In case 14, the development phenomenon is similar to that in case 12, the difference is that its velocity development is slower and a more obvious M-shape appears due to the stronger buoyancy force effect. Its M-shape profile vanishes only around the outlet of the tube. Compared to the velocity profiles with different Reynolds numbers, the velocity boundary layer in low Reynolds are thicker than that of high Reynolds number, as can be seen from the slope of velocity profile. The thickness of velocity boundary layer in the low Reynolds number experiences a process of initial increase and a decrease at the end of the tube. It can reflect the variation of the turbulence intensity, which will be discussed in the later. It is worthy to note that the negative values near the wall show the influence of the falling film.

The development of temperature and vapor mass fraction along the tube are shown in Fig. 5.6 and Fig. 5.7, respectively. In case 3, the inlet temperature of liquid film is relatively higher and air-vapor mixture energy level increases due to the convective heat transfer and evaporation on the interface of the film. Consequently the temperature and concentration profiles show monotonical increase trend along the tube. Through the comparisons between case 2 and case 3 with the same inlet temperature of liquid film, even the heat flux of case 3 is 2.22 times of the one of case 2. The temperature ΔT_3 of mixture in case 3 does not increase by the corresponding times than case 2, instead only by approximate 25%. The main reason could be explained from the heat distributions. With the higher heat flux, the bigger part of the heat flux (approximately 1.6 times as case 2) is used for evaporation transport (see Fig. 5.9). Therefore the concentration profile of outlet in case 3 is higher than case 2.

For case 9, the temperature near the wall does not show a monotonical trend. It is because that it is strongly influenced by the liquid film temperature. The liquid film temperature experiences a increasing process from the top and then a slight reduction trend at the bottom of the tube. From the energy distribution in case 9 (Fig. 5.9), it can be seen that the latent heat transfer is almost equal to the heat flux imposed on the wall at the bottom part of the tube (125% − 80% of heat flux from the bottom

to x=40D is used for evaporation), so the film temperature is almost constant till $x = 50D$. However as the inlet film temperature is lower at the top of tube, the gradient of concentration is small and the evaporation is weak at the interface. The most part of heat transfer imposed on the heat flux (102% − 67% from x=100D to 80D) is converted into the internal energy of the falling film. As a result the temperature shows a increase trend with its falling.

From the comparison of the high-Reynolds number and low-Reynolds number, the effects of buoyancy force on the temperature and concentration development can be observed. In cases 2, 3 and 11, the temperature and concentration develop quickly along the radial direction and it shows the thin thermal sublayer in the turbulent flow. In case 12 and case 14, the temperature and concentration variation is more gradual along the radial direction and thermal boundary layer is much thicker. The thicker boundary layer is consistent with theory of the laminar flow.

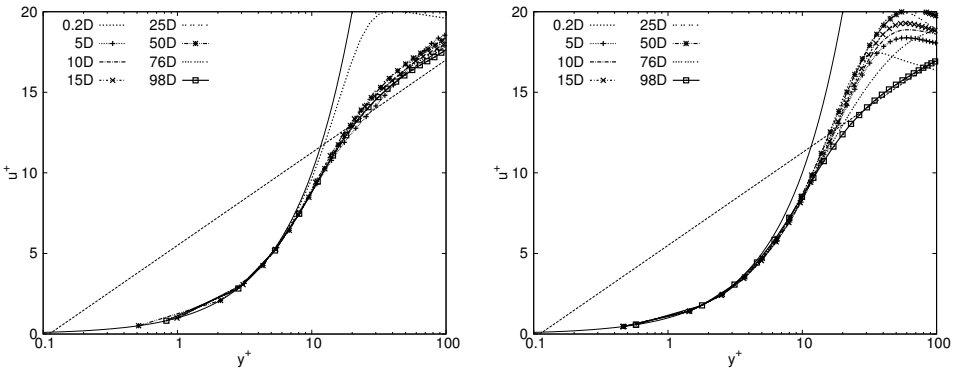

(a) case 3 (b) case 12

Figure 5.8: Mean velocity in wall coordinates

In order to better understand the variation of velocity along the tube, we present the velocity profiles in wall coordinates in Fig.5.8. Although the velocity at interface is negative, the velocity at interface can be considered as a reference. Accordingly, the velocity inside the tube is increased by the absolute velocity of interface. In case 3, all the profiles except x=0D are close to the fully developed turbulent curve. It confirms the fast development of velocity in case 3. Compared to case 3, the profiles in case 12 present a different performance. Its development is slow and all the profiles except x=98D do not obey the fully developed turbulent curves. The profile at x=98D shows it is approximately at hydrodynamically fully developed state.

Table 5.2: Evaporation balance (Unit kg/s)

Case	2	3	4	5	9
Water side	1.465e-3	1.828e-3	1.427e-3	9.546e-4	3.616e-4
Air side	1.467e-3	1.839e-3	1.438e-3	9.662e-4	3.620e-4
Error	0.81%	0.56%	0.77%	1.12%	0.13%
Case	10	11	12	14	
Water side	7.834e-4	1.324e-3	9.051e-4	1.358e-3	
Air side	7.847e-4	1.337e-3	9.099e-4	1.345e-3	
Error	0.16%	0.97%	0.53%	-0.94%	

5.5.4 Heat transfer distribution

As explained in Chapter 3, the heat flux imposed on the wall is composed of three parts in terms of energy balance:

$$\dot{q}_f \mathrm{d}y = \dot{m} c_p \mathrm{d}T_w + \dot{q}_l \mathrm{d}y + \dot{q}_s \mathrm{d}y \tag{5.23}$$

$\dot{q}_l$ for the latent evaporation, $\dot{q}_s$ for the convective heat between the liquid film and air-vapor mixture and $\dot{q}_m = \dot{m} c_p \mathrm{d}T_w$ for the energy carried away by the liquid film. The distribution of the energy can provide the information for us to improve the efficiency of evaporation. The energy distribution is given in Fig.5.9. It can be concluded from all the cases that the convection heat transfer between the liquid film and air-vapor mixture is small. In the case 2, 3, 11, 12 and 14 where the inlet temperature is high, the latent evaporation is stronger and all the heat flux imposed on the wall is removed through the evaporation. Meanwhile due to the high liquid temperature, the released internal energy of the liquid film is large. In that situation, the "evaporation mode" [11] dominates. In case 9, the evaporation hear transfer $\dot{q}_l$ and energy $\dot{q}_m$ carried by liquid film are significant at the bottom region of the tube. The negative $\dot{q}_m$ shows that its internal energy is released and temperature is reduced. As the air-mixture flow evolves, the evaporation heat transfer is reduced linearly to a approximate zero value while the energy $\dot{q}_m$ carried out by film increases. But the heat carried by the falling film increases to a high level after proceeding low level. It means that at the top of the tube the evaporation is weak and the main part of heat flux imposed on the wall is carried out by the falling liquid film.

During the simulation of the evaporation or condensation, the mass transfer on the falling liquid film side should be equal to the increase or decrease of moisture flow rate on the air side. The energy lost on the water side should equal to the energy increase of air side. Tables.5.2 and 5.3 list the mass and energy balance for different cases. The mass conservation and energy balance perform very well in all the simulations. The maximum error on mass balance is only 1.12% appearing in case 5 and the maximum

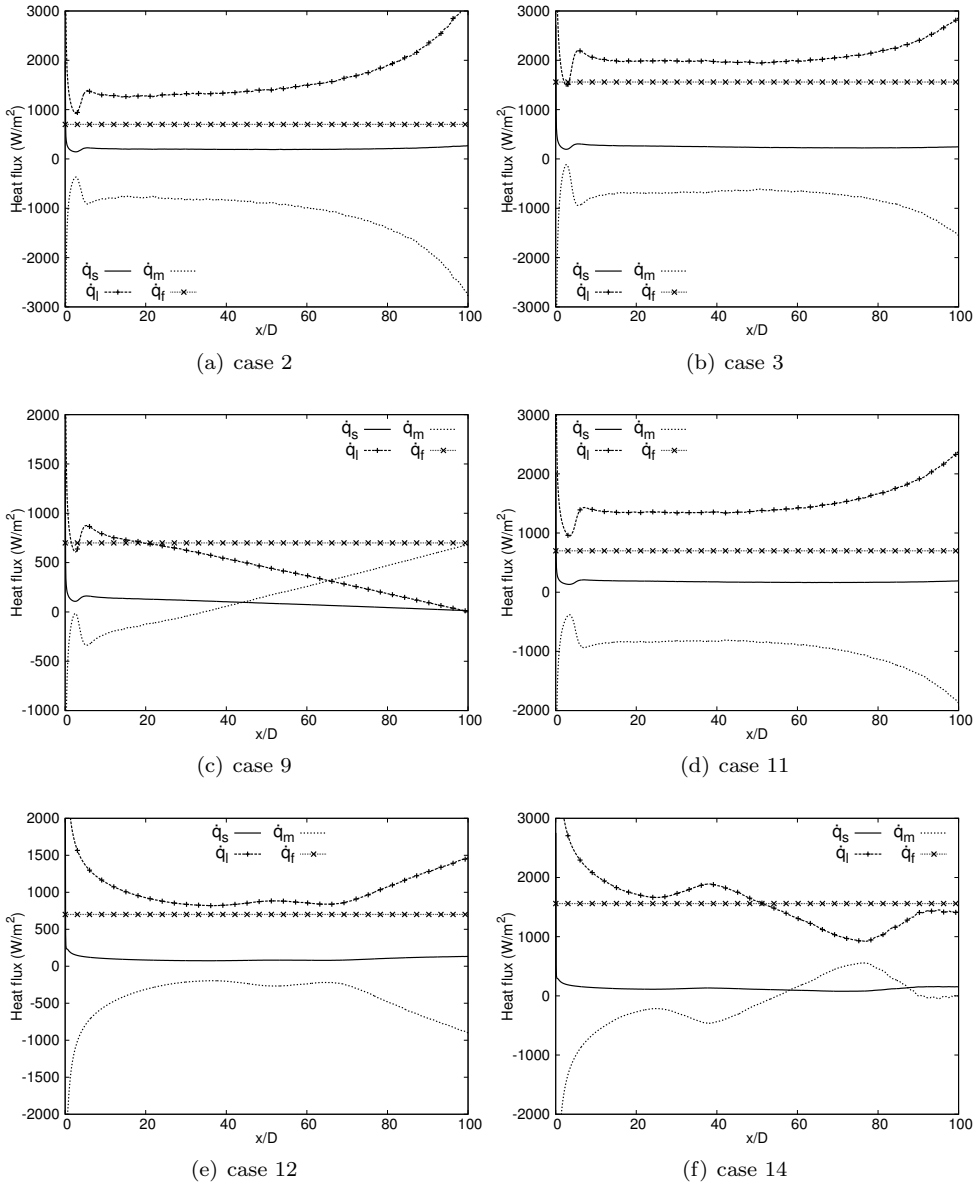

(a) case 2 (b) case 3

(c) case 9 (d) case 11

(e) case 12 (f) case 14

Figure 5.9: Energy distribution

Table 5.3: Energy balance (Unit W)

Case	2	3	4	5	9
Water side	3654.5	4560.8	3614.5	2426.6	1027.2
Air side	3715.4	4596.1	3676.0	2439.1	1019.9
Error	1.61%	0.77%	1.70%	0.52%	0.72%
Case	10	11	12	14	
Water side	2379.5	3675.2	2740.4	3791.6	
Air side	2397.3	3724.0	2777.6	3719.1	
Error	0.75%	1.33%	1.36%	-1.91%	

error on energy is -1.91% in case 14. From the table, it can be concluded that the evaporation rate in case 9 is minimum.

The total convective heat transfer rate from the film interface to the air-vapor mixture flow consists of two parts: $\dot{q}_s$ and $\dot{q}_l$. Therefore the local total Nusselt number can be obtained from two Nusselt numbers, sensible Nusselt number and latent Nusselt number, namely, $Nu_{total} = Nu_s + Nu_l$ (see chapter 3 for their definitions). Fig. 5.10 presents the sensible and latent Nusselt numbers Nu_s, Nu_l for the cases under study. The sensible Nusselt number directly depends on local Reynolds number and Buoyancy force for a given geometry. Therefore with low Reynolds number (case 11, 12 and 14), the sensible Nusselt numbers are clearly less than other cases with higher Reynolds number. The sensible Nusselt numbers in the cases of high Reynolds number are clearly similar except case 9. Compared to other cases with same Reynolds number, the buoyancy force in case 9 shows a clear deviation near the outlet of tube (Fig. 5.4). The reduced buoyancy force directly leads to a reduction in sensible Nusselt number. Based on the calculation correlation $Nu_s = \dot{q}_s\Phi/[\lambda(T_w - T_m)]$, it is indirectly influenced by the temperature difference between the bulk and film. The inlet film temperature in case 9 is low and the temperature difference between the bulk and film is very small at the top of the tube (seen from the mean temperature in Fig.5.6). Thus the convection heat transfer between the mixture and film is less and its sensible Nusselt number is reduced greatly at the top of the tube.

The condition of the latent Nusselt number is more complicated. It depends on not only the Reynolds number but also heat flux and inlet film temperature since these parameters are directly related to the evaporation rate. The evaporation rate is directly affected by the Reynolds number, inlet water temperature, water flow rate and heat flux imposed on the wall. With the same Reynolds number and inlet water temperature, the latent Nusselt number is enhanced with higher heat flux (comparisons between case 2&3, case 5&4, case 12&14). The latent Nusselt number is enhanced with the rise of inlet water temperature and with the others parameters fixed (the comparison of case 9, 10, 2).

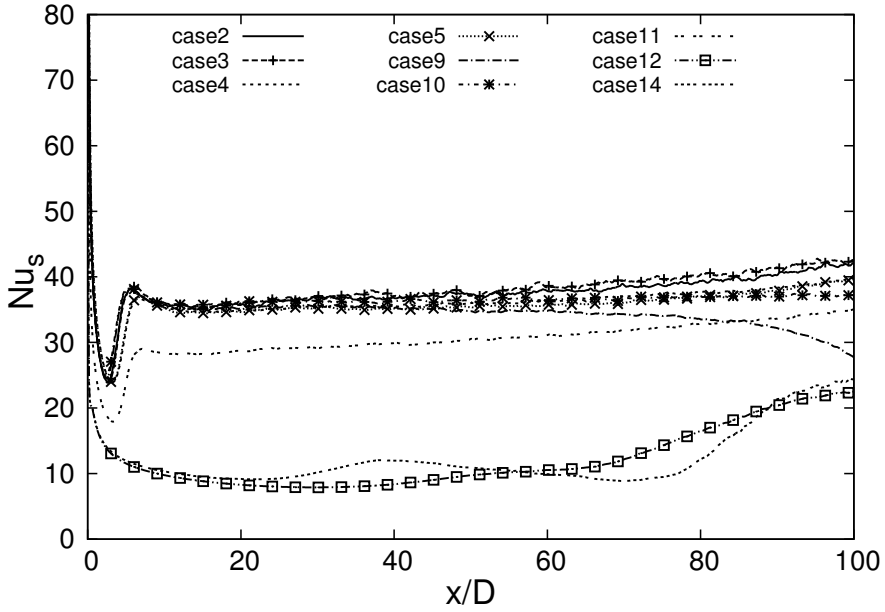

(a) Sensible Nusselt number

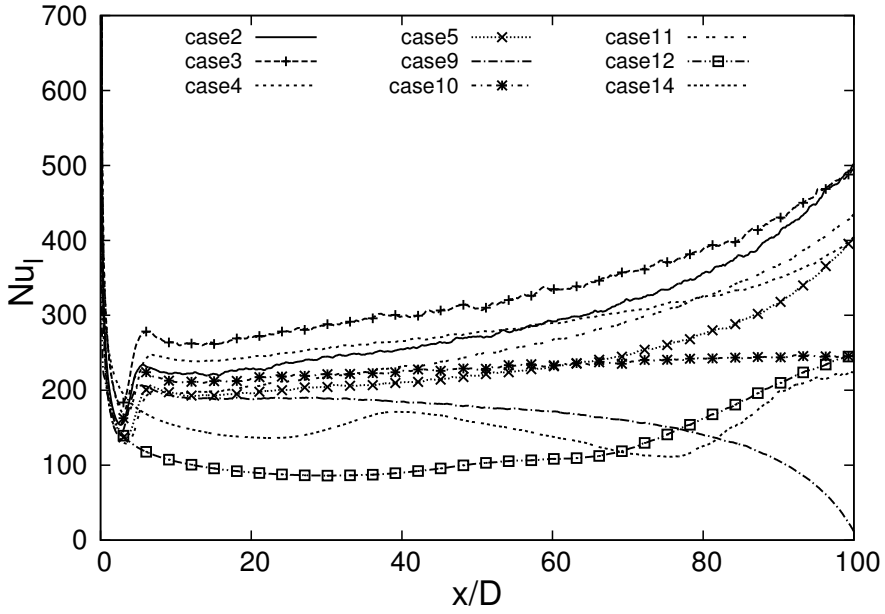

(b) Latent Nusselt number

Figure 5.10: Variation of Nusselt number along the tube

In general, the variation trend of latent Nusselt number is similar with the latent heat transfer.

5.5.5 Turbulent shear stress

The shear stress contributions were calculated by

$$\tau_{res} = - < \rho u^{''} u_r^{''} > \tag{5.24}$$

$$\tau_{vis} = - < \mu \frac{\partial u}{\partial r} > \tag{5.25}$$

$$\tau_{sgs} = \overline{\tau}^t = - < \mu_t \frac{\partial u}{\partial r} > \tag{5.26}$$

$$\tau_{total} = \tau_{res} + \tau_{vis} + \tau_{sgs} \tag{5.27}$$

where the three equations represent the resolved Reynolds shear stress, resolved viscous shear stress and modeled SGS shear stress, respectively. Fig. 5.11 presents the distributions of the four shear stresses normalized by the interface shear stress for case 3 and case 12. For case 3, the resolved shear stress is very low at the inlet and then the turbulent intensity is enhanced rapidly from inlet to 5D near the wall. Although the turbulence intensity jump happens near the wall, the resolved shear stress at the core of the tube varies more slowly. It increases gradually from inlet to 15D-20D from where the turbulence intensity changes little. The variation phenomena corresponds to the boundary condition imposed on the wall - evaporation on the interface and heat transfer between the film and air-vapor mixture. The development distance is consistent with the variation of the mean velocity. The small negative value at the core shows that a weak M-shape velocity exist at the 5D since the strong evaporation near the interface.

In the condition of the hydrodynamically fully developed flow and a statistically steady state with solid wall, the total shear stress must be linear and the normal-to-the-interface gradient of total shear stress must balance the pressure gradient [18,19]. Although a radial velocity is imposed at the interface, it is very small and can be neglected. Therefore, we think, the total shear stress still satisfies the theory of the fully developed flow. In this sense the total shear stress can illustrate the deviation extent from the hydrodynamically fully developed flow. For case 3, the viscous shear stress only change from inlet to 5D. After that, their variation is not obvious till the outlet of the tube. The variation trend of the modeled SGS shear stress is similar with the resolved shear stress but its value is very small. The total shear stress shows a quick developing trend towards the fully developed state. At around 15D, the total shear stress normalized by the wall shear stress is nearly linear and it confirms that the hydrodynamically fully developed condition is reached.

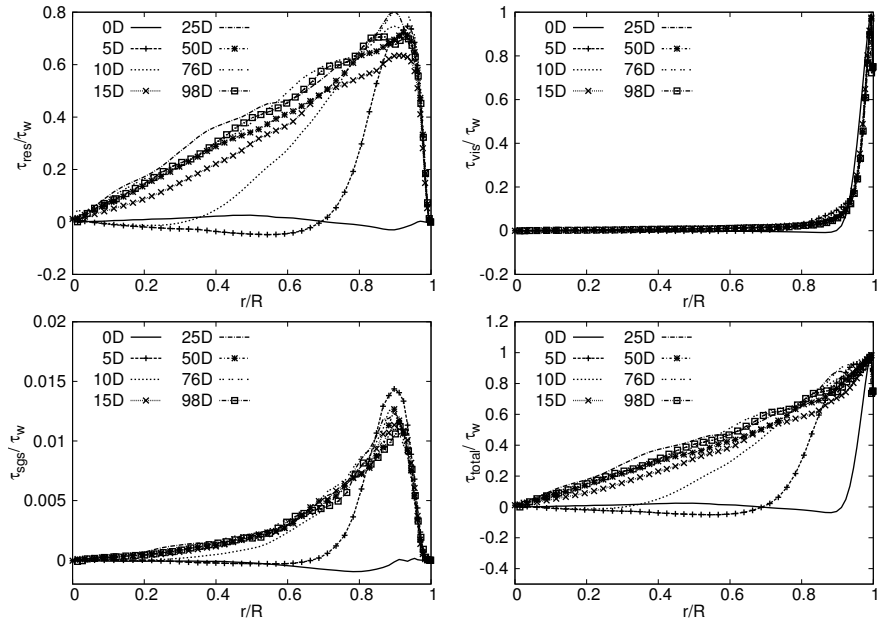

(a) case 3

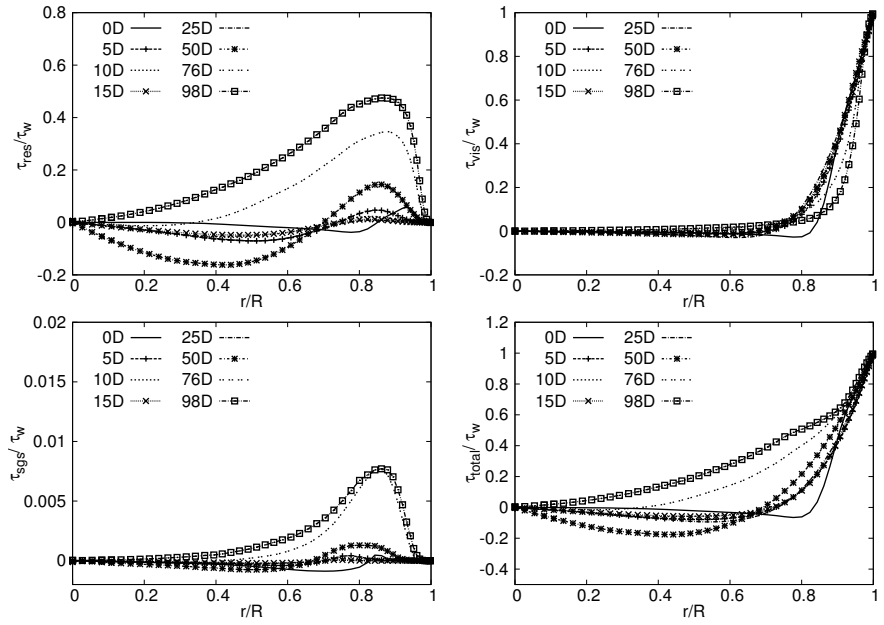

(b) case 12

Figure 5.11: Shear stress distribution normalized by the wall shear stress

On the contrary, the flow development in case 12 is very slow. The turbulent resolved shear stress firstly shows negative value from inlet to 50D, it corresponds the M-shape velocity profiles although the value is large. From 80D, the turbulence intensity becomes a large positive value. The resolved shear stress is increasing till near the outlet and it shows the developing process. From the total shear stress, it can be seen that its normalized value is nearly linear at the outlet, it shows that the flow only approaches the hydrodynamically fully developed state near the outlet. The observation is consistent with the assessment of development state.

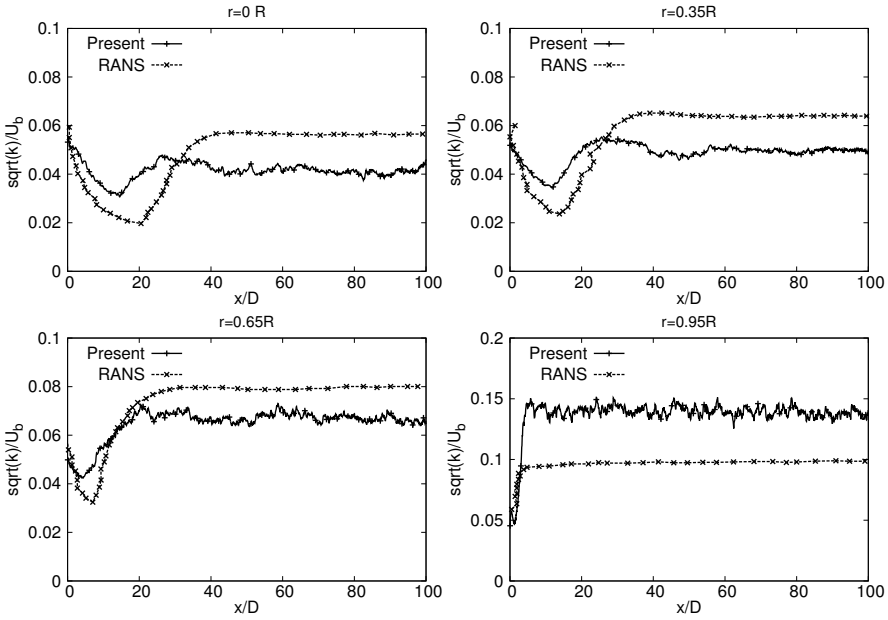

Figure 5.12: The turbulent kinetic energy profile for case 3

Since the profiles of all the cases with high Reynolds number are similar, case 3 is chosen as a comparison with RANS model [11]. Fig. 5.12 shows the variation of the turbulent kinetic energy (TKE) along the axial direction at different radial locations. Near the wall (r=0.95R) the turbulence kinetic energy presents a rapid jump process within five diameters, which responds to the boundary condition - strong heat flux and evaporation. Towards the core, the influence of boundary condition on the flow is weak and delayed. The trend of turbulent kinetic energy at far from the boundary is different from near the wall. They show a decrease trend at the beginning and then is recovered to the inlet level. At the different radial positions, the locations where

the minimum value appears are different and also the extents they are reduced are different. At r=0R core of the tube, the location of minimum value is around 15D while it moves to around 5D at r=0.65R. It can also be seen that the general trend is similar with RANS model although turbulent intensity levels are different. Near the wall the turbulence intensity is stronger than RANS model while it is weaker in other locations.

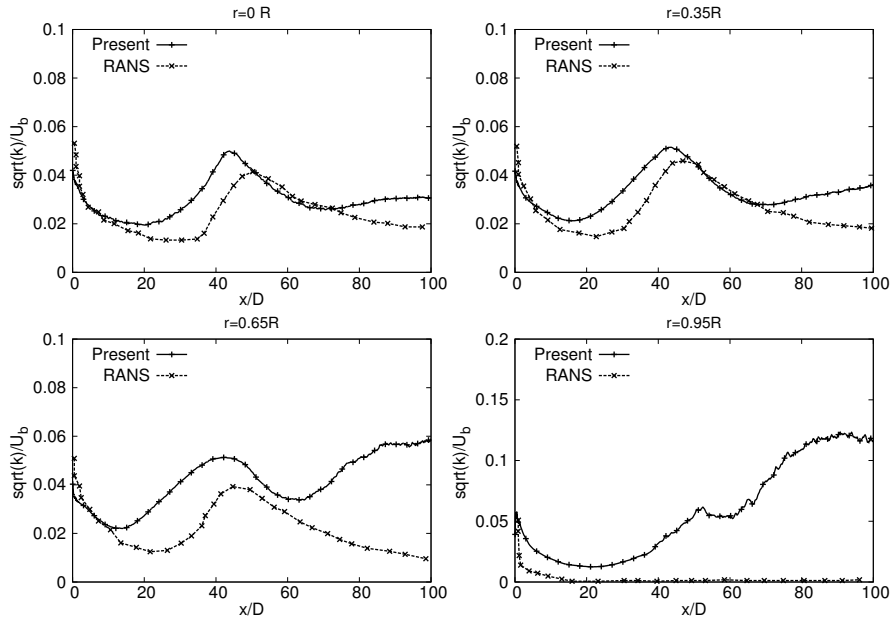

Figure 5.13: The turbulent kinetic energy profile for case 12

The performance of TKE in low Reynolds number (case 12) are different. Fig. 5.13 gives the comparison on TKE between the present simulation and RANS model. The observation obtained in the present study is different with the one by He et al. [11] using the Launder-Sharma model. At the locations closer to the wall, the clearer difference can be observed. In the core of the tube ($r = 0R$), TKE shows a similar trend, in particular in the upstream region. Both TKEs arrive at the first peak at around x=40D. Afterwards it proceeds another slow reduction process until end of the pipe. It is observed that a slight recover of TKE appears near the end of the pipe in the present simulation. At $r = 0.65R$, the deviation happens near the initial distance of the pipe and TKE is strongly recovered near the outlet. Near the region next to the wall, the trend is completely different. In RANS model, it monotonically

decreases along the streamwise while it experiences a process of reduction and recover in LES. Finally, TKE remains a high level which is same as the one of fully developed state. Under the condition of strong buoyancy force, RANS model overpredicted the laminarization which does actually not exist in the experiments. In particular in the turbulent shear flow, the turbulent should be generated in the near wall region where turbulence energy decayed in RANS model. That difference results in a lower film temperature in the present simulation compared to the Launder-Sharma model. Generally speaking, LES gives better prediction of this transitional process with strong buoyancy force.

5.5.6 Turbulent heat transfer and moisture transfer

Corresponding to the shear stress components, the turbulent heat flux contributions are calculated as,

$$\dot{q}_{res} = - < \rho u_r^{''} h^{''} > \tag{5.28}$$

$$\dot{q}_{con} = - < \frac{\mu c_p}{Pr} \frac{\partial T}{\partial r} > \tag{5.29}$$

$$\dot{q}_{sgs} = \bar{\dot{q}}^t = - < \frac{\mu_t c_p}{Pr_t} \frac{\partial T}{\partial r} > \tag{5.30}$$

$$\dot{q}_{total} = \dot{q}_{res} + \dot{q}_{con} + \dot{q}_{sgs} \tag{5.31}$$

where the three heat flux components represent the resolved heat flux, heat conduction and modeled SGS heat flux, respectively. The sum of the three heat flux is the total heat flux or the convection heat transfer at the interface.

Corresponding to the shear stress components, the turbulent moisture diffusive flux contributions are calculated as,

$$\dot{J}_{res} = - < \rho u_r^{''} c^{''} > \tag{5.32}$$

$$\dot{J}_{con} = - < \rho D \frac{\partial c}{\partial r} > \tag{5.33}$$

$$\dot{J}_{sgs} = - < \rho D_t \frac{\partial c}{\partial r} > \tag{5.34}$$

$$\dot{J}_{total} = \bar{\dot{J}}^t = \dot{J}_{res} + \dot{J}_{con} + \dot{J}_{sgs} \tag{5.35}$$

where the three moisture diffusive flux components represent the resolved moisture flux, diffusion and modeled SGS moisture flux, respectively. The sum of the three moisture flux is the total moisture diffusive flux. It is worth to note that the total

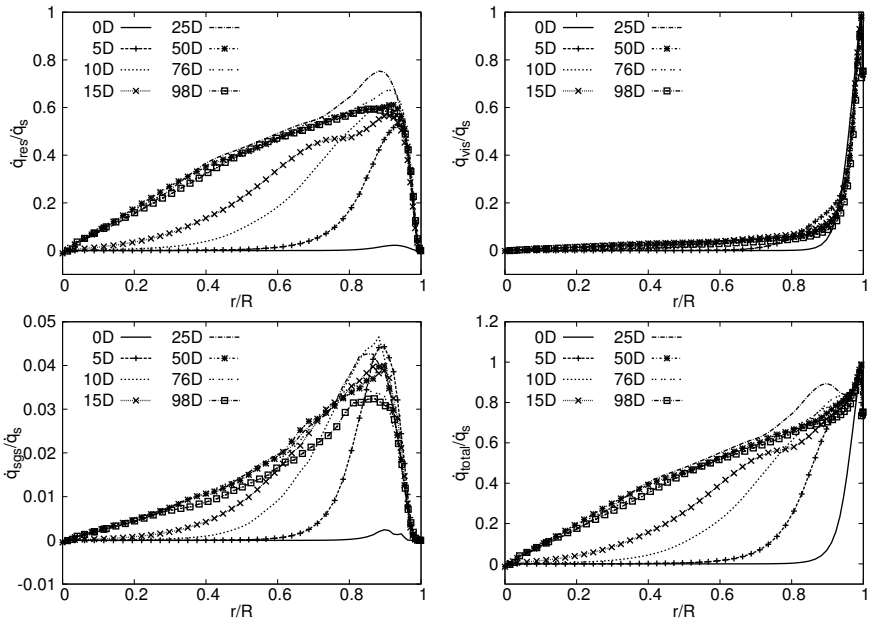

(a) case 3

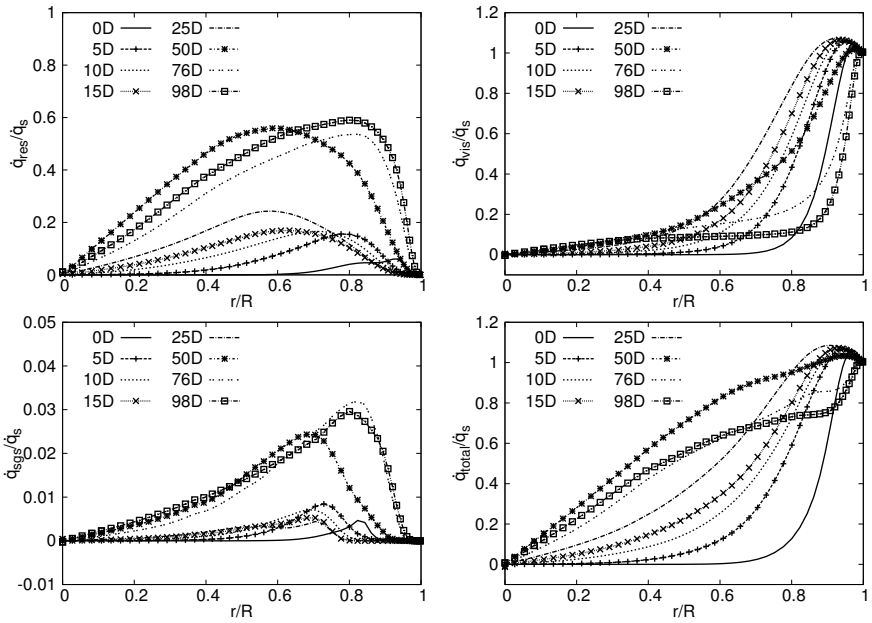

(b) case 12

Figure 5.14: Heat transfer distribution normalized by the convection heat transfer between the interface and air

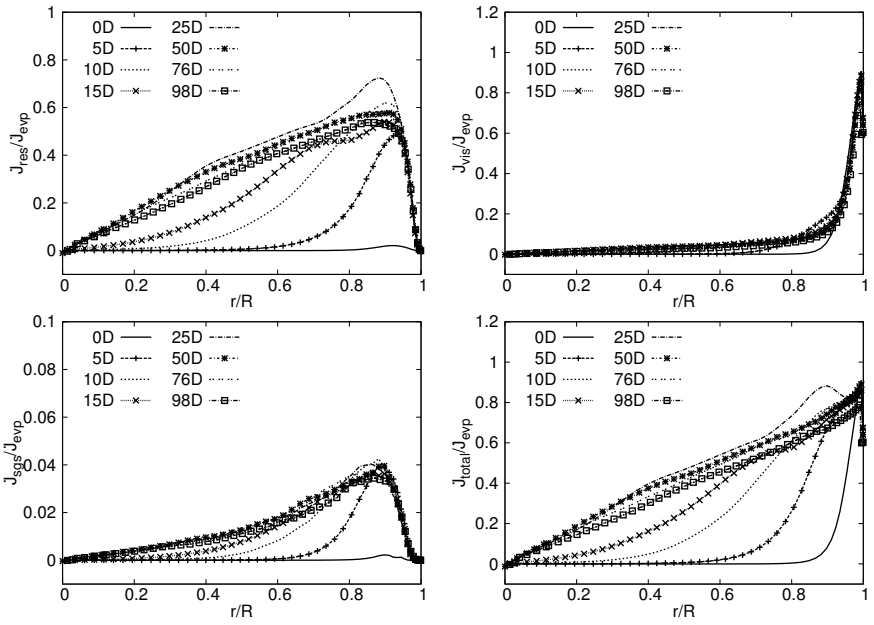

(a) case 3

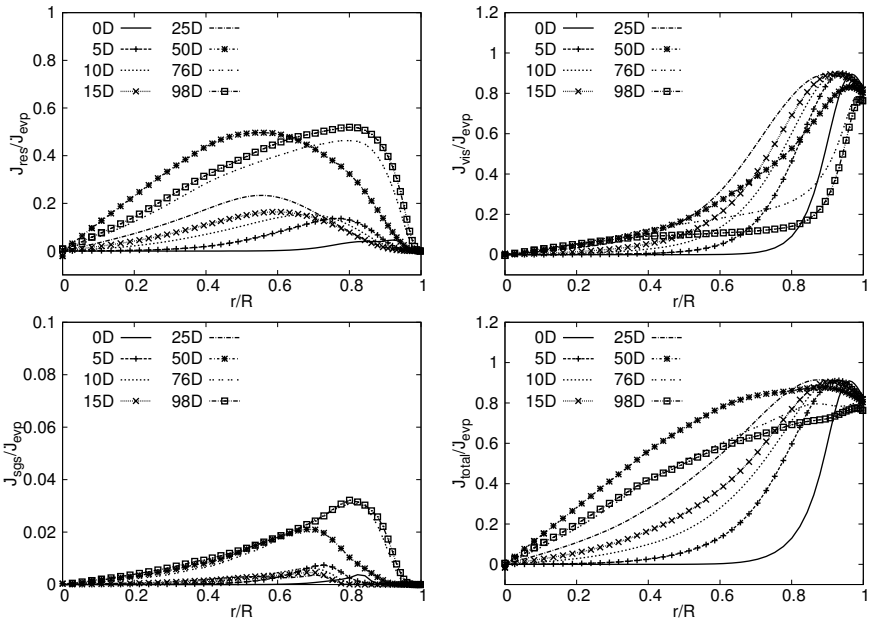

(b) case 12

Figure 5.15: Moisture transfer distribution normalized by the evaporation at the interface

moisture diffusive flux is not equal to evaporation rate at the interface since the interface is considered as a semipermeable plane.

The four heat flux distributions normalized by the convection heat transfer at interface are shown in Fig. 5.14. The four moisture flux distributions normalized by the evaporation rate at the interface are shown in Fig. 5.15. In general, the performance of turbulent heat transfer is similar as the one of turbulent moisture transfer.

In case 3, the resolved heat transfer and moisture diffusive flux show a slow increasing trend with the distance from inlet to 20D. But the increase is rapid near the wall while it is slow at the core of the tube corresponding the convection heat transfer and evaporation at the interface. From 20D, the variations of the resolved heat transfer and moisture transfer are not significant any more. The viscous heat and moisture transfer are mainly concentrated near the region next to the wall, and their variations only happen from inlet to 5D. The total heat flux and moisture flux are more dependent on the resolved heat transfer or moisture transfer at the core of the tube while they are largely decided by the viscous heat transfer and moisture transfer contributes in the region next to the wall. The variations of turbulent heat transfer and moisture transfer from 0D to 20D show the thermally developing process along the tube. The approximately linear profile from 20D shows that the thermally fully developed state is obtained from 20D.

The variation of turbulent heat transfer and moisture transfer in case 12 are more complicated as shown in Fig. 5.14(b) and Fig. 5.15(b). From the entrance to 20D, the maximum resolved heat transfer and moisture transfer almost keep constant while its peak value moves towards the centre of the tube. Afterwards, it proceeds a rapid increasing process from 20D to 50D. It reflects the turbulence variation along the tube. The viscous heat and moisture transfer represents for the thickness of viscous sublayer. From their variation, it can be seen that the viscous sublayer is increasing from inlet to 25D and then reduces from 25D to outlet.

5.5.7 Flow Structure

The variation of turbulent intensity in the flow field of case 12 is illustrated in Fig. 5.16 where the instantaneous isosurface of the vorticity for $\omega = 20$ is shown. In the axial sectional views, the variation of the vorticity along the tube can be clearly seen. Due to the velocity fluctuation imposed on the inlet, a clear turbulent characteristic appears at the entrance of the tube. The fluid vorticity decreases gradually in the flow direction from the inlet to around 1m. It shows the laminarization trend due to the effect of strong evaporation. From 1m, the fluid vorticity shows a trend of slight enhancement. Although the fluid vorticity shows a fluctuation within the first 2m, its variation is not clear with a low level of turbulence intensity. The variation can also be seen from Fig.5.13. From 2m, it is enhanced clearly and reaches a peak around 4m where the turbulence characteristic is very apparent. The fluid vorticity at 5-6m

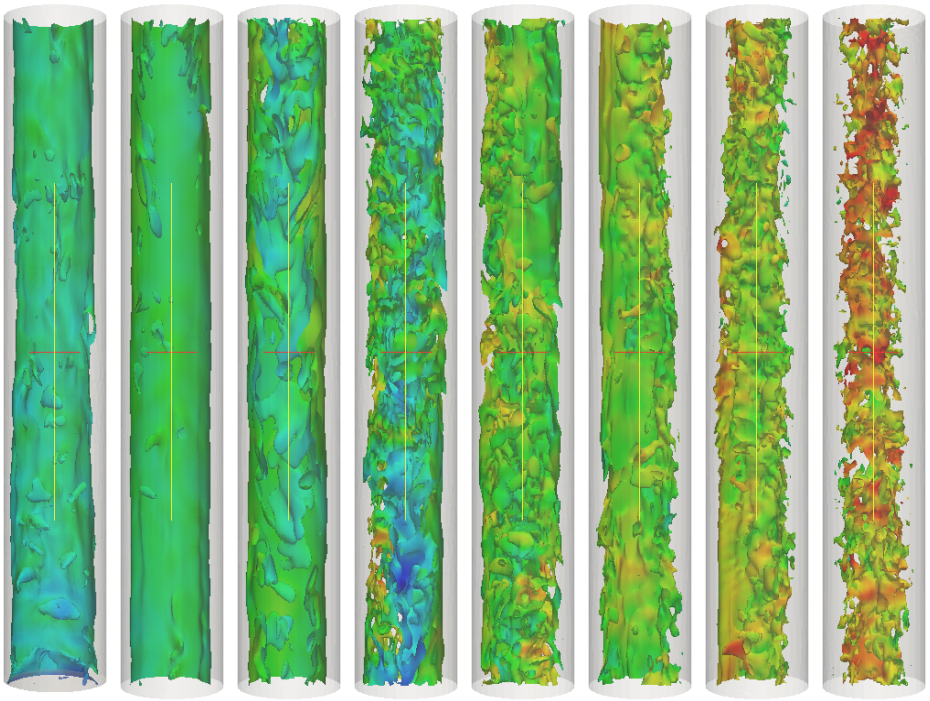

(a) 0-1m (b) 1-2m (c) 2-3m (d) 3-4m (e) 4-5m (f) 5-6m (g) 6-7m (h) 7-8m

Figure 5.16: Instantaneous isovorticity surfaces for $\omega = 20$ colored by velocity for case 12

presents another recession. After that, the fluid vorticity increase gradually again till the outlet.

The instantaneous cross sectional views of velocity vector fields are shown in Fig. 5.17. It can be seen from the sectional velocity vector fields, the large scale motion does not appear at the inlet although the velocity vector at the cross section is apparent. It is because of the imposed uniform velocity. The variation of velocity vector field is weak and there does not exist the large scale eddies even there is a weak fluctuation within the first distance of 40D. At x=40D, the large scale eddies are captured only at the core of the tube. It shows the thickening of the viscous sublayer. At x=50D and x=60D, the vortical structure become ambiguous in the core of the tube while the large scale motion begin to form near the wall. As the flow develops, the larger eddy motions are observed near the wall. At the section of x=100D, the

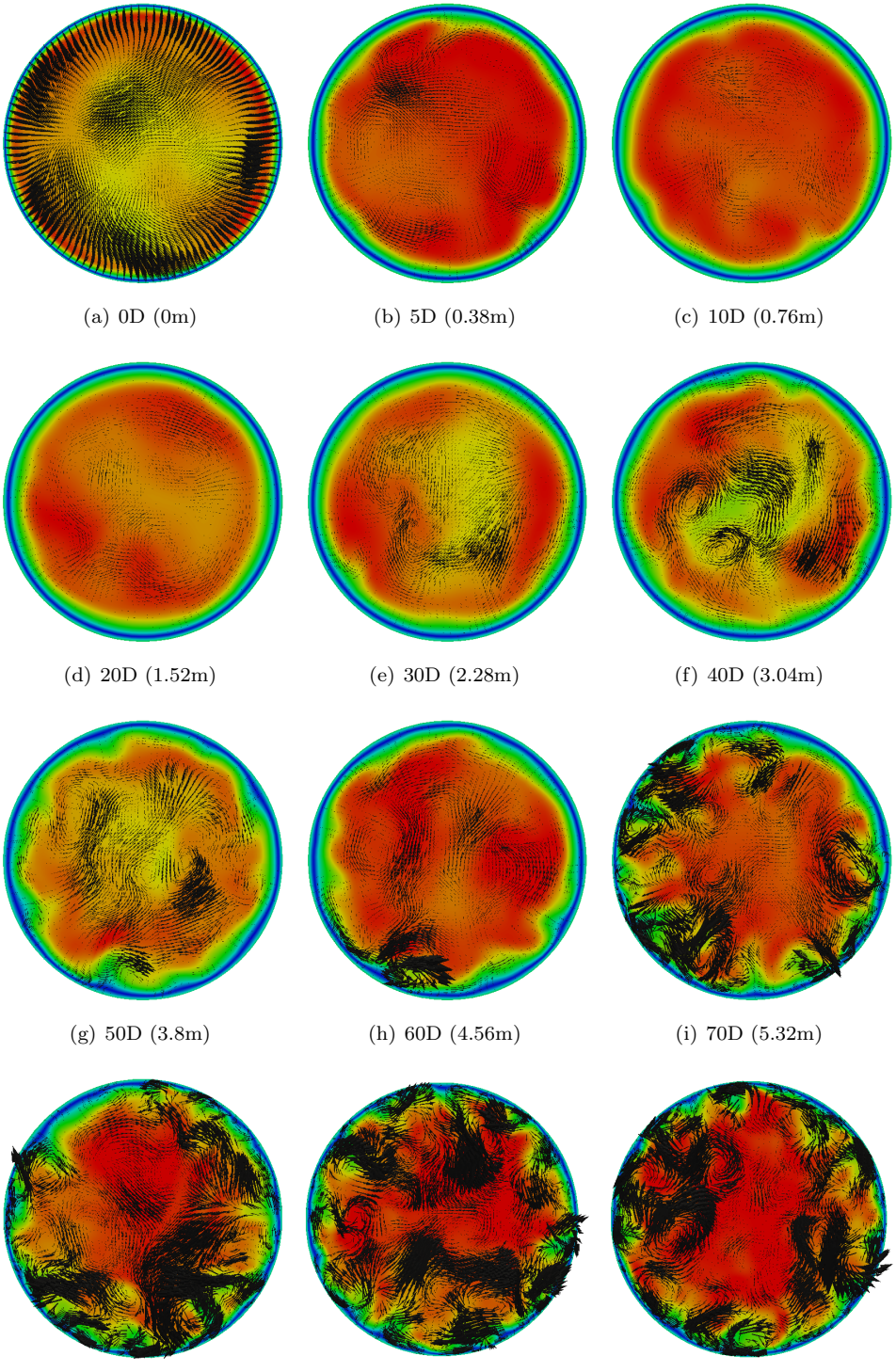

(a) 0D (0m) (b) 5D (0.38m) (c) 10D (0.76m)

(d) 20D (1.52m) (e) 30D (2.28m) (f) 40D (3.04m)

(g) 50D (3.8m) (h) 60D (4.56m) (i) 70D (5.32m)

(j) 80D (6.08m) (k) 90D (68.4) (l) 100D (7.6m)

Figure 5.17: Instantaneous velocity field and vector in cross section for case 12

characteristics of velocity distributions is very similar with that at inlet in the chapter 4, where the hydrodynamically fully developed velocity is imposed on the entrance. It shows that the flow is approaching the fully developed state in the case 12.

5.6 Conclusion

In this part, the validated turbulent model in the pure air flow is extended to evaporation in turbulent flow. The validated simplified model for a falling film in the chapter 3 is employed as the solution of the falling film. Both models are coupled to simulate the experiments conducted by An et al. [1]. In these experiments, the fluids flow upwards in a vertical pipe with a falling film. The heat and mass transfer happens in the experiments and the flow is strongly influenced by the buoyancy force in some conditions. The evaporation process involves the laminar and turbulent mixed convection flow and detailed flow characteristics were obtained.

To the author knowledge, this is the first work that the turbulent mixed convection heat and mass transfer in a vertical tube is simulated using LES. All the previous simulations are conducted using RANS models. This is the main contribution of the paper to the kind of evaporation flow. The results are compared with the experimental data. It is found that the WALE model in LES is generally able to respond well to the turbulent flow under the condition of mixed convection, in which the complex combined heat and mass transfer exists. The obtained results are also compared with the one obtained by the Launder-Sharma turbulence model [11]. However the LES result still overpredicted the influence of buoyancy force in some cases (case 12 and case 14) although it presents a advantage over the Launder-Sharma model. The film temperature obtained using LES model shows a better result than the Launder-Sharma model in case 12. The main reason is that it shows a certain level of turbulence intensity near the wall in present simulation while it almost is completely laminar in the zone with the Launder-Sharma model. In addition, the strong turbulent flow (approximately fully developed flow) is approached near the end of the tube in the present work while it does not appear in the Launder-Sharma model.

Like the observation with the Launder-Sharma model, the velocity is re-organized with the entrance region of the tube for all the cases under study. The distance in the present simulation is close as the Launder-Sharma model (20D). The turbulence intensity proceeds a reduction process within the entrance region. After the entrance region, the turbulence is enhanced greatly, in particular near the wall.

References

[1] P An, J Li, and JD Jackson. Study of the cooling of a uniformly heated vertical tube by an ascending flow of air and a falling water film. *International journal*

of heat and fluid flow, 20(3):268–279, 1999.

[2] Wei-Mon Yan. Effects of film vaporization on turbulent mixed convection heat and mass transfer in a vertical channel. *International Journal of Heat and Mass Transfer*, 38(4):713 – 722, 1995.

[3] Wei-Mon Yan. Evaporative cooling of liquid film in turbulent mixed convection channel flows. *International Journal of Heat and Mass Transfer*, 41(23):3719 – 3729, 1998.

[4] Jer-Huan Jang and Wei-Mon Yan. Thermal protection with liquid film in turbulent mixed convection channel flows. *International Journal of Heat and Mass Transfer*, 49(19 - 20):3645 – 3654, 2006.

[5] M Feddaoui, A Mir, and E Belahmidi. Cocurrent turbulent mixed convection heat and mass transfer in falling film of water inside a vertical heated tube. *International Journal of Heat and Mass Transfer*, 46(18):3497 – 3509, 2003.

[6] M. Feddaoui, H. Meftah, and A. Mir. The numerical computation of the evaporative cooling of falling water film in turbulent mixed convection inside a vertical tube. *International Communications in Heat and Mass Transfer*, 33(7):917 – 927, 2006.

[7] F. Nicoud and F. Ducros. Subgrid-scale stress modelling based on the square of the velocity gradient tensor. *Flow, Turbulence and Combustion*, 62(3):183–200, 1999.

[8] O. [et al.] Lehmkuhl. Termofluids: A new parallel unstructured cfd code for the simulation of turbulent industrial problems on low cost pc cluster. In *Proceedings of the Parallel CFD 2007 Conference*, pages 1–8, Ismail H. Tuncer, 2007.

[9] Habib N. Najm, Peter S. Wyckoff, and Omar M. Knio. A semi-implicit numerical scheme for reacting flow: I. stiff chemistry. *Journal of Computational Physics*, 143(2):381 – 402, 1998.

[10] F. Nicoud. Conservative high-order finite-difference schemes for low-mach number flows. *Journal of Computational Physics*, 158(1):71 – 97, 2000.

[11] S He, P An, J Li, and JD Jackson. Combined heat and mass transfer in a uniformly heated vertical tube with water film cooling. *International journal of heat and fluid flow*, 19(5):401–417, 1998.

[12] M Klein, A Sadiki, and J Janicka. A digital filter based generation of inflow data for spatially developing direct numerical or large eddy simulations. *Journal of computational Physics*, 186(2):652–665, 2003.

[13] L Di Mare, M Klein, WP Jones, and J Janicka. Synthetic turbulence inflow conditions for large-eddy simulation. *Physics of Fluids (1994-present)*, 18(2):025107, 2006.

[14] Thomas S Lund, Xiaohua Wu, and Kyle D Squires. Generation of turbulent inflow data for spatially-developing boundary layer simulations. *Journal of Computational Physics*, 140(2):233–258, 1998.

[15] YL Tsay and TF Lin. Evaporation of a heated falling liquid film into a laminar gas stream. *Experimental thermal and fluid science*, 11(1):61–71, 1995.

[16] Ernst Rudolf Georg Eckert and Robert M Drake Jr. Analysis of heat and mass transfer. 1987.

[17] JD Jackson and WB Hall. Influences of buoyancy on heat transfer to fluids flowing in vertical tubes under turbulent conditions. *Turbulent forced convection in channels and bundles*, 2:613–640, 1979.

[18] Xu. Xiaofeng. *Large eddy simulation of turbulent pipe flow with property variations*. PhD thesis, Iowa State University, 2002.

[19] Stephen B Pope. *Turbulent flows*. Cambridge university press, 2000.

6

Conclusions and future work

As written in the introduction, the present study focuses on the multiphase and multicomponent flows, especially on mixed transitional/turbulent flow with strong buoyancy force. In order to finalize this dissertation, the conclusions drawn from the present work and the recommended future work are presented in this chapter.

6.1 Conclusions

In Chapter 2, the two-fluid model has been solved by means of the explicit Fractional Step method avoiding the problem of implicit formulation under pressure-based iteration method. Surface tension is also solved, while diffusion effects have been reduced, considering high resolution schemes and implementing interface sharpening method. Verification tests of mesh density and numerical schemes are carried out in order to confirm the influence of discretization scheme. The capability of the two-fluid model with Fractional Step method in flow with small or large scale length interface has been assured by means of different numerical and experimental cases with and without interface sharpening method. In order to highlight the capability of the two fluid model in flow with large scale length, Rayleigh-Taylor instability, Dam break, droplet and rising bubble have respectively been implemented. The results obtained are all consistent with the referred data. The case of Rayleigh-Taylor instability illustrates clearly the advantages of Vanleer flux limiter and interface sharpening on controlling the diffusion. Dam break cases shows the good performance in the flow with high density ratio and high viscosity. Through the simulation of pressure jump over droplet interface, oscillating droplet and rising bubble, the capability of the two-fluid model where surface tension dominated was validated. The capability of the two-fluid model in the flow with small scale length interface is presented in the case of sedimentation. Overall, the present simulations and results conclude that, the two

fluid model with small or large characteristic scales can be solved successfully to obtain the accurate results through Fractional Step Method algorithm, and it can also be applied to simulate the free surface flow if appropriate formulations and parameters are used. The fractional step method is able to solve the large characteristics scale problems without interface sharpening even with coarse meshes, reducing the diffusion and sharp the interface in all situations

In Chapter 3, simultaneous heat and mass transfer in laminar flow is studied. Three cases are included: a horizontal flow with constant physical properties, natural convection with variable properties and mixed convection with variable properties. In the first case, a static wet boundary condition is applied while liquid film boundary condition is imposed in the last two cases. During the work, a simplified method of solving liquid film equations has been applied which takes into account of the transfer in liquid film and also between the film and the flowing air-vapor mixture. The mixture model and simplified liquid film model are tested in the laminar flow. The influence of different parameters on film temperature, evaporated ratio and thermal efficiency have been studied in details. The mixture model can accurately predict the laminar flow with constant and variable physical properties. In the first case, a spanwise boundary layer is also observed, which results in the non-uniform temperature field along spanwise direction. Meanwhile a small vortex has been seen near the corner to bottom wall due to the imposed transverse velocity and evaporation. In the second case, the simplified model from energy balance is developed to calculate the boundary condition and it gives good results compared to the experimental ones. The mixture model with variable physical properties provides more accurate than the one with constant properties. Meanwhile the condensation in the film side is also considered and it could have an impact on the heat flux profiles and the detailed values. Multiple vortex have been observed in the natural cavity flow in the present study and they move upwards with heat flux. In the third case, the mixed convection has been studied. It is found that the evaporation thermal efficiency at low inlet velocity does not change greatly with heat flux. The behavior is different to the one in natural convection. The thermal efficiency is influenced by the forced convection through the imposed inlet velocity. The temperature drop across the liquid film is very small and can be neglected.

In Chapter 4, large-eddy simulation of heated vertical air flows in the turbulent mixed convection have been performed for the experimental conditions of Shehata [1] and Li [2]. WALE model is used as the SGS model and symmetry-preserving scheme discretization were adapted, with which a relative coarse mesh could be chosen. In the simulation for Shehata case, the detailed data in the whole field were compared with experiment and DNS results. It covered the complete laminarization transition. Good agreement shows that the present model can be successfully applied to the turbulence-laminar transitional flow with high heating. Furthermore, a series of flows

in a very long tube which proceed turbulence-laminar and reverse transition were simulated. The change after the reverse transition to the fully developed state were obtained. Meanwhile the downward flow under the same conditions were compared. The obtained Nu or Nu ratios agree well with the experimental results. The variable parameters in the whole tube were studied. In general, the present model could be successfully applied to the transition flow with the heating, capturing the transition and accurately predicting the heat transfer and flow structure.

In Chapter 5, the validated turbulent model in the pure air flow is extended to evaporation in turbulent flow. The validated simplified model for a falling film in Chapter 3 is employed as the solution of the falling film. Both models are coupled to simulate the experiments conducted by An et al. [3] with strong buoyancy force. To the author knowledge, this is the first work that the turbulent mixed convection heat and mass transfer in a vertical tube is simulated using LES. All the previous simulations were conducted using RANS models. This is the main contribution of this thesis to the kind of evaporation flow. It is found that the WALE model in LES is generally able to respond well to the turbulent flow under the condition of mixed convection, in which the complex combined heat and mass transfer exists. The obtained results are also compared with the one obtained by the Launder-Sharma turbulence model [4]. However the LES result still overpredicted the influence of buoyancy force in some cases (case 12 and case 14) although it presents a advantage over the Launder-Sharma model. The main reason is that it shows a certain level of turbulence intensity near the wall in present simulation while it almost is completely laminar in the zone with the Launder-Sharma model.

6.2 Future work

Based on the present work and our long-term objective, the following recommendations can be made for the future work.

- In the present work, the two phase model coupled with interface sharpening method is only applied to the two-dimensional simulation. In the following, it could be extended to three-dimension so that more general geometries can be considered.
- In the present simulation, the study on two phase flow is only limited to laminar flow. However, the turbulent two phase flow exists widely in engineering applications. Therefore the extension of the two phase model to turbulent flow should be studied further.
- In the present simulation of two fluid model, the continuity equation and momentum equations are only included while the phase change is not involved. In the future, the energy equation can be added. The two phase model including

energy equation can be used as the simulation of the nucleate boiling that may happen between the falling liquid film and solid wall.

- In the present solution of evaporation with falling film, the falling film is solved only by a simplified energy balance equation, instead of the full governing equation for the water. In the many engineerings, the interface is not smooth and there exist capillary waves on it. It could result in the enhanced heat and mass transfer. In order to solve it, the thin film flow has to be solved using full Navier-Stokes equations. In the following research, the two phase model can be coupled with the mixture model to solve the complicated flow, in which the nucleate boiling and surface evaporation are included.
- In the present simulation, the Reynolds number is low inside the falling film and it is assumed to be laminar flow. The turbulent falling film with high Reynolds number could be considered for the future.
- Based on the validation of the model adopted in the transitional/turbulent mixed convection flow, the mixed convection model with strong buoyancy force can be applied to industrial engineering with complex configurations, such as noise reduction, fan consumption reduction in low-speed velocity air-conditioner, air-cooled heat exchanger optimization, passive cooling and so on.
- Regarding to the evaporation model with or without falling film, it can be the first stage for future study on desalination, absorption, cooling tower, air-conditioner, refrigerator evaporator/condensor, heat exchanger with heat and mass transfer and so on.

References

[1] A.M. Shehata and D.M. McEligot. Mean structure in the viscous layer of strongly-heated internal gas flows. measurements. *International Journal of Heat and Mass Transfer*, 41(24):4297–4313, 1998.

[2] JianKang. Li and J.D. Jackson. Buoyancy-influenced variable property turbulent heat tranfer to air flowing in a uniformaly heated vertical tube. In *2nd International Conference on Turbulent Heat Transfer*, Manchester, UK, 1998.

[3] P An, J Li, and JD Jackson. Study of the cooling of a uniformly heated vertical tube by an ascending flow of air and a falling water film. *International journal of heat and fluid flow*, 20(3):268–279, 1999.

[4] S He, P An, J Li, and JD Jackson. Combined heat and mass transfer in a uniformly heated vertical tube with water film cooling. *International journal of heat and fluid flow*, 19(5):401–417, 1998.

Appendix A

Physical properties

A.1 Physical properties

Air and water vapor

The properties of dry air and water vapor are calculated by using the following equations,

–Density. Air and water vapor are assumed to be a prefect gas, the ideal gas equation of state is used to calculate the density,

Dry Air:

$$\rho_a = \frac{28.966}{8314.472}\frac{P}{T}, \quad 150 < T < 2500K \tag{A.1}$$

Water Vapor

$$\rho_v = \frac{18.01528}{8314.472}\frac{P}{T}, \quad 150 < T < 647K \tag{A.2}$$

–Heat capacity.

Dry Air. Eckert [1] and Rohsenow [2] polynomial expressions are chosen to calculate the property.

$$cp_a = A_0 + A_1T + A_2T^2 + A_3T^3 + A_4T^4 \tag{A.3}$$

Water Vapor. The polynomial expression from CRC [3] is considered,

$$cp_v = \frac{1000}{18.01528}(A_0 + A_1T + A_2T^2 + A_3T^3) \tag{A.4}$$

–Dynamic viscosity

The dynamic viscosity of dry air and water vapor are calculated by using Hilsenrath [4] equations recommended by NASA [5]

Dry Air.

$$\mu_a = 1.0e-8A_0T^{1.5}/(T + A_1) \tag{A.5}$$

Water Vapor.

$$\mu_v = \begin{cases} 1.0e-7(A_0T - A_1) & \text{if } T < 800\text{K} \\ 1.0e-7(A_2 * T^{1.5}/(A_3 - T + A_4 * T^2)) & \text{else} \end{cases} \tag{A.6}$$

Table A.1: Coefficients of the polynomial expression for dynamic viscosity

	T Range (K)	A_0	A_1	A_2	A_3	A_4
Dry Air	100-1900	145.8	110.4	—	—	—
Water Vapor	200-1500	0.361	10.2	39.37	3315.0	0.001158

–Thermal conductivity

The thermal conductivity of dry air and water vapor are calculated by using Hilsenrath [4] equations recommended by NASA [5]

Dry Air.

$$\lambda_a = 418.7 * (A_0T^{0.5}/(1.0 + (A_1 * 10^{-A_2/T}))) \tag{A.7}$$

Water Vapor.

$$\lambda_{ref} = \frac{A_2T^{0.5}}{1.0 + A_3/T * 10^{-12/T}}$$

$$\lambda_v = 418.7(\lambda_{ref} + A_0(10^{A_1P_v/T^4} - 1.0))$$

Table A.2: Coefficients of the polynomial expression for thermal conductivity

	T Range (K)	A_0	A_1	A_2	A_3
Dry Air	80-1000	0.6325e-5	245.4	12.0	—
Water Vapor	200-800	1.097e-5	0.934e9	1.5466e-5	1737.3

–Moist Air Mixture

Density. The most air is considered as a perfect gas mixture that accomplish adding pressures law,

$$M_{mix} = y_aM_a + y_vM_v, \qquad \rho_{mix} = \frac{p}{TR/M_{mix}}$$

where y is mole fraction, M is molar mass and R is gas constant.

Heat capacity. Same as density calculation, the moist air is also assumed as an ideal mixture of dry air and water vapor

$$cp_{mix} = x_acp_a + x_vcp_v \tag{A.8}$$

where x is mass fraction.

Dynamic viscosity. The expression of Studnikov are recommended in NASA report [6] and [7] for calculation of the mixture property.

$$\mu_{mix} = (y_a\mu_a + y_v\mu_v) * (1 + (y_v - y_v^2)/2.75) \tag{A.9}$$

Thermal conductivity. The same formula is used to calculate the mixture thermal conductivity

$$\lambda_{mix} = (y_a\lambda_a + y_v\lambda_v) * (1 + (y_v - y_v^2)/2.75) \tag{A.10}$$

Mass diffusivity. A polynomial formula based on ASHRAE[NASA1993] data is used to calculate the mass diffusivity into air. It is only valid for 1atm. The pressure fluctuation in the computations is assumed negligible and the formulation is only a function of temperature of the mixture.

$$D_{av} = A_0 + A_1T + A_2T^2 + A_3T^3 + A_4T^4 + A_5T^5 \tag{A.11}$$

Table A.3: Coefficients of the polynomial expression for heat capacity

	T Range (K)	A_0	A_1	A_2	A_3	A_4
Dry Air-Eckert	200-400	8.85804e+02	1.83710e+00	-1.01113e-02	2.35326e-05	-1.93327e-08
Dry Air-Rohenow	150-1000	0.10341e4	-0.28489e0	0.78168e-3	-0.49708e-6	0.107702e-9
Water Vapor-CRC	200-800	33.80	-0.00795	2.8228e-5	-1.3115e-8	—

Table A.4: Coefficients of the polynomial expression for mass diffusivity

T Range (K)	A_0	A_1	A_2	A_3	A_4	A_5
200-530	-6.20070e-6	8.23209e-8	-7.30863e-12	4.87099e-13	-7.41271e-16	4.39276e-19

References

[1] Ernst Rudolf Georg Eckert and Robert M Drake Jr. Analysis of heat and mass transfer. 1987.

[2] Warren M Rohsenow, James P Hartnett, and Young I Cho. *Handbook of heat transfer*, volume 1. 1997.

[3] David R Lide and Henry V Kehiaian. *CRC handbook of thermophysical and thermochemical data*, volume 1. CRC Press, 1994.

[4] Joseph Hilsenrath, Harold J Hoge, Charles W Beckett, JF Masi, WS Benedict, RL Nuttall, L Fano, YS Touloukian, and HW Woolley. *Tables of thermodynamic and transport properties of air, argon, carbon dioxide, carbon monoxide, hydrogen, nitrogen, oxygen, and steam.* Pergamon Press New York, 1960.

[5] ASHRAE Handbook. Fundamentals. *American Society of Heating, Refrigerating and Air Conditioning Engineers, Atlanta*, 111, 2001.

[6] T.E.Fessler. *Wetair - a computer code for calculating thermodynamic and transport properties of air water mixtures.* Tech.Report, NASA, 1979.

[7] D.R.Richards and L.W.Florschuetz. *Forced convection heat transfer to air/water vapor mixtures.* Tech.Report 3769, NASA, 1984.

Appendix B

Numerical Procedure

B.1 Numerical Procedure

Numerical results are carried out by using the CFD&HT code–Termofluids [1] which is an intrinsic 3D parallel CFD object-oriented code applied to unstructured/structured meshes, which can handle the thermal and fluid dynamic problems in complex geometries. The governing equations were discretized on a collocated mesh in Cartesian coordinates. The numerical integration was performed by a finite volume method.

In problems with very Low Mach numbers and where acoustic phenomena are not of interest, the common strategy is to use a variant of the Predictor-Corrector scheme shown by Najm et al. [2].The pressure-velocity coupling is solved by a fractional step as described by Nicoud [3] where a constant coefficient Poisson results. In the Predictor step a second-order Adams-Bashforth time integration scheme is used to calculate the intermediate scalar fields and the velocity and it incorporates a pressure correction step to satisfy the continuity equation. The Corrector step uses a Crank-Nicolson integration to advance the scalar fields, and it also involves a pressure correction step. The specific algorithm scheme is as follows

B.1.1 Predictor

- Assume an initial estimated temperature, enthalpy and velocity field and evaluate scalar transport equation(energy or moisture) to obtain the predictor temperature(enthalpy) T^* and mass fraction C^*. Scalar transport terms discretization involves a second order backward difference scheme for the temporal term, and an Adams-Bashforth for the other terms.

$$\rho^n \frac{\phi^* - \phi^n}{\Delta t} = \frac{3}{2}(\rho^n \frac{\partial \phi}{\partial t}|^n) - \frac{1}{2}(\rho^{n-1} \frac{\partial \phi}{\partial t}|^{n-1}) \tag{B.1}$$

- Evaluate the density ρ^* through the equation of state based on temperature T^* and thermodynamical pressure P_0

- Solve the Poisson equation to obtain the pressure field

$$\nabla^2 p^* = \frac{1}{\Delta t}[\nabla \cdot (\rho^* \hat{u}) - \nabla \cdot (\rho^* u^*)] \tag{B.2}$$

where the pseudo velocities is

$$\frac{\rho^* \hat{u} - \rho^n u^n}{\Delta t} = \frac{3}{2}(\rho^n \frac{\partial u}{\partial t}|^n) - \frac{1}{2}(\rho^{n-1} \frac{\partial u}{\partial t}|^{n-1}) \tag{B.3}$$

$$\nabla \cdot (\rho^* u^*) = -\frac{\partial \rho}{\partial t}|^* \tag{B.4}$$

The time derivative of density is approximated by

$$\frac{\partial \rho}{\partial t}|^* = \frac{1}{2\Delta t}(3\rho^* - 4\rho^n + \rho^{n-1}) \tag{B.5}$$

- Based on the obtained the predictor pressure, the first estimated predictor velocity field is calculated

$$\frac{\rho^* u^* - \rho^* \hat{u}}{\Delta t} = -\frac{\partial p^*}{\partial x} \tag{B.6}$$

With the above values computed a Predictor step ϕ^*, ρ^*, p^*, u^*, the fluid property fields are updated by means of state equation. The time derivative of the predictor scalar $\rho^* \frac{\partial \phi}{\partial t}|^{**}$ are calculated using the energy or moisture equation.

B.1.2 Corrector

- The time derivative of the scalar field h and c at the next time is evaluated using a Crank-Nicolson scheme

$$\rho^n \frac{\phi^{n+1} - \phi^n}{\Delta t} = \frac{1}{2}(\rho^n \frac{\partial \phi}{\partial t}|^n) - \rho^* \frac{\partial \phi}{\partial t}|^{**}) \tag{B.7}$$

- Evaluate the density ρ^* at the next time step through the equation of state based on temperature T^{n+1} and thermodynamical pressure P_0

- Solve the Poisson equation

$$\nabla^2 p^{n+1} = \frac{1}{\Delta t}[\nabla \cdot (\rho^{n+1} u^{'}) - \nabla \cdot (\rho^{n+1} u^{n+1})] \tag{B.8}$$

where the pseudo velocities is

$$\frac{\rho^{n+1} u^{'} - \rho^n u^n}{\Delta t} = \frac{3}{2}(\rho^n \frac{\partial u}{\partial t}|^n) - \frac{1}{2}(\rho^{n-1} \frac{\partial u}{\partial t}|^{n-1}) \tag{B.9}$$

$$\nabla \cdot (\rho^{n+1} u^{n+1}) = -\frac{\partial \rho}{\partial t}|^{n+1} \tag{B.10}$$

The time derivative of density is approximated by

$$\frac{\partial \rho}{\partial t}|^{n+1} = \frac{1}{2\Delta t}(3\rho^{n+1} - 4\rho^{n} + \rho^{n-1}) \tag{B.11}$$

- Based on the obtained the predictor pressure, the velocities at the next time step is calculated

$$\frac{\rho^{n+1} u^{n+1} - \rho^{n+1} u^{'}}{\Delta t} = -\frac{\partial p^{n+1}}{\partial x} \tag{B.12}$$

Due to the use of a dual stepping the computational cost per iteration is increased, as a Poisson equation has to be solved in each sub-step. On the other hand the Courant-Friedrich-Lewy like condition for the time step can be relaxed, allowing to increase the time step. Tests where the time step was multiplied by a factor showed it was feasible. It has been seen that multipliers higher than ten were not stable.

The collocated discretization is employed in the paper. The computation of the convective term requires that the mass fluxes at the control volume faces and the cell centred velocity be corrected in order to conserve the kinetic energy. The reason of these corrections is that the solution variables of the problem are located at the centre of the control volume while the mass fluxes are interpolated at the faces. The pressure field obtained through the resolution of the Poisson equation ensures mass conservation at the faces, but to assure that the cell centred velocity remains solenoidal a pressure is necessary.

Convective terms of the scalars equations have been discretized using the Upwind differencing scheme. Diffusive terms of all the equations are discretized using a second central difference scheme(CDS). The convective terms of the momentum equations are discretized using second order Symmetry Preserving scheme [4]. With the scheme, the unstructured spatial discretization schemes are conservative, that is, they preserve the kinetic energy equation, and doing so, it is possible to assure good stability properties even at high Reynolds numbers with coarse meshes.

References

[1] O. [et al.] Lehmkuhl. Termofluids: A new parallel unstructured cfd code for the simulation of turbulent industrial problems on low cost pc cluster. In *Proceedings of the Parallel CFD 2007 Conference*, pages 1–8, Ismail H. Tuncer, 2007.

[2] Habib N. Najm, Peter S. Wyckoff, and Omar M. Knio. A semi-implicit numerical scheme for reacting flow: I. stiff chemistry. *Journal of Computational Physics*, 143(2):381 – 402, 1998.

[3] F. Nicoud. Conservative high-order finite-difference schemes for low-mach number flows. *Journal of Computational Physics*, 158(1):71 – 97, 2000.

[4] RWCP Verstappen and AEP Veldman. Symmetry-preserving discretization of turbulent flow. *Journal of Computational Physics*, 187(1):343–368, 2003.

Appendix C

The application of mixture model in complex geometry

The part contents of this chapter have been published as:
Xiaofei Hou, Rigola Joaquim, Lehmkuhl Oriol, Oliet Carles and Pérez-Segarra Carlos D. Numerical modeling of simultaneous heat and moisture transfer under complex geometry for refrigeration purposes. *Journal of Physics: Conference Series*, Vol. 395, No.1, 2012

C.1 Problem description

As an application of mixture evaporation model, simultaneous heat and mass transfer process during the moist air flow through a refrigerator is simulated and temperature and humidity distributions are obtained. It is helpful to gain a better insight into heat and moisture transfer in refrigerator.

As an illustrative case of mixture model, an inner refrigerator chamber has been simulated with mixing between two air streams of different temperatures and concentration levels. The complex geometry is actually an inner evaporator chamber of the model refrigerator shown in Fig. C.1(a). The main dimensions are width=0.06m=L, length=7L, height=7L. The inlet parameters are $T_2 = 253.5K, T_1 = 1.1T_2, Re_1 = 3135, Re_2 = 1065, RH_1 = 18.4\%, RH_2 = 5RH_1, m_2 = 2m_1$. The walls except inlet and outlet are solid walls with zero velocity, Neumann boundary condition for temperature and concentration are imposed on them. In the actual application, a certain number of fins are installed inside the chamber. In the present simulation, 9 fins with a length of 3.2L are used to study its influence on mixing of flow. Fins are treated as

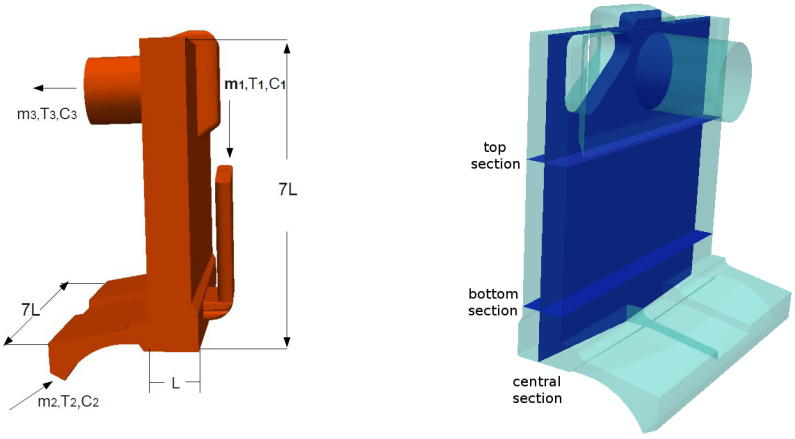

(a) Geometry of inner chamber (b) Cross sections

Figure C.1: Geometry of chamber

solid wall and Neumann boundary conditions are also imposed on them for temperature and concentration parameters. All the simulations were implemented on around one million control volumes.

C.2 Result

Fig. C.2 shows the instantaneous temperature and concentration distributions of central section without fins at statistically steady state. It can be observed that the two inlet fluids mix around the central part of the bottom chamber, then the mixed fluids flow towards the top of the chamber. As they flow upwards, the mixing area is more concentrated as seen in Fig. C.2.

In order to illustrate the mixing process inside the refrigerator chamber without fins, two cross sections perpendicular to y direction are taken (shown in Fig. C.1(b)). Their instantaneous temperature and humidity fields are shown in Fig. C.3. It can be seen from Fig. C.3(a) and C.3(b) that, the fluids from inlet 1 and inlet 2 flow into the chamber and the mixing happens at most parts of the bottom section, instead of all the section area. The fluid from inlet 1 is relatively concentrated on the left wall due to the higher velocity. As the mixed fluids flow upwards, they are mixed further and there is no significant concentration along x direction at top section, which is shown in Fig. C.3(c) and C.3(d). However the mixing area at top section is less than the bottom section. The temperature and moisture are mainly concentrated only on an

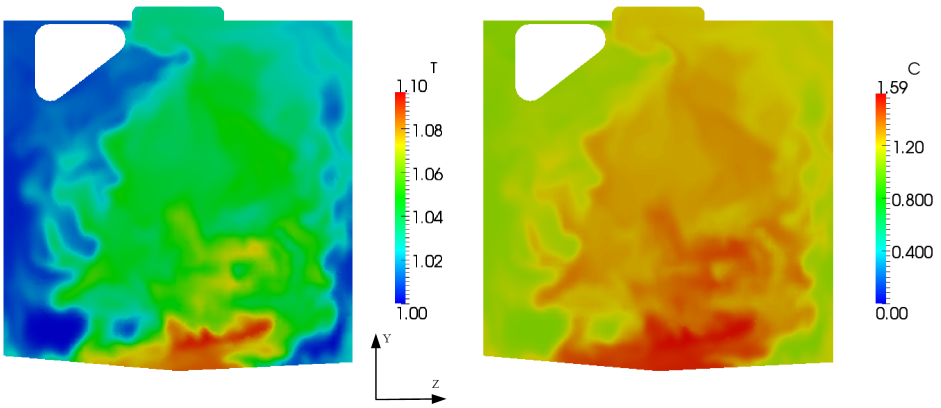

(a) Temperature field (b) Concentration field

Figure C.2: Instantaneous temperature and concentration fields at central cross section without fins

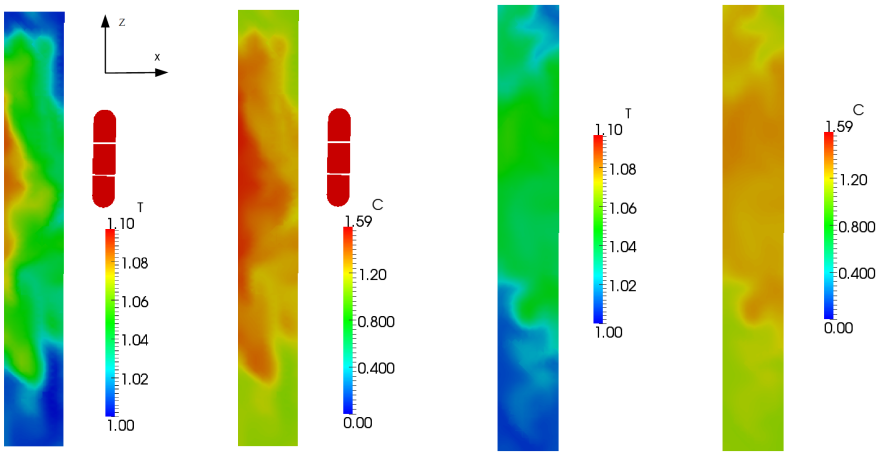

(a) bottom section (b) bottom section (c) top section (d) top section

Figure C.3: Instantaneous temperature and humidity fields at top and bottom cross sections without fins

approximate 65% zone of the section along z direction.

The mixing process with 9 fins is simulated and its influence on the mixing is studied. In the study, 9 fins are uniformly set up in the refrigerator evaporator chamber. Their top edges are located at the same level as the top section while their bottom edges are slightly lower than the bottom section (0.1L) (See Fig. C.1(b)). It can be seen from Fig. C.4 that fins avoid the mixing to continue in spanwise direction (z). Therefore compared to Fig. C.2, maldistribution between channels is found, with great impact on both heat and mass transfer in the real application.

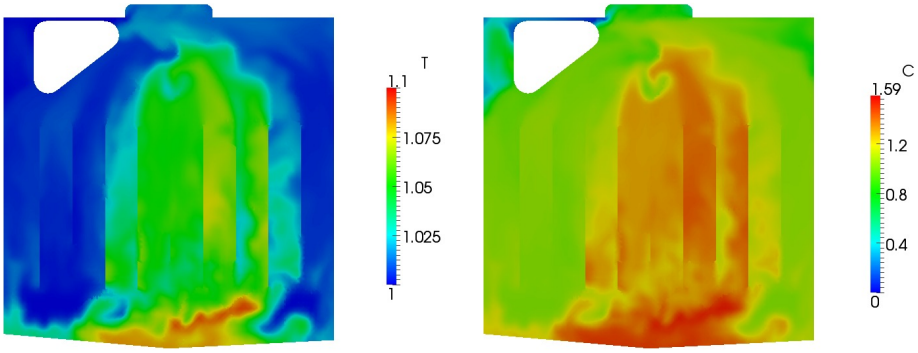

(a) Temperature field (b) Concentration field

Figure C.4: Instantaneous temperature and concentration fields at central cross section

The instantaneous temperature and humidity fields at the top and bottom sections with 9 fins are given in Fig. C.5. Compared to the temperature and concentration distributions without fins in Fig. C.3, their difference at the bottom section is not clear while the difference is relatively obvious at the top section. At the top section, the mixing is more concentrated in a small area with only approximate 40% zone of the section. It confirms that with the inclusion of fins, the mixing in z direction is clearly reduced because of flow confinement.

In order to illustrate quantitatively the temperature and concentration difference between without fins and with fins, average profiles at centerline of top section are given in Fig. C.6, which reveals clearly the fin-effect. The temperature and concentration profiles with 9 fins are obviously higher in the zone of 0.25m to 0.4m than without fins. Although the mixing exists within each passage, the fins eliminate the overall z direction mixing from its inlet, therefore the central fins capture the hot/humid flow.

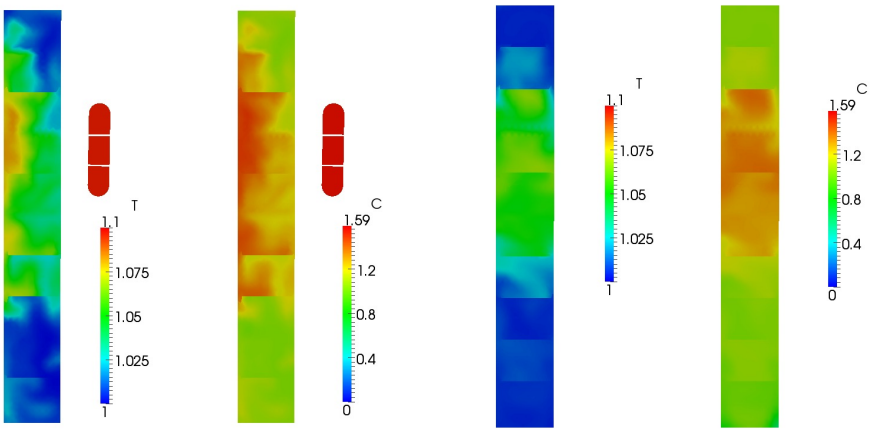

(a) bottom section (b) bottom section (c) top section (d) top section

Figure C.5: Instantaneous temperature and humidity fields at top and bottom cross sections

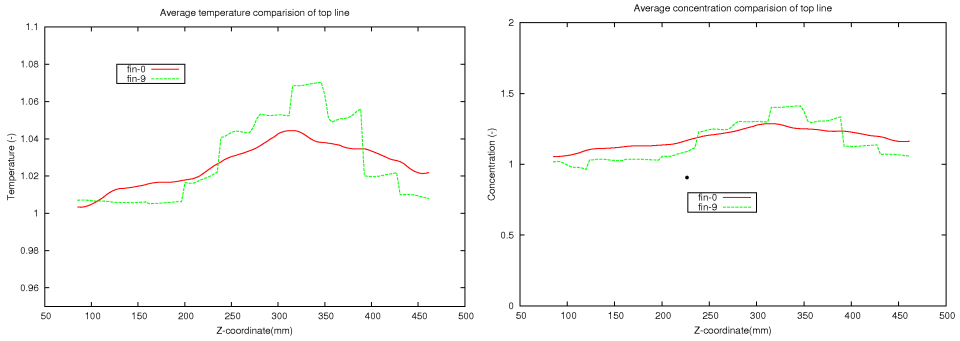

(a) Temperature (b) Concentration

Figure C.6: Average temperature and concentration comparison of top line between with and without fins

C.3 Conclusion

Comparison of different geometrical configurations of the inlet ducts and conditions can be compared in terms of inlet-nonuniformity with the presented methodology. Through the comparison with fins and without fins, maldistribution between

channels is observed and fins deteriorates the mixing process. The results illustrate clearly the mixing process and provide a fundamental basis to optimize the complex geometry configuration for improvement of heat transfer.

List of Publications

This is a list of publications carried out within the framework of the present thesis.

Papers and Articles published

Xiaofei Hou, Joaquim. Rigola, Oriol.Lehmkuhl and Carles.Oliet and Pérez-Segarra Carlos D. Numerical modeling of simultaneous heat and moisture transfer under complex geometry for refrigeration purposes in Journal of Physics: Conference Series, vol.395, no.1, p.012178. IOP Publishing, 2012.

Xiaofei Hou, Joaquim. Rigola, Oriol.Lehmkuhl and Assensi.Oliva. Simulation of the two-fluid model on incompressible flow with Fractional Step method for both resolved and unresolved scale interfaces International Journal of Heat and Fluid Flow, vol.52, p.15-27,2015.

Papers in preparation

Xiaofei Hou et al., Large eddy simulation of spatially-developing transitional flow in a vertical tube with buoyancy effects (Chapter 4). To be submitted: International Journal of Heat and Mass Transfer

Xiaofei Hou et al., Numerical study of heat and mass transfer for turbulent flow in a vertical tube with a falling film (Chapter 5). To be submitted: International Journal of Heat and Mass Transfer